THE IMPACT OF SHALE PRESSURE DIFFUSION ON 4D SEISMIC INTERPRETATION

RICARDO ELIAS RANGEL GONZALEZ

SUBMITTED FOR THE DEGREE OF DOCTOR OF PHILOSOPHY

HERIOT-WATT UNIVERSITY
INSTITUTE OF PETROLEUM ENGINEERING
SCHOOL OF ENERGY, GEOSCIENCE, INFRASTRUCTURE AND SOCIETY

SEPTEMBER 2016

Abstract

Shale typically has a low but non-negligible permeability of the order of nanodarcys (recognized an appreciated in production of unconventional resources), which could affect the magnitude and pattern of the pressure in conventional reservoirs over the lifetime of a producing field. The implications of this phenomenon for reservoir monitoring by 4D seismic can be significant, but depend on the geology of the field, the time-lines for production and recovery, and the timing of the seismic surveys. In this PhD thesis I developed an integrated workflow to assess the process of shale pressure diffusion and its elastic implications in the 4D seismic interpretation of four conventional reservoirs (three North Sea case studies and one from West Africa), with different geological settings (shallow marine and turbidites) and production mechanisms. To accomplish that, first, a detailed petrophysical evaluation was performed to characterize the overburden, intra-reservoir and underburden shales. Next, the simulation models were adjusted to activate the shale-related contributions, and then, applying simulator to seismic workflows, 3D and 4D synthetic seismic modelling were performed, for comparison with the observed seismic data and to establish the impact of the shale pressure diffusion in the elastic dynamic behaviour of the reservoir. This work also includes a case study where evaluation of shale pressure diffusion was integrated with geomechanical simulations to assess the propagation of time shifts and time strain in the overburden of a high pressure/high temperature reservoir under compaction, improving the understanding of the distribution and polarity of the observed seismic time strain.

Fluid flow simulation results of this work indicate that activation of the shale improves the overall reservoir connectivity, enhancing model prediction (production history matched data). The fit to observed 4D seismic data was improved in all the field applications with a noticeable reduction (up to 6%) in the mismatch (hardening and softening signal distribution) for the models with active shales. In reservoirs where the saturation was very sensitive to changes in pressure, shale activation proved to impact strongly on the breakout and distribution of gas liberated from solution. Overall, this work found that inclusion of shale in the 3D and 4D reservoir seismic modelling can provide valuable insights for the interpretation of the reservoir's dynamic behaviour and that, under particular conditions such as strong reservoir compartmentalization, shale pressure diffusion could be a significant process in the interpretation of the 4D seismic signature.

I dedicate this work to my family and to all the little, good and bad coincidences that brought me here.

Acknowledgements

I want to thank my wife Marie-Helene and my kids Rodrigo and Marion for all the patience, love, support and understanding during these years. You are my inspiration, my pride and the source of my energy.

I would like to thank my supervisor, Professor Colin MacBeth for his wonderful technical guidance and unconditional support throughout my PhD project, all my respect and gratitude for him; research is definitely easier when you have an excellent role model close to you. I thank to Dr Asghar Shams for his guidance, friendship, support and the opportunities provided. Also all my gratitude to Dr Maria Mangriotis for her efforts into shape this thesis.

I thank the Edinburgh Time Lapse Project (ETLP) sponsors of Phase V and VI, for their support and for providing the datasets used in my research (BG, BP, Chevron, CGG, ConocoPhillips, ENI, ExxonMobil, Hess, Ikon Science, Landmark, Maersk, Nexen, Norsar, RSI, OMV, Petoro, Petrobras, Shell, Statoil, Suncor, Taqa, TGS and Total). Thanks to Schlumberger for provision of the Petrel and Eclipse software. I thank the Roberto Rocca Education Program for awarding me with their fellowship during 2013 and 2014. I am also grateful to the Society of Exploration Geophysicists (SEG) for awarding me the prestigious SEG/Ian G. Jack scholarship for academic excellence in the Reservoir Geophysics domain in 2014.

My appreciation goes to all my ETLP colleagues for their friendship and the technical discussions, life during these years wouldn't have been the same without Angel Briceno, Dennis Obidegwu, Danil Khakimov, David Yin, Lu Ji, MingYi Wong, Maria Daphne Mangriotis, Niki Obiwulu, Phung Nguyen, Sean Tian, Veronica Omofoma, Ilya Fursov, Hamed Amini, Olarinre Salako, Erik Alvarez, Justin Chong, Romain Chassagne, Mathieu Chamberfort and Juliana Santos.

I want to express my gratitude to my friend Ramon Moreno, for his unconditional support and brotherhood. Also to my Venezuelan friends Honeidy, Carlos, Andres, Humberto, Jorge, Marcos, Rafael, Lidia and Leonardo for making me feel always at home.

I am very grateful to my parents, for the way that they taught me to see and live life, for my brothers and sisters and for their love. I also thank Jose Antonio, Maruja and Pascal Alvarez who opened the door of their home to make me feel truly part of the family.

Ricardo Rangel, September 2016

Declaration Statement

ACADEMIC REGISTRY
Research Thesis Submission

Name*:*	Ricardo Elias Rangel Gonzalez		
School/PGI:	Energy, Geoscience, Infrastructure and Society		
Version: *(i.e. First, Resubmission, Final)*	Final submission	Degree Sought (Award **and** Subject area)	Doctor of Philosophy Reservoir Geophysics

Declaration

In accordance with the appropriate regulations I hereby submit my thesis and I declare that:

1) the thesis embodies the results of my own work and has been composed by myself
2) where appropriate, I have made acknowledgement of the work of others and have made reference to work carried out in collaboration with other persons
3) the thesis is the correct version of the thesis for submission and is the same version as any electronic versions submitted*.
4) my thesis for the award referred to, deposited in the Heriot-Watt University Library, should be made available for loan or photocopying and be available via the Institutional Repository, subject to such conditions as the Librarian may require
5) I understand that as a student of the University I am required to abide by the Regulations of the University and to conform to its discipline.

* *Please note that it is the responsibility of the candidate to ensure that the correct version of the thesis is submitted.*

Signature of Candidate*:*		Date:	

Submission

Submitted By *(name in capitals):*	
Signature of Individual Submitting:	
Date Submitted:	

For Completion in the Student Service Centre (SSC)

Received in the SSC by *(name in capitals):*			
Method of Submission *(Handed in to SSC; posted through internal/external mail):*			
E-thesis Submitted **(mandatory for final theses)**			
Signature:		Date:	

Table of contents

Table of Figures

1 Chapter:

Introduction: Shale Activation and Shale Pressure Diffusion

This chapter discussess the perception of shale in the geophysics comunity and how it relates to reservoir characterization and 4D seismic interpretation. The recognition of heterogeneity and a complex internal achitecture inside shales in conventional reservoirs lays the foundation to consider that this lithology may play an active role in the dynamic reservoir behaviour and its elastic expression recorded in the 4D seismic, in addition to the reservgoir facies (sandstones). The processes and parameters involved in the reservoir-shale interactions are described in this section, together with the workflow developed during my research project for the evaluation of the shale pressure diffusion and its elastic implications in the 4D seismic interpretation.

1.1 Overview

Time lapse seismic monitoring has been a valuable analysis and decision tool since its commercial implementation in the early 1990's [*Lumley*, 2001]. Variations in the reservoir elastic properties recorded in the monitor seismic surveys are linked to changes in pressure and saturation induced by production and injection, providing a useful insight into the reservoir's dynamic behaviour [*Johnston*, 2013]. The interpretation of the 4D seismic signature demands deep knowledge of the reservoir geology that conditions the spatial distribution of facies, properties and connectivity, determining the reservoir's stress sensitivity and its response to the induced production / injection. As changes observed in the 4D seismic response have to be correlated to corresponding variations in rock-fluid properties, the interaction between the components of this system needs to be characterized properly. In this process it is paramount to define the reservoir boundaries, where the criterion of reduction in the fluid flow usually prevails. These boundaries are defined where reservoir conditions such as porosity, permeability and hydrocarbon saturation decrease drastically, limiting the fluid interaction between rock units. As a consequence, the reservoir boundaries usually correspond to sealing faults, fluid contacts and lithology changes linked to permeable-impermeable rock contacts.

The typical intrinsic properties of shale have contributed to this lithology being regarded as an impermeable rock during modelling and simulation, and as such, shale is commonly excluded from the reservoir definition and represented as inactive cells. This assumption may be considered valid, as conventional fluid flow through pure shales is almost negligible during the hydrocarbon production time-scale. Classical reservoir characterization treats all shales as pure mudstones (almost 100% clay), whereas most intra- and inter-reservoir shales are heterogeneous and anisotropic. It has been shown that shale permeability, even in the order of a few nanodarcys, permits pressure diffusion that impacts production-induced elastic changes in the reservoir, recorded in time–lapse seismic monitoring [*MacBeth et al.*, 2011; *Ricard et al.*, 2012]. This research project, explore the response of shale pressure diffusion in different reservoir and geological scenarios, selected as representative of the clastic conventional reservoirs under time-lapse surveillance, using a broader (pressure dependent) reservoir definition where the boundaries include overburden, underburden, sideburden, intra- and inter-reservoir shales, all characterized and recognized as heterogeneous, with lateral and vertical variability in their static (porosity, net-to-gross) and dynamic (permeability, transmissivity, pore pressure) properties: parameters which are included in the reservoir

modelling and simulation processes for saturation and pressure prediction. This research includes four field case studies: Heidrun (Jurassic shallow marine), Girassol (Oligocene turbidite), Schiehallion (Palaeocene turbidite) and Shearwater (Jurassic high pressure/high temperature shallow marine) fields and the application of a workflow for shale activation in conventional clastic reservoirs to analyse the impact of pressure diffusion in processes such as reservoir connectivity, gas exsolution and strain propagation in the overburden, and their correspondent implications in the 4D seismic signature and interpretation (Figure 1-1).

The different sedimentological environments, structures, geological settings, reservoir types, and depletion and production mechanisms of the field applications involve the activation and modelling of a large variety of shales, with different static and dynamic properties, thickness, internal architecture, degrees of heterogeneity and sand-shale geometry. Case by case, these parameters determine the magnitude and extent of pressure diffusion into the shale and the contribution of this process in the overall dynamic and elastic behaviour of the reservoir. In order to analyse the contribution of active shale, the predicted pressure and saturation from the numerical simulations of the modelled scenarios were used to build synthetic seismic volumes and compute 4D differences. The comparison of the predicted to the observed 4D seismic shows the validity of the assumption of pressure diffusion being an active process in the reservoir time lapse behaviour. In general, the match between observed and predicted seismic volumes is better when shales are included in the reservoir modelling. In terms of 4D differences, in some cases shales do not have a major impact on the elastic signature of the induced reservoir changes, whereas in others only shale activation can explain the distribution of the hardening and softening signal, as pressure diffusion through shale better explains the reservoir connectivity.

This thesis is structured in 7 chapters, the initial contains a general introduction to the topic and some concepts of shale activation; the chapter 2 consist of the description of the applied methodology for the characterization of shale and the modelling of its static and dynamic properties; chapters 3, 4, 5 and 6 corresponds to field applications (Heidrun, Girassol, Schiehallion and Shearwater fields), each one was written as an independent case study containing from shale characterization and activation to numerical simulations, synthetic seismic modelling and 4D seismic interpretation; finally, chapter 7 corresponds to the conclusions and recommendations of this work.

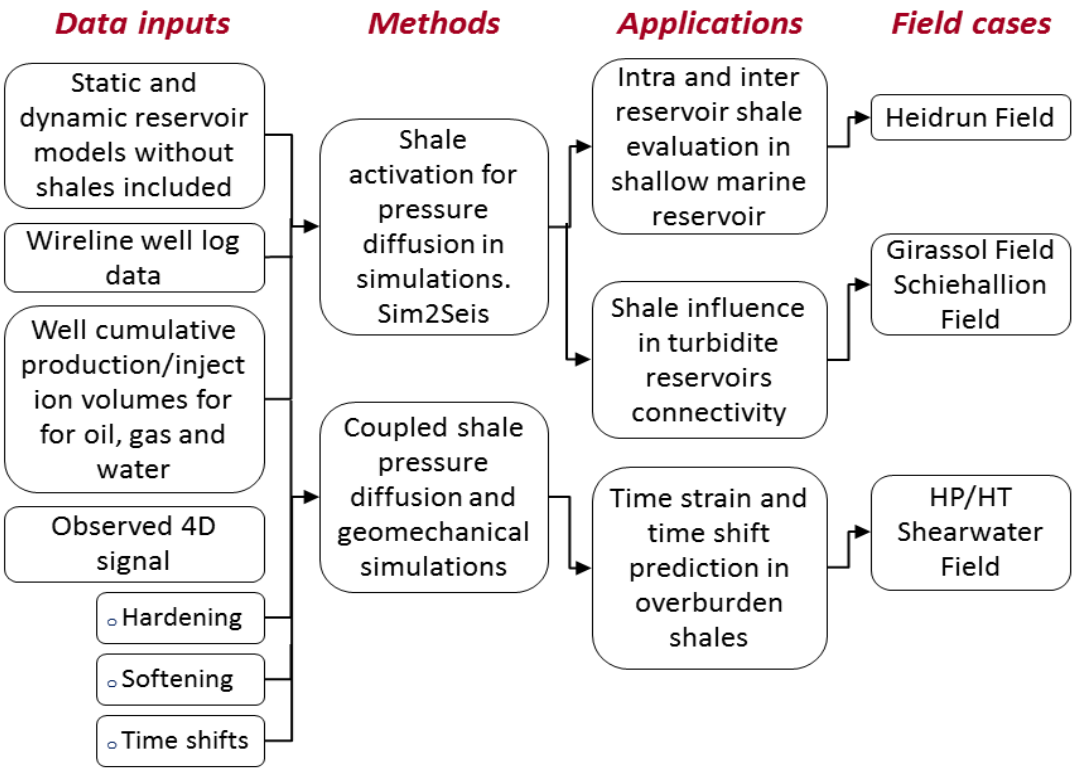

Figure 1-1 *Diagram of the thesis workflow showing data input, methods, applications and field cases*

1.2 The geology of 4D fields

The 4D seismic can be used for monitoring the reservoir dynamic behaviour in any type of geological environment; however, certain conditions determine the scope of its use. The key is the reservoir's stress sensitivity (changes in density, P-wave and S-wave velocities), which relies on three parameters: the rock frame stress sensitivity, pore pressure, and saturation [*MacBeth*, 2004], and specifically, on the evolution of these three parameters during production. As a consequence of the production mechanism applied to the reservoir, the effective stress transmission and the overall reservoir elastic properties are changed, resulting in differences that may be captured in the time lapse seismic. The rock frame stress sensitivity is intrinsically related to rock composition and the relationships between its components (geometry, sorting, packing, contacts and porosity), which are determined by the sediment source, transport, deposition environment (sedimentological context) and burial history (compaction, cementation and diagenesis). The reservoir saturation and pore pressure depend largely on the burial history and fluid migration, which are linked to the basin's thermal and tectonic evolution. Induced changes in the reservoir pore pressure and saturation are responsible for the majority of the 4D signal recorded during the seismic monitoring, with variations in these two

parameters resulting in changes in the elastic properties of the pore space that supports a very important fraction of the reservoir's stress field.

The seismic records are a reflection of the elastic contrast between different media. When the properties of the pore space in a specific area or layer are changed, the contrast between the elastic properties (density, P-wave and S-wave velocity) of that interval and the adjacent media changes as well, modifying the seismic response and consequently the seismic attributes (amplitude and frequency) corresponding to the contrast interface. If the pore space increases its elastic moduli (such as in the case of a denser fluid replacing a lighter one, or an increase of pressure making the fluid's particles tighter), the interval becomes "faster" or "harder". If the elastic moduli from the pore space decreases (such as in the case of a lighter fluid replacing a denser one or in the case that pressure is decreasing), the interval becomes "slower" or "softer" (compared with its previous contrast with the adjacent media). The polarity of the 4D seismic signal depends on the specific seismic attribute used to highlight the seismic character of the reservoir in a defined TWT (two-way time) interval. The computation of the 4D differences consists of the subtraction of a specific amplitude attribute of the monitor survey from the one extracted from the base seismic survey. As an example, the computed 4D differences calculated using RMS (root mean square) amplitude show negative values for hardening as the contrast of the reservoir with the surrounding non-reservoir layers decreases (the respective amplitude decreases too) for the monitor survey and thus its subtraction from the base, where the contrast and reflection amplitude are higher, results in negative values. In the opposite way, softening using RMS amplitude has a positive polarity.

If production / injection induces changes in the rock frame (also known as matrix), the reservoir, overburden and underburden intervals may experience geomechanical effects. This happens when variations in pore pressure and saturation produce weakening of the rock matrix structure, affecting the transmission of the effective stress, causing compaction or expansion. This effect may not only change the elastic moduli and seismic attributes corresponding to the interval, but may also change the vertical position of the geological events, producing "time shifts" between the monitor and base, as a result of velocity change and interface position change. Time shifts can be positive or negative, depending on whether the reflection corresponding to an event is recorded in the monitor survey some milliseconds after or before (below or above) its original TWT position in the base seismic survey. Time shifts are measured in seismic traces that involve interference between interface reflections. As a result, they not only reflect kinematic

changes of the medium (velocity variations), but also considers spatial changes in the position of the interface, changes in the contrast (reflectivity) between the interfaces and lastly changes in the interference between reflection events.

The distribution of hardening, softening and time shifts in seismic volumes has proved to be, in the three last decades, an excellent indicator of reservoir connectivity and compartmentalization, contact fluid movement, bypassed oil, injection efficiency and reservoir compaction, to name few examples. In short, amplitude, time shifts and more generally 4D seismic attributes capture almost fully the reservoir dynamic behaviour. As different processes can cause the same type of 4D signal (equal polarity), separating the effect of changes in pore pressure, saturation and rock frame in the 4D signal is sometimes not straightforward. Frequently, the 4D signal is the combined response of all of these parameters, and only knowledge of the reservoir's sensitivity to each variable may help in the right interpretation. Time lapse seismic monitoring brings added interpretation value when the combination of geological factors generates a pronounced stress sensitivity. Also the 4D seismic response depends on the type of mechanism applied to support production and how the reservoir stress sensitivity responds to it, creating substantial and measurable variations in the elastic properties. Finally, the timing of the monitors' acquisition related to the specific stage of the field development is very important [*Calvert*, 2005; *Johnston*, 2013], as the spatial distribution of the induced changes varies with time and may mask the effect of a previous elastic change in the reservoir. The signal related to those changes should be above seismic noise and the effect of attenuation [*Kragh and Christie*, 2002]. The interpretation of the 4D seismic response only can be considered valid after a rigorous analysis of repeatability, as similar geometry and positioning between compared seismic volumes has to be ensured, as well as another acquisition parameters such as energy source, weather and environmental conditions. Also is important that both seismic volumes share the same processing routine as many parameters can create differences between the surveys and bias the reservoir related time lapse signature.

For the abovementioned reasons, in the early applications of 4D seismic, the reservoir candidates for time lapse monitoring had to fulfil most of the following characteristics: large remaining reserves (to justify the seismic acquisition and processing costs); recovery factors below the ones initially predicted; high porosity and permeability (to be sure that the pore space elastic changes were easy to record); production supported by the injection of a fluid with elastic properties different from those of the hydrocarbon in place

(to ensure that the contact between fluids was mappable, due its elastic contrast); early water cuts; reservoir pressure very close to bubble point (to identify gas coming out of solution), and finally, reservoirs with rigorous feasibility study to establish a good repeatability in the acquisition of the monitor survey. Today with the proven success of 4D [*Landrø et al.*, 1999; *Lumley*, 2001; 2004; *Calvert*, 2005; *Johnston*, 2013] in a wide range of applications worldwide (Figure 1-2) and with the advancement of techniques for seismic acquisition and processing, some reservoirs have permanent seismic monitoring, even from early stages of development, to test in real time the effectiveness of a production technique before it has been applied in the whole field.

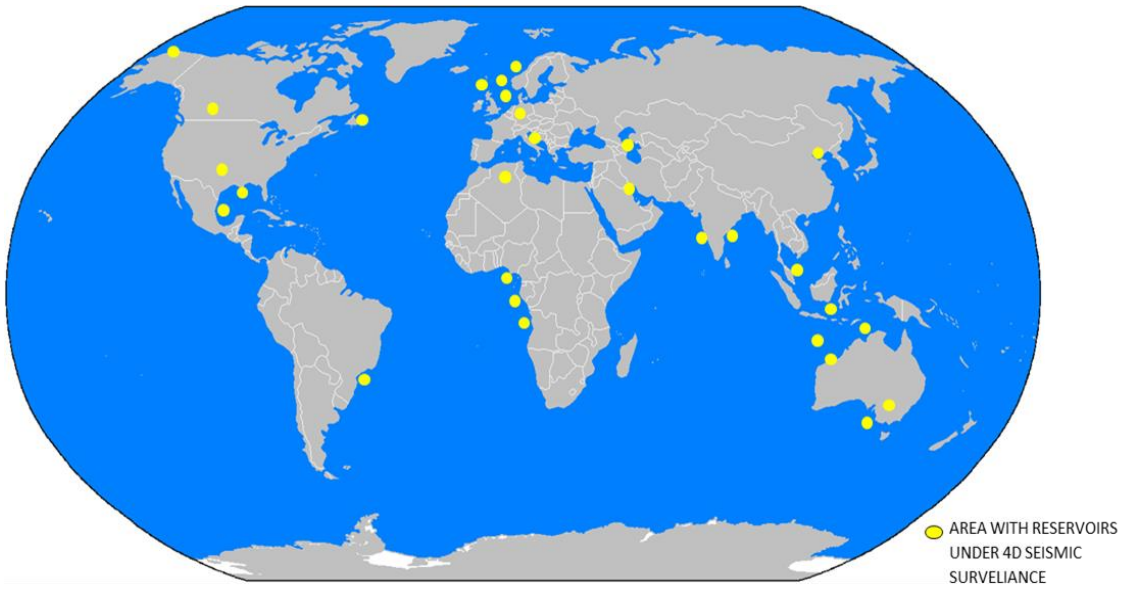

Figure 1-2 *Distribution of fields under 4D seismic monitoring according to the elaborated database in the Appendix A (until 2014).*

In order to have a better perspective of the uses of 4D seismic in specific geological scenarios, was created a field database that comprises 146 conventional reservoirs around the world with seismic time lapse monitoring (Appendix A). This database was backed up by the Edinburgh Time Lapse Project (ETLP) field's database (12 4D fields) and with the results of an extensive literature review, including papers, web pages and reports of oil companies, news and bibliography. In this compendium some statistics are obvious, such as the predominance of offshore 4D reservoirs over onshore. There are several reasons behind this, the main is related to seismic acquisition: offshore conditions imply

the presence of an upper layer of water (the effect of salinity, temperature, currents and wave energy has to be taken into account during the elastic modelling of this layer), that favours wave energy transmission and signal processing, allowing the recovery of a wider range of frequency and therefore better seismic quality and resolution. Offshore acquisition also has lower seismic noise, which increases survey repeatability, and the cost of acquisition is much cheaper than onshore [*Vermeer*, 2003]. Permanent seismic monitoring is more reliable and requires less maintenance when installed in the seafloor (Ocean Bottom Nodes and Ocean Bottom Cables). Moreover, for the case of Tertiary reservoirs, offshore fields are better positioned regarding active petroleum systems. In addition, the 4D seismic technology was developed by companies that are major operators in offshore basins such as the North Sea and Gulf of Mexico, where the number of 4D seismic surveys is obviously higher than anywhere else.

As previously mentioned, for the case of offshore reservoirs, the presence of free water over the reservoir constitutes an advantage for seismic quality, resolution and signal processing. If the overburden (sediment column over the reservoir) favours wave energy transmission and has a monotonous lithology, the contrast with the top reservoir (that has different saturation and therefore different elastic properties) will be higher and better illuminated. Highly reflective intervals or strong elastic contrasts in the overburden transmit only a small amount of wave energy beneath, making difficult the acquisition of good quality seismic in the reservoir and certainly limiting the interpretation and use of attributes. This is the case of salt, a very reflective lithology, that under active tectonic regimes intrudes easily (due to its plasticity and mobility) into adjacent sediments, creating pinch-outs and excellent lateral and vertical permeability barriers (diapirism), which although they are ideal elements for hydrocarbon traps, result in very low-quality seismic imaging beneath them. It is just recently, with the application of new techniques such as wide azimuth seismic acquisition, that pre-salt events are now recorded with better quality and resolution, allowing the development of pre-salt reservoirs (i.e. Campos Basin in Brazil) and their time-lapse monitoring.

Regarding sedimentary environments, shallow marine and turbidite constitute by far the most common 4D reservoirs (Table 1-1), and it is easy to understand why: both have sandy facies deposited during high energy regimes, the sediments are reworked (by waves and tides in the case of shallow marine, and by turbidite flows in turbidites) which enhance sand sorting and packing, favouring high primary porosity development and good pore connectivity, which are linked to high stress sensibility. The reservoir

configuration is essentially stratigraphic for turbidites, and usually mixed (structural and stratigraphic) for shallow marine. In addition, for turbidites and shallow marine environments, may be interbedded in active source hydrocarbon kitchens, with migration pathways. At the same time, the elastic contrast between reservoir and surrounding rocks is excellent, with higher lateral contrast variability for turbidites (between the reservoir's sands and pelagic shales), while the shallow marine reservoirs have more vertical contrast variability, due their geographic position that makes them more sensitive to eustatic changes (the contrast between the reservoir's sands and episodic transgressional shales).

Geology of the Reservoirs	# of 4D fields
Turbidites	53
Fluvio - Deltaic	43
Shallow marine	32
Carbonate shelf	16
Aeolian	2

Table 1-1 *Typical geological environments of the reservoirs under 4D seismic monitoring statistics according to the Appendix A fields database*

Shallow marine environments are very common during the development of rift systems, following the breaking up of the super continent Pangea during Triassic–Jurassic (under a divergent plate tectonic regime). In these high energy tectonic settings, shallow marine environments rich in sands were developed, with the continuous tectonic expansion favouring the generation of marine conditions which, combined with a global transgression event during the Cretaceous, created an organic rich carbonatic and pelagic sequence overlapping the Triassic–Jurassic shallow marine sequence. The transgressive Cretaceous sediments constitute the most prolific source rock of hydrocarbon in the entire geological record and their assemblage with the underlying sand-rich shallow marine deposits constitutes the petroleum system par excellence in many basins around the world. Turbidite deposition occurs with relative frequency in passive margins that have short platforms in front of fluvial systems with important sedimentary load, but their configuration as hydrocarbon reservoirs is more common for Palaeocene and younger sediments. There are also 4D seismic monitoring applications in chalk reservoirs (bioclastic limestone composed almost entirely of coccoliths), this carbonate lithology has a high stress sensitivity due to weakening of the rock frame as a consequence of chemical interaction of the matrix mineral with the injected fluids to support pressure

maintenance and affective fluid sweep. Rock frame weakening in these reservoirs leads to compaction and successive strain propagation in the overburden, processes that in 4D seismic monitoring are evidenced as time shifts. The distribution and polarity of the time shifts are paramount to understanding the geomechanical behaviour of the reservoir, and only after the removal of the time shift signal, can pressure and saturation driven changes in the 4D seismic be interpreted.

There is a historic reason for the predominance of shallow marine and turbidite reservoirs in 4D seismic applications: these two environments constitute the most common type of reservoirs in the North Sea (shallow marine Jurassic sediments of the Brent Group and Tertiary turbidites of the Forties Group and Lista Formation) and the Gulf of Mexico (Palaeocene to Miocene turbidites), which are the basins where the major oil companies that developed the 4D seismic technique operate. This work pays special attention to describing the role of shales in shallow marine and turbidite reservoirs, because all the field applications (the four study cases) of the workflow developed in this research were applied to these types of reservoirs. From the twelve 4D fields of the ETLP database (4 shallow marine, 5 turbidite and 3 chalk reservoirs, included in the Appendix A) were selected four fields as case studies: the Heidrun Field due to its sand-shale 'layer cake' stratigraphy and fault tilted block configuration, typical in many Jurassic shallow marine reservoirs of the North Sea, this configuration involve high degree of compartmentalization and sand-shale pressure imbalance; the second reservoir selected was the Girassol Field, an unconsolidated Oligocene turbidite reservoir in the West Africa Slope with coalescent channels and plenty of reservoir-shale lateral contacts, scenario to study sideburden pressure diffusion into shales; the third option was the Schiehallion Field, a Palaeocene turbidite reservoir with a complicated facies connectivity and a complex distribution of gas exsolution, ideal to test the influence the effect of shale pressure diffusion in reservoirs with a narrow window between the field's pressure and the bubble point; finally the last application consisted in the high pressure / high temperature Shearwater Field, a Jurassic shallow marine condensate reservoir under compaction, appropriate scenario to study the effect of pressure diffusion in the propagation of strain in a shaley overburden.

1.3 Shale in conventional reservoir modelling and characterization

With the conventional reservoir definition usually linked to hydrocarbon fluid flow, it is easy to understand that shales have historically been used as boundaries, as their intrinsic properties (very low permeability and extremely high capillary forces) forbid considerable fluid flow through this lithology during the reservoir production lifetime (from a few years to a couple of decades). To save computing time and avoid complications with the modelling and upscaling of shale properties, classical reservoir modelling regards shales as inactive cells, only considering them as part of the models when evaluation of the reservoir seal integrity is included in the numerical simulations and geomechanical analysis. In most models, cells corresponding to intra- or inter-reservoir shales are represented as inactive, using switch-off tools as multipliers (e.g. ACTNUM in the Eclipse software), or just as cells without any static and dynamic properties assigned.

Shale characterization and modelling is, in itself, more complicated than the equivalent process for sands, with the larger variety of mineral components making impossible the use of most equations, tables and empirical functions widely applied for sands [*Wu and Aguilera*, 2013]. With composition, porosity and permeability not directly determined from wireline log data, shale characterization necessarily involves a complex analysis at large scale, sometimes at basin level, but also at smaller scales, below the petrologic and petrographic level, as the size of the shale components, their disposition and diagenetic architecture are only visible under the application of advanced optical techniques capable of high focus and magnification. In conventional reservoirs, shales usually are not included as target during core acquisition operations, and in those cases where are acquired (thin intra-reservoir shales), the recovery of shale samples is usually poor due to damage during the coring process, which makes difficult and not representative the recreation of shale sample original conditions in the laboratory (known as loading). Moreover, the pressures needed to perform classical porosity and permeability tests are very high, only available in very specialized facilities, besides which, the test duration can last several days, increasing the cost of the analysis per sample. In short, reliable laboratory data for shale properties usually comes from shale research groups in institutes and universities dedicated to the study of shale seal integrity in nuclear waste disposal or CO_2 storage, or from companies involved in shale gas unconventional projects, where the shale pore space constitutes the main reservoir. For this reason, it is common that the database of a conventional reservoir has very poor information about the characterization

of shales, with the exception of fields where the presence of overpressured or swelling shales constitutes risk for drilling operations and well stability. However, even in those cases, the characterization of shale barely goes further than a basic composition analysis, as the information is only used in the design of mud drilling properties.

Due to these challenges, the most used methods within the oil industry to estimate shale properties are empirical relationships built from a very limited laboratory database [*Yang and Aplin*, 2007], or through application of correction coefficients and weighting functions to well-known sand-derived equations [*Schön*, 2011; *Pang et al.*, 2013]. However, estimation of properties is just the first step in the task of shale representation in conventional reservoir modelling, as the scale of shale heterogeneity and internal architecture is very small when compared with the scale of the reservoir model grid. The problem arises in the strong anisotropy of the shale properties, making the average and upscaling to the reservoir model grid a real challenge. Lateral variations in shale static and dynamic properties can be considered above the horizontal typical cell dimensions (between 50 and 100 metres). However, vertical variations are in the range of millimetres and centimetres, while minimum layering thickness in reservoir modelling is usually over 1 or 2 metres. Averaging techniques do not completely solve the problem, as the differences between the heterogeneous laminations within a shaly interval (e.g. interbedded shale, silt and very fine sand) in terms of properties can be very large, even different by several orders (permeability case). The upscaling of shale static properties such as NTG and porosity estimated from the well at wireline log sampling scale can be performed with the Backus average [*Backus*, 1962], but for shale dynamic properties such as permeability, the fluctuations in the property value between the different layers are too large and some assumptions, such as weak anisotropy, are no longer valid [*Thomsen*, 1986]. Thus it is clear that the modelling of shale at the reservoir simulation model scale involves large uncertainties, especially for the dynamic properties.

Shales are not entirely excluded from the conventional reservoir models, their presence is actively used as a multiplier (Vshale and NTG fraction values) to constrain the fluid flow and define the reservoir quality. So, for example, when the NTG of a cell is defined as 0.7 that means that a fraction equivalent to 30% of the total volume is inactive, so dispersed or laminar shale within a sandy interval is considered in conventional reservoir modelling as a solid component, without porosity, permeability and saturation. The question of whether the internal heterogeneity (silt laminations) within the intra-sand shales should be taken into account for volumetric and dynamic properties estimation of

the cell is usually ignored. The distribution of the shale, whether dispersed or laminar continuous (stochastic or deterministic) within the sandy intervals, does not have a major impact on the estimation of the static properties, as shale is treated as a clast, a component of the sands. However, for permeability, especially the vertical form, shale distribution can increase pore tortuosity (in the case of dispersed shale) and entail only a decrease in permeability, or it may constitute a fluid flow barrier (laminar and continuous distribution), reducing the vertical permeability of the interval to the range of a few nanodarcys. The importance of shales in the reservoir characterization is also evidenced in the estimation of the effective porosity, which is the product of multiplying NTG by the porosity, which is a parameter widely used for the spatial propagation in the reservoir of the core calibrated poro-perm relationship.

1.4 Shale activation

The principles behind the concept of shale activation in this work are very simple, shale has static and dynamic properties, the population of their correspondent cells (initially inactive and empty) in the simulation model with those properties enables interaction between shale cells and reservoir cells (sandstones) during the numerical simulations. Shales, as with any clastic sedimentary rock, have finite porosity and permeability. It is true that the shale pore space geometry is complicated, the connectivity is poor, the permeability is very low (but finite) and the capillary forces are also very high, nevertheless under the effect of specific gradient conditions, these properties may enable interaction between sections of shale in contact with another porous lithology. To explore one of those particular interactions, mathematically defined as the pressure diffusion, in this research shales were included in the reservoir numerical simulations, to study the impact of this process on the reservoir dynamic behaviour, using the 4D seismic as tool to corroborate the validity of the modelled scenarios. The first step in the process of shale activation is to recognize that the most accepted perception in the oil industry of the characterization of this lithology comes from the petrophysical domain, which regards shale as the end member of the clean sand / shaley sand / sandy shale / shale lithologic spectrum in the clastic reservoir evaluation. With shales often perceived as an inhibitor, and once the effect of this lithology is deemed non-profitable (usually evaluated with very conservative criteria), a “cut off” or base line is established and intervals with higher proportions of shale within them are discarded from the reservoir definition. Usually the

shale base line excludes fine laminated interbedded intervals of shale with silt and fine sands, treating anything above the cut off as a pure mudstone. The petrophysical approach developed in this project for the evaluation of shale heterogeneity (Figure 1-3) considers that the shale base line must be defined in a true pure mudstone, where the clay content is really high, and if possible, in an interval corresponding to a maximum flooding surface (MFS). The difference between the classical shale cut off (which marks the end of the domain of shaly sandstones) and the pure mudstone can be used to define shale heterogeneity, volume of shale and shale NTG, all this keeping unaltered the definition of the opposite lithological end member, the cleanest sand.

The shales activated in the field applications showed in this thesis, consist of laminar and structured shales, also known as deterministic shales [*Haldorsen and Lake*, 1984] disperse shale embedded within sand facies, also known as stochastic shales, were not included in the process of shale activation. As the process of shale activation involves a detailed characterization of shale static and dynamic properties, a complete description of the applied techniques and criteria used to estimate shale properties and to represent them at the simulation model scale is included in Chapter 2 of this thesis. At this point, it is very important to clarify that the modelling of shale properties, specifically with capillary pressures much higher than the induced reservoir depletion, makes the occurrence of fluid flow from and within shale impossible, with only pressure diffusion being the sole dynamic process occurring within shales. Although it is possible that natural and frequent discontinuities such as fractures and bioturbation may constitute preferential permeability paths that can allow fluid flow between shales and the reservoir, the accurate modelling of the occurrence and distribution of such geological features is very complicated in the simulation models.

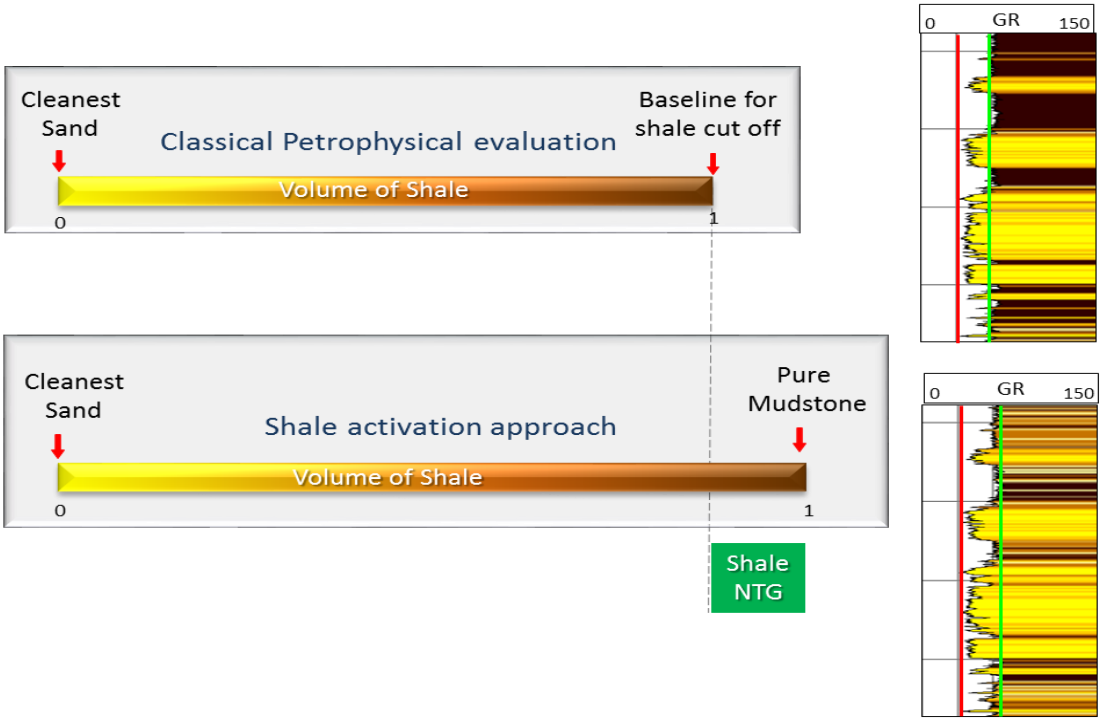

Figure 1-3 *Shale activation approach for shale base line definition; note how the displacement of the shale base line highlights the internal shale heterogeneity and architecture. Criteria for clean sand definition were not changed.*

1.5 Pressure diffusion in shale

Pressure diffusion in shales has been studied widely at various scales when addressing different issues in the oil industry, such as its implications in wellbore stability [*Horsrud et al.*, 1994; *Fam and Dusseault*, 1998; *Simpson and Dearing*, 2000; *Asef and Farrokhrouz*, 2013; *Arain*, 2015;], shale as a transport agent in the reservoir [*Wei et al.*, 2013], and even pressure communication between neighbouring fields through shale [*Da Fontoura et al.*, 2007]. Shale's intrinsic characteristics make fluid flow negligible at the scale of a reservoir's hydrocarbon production lifetime; however, at the geological time scale, fluid flow through shales does occur. Fluid flow is not the only possible interaction between two sections of porous and saturated media, if there is a gradient, thermal, chemical and pressure diffusion also occur. Out of those processes, this project explores pressure diffusion in shale for different scenarios and its implications, using a numerical simulator to predict results and observed 4D seismic to evaluate the validity of the assumptions during the modelling of the shale's properties. But how exactly does pressure diffusion operate in shales? Assuming, for example, a typical clastic reservoir with some interbedded shale layers (Figure 1-4), in pre-production conditions sand and shale are at the same pressure, then, when production starts, the pressure profiles of sands and shales

behave differently. While in sands the depletion is instantaneous, the process of pressure diffusion in shales is much slower, as shale's low permeability limits diffusion.

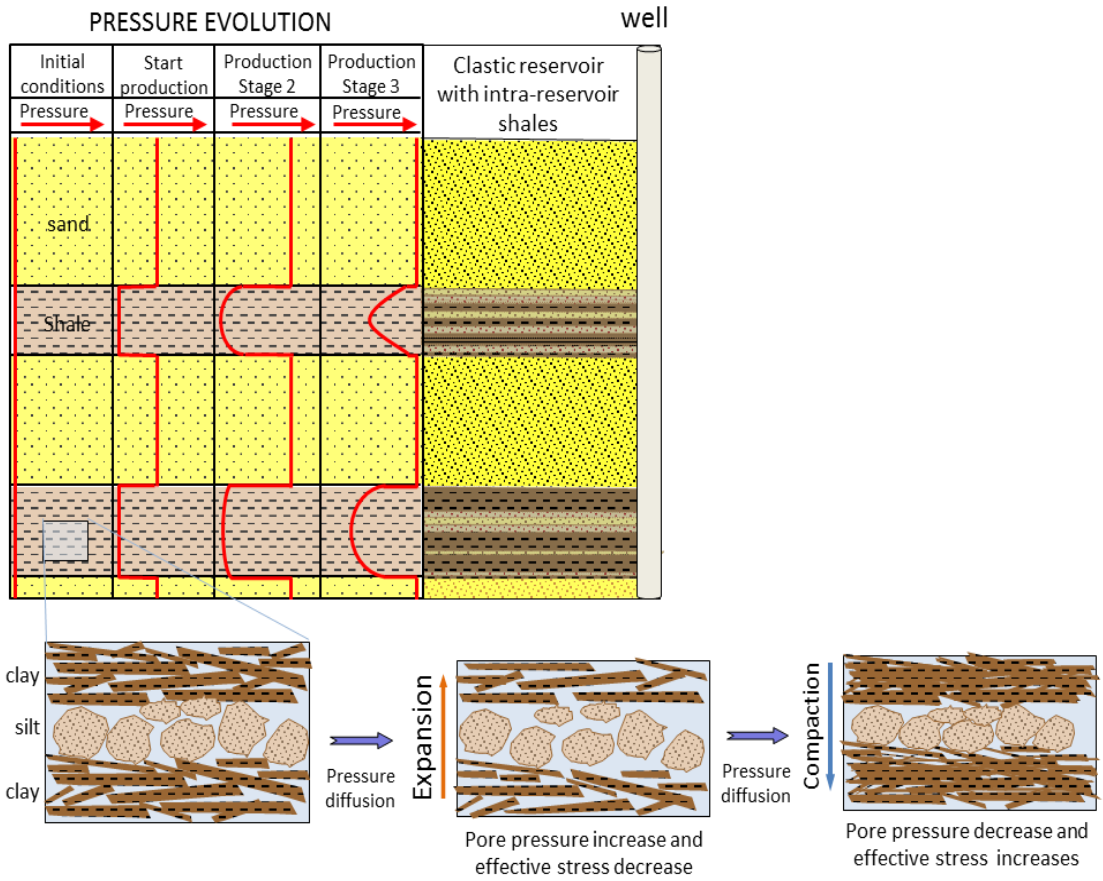

Figure 1-4 *At the top, schematic diagram showing the pressure evolution in a clastic reservoir with two layers of intra-reservoir shales, under the depletion induced by a well producer. At the base, detail of the two phases in shale geomechanical behaviour*

The beginning of pressure diffusion into shales is more linked to the production induced geomechanical effect in sands than to the increasing pressure gradient as a consequence of depletion. Depleted sands compact as a portion of the fluid that supports part of the effective stress in the pore space is extracted and the sand rock frame has to assume the effective stress load, which increases the grain contact surface and reduces sand porosity. Sand compaction causes expansion in the adjacent shale intervals (especially in overlying layers). The expansion process in shales causes a change in the shale pore space geometry, enhancing pore connectivity and permeability, which favours pressure diffusion from the adjacent depleted sand into the shale (Figures 1-4 and 1-5). After this initial extensional regime, the shale starts to compact in a subsequent phase, as a consequence of the effective stress transmission and pressure diffusion, leading to pore pressure decrease and

an increment in the effective stress supported by the shale rock frame. The coupled geomechanical- pressure diffusion process (Figure 1-5) defines a strain path for shales that gradually evolves into compaction, crossing over between an extensional and compactional regime in a period of time considerably longer than that for sand compaction.

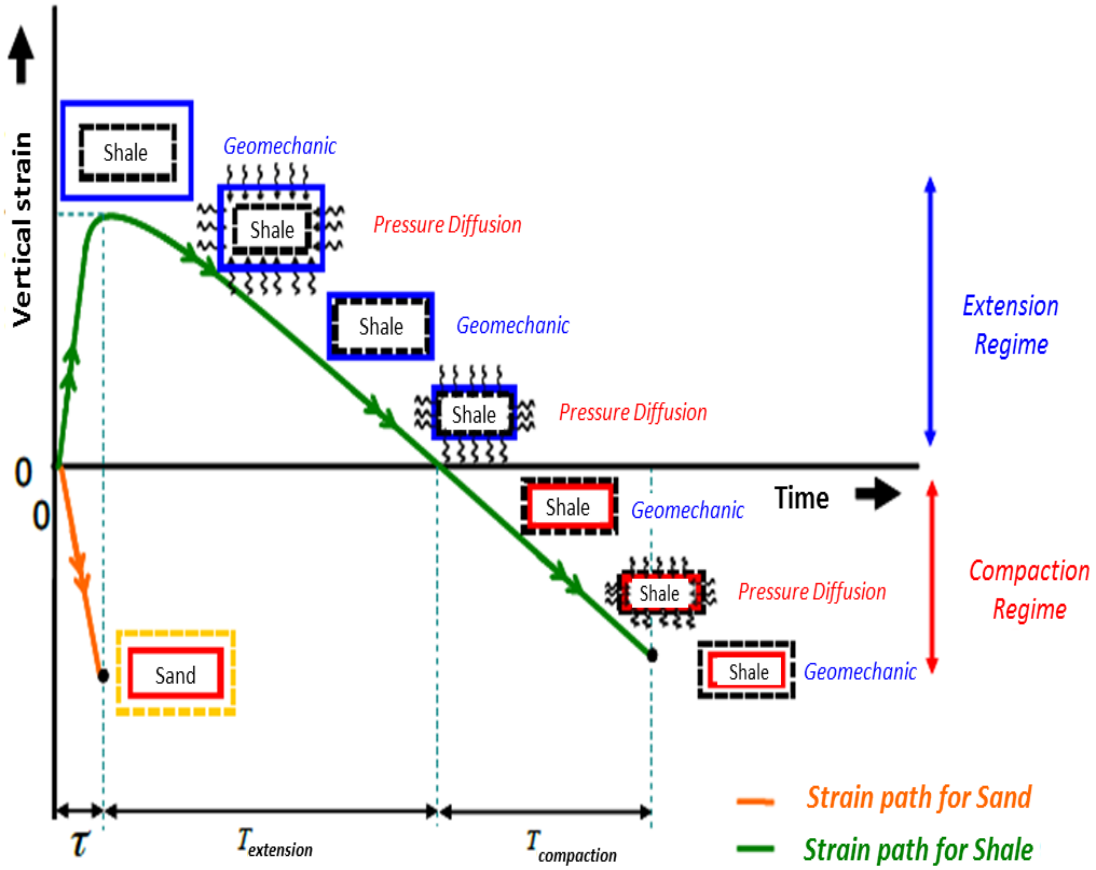

Figure 1-5 *Strain paths for the shales and sand in an instantaneously depleted sand body. The shales slowly evolve to a strain condition similar to the compaction in the sands, crossing over between an extensional and compactional regime. Taken from HajNasser, 2012*

Shale pressure diffusion is strongly dependent on time, sand-shale geometry, thickness and, of course, shale permeability. For these reasons the penetration distance and the amount of pressure drop (or build up) varies from one reservoir to another and even from one shale to another within the same reservoir. Table 1-2, presents a summary of some analytic computations from a previous ETLP thesis [*HajNasser*, 2012] of shale pressure diffusion for two scenarios: a shale interval adjacent to a depleted sand and a single shale layer interbedded between two depleted sand intervals (Figure 1-6). Pressure diffusion penetration distance and timing to achieve pressure diffusion in shale layers of different

thickness are estimated for shale permeabilities of 1 microdarcy and 1 nanodarcy; shale porosity, fluid viscosity and rock compressibility are assumed constant, and shale permeability anisotropy is not considered. The corresponding equations for these computations are shown in Appendix B.

Model / boundary conditions	Description	Shale permeability	Diffusivity constant D (m^2/day)	Time	Penetration / Shale layer thickness
Linear depletion, semi-infinite model	This scenario describes the diffusion in a semi-infinite model created at a sand-shale boundary	1 µD	2.61	3 months	32.32 metres of penetration
				30 years	323.30 metres of penetration
		1 nD	2.61E-3	3 months	1.02 metres of penetration
				30 years	10.22 metres of penetration
Linear depletion, single shale layer	This scenario describes the diffusion in a single shale layer between two depleted sand intervals	1 µD	2.61	2.14 hours	1 metre of thickness
				8.92 days	10 metres of thickness
		1 nD	2.61E-3	89 days	1 metre of thickness
				25 years	10 metres of thickness

Table 1-2 *Analytical pressure diffusion estimation for an infinite shale layer adjacent to a depleted sand (linear depletion, semi-infinite model) and a single shale layer interbedded between two depleted sands (linear depletion, single shale layer). Pressure diffusion estimation was accounted as a minimum 10% shale pressure drop compared with the final sand depletion. In both cases, shale porosity is 10%, the saturation is 100% water with a viscosity of 0.38 centipoise and compressibility of 3.0 (1/psi.10^{-6}). Modified from HajNasser 2012.*

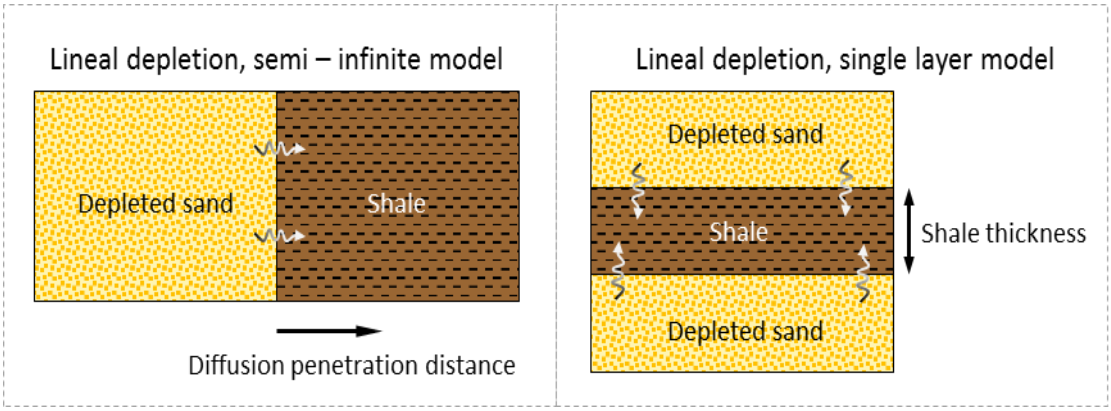

Figure 1-6 *Scenarios for analytical estimation (Table 1-1) of pressure diffusion in shale*

As the analytic results shows, sand-shale geometry matters, as it defines the number of diffusion fronts acting on a shale body. When shale permeability anisotropy is taken into account in this analysis, sand-shale geometry becomes even more important, as shale horizontal permeability is higher (even an order of magnitude higher if the shale contains silt layers and laminations) than the vertical permeability; thus if the sand-shale interface is a lateral contact, the penetration distance of the pressure diffusion will be considerably higher than for a shale overlying a depleted sand; also, the timing for pressure diffusion will be much lower. Shale thickness is also very important, as I show in one of the case studies; pressure equilibrium between reservoir sands and intra-reservoir shales can be achieved during production lifetime if those shales are relatively thin.

1.6 Shale Geomechanics

With a wide range of components and rheological responses under stress changes, the study of shale geomechanical behaviour should be considered a complex topic, worthy of a separate and fully dedicated research study. Production and injection processes change the reservoir pore pressure and hence alter the stress field acting on the reservoir and the surrounding rocks [*Grasso,* 1992; *Addis et al.*, 1998; *Hettema et al.*, 1998]. The impact of those alterations is certainly stronger and faster inside the reservoir, where major changes in the pore space occur. But after the initial adjustment of the new induced stress field conditions, the perturbations propagate to the surrounding rocks, especially in the vertical direction, as the effective stress is the main affected component. For this reason, the immediate reservoir overburden (which for clastic reservoirs is generally constituted by sealing shales), although it is outside the reservoir, is the area with higher geomechanical perturbations, which is reflected in changes recorded as time shifts in the time lapse seismic monitoring [*Geertsma*, 1973; *Hatchell et al.*, 2003; *Herwanger and Horne*, 2009]. Small geomechanical effects linked to hydrocarbon production are common in almost every reservoir, but moderate and severe effects, compromising the well's stability and seal integrity, and with considerable measurements of time shift recorded in the 4D, are more frequent in recent, unconsolidated reservoirs, such as the Tertiary turbidites from the Gulf of Mexico and West Africa. These effects are also found in the chalk reservoirs in the North Sea, due to rock matrix weakening produced by chemo-mechanical reactions related to water injection, and high pressure/high temperature clastic reservoirs (HP/HT) in the North Sea, as large pressure gradients occur

due to depletion used as production mechanism and compaction of the reservoir can be an important process [*Herwanger and Horne*, 2009].

Out of the four case applications of this thesis, only the Shearwater Field (HP/HT) was considered geomechanically active, as the effect of the Fulmar reservoir compaction into the overburden shales is taken into account, coupled with the process of pressure diffusion within the overlying shales from Heather and Kimmeridge Clay formations, to explain the time shift and time strain propagation and distribution in the overburden observed in the 4D seismic signature. In the Shearwater Field case study, to avoid complications in the estimation of the overburden mechanical properties related to shale anisotropy [*Herwanger and Horne,* 2009], shales were considered to be isotropic in terms of mechanical properties. In the other 3 case studies (Heidrun, Girassol and Schiehallion fields), compaction in the reservoir is not considered to be a dominant process in the dynamic elastic behaviour of the reservoir (without denying its existence), and shales are only activated for pressure diffusion, excluding any geomechanical effect on them in the numerical simulations, synthetic seismic modelling and 4D seismic interpretation.

Shale's mechanical properties are strongly affected by burial history, pore pressure, fabric and mineralogical composition: for that reason, shale has a wide range of values for the unconfined compressive strength (UCS), Young's moduli and Poisson's ratio[*Dewhurst et al.,* 2008]. As shale mechanical characterization is not part of the core in this research, the values used to define shale properties for the material library of the geomechanical simulations in the Shearwater Field are taken from previous studies in the area [*De Gennaro et al.,* 2010], and the only parameter taken into account for variations in the mechanical properties of the shale and the acting stress field is the pore pressure induced change [*Geertsma*, 1973].

1.7 Shale and 4D seismic interpretation

The presence of shale can be observed in the seismic interpretation of every single clastic reservoir under time lapse seismic monitoring. The distribution of this lithology and its geometric relationships with the sand units determine the architecture of the reservoir, its connectivity and compartmentalization, and with that, part of the dynamic behaviour of the reservoir and hence the distribution of the 4D seismic signature. The elastic differences recorded in 4D are related to changes in the reservoir pore space, but circumscribed laterally and vertically by variations in facies (controlled by the sand-shale

ratio and sedimentological structures), the presence of impermeable barriers (faults, shale or cemented intervals) and the dynamic distribution of fluids and pressure fronts. The distribution of thin (sub-seismic) intra-reservoir shale layers and its drastic effect on the reservoir vertical connectivity and permeability can produce interesting features in the 4D seismic signature, as differential movements of fluids contact in highly tilted reservoirs [*Park et al.,* 1996; *Kloosterman et al.,* 2003*; Staples et al.,* 2006]. Moreover, in very heterogeneous reservoirs, only an understanding of the geology and shale distribution allows the understanding of the 4D seismic signal [*Landrø et al.,* 1999; *MacLellan et al.,* 2006].

The analysis of the pressure diffusion process into shale and its elastic implications is a relatively new concept in 4D seismic interpretation, with most of the similar work generated in the Edinburgh Time Lapse Project [*MacBeth et al.,* 2011; *HajNasser,* 2012; *Ricard et al.,* 2012; *Rangel and MacBeth,* 2015]. The approach of my thesis consists of the inclusion of the analysis of the internal architecture of the shale in the classical 3D and 4D forward reservoir modelling workflow (Figure 1-7). The starting point is to recognize how the geological and simulation models represent shales, and how to make them active by populating shale cells with static (NTG, porosity) and dynamic (permeability and transmissivity) properties estimated from a detailed geological analysis, upscaling and honoring the log data. Including lithological and dynamic property variation inside shales in the simulation model enables pressure interaction with the reservoir. In this workflow, the modelling of the shale's capillary pressure inhibits fluid interaction between shales and the reservoir (the pressure gradient is not high enough to change the shale's saturation). Activating shales in the simulation model enables pressure diffusion with the reservoir. To analyze the effect of this process, the simulation model outputs and rock physics analysis applied to the shale are integrated in a simulation to seismic workflow to generate synthetic seismic volumes.

Comparison of the mismatch between the observed 4D seismic differences and the synthetic seismic responses for active and inactive (control or base scenario) shale models, determines whether the pressure diffusion in shales is an important process in the dynamic elastic behavior of the reservoir, its compartmentalization and connectivity. As shale architecture and its spatial relationships with the reservoir depend on the specific sedimentological setting and its geologic evolution, in this project I apply my workflow for shale contribution evaluation in four conventional hydrocarbon reservoirs, each one with different geology and sand-shale geometries.

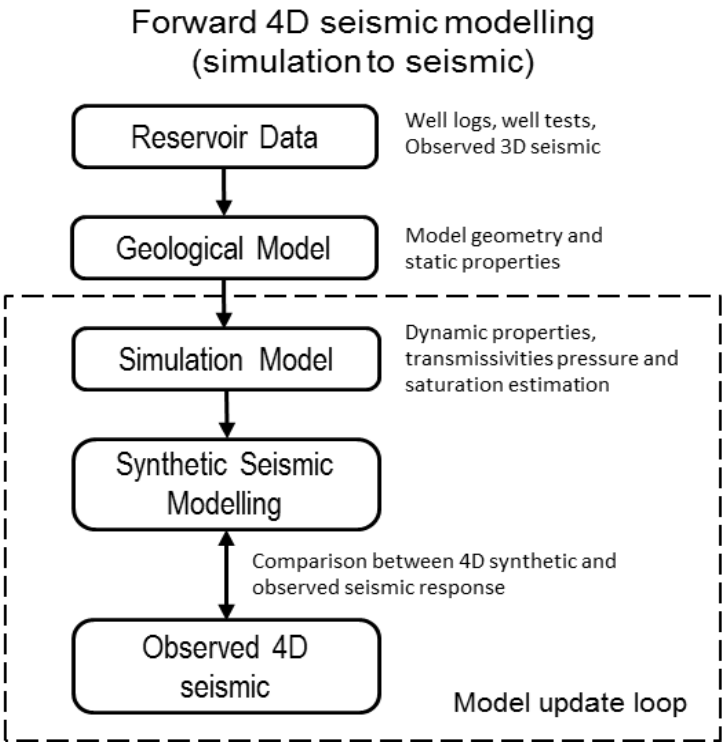

Figure 1-7 *Forward 4D seismic modelling workflow. Modified from published literature [Davies and Maver, 2004; Eggenberger et al., 2015]* .

1.8 Contributions of this work

This thesis presents the evaluation of the impact of shale pressure diffusion in the 4D seismic interpretation, highlighting the importance of a comprehensive characterization of shale, its composition, internal architecture, and static and dynamic properties. This research includes a detailed guide for the study of shales using wireline log data, which in conventional reservoirs is the most common source of information acquired in shale intervals. Also this work presents a series of equations and empirical relationships for the estimation of the main static (NTG and porosity) and dynamic (permeabilities, capillary pressure, saturation and transmissivity) properties of shales at the well location, and methods for the upscaling and spatial propagation of those parameters across the reservoir simulation grid. Special attention was paid to the estimation and modelling of shale permeability, as it is one of the main parameters controlling the shale-reservoir interaction, through pressure diffusion. The main contribution of this project relies on the presentation of four case studies where shales were activated and included in the reservoir numerical simulations, changing the geometry of the previous models to include underburden, sideburden and overburden [*Olden et al.*, 2001] shales in order to study their pressure related interactions with the reservoir. Rock physics analysis and elastic

modelling was performed to study the influence of the pressure diffusion in the 4D seismic signal of the fields and its interpretation. The diversity of geological scenarios in the field applications, the types of shale, sand-shale geometry and reservoir mechanisms determine the particular contribution of shale activation in each field. The responses range from reservoirs where shale pressure diffusion has a weak effect on the reservoir dynamic behaviour, and hence the 4D seismic interpretation, to cases where the reservoir connectivity and its impact on the distribution of pressure, saturation and 4D seismic signature can only be understood if pressure diffusion occurs through shales.

Regardless of the degree of contribution of shale pressure diffusion to the 4D seismic interpretation, the results of this work prove the advantages of the inclusion of shale analysis in 3D and 4D seismic modelling, as the accurate characterization of this lithology allows to capture better the elastic contrasts and the imaging of the seismic events within the reservoir, the immediate overburden and the underburden. Finally, I expect that the exposure of the readers to this material, will make them aware of the particular conditions in which the shale pressure diffusion can be an important process to explain the dynamic seismic response of a reservoir. And lastly, I hope this work further arouses interest in the study of shale in conventional reservoirs.

2 Chapter:

Shale Characterization and Properties Estimation

This section covers definitions of essential concepts concerning shale and the methodology used in this research to perform the static and dynamic characterization of this lithology. It also includes the main instructions for the application of the developed workflow for shale activation, procedures and constraints established for the engineering modelling of the pressure diffusion process in shales. Finally, this chapter also describes the estimation of shale elastic properties and parameters used for the synthetic seismic modelling with shales activated.

2.1 Introduction

Shales are the most abundant sedimentary rock covering the earth's surface and constitute 60% of the entire sedimentary column of our planet [*Potter et al.*, 1980]. Shale's small sized mineral components are a challenge for naked eye petrological analysis, and their sedimentary structures (very useful to describe a rock history) are only apparent when silts and fine sands are interbedded within their lithology. Technological improvements in the last century helped to address some of the scale issues in shale analysis, mainly those concerning mineral composition and porosity estimation, but still shale's dynamic properties and behaviour (permeability, fluid flow and pressure variations) remains largely unknown, or at least not very well represented by conventional physical laws, with empirical relationships often presenting the best approach currently available for shale characterization [*Yang and Aplin*, 2007].

Due to shared low energy conditions for shale deposition and organic matter preservation, shales contain the largest portion (around 90%) of preserved organic matter in all sedimentary rocks (shale organic content ranges from 0.2 to 0.5% for oxygenated deposits to 15 and even 25% for black shales deposited under anoxic conditions). As a result, shales are the main rock source of hydrocarbons; therefore, the study of their depositional processes, burial and structures is paramount to the exploration of oil and gas reservoirs. Currently, with shale gas industry development, the characterization of these rocks is becoming increasingly important, with their classic role as bedrock and seal in conventional fields now extended into their reservoir role in unconventional oil and gas. This has opened an entire research field, with enormous economic resources, that is developing increasingly towards smaller scale analysis in shale characterization.

The recognition of the existence of different levels of heterogeneity inside shale bodies has begun to dispel the old perception of shales as impermeable barriers which were not taken into account in fluid flow simulations. Recent studies [*MacBeth et al.*, 2011; *HajNasser*, 2012;], have shown that the very low (but finite) permeability of shales enables pressure equilibrium with the surrounding rocks; this effect is sizable over production time scales and time lapse seismic monitoring, and can be the key to explaining some problems in reservoirs related to pressure and saturation.

2.2 Shale definition

Shale is the widespread term used to name indurated, laminated, fine-grained detrital argillaceous rocks that contain 50% or more of terrigenous components with a size less than 4 micrometres [*Tourtelot*, 1960; *Potter et al.*, 2005]. Clays are the main component of this fine terrigenous rock, but shales also can contain a broad spectrum of particles that include silt, carbonate mud (micrite), volcanic ash, kerogen, fragments of bioclasts, diatoms, pellets and small size clasts of quartz and feldspar. Silt, detrital grains (mainly quartz) with size between 4 and 64 micrometres, represents a significant fraction of shale, and when their volume exceeds that of clays, the deposits are called siltstones, sedimentological units linked with shales that are usually interbedded and give evidence of abrupt or gradational changes in the depositional energy regime. As the term shale (Teutonic word) has been originally applied to *laminated* argillaceous rocks [*Hooson*, 1747], some geoscientists [*Potter et al.*, 2005] have proposed the use of mudstone as the generic term for all fine-grained argillaceous rocks, laminated or not. There are other terms for fine-grained sedimentary rocks, like mudrock, claystone, loam, pelite, lutite, argillite, phylite and slate, but they are only textural and maturity (metamorphic) variations of shales and mudstones. The mudstone term has become more popular in academia, while shale remains in use in the oil and gas industry, chiefly because it is also used on many occasions in the stratigraphic nomenclature as part of formation names, i.e. Marcellus Shale, Barnett Shale, etc.

2.2.1 Shale Classification

Among the numerous classifications for shales and mudstones, this research adopt the criteria of lamination thickness and clay content used by *Potter, et al*. 2005 (Table 2-1), with some changes. Note that although the above shale definition highlights the content of 50% or more clay-sized particles, the table below includes siltstones. The reason for this is that this research is focused on the effect of shale architecture on reservoir behaviour during production, and the key feature in the shale heterogeneities is the presence of interbedded siltstones, creating preferential flow paths for pressure diffusion and fluid saturation changes. For practical purposes in this project, mudshales and clayshales will be regarded as simple shales; mudstones and claystones as massive shales or simple mudstones, while the siltstones (laminated or bedded) keep their place in the classification but as a different type of fine grained rock.

		Clay size constituents (%)	0 - 32	33 - 65	66 - 100
Indurated	Beds	Greater than 10 mm	Bedded Siltstone	Mudstone	Claystone
	Laminae	Less than 10 mm	Laminated Siltstone	Mudshale	Clayshale

Table 2-1 *Shale clastic classification based on clay/silt percentage and bedding thickness, redrawn from published literature [Potter et al., 2005].*

2.3 Composition

Shale composition can encompass a wide range of mineral assemblage (Table 2-2), and, as mentioned in shale definition, the only constraint is having a 50% or higher proportion of clay-sized constituents. Even though the number of components can be large, almost the whole rock volume (around 90% or higher most of the time) can be grouped into two fractions: the clay fraction that is usually a mixture of at least two types of clays (100% clay monomineralic scenarios are near impossible in nature) and the silt fraction that most of the time consists of quartz (in higher proportion) and feldspar. Calcite and organic matter are almost always present, but in lower proportions; a moderate or high amount of these components can imply the occurrence of marls (calcite case) or hydrocarbon rock source (high organic matter content) if the thermal maturity of the shale allows organic matter transformation into kerogen and cracking into hydrocarbon. Before starting with shale composition analysis, it is convenient to first establish the type of shales to study in the reservoir. Shales are very consistent laterally, but can vary a lot vertically. In a classic clastic reservoir there are shales in the overburden (seal), and intra- and inter-reservoir shales; specific marine reservoirs such as turbidites have underburden and sideburden shales. Overburden, underburden and sideburden shales are usually deposited in lower energy conditions; consequently their clay fraction is usually higher than that of reservoir shales that have a higher silt content, due to higher energy deposition.

	Mineral	Origin and significance
Silt Fraction	Quartz	Ever present component (at least 15 to 30%), almost always with a detrital origin, its proportion in shales is an indicative of shoreline (with some aeolian transported exceptions).
	Feldspar	Less abundant than quartz, with plagioclase as the most abundant type of feldspar; can be detrital or autigenic
Clay Fraction	Illite	Non-expansive clay, occurs as the alteration of feldspar, micas and pre-existing shales; can also occur due smectite transformation by burial and diagenesis. Illite is by far the most abundant clay mineral.
	Smectite - montmorillonite	Hydrate expandable clay, commonly formed by the alteration of volcanic glass (bentonites) or by weathering of very alkaline soils.
	Kaolinite	Characteristic of tropical and subtropical weathering with abundant rainfall; in marine basins is a very good indicator of shoreline.
	Chlorite	More common in temperate and high latitude areas, created by the alteration of mafic minerals; or by diagenetic burial. Chlorite is very common in Palaeozoic shales.
	Glauconite	Iron-rich product of the smectite-illite transformation; only occurs in marine environments with slow deposition.
	Carbonates	Calcite/dolomite/siderite: common in marine shales deposited above the calcite compensation depth; is an important cement agent in shales.
	Oxides	Mostly autigenic pyrite and siderite, indicative of reducing environmental conditions.
	Organic matter	Present in almost all shales (except red ones), usually lower than 2% of rock volume: higher corresponds to potential source rock. Content can vary according to organic supply and oxygen during deposition, very useful for basin thermal history reconstruction. Coal laminations interbedded within shale internals are also very common in Fluvio-deltaic and estuarine environments.
	Other	Gypsum, heavy minerals, volcanic ash.

Table 2-2 *Most common shale mineral components*

Using current advanced methods and technology, a series of very accurate laboratory tests can be conducted if physical samples are available to determine shale components and proportions. The most popular methods are X-Ray diffraction and mass spectrometry, where even trace elements can be identified and used to identify source provenance (protolith). In addition, petrographic analysis of thin sections can characterize the silt fraction, but not the clay size, which in most cases is below the petrographic analysis scale. As shales in conventional reservoir characterization are not considered part of the reservoir, shale intervals are not selected to be cored, and even if they are, most of the time the samples are not included in the laboratory core analysis routine, so shale composition, static and dynamic properties frequently remain unknown, with the

exception of some overburden overpressured or swelling shales that are characterized due to their geomechanical implications during drilling. The available database for the fields studied during this research lacked any information related to shale composition (the exception is the Heidrun Field). Due to this, a methodology to characterize shale composition based on well log analysis was developed. As the silt fraction (quartz and feldspar) properties variation is low, this methodology pays special attention to the clay fraction and its components that are the most variable.

2.3.1 Shale composition estimation based on well log analysis

The first step involves the following procedures: to create an inventory of available well logs, and consider which logs are more useful in identifying particular shale components; to delimitate the interval to study, as, due to changes in deposition energy, shale composition can vary vertically; to establish shale baselines for each well and log measured in the field, and to compare them; and finally to identify trends (in compaction or eventually in composition). Below is a detailed analysis of the available logs, their features and uses for shale composition estimation

Gamma Ray (GR): this log is a direct measurement of rock radioactivity (presence of radioactive components). It is used to establish how "pure" the shale is, based on the analysis of shale electrofacies homogeneity, and also to define the clay-silt relation or relative percentages (as quartz and feldspar are not radioactive and clays are); and coarsening up or fining up trends (silt and sand content vertical variation in an interval). Radioactivity can vary in clays (see Table 2-3), according to their content of uranium, thorium and potassium. Special attention needs to be paid to the GR log interpretation when the borehole was drilled using bentonite (a type of smectite) based mud fluid, as this material is radioactive and GR measures can be affected, especially under bad hole conditions (washouts), where more drilling fluid is accumulated in the borehole cavity.

Clay Mineral	°API
Illite	182
Kaolinite	155
Smectite	90
Chlorite	50

Table 2-3 *Typical GR values in shales were a specific type of clay is dominant (not 100% monomineralic measures). Taken from published literature* [*Chitale,* 2009].

Spectral Gamma Ray: is a radioactivity measure that differentiates uranium, potassium and thorium signals, and hence proportions. Potassium and thorium content are used to identify clays (see Table 2-4), while uranium abundance is indicative of organic matter content.

	Potassium content		Thorium content
Mineral	% by weight	Average %	Average (ppm)
Illite	3.51 – 8.31	5.20	6 - 22
Glauconite	3.20 – 5.80	4.50	2 - 8
Kaolinite	0.00 – 1.49	0.63	18 - 26
Smectite	0.00 – 0.60	0.22	10 - 24
Chlorite	0	0	0 - 7

Table 2-4 *Potassium and Thorium content by clay, taken from published literature* [*Rider and Kennedy,* 2013]

Density: this log measures formation bulk density (recording gamma ray scattering), which is the overall density record including solid matrix and fluid enclosed in the pore space. Shales in conventional reservoirs are water saturated, so by knowing water properties it is easy to determine the occurrence and proportion of mineral components of the rock solid matrix and their bulk density (see Table 2-5). Density log measures are apparent (low readings) in washout sections (borehole enlargement) because the tool is recording mud properties instead of true formation, and needs to be corrected through accurate analysis. As can be observed in Table 2-5, the bulk densities of clays have a wide range of values, depending on consolidation and bound water content, so compaction needs to be assessed prior to using a clay distinctive bulk density for shale composition differentiation, as some clay densities' values overlap each other.

	Mineral	Bulk Density (g/cm^3)
Silt Fraction	Quartz	2.65
	Feldspar (average)	2.62
Clay Fraction	Illite	2.5 – 3.0
	Glauconite	2.67
	Kaolinite	2.2 – 2.6
	Smectite (Montmorillonite)	2.0 – 3.0
	Chlorite	2.6 – 3.3
	Calcite	2.71
	Organic matter (kerogen)	1.3

Table 2-5 *Main shale components' bulk density, values taken from published literature [Mavko et al., 2009; Rider and Kennedy, 2013]*

Caliper: This is a contact tool that measures inner borehole diameter variations, which is used in quality control of other logs, to ensure that the tool is recording formation properties instead of mud filtrate. Sloughing (borehole diameter reduction or 'tight spots') is usually related to the presence of swelling clays, such as smectite (montmorillonite and bentonite). Washouts or increases in the borehole diameter in shales are generally related to poorly consolidated shaly intervals, but are more common in illite and kaolinite clay dominated intervals.

Sonic: this log measures P-wave and S-wave (dipole tools) propagation in the formation (in fact, the tool measures acoustic slowness or interval transit time). Each mineral has different P-wave and S-wave velocities, which can be used to corroborate shale mineral composition (Table 2-6). These reference values can increase or decrease according to compaction and bound water content, but the values do not overlap each other. The sonic log is an excellent indicator of compaction and porosity reduction in shales; it is also used to detect overpressured or underpressured intervals, expressed by an anomalous decrease or increase in the shale compaction trend (naturally velocity gradually increase with depth).

	Mineral	P-wave Velocity (m/s)	S-wave Velocity (m/s)
Silt Fraction	Quartz	5760	3660
	Feldspar (average)	4680	2390
Clay Fraction	Illite	4320	2540
	Glauconite	5640	3830
	Kaolinite	1440	930
	Smectite (Montmorillonite)	3600	1850
	Chlorite	5490	3730
	Calcite	6640	3440
	Organic matter (kerogen)	2250	1450

Table 2-6 *Main shale components' P-wave and S-wave velocities, values taken from published literature [Mavko et al., 2009; Rider and Kennedy, 2013]*

Resistivity: this log measures the formation's ability to conduct electricity. Most rock frames do not play an active part in determining the formation resistivity. The conductivity is basically related to the fluid contained in the pore space, (water, oil or gas) and their amount of associated ions (salinity); however, in the case of shales, the clay fraction introduces an *excess of conductivity*, due the presence of brine in their pore space and negatively charged molecules of water in the clay crystalline structure. The

phyllosilicate structure determines the clay's cation exchange capacity, CEC (Table 2-7), and hence its conductivity. As can be observed, kaolinite and chlorite are more resistive than illite, smectite clays, due their lower water content. As micro resistivity logs have one of the highest vertical resolutions, the microspherical resistivity log (MSFL) can be used to determine a shale's heterogeneity, allowing silt and fine sand interbedded laminations and layers to be detected and differentiated from most clays (quartz and feldspar do not conduct electricity).

Mineral	Average CEC (meq/g)
Illite	0.25
Kaolinite	0.04
Smectite	1
Chlorite	0.04

Table 2-7 *Clay cation exchange capacity, taken from published literature* [*Dewan,* 1983]

Photoelectric Factor (PEF): this is a continuous record of the effective photoelectric absorption per electron index of a formation. As this measurement is dependent on the atomic number of the formation, PEF readings are not influenced by fluids and are very responsive to heavy elements such as iron (high atomic numbers), and can be used as shale and clay composition discriminators, due to the variable heavy element composition inside their crystalline structure. As can be seen in Table 2-8, the PEF log can be very useful to differentiate most clays (only kaolinite and smectite values overlap). Some corrections in PEF readings may be necessary if the borehole was drilled with a barite based mud.

	Mineral	PEF (barn/gr)
Silt Fraction	Quartz	1.806
	Feldspar	2.86
Clay Fraction	Illite	2.837
	Glauconite	5.32
	Kaolinite	1.635
	Smectite	1.636
	Chlorite	9.973
	Calcite	5.084

Table 2-8 *Photo Electric Factor (PEF) for main shale components, taken from published literature* [*Rider and Kennedy* 2013]

Neutron: this measures the *Hydrogen Index*, which is related to the formation's hydrogen content. The log is given in neutron porosity units. While, in sands, the hydrogen is strictly related to water and fluids contained in the pore space, in shales there is also hydrogen associated with the bound water in the clay crystalline structure, so the neutron porosity measured is overestimated. A typical neutron log will indicate Neutron Porosity values for shales between 25 and 75% (average is between 40-50%), while the range for sands is 0-30% and for limestone is from 0-35% [*Rider and Kennedy*, 2013]. The interstitial water in clays also can be used to differentiate them (Table 2-9). When Neutron-Porosity and Density logs are plotted in the same track at specific scales (Density from 1.95 to 2.95 g/cm^3 and Neutron-Porosity from 0.45 to -0.15 fraction in reverse scale), the separation between both curves can be used as indicative of shale silt and clay content. If the separation decreases, that implies that the silt content is higher, while if the separation increases, the clay fraction content dominates the shale composition.

Mineral	% water (average)	Hydrogen index	Neutron Porosity
Illite	8	0.09	30
Kaolinite	13	0.37	37
Smectite	18 - 22	0.64	52
Chlorite	14	0.32	44

Table 2-9 *Clay water content and Neutron Porosity measures, taken from published literature* [*Rider and Kennedy*, 2013]

Nuclear Magnetic Resonance: this log records the behaviour of protons (hydrogen nuclei) under an induced magnetic field, as a measure of their relaxation time (the protons' rotation and alignment time after the induced magnetic field is removed and hydrogen nuclei return to their original position, which is aligned with the Earth's natural magnetic field). As the hydrogen protons contained in the clay bound water are quite tight, the relaxation time is very fast and the T2 distribution (one of the relaxation time parameters measured by the tool) is unimodal for most of the clays. Only very high smectite concentrations could give some differentiation in the T2, due to higher water content [*Rider and Kennedy*, 2013].

Dipmeter: this log provides a continuous record of formation dip and azimuth. The tool acquires four microresistivity curves in orthogonal position in the borehole; a correlation

between them is then used to calculate the dip and the azimuth. Depending on the vertical resolution of the processing (which is usually very high), the dipmeter can be used in sedimentological and stratigraphic studies to analyse paleocurrents and sedimentary structures such as lamination and bedding (which in the specific case of shales can be used to infer shale heterogeneity, i.e. sand and silt content).

Image logs: images can be produced from electrical, acoustic, density, photoelectric, gamma ray and calliper measurements, but the higher resolution comes from electrical (multi pad) and acoustic logs. Based on 0.5-centimetre vertical resolution, bedding, and even textural analysis can be performed, thin-bedded sequences that can look like shaly intervals can be better characterized and shale, silt and fine sand lithofacies can be separated.

It is clear that qualitative analysis of shale composition can be performed using a single or more integrated logs to discriminate between clay and silt mineral properties. On the other hand, quantitative shale composition analysis based on logs requires the integration of a minimum number of logs and a weighted relationship between the different parameters, which is usually calibrated from previous knowledge about the basin stratigraphy and even core laboratory tests performed to representative lithologies of the area: this is basically what most wireline log service companies offer as part of their portfolio under the "Lithologic log". Given that, for this research, there were no calibration algorithms available, the quantitative analysis of shale composition was based on assumptions for the clay type proportions, based on the study of clay provenance, which is explained next.

2.4 Clay provenance

The analysis of clay provenance with the purpose of identifying clay fraction proportions can be perform through the integration of laboratory analysis or wireline well log data with a regional geology analysis. If shale samples are available, the laboratory tests that can be performed to determine provenance are: ***Ion microprobe analysis***, to estimate Pb^{207}/Pb^{206} isotope proportions. which is a good indicator of the age of detrital zircons (to identify primary source rock and recycling); ***Pollen concentration decay***, to determine distance from land source (valid only for rocks younger than Devonian), assuming

palynomorph content in shales as indicative of continental proximity; and ***Radiogenic isotopes***, which behave like a rock footprint that can be compared to those from eroded areas contemporaneous with the shale deposition, for source determination [*Potter et al.*, 2005]. Test results have to be integrated with the paleogeography of the basin and its dynamic evolution. Since shale samples and laboratory tests were not available for the studied reservoirs, the clay provenance analysis was conducted by integrating well log and seismic data with a more extensive regional geology study, with the following methodology:

Basin Analysis: the first step is to establish the basin and depocentre geometry, to then recognize the location of the reservoir in this regional frame. To this end, a paleogeography documentation that establishes chronostratigraphic limits wider than the interval of interest is preferable (older for the base reservoir and younger for the top) in order to have a better picture of the basin evolution. The analysis of basin geometry and the surrounding exposed areas around it can give hints about sediment source and transport mechanisms. A regional stratigraphy review will reveal the architecture of the basin fill, with the study of the sediments' stacking patterns (progradational, aggradational or retrogradational sequences) helping to understand major eustatic changes and hence the evolution of energy during the reservoir deposition, which is the paramount factor for studying shale sedimentation and vertical heterogeneity.

Reservoir Analysis: in order to establish the local stratigraphic column a lithology analysis in the well logs needs to be conducted, to establish the reservoir position in the basin and its correlation with the regional stratigraphic and tectonic processes, with the aim of understanding better the prevailing sedimentary conditions during the reservoir deposition (Figure 2-1). Also a seismic local and regional analysis can be conducted to establish the clinoform geometry (seismic reflection termination), which is very useful for determining the direction of deposition and depocentre geometry. The validity of this analysis depends on whether the clinoforms are still in their post-depositional position or if they have been deformed and rotated by major tectonic events, in which case a palinspastic structural restoration may be necessary.

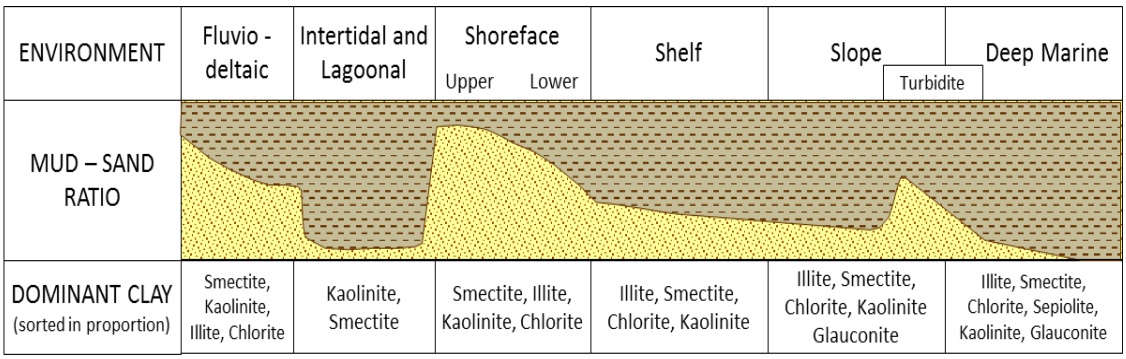

Figure 2-1 *Dominant clay deposition (organized by proportion) and mud-sand ratio according to sedimentological environment, with data from published literature* [*Biscaye*, 1965*; Potter et al.*, 1980; *Lisitzin*, 1996].

Source identification: with the basin paleo-geometry and direction of deposition established, it is easy to establish the exposed area where erosion gave origin to the reservoir sediments. Paleogeographic analysis allows us to establish transport and distance from source to depocentre, which is critical in understanding the clay settling process. The geographical location of the exposed area in terms of latitude and climate, coupled with the photolith mineral composition and tectonic setting is paramount to establish the weathering and dominant clay generation process (see Figure 2-2 and Table 2-10).

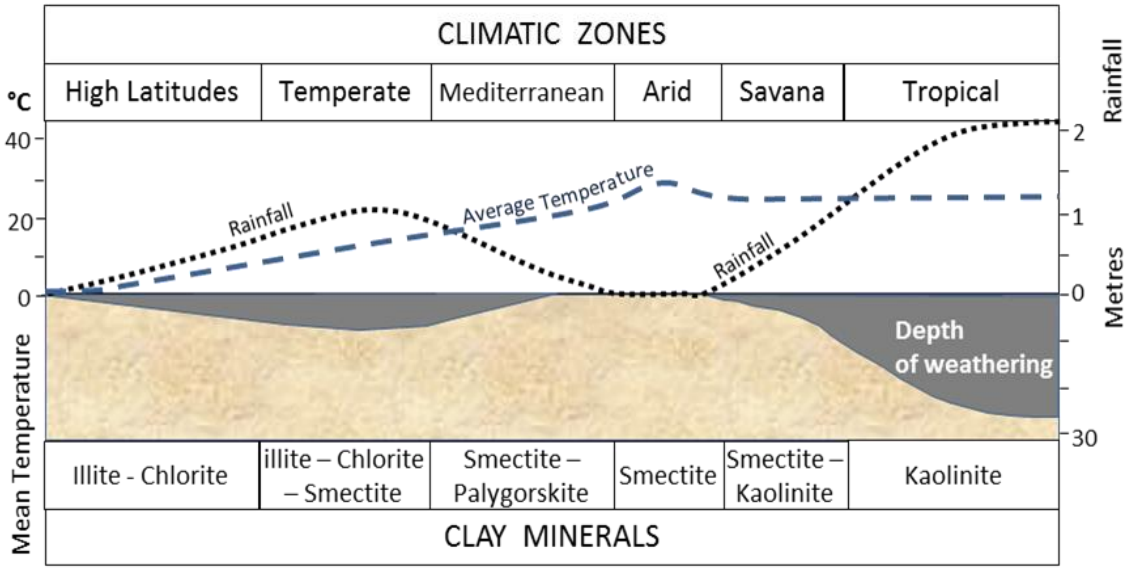

Figure 2-2 *Clay mineral generation according to climate zones, modified from published literature* [*Potter et al.*, 2005]

Tectonic Setting	Moderate Weathering	Strong Weathering
Igneous Rocks		
Plateau basalts	Fe oxides, smectite, little sand	Fe oxides, some smectite with kaolinite and gibbsite
Island arcs	Smectite with volcanoclastic sands	Smectite and kaolinite with volcanoclastic sands
Continent-margin arcs	Smectite and illite with quartz-feldspar and volcanoclastic sands	Smectite, illite and kaolinite with quartz-feldspar and volcanoclastic sands
Basement uplifts	Illite with quartz-feldspar sands	Kaolinite with quartzitic sands
Sedimentary Rocks		
Fold-thrust belts & strike slip terranes	Recycled illite, chlorite, kaolinite plus some new smectite; quartz-feldspar sands	Recycled illite, chlorite, kaolinite plus abundant new kaolinite; quartzitic sands
Craton interiors	Recycled illite, chlorite, and kaolinite; quartz-feldspar sands	Recycled illite, chlorite, kaolinite plus abundant new kaolinite; quartzitic sands
Metamorphic Rocks		
Mountain belts	Recycled chlorite, muscovite, illite; quartz-feldspar sands	Recycled chlorite, muscovite, illite with new kaolinite; quartzitic sands
Precambrian shields	Recycled muscovite, illite; quartz-feldspar sands	Recycled muscovite, illite with new kaolinite; quartzitic sands

Table 2-10 *Weathering products according to rock type and tectonic setting, taken from published literature* [*Potter et al.,* 2005].

For shales deposited in deep marine environments, the clay provenance definition is more complex. In this case, the majority of sediment load will come from closer inland eroded areas (according to transport agents), but depending on the intensity and direction of marine currents, an important percentage of a shale's composition can come from clays travelling in suspension from a more distant origin, as far as a couple of thousand kilometres in some particular cases [*Schieber et al.*, 1998]. In Figure 2-3 one can observe the influence of oceanic currents in the clay distribution, e.g. the effect of the south Atlantic current in today's marine smectite distribution. As flocculation processes are different for each clay, some of them can travel further in suspension, while others settle quicker. Aeolian sediments can also create confusion in the process of provenance determination, but the silt fraction transported by the wind has a very distinctive signature, the sorting and sphericity of their grains being very high, due to aeolic abrasion. Provenance of volcanic dust can be also challenging to track, when it is present as shale component.

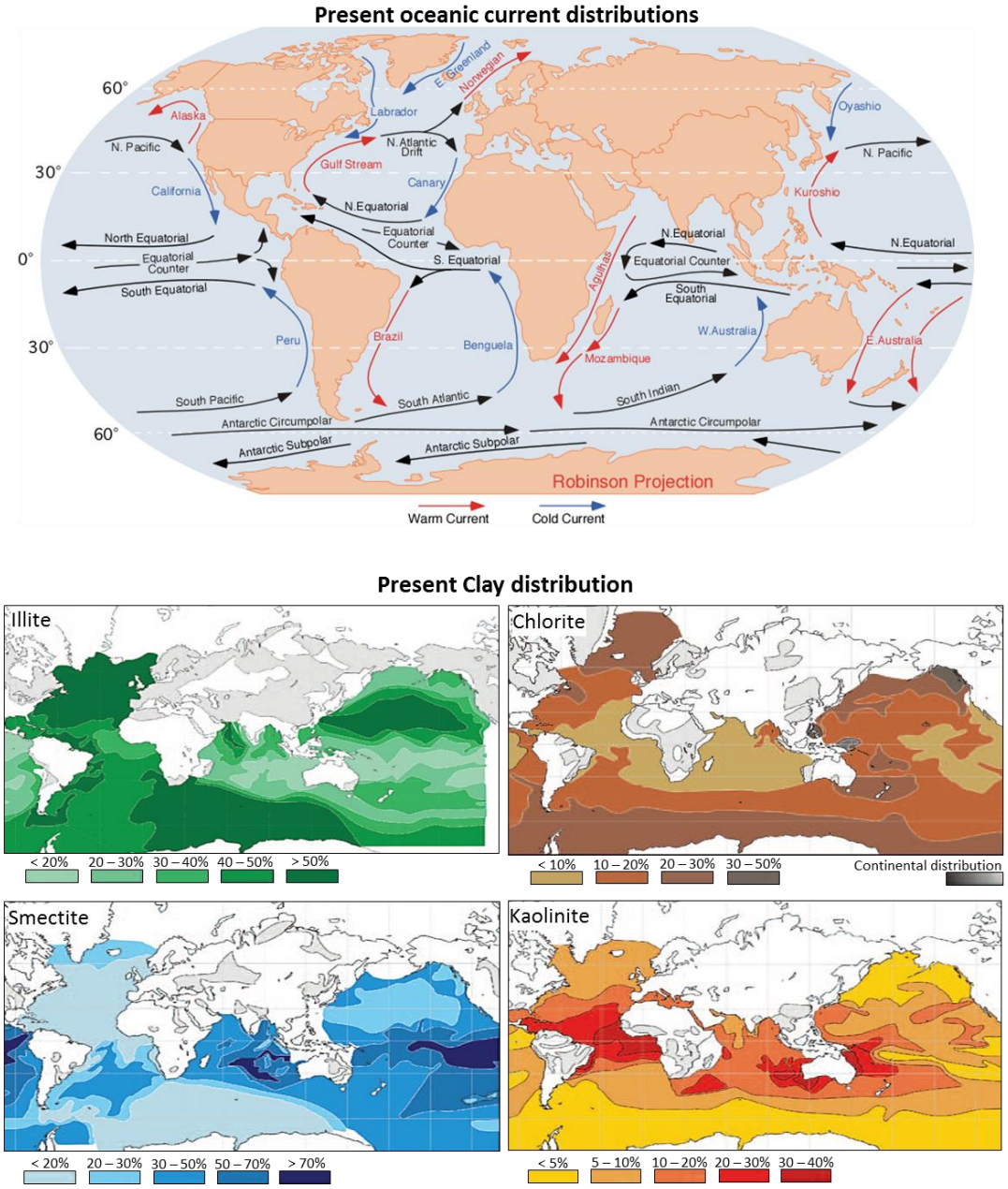

Figure 2-3 *Present day oceanic currents and clay distributions, modified from published literature* [*Lisitzin*, 1996; *Fagel*, 2007].

2.5 Shale deposition

In contrast to sands, the deposition of shale is not primarily governed by particle size and flow velocity; instead, inter-particle interaction and cohesion play a major role [*Schieber et al.*, 1998], as the fall velocity of single clay-sized particles in suspension rarely exceeds the effects of viscosity and turbulence characteristics of moving water [*Allen*, 2012]. Mud deposition from suspension commonly occurs when particles flocculate and settle as aggregates, which are much larger than single clay grains. Also important is the aggregation and pelletization of mud by organisms, as faecal matter can act as a binding

agent for clay particles. Clay platelets have naturally occurring electrically charged surfaces that tend to repel each other while they are in suspension, and as a result, changes in water chemistry (salinity increase) may affect clay's exchangeable cation population [*Potter et al.*, 1980] thereby enhancing the electrical affinity between platelets, which favours the aggregation processes (Figure 2-4). Floccule formation and size are enhanced by high-suspension concentrations and agitated, turbulent waters, as this produces a higher rate of inter-particle collisions. Both estuarine and transitional environments fulfil these conditions, and, coupled with the fact that they host a large association of mud feeding organisms, these environments promote chemical and biological aggregation of mud. Not all clays flocculate under the same conditions. Kaolinite for example only needs small salinity concentrations to change platelet electrochemical attraction; in addition, its particles are of the largest clay size, which allows flocculation and deposition to occur almost in the river mouth; thus, very often the distribution of this clay in the stratigraphic record is used as a reference of shoreline position (in tropical areas, where kaolinite is generated). In contrast, illite and smectite clays need higher salinity concentrations to aggregate, and for that reason, are transported further into the sea in suspension.

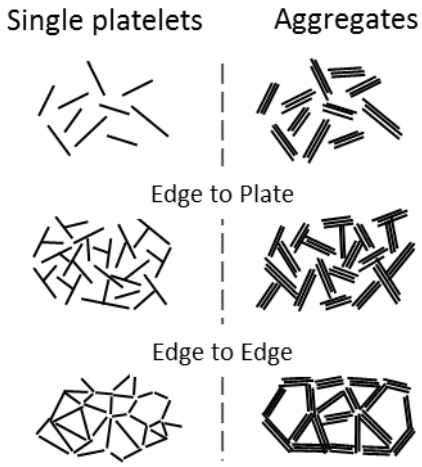

Figure 2-4 *Different forms of flocculation; note how the open fabric favours water trapping; modified from published literature [Allen, 2012]*

Continental deposition of shale may occur by single clay particles settling when water evaporates, or through particles sinking into the ground in lake beaches and in ephemeral river floods and also under extremely stagnant conditions in swamps and lagoons; however, marine processes are responsible for the largest shale volume deposition. As in this research all case studies are marine reservoirs, this research is focussed on shale

characterization under marine conditions, specifically shallow marine and turbidite environments.

2.5.1 Shallow marine environments

Shale deposition in shallow marine environments depends on river water density versus sea water density, particle aggregation processes, the dominant energy regime in the environment and major eustatic changes. If the concentration of suspended particles at a river mouth makes the water flow less dense (the most common scenario) than the sea water in the basin receiving it (sea water is usually denser because of the large amounts of dissolved components), hypopycnal flow occurs, which means than the river water is buoyant and flows above the basin water. This condition enables clay to remain longer in suspension and travel further into marine hemi-pelagic and pelagic conditions while sand and silt are deposited. In the opposite scenario, a hyperpycnal flow, denser river water flows beneath the basin water (this occurs during floods), in which case, the higher concentration of particles favours flocculation and faster aggregate settlement [*Boggs*, 2006]. In this scenario, the structure of the deposits is usually chaotic, as clay, sand and silt are mixed, and in general, the gravitational differentiation based on granulometry goes from poor to moderate.

Clay flocculation (by water salinity increase) and biogenic pelletization are certainly very active processes in shallow marine environments, but usually the high energy of these environments exceeds aggregate fall velocity, which allows particles to remain in suspension and to then be transported and slowly settled in the prodelta, platform and deep marine environments, so very little shale is deposited in shoreface and wave/river dominated deltas. Tide dominated areas are the high energy exception in shallow marine environments, as clay is deposited when water sinks during receding tide and shale laminations form part of heterolithic intervals deposited during the cyclic high and low tide. Shale deposition may also happen in some particularly shallow marine environments with low energy, such as marine lagoons, where restricted saline waters speed up flocculation and deposition of fine clastics; in secluded conditions, water evaporation also favours shale deposition (red sediments due to oxidation processes).

Due to their geological and geographical positions, shallow marine environments are particularly sensitive to eustatic changes, especially to the rise of sea level which moves inland the high energy line represented by the shoreface. During transgressions, the

energy in general decreases, so waters carry only sedimentary loads in suspension, which flocculate and settle in very homogeneous and lateral continuous shale layers. Therefore, most of the shallow marine shales (that constitute excellent inter-reservoir and seal barriers) are deposited during transgressive pulses, as flooding surfaces. Lower energy associated with summer and drought seasons may lead to deposition of shale laminations, which, however, remain likely to be eroded by subsequent flooding or rainy season deposits.

2.5.2 Turbidite environments

To understand shale deposition in turbidite environments, first it is necessary to clarify that turbidite sedimentation occurs inside a bigger frame, consisting of both the slope-abyssal plane and deep marine conditions, where slow pelagic deposition of clay aggregates is the dominant process. In deep marine environments, the low energy favours clay aggregate settlement. The distribution of this material is conducted by marine and submarine currents. During seasonal or an exceptionally high influx of sediments into the basin, and depending on the platform geometry and length, very fine sand and silt layers and laminations may be deposited, inducing vertical heterogeneity in the sediments. The occurrence of turbidite flows depends on several parameters: the most important factor is fast and abundant sedimentation in the platform, which reduces the time for water expulsion from the clay open fabric aggregates, as the deposition of successive clay, sand and silt layers blocks water expulsion paths, ending up with a thick and very unstable sequence of sediments (due to the high content of water). Relatively short platforms in front of river mouths with big sedimentary loads is in general the ideal combination for turbidite development (good examples are Tertiary turbidite systems in the Gulf of Mexico developed by Mississippi River sediments, North Atlantic Slope in the United Kingdom Continental Shelf and the lower Congo River fan system in Angola Offshore). Dip changes in the platform edge (just a couple of degrees is needed), tremors and the weight of the oversaturated sediment sequence favour slope failure and lateral displacement, creating gully-like detachment surfaces through which the sediment column collapses and flows down-dip towards the platform slope and abyssal plain. As the intruding current is denser than the sea water [*Potter et al.*, 2005] the turbidite flow follows the sea bottom topography. The high energy flow carries a mixture of fine but very well sorted sand (medium and coarse sand usually do not reach the platform edge),

silt and clays from the collapsed sequence, and in its path this mixture incorporates eroded clays and silt deposited in deep marine pelagic conditions. As the sediment mass moves, some grain differentiation starts to occur, with poorly aggregated clay floccules going back into suspension, while silt and sand are transported as bottom load in the current. Large and highly consolidated clay aggregates may behave like clasts and travel as heavier particles, together with sand, and are thereafter deposited as dispersed shale inside main turbidite sand channels. The re-suspended clay aggregates will settle gradually over the high-energy sand bodies, giving to turbidite deposits their very distinctive fining up pattern profile [*Bouma et al.*, 1962]. The upper section of that sequence is sometimes eroded by the subsequent turbidite flow in stacked systems. Due to aggregate size and weight, re-suspended clay settles faster than pelagic flocculate, and traps more water in its fabric. Levee and overbank turbidite deposits present vertical and lateral grain-size gradation, creating a transitional fining up profile of sand – silt – resettled shale – pelagic shale.

Due to the intrusive character of the turbidite flow into the deep marine environment, pelagic shales constitute the underburden substratum of the sandy facies; re-settled shale carried by the turbidite current creates an immediate cover that can constitute the turbidite seal – the overburden or just intra-reservoir shales (if they are not eroded) in the case of stacking and coalescence between channels from different flows. If the time between turbidite current depositions is long enough, some inter-reservoir shales may be composed mainly of pelagic sediments. When changes in the basin dynamics do not favour the generation of turbidite flows, (for example, due to lower sediment influx from the continent), the overburden is constituted initially by resettled clays and overlying them, homogenous pelagic shale. The configuration of the sideburden is mostly gradational between resettled clays and pelagic shales. It is important to clarify that during turbidite deposition, pelagic processes never stop, but the amount of sediments and energy in the deep marine environments rarely interferes with the fabric and distribution of the turbidite deposits. Some exceptions are related to the presence of strong submarine currents parallel to the slope, which may re-work part of the unconsolidated sediments, creating contourite deposits.

2.6 Shale heterogeneity and internal architecture

In conventional reservoir characterization the common perception is that below the petrophysically defined rock cut-off, shales are pure mudstones, homogeneous intervals composed of almost 100% clays, when most of the time conditions to deposit such rocks are far from those to deposit a clean package of reservoir sand [*Potter et al.*, 1980]. A common assumption is that environmental conditions change extremely fast, creating an abrupt lithological contrast between clean sand and pure shale, which however, does not correspond to the majority of scenarios in nature (intrusive turbidite flows into deep marine conditions are one of the very few exceptions). So, based on logic and observation of the dynamic conditions, one concludes that there are transitionality, seasonality and cyclicity between high and low energy regimes in a specific sedimentological environment, and even though the two lithological end members (clean sand and pure shale) may exist in the same sequence, there is a high probability that an intermediate lithological spectrum is deposited as a consequence of the evolution of the energy from very low to high or vice versa. Based on this argument, it is fair to assume that shales associated with conventional clastic reservoirs are heterogeneous, as a consequence of gradational changes in energy, which can be easily evidenced by the presence of fining up or coarsening up trends in the electrofacies of shale intervals.

Excluding overbank shaly sediments associated with river flooding and tide-influenced deposits, low energy is predominant during shale sedimentation. Under conditions of low energy, similar patterns of sedimentation tend to occur over a wider area of influence. For this reason, at the outcrop and reservoir scale, shales are believed to have more lateral continuity than sandstones. The study of the internal architecture of shales involves recognizing elements in their structure that point to deviations from the typically low energy conditions: these can include interbedded deposits of sand and silt layers or laminations (high energy perturbations) and calcite streaks (from an increase of carbonatic influx or conditions), together with shale. The presence of these heterogeneous deposits reveals shale hydraulic structures such as stratification, bedding and lamination, which are all used for description, characterization, correlation and prediction purposes, usually below log and petrographic scales of analysis. The depositional hydraulic structures of shales are commonly affected by bioturbation, which consists in the disturbance of sedimentary deposits by living organisms (animals and plants). Faunal activities, such as burrowing, ingestion and defecation of sediment grains, construction and maintenance of galleries, and infilling of abandoned dwellings, all displace sediment

grains and mix the sediment matrix [*Meysman et al.*, 2006]. The occurrence of bioturbation in shales increases their anisotropy and may contribute to increase shale connectivity and permeability, especially in the vertical direction.

Shale's compositional variations in the clay/silt ratio, type of clay (change of provenance) and organic content can also be reflected in the internal architecture. As these material changes involve density, P-wave velocity, and hence impedance, increases or decreases, some large variations may be enough to create important elastic contrast and be appreciated at the seismic scale [*Singh et al.*, 2009; *MacBeth et al.*, 2011]. Embedded fossils, bioturbation and fractures, which are mostly relatively small features, can cause partial or even total destruction of the shale's original fabric and can have a large impact on its dynamic behaviour, as they create vertical transmissibility paths, commonly absent due to the strong alignment of clay platelets and the narrow/complicated shale pore geometry.

To evaluate the internal architecture of shale, a qualitative analysis can be performed using well logs. As Gamma Ray is one of the field measurements that is most responsive to shale, its analysis constitutes an excellent starting point for shale characterization, with variations in radioactivity related to the presence of heterogeneous lithology. Due to its vertical resolution, GR analysis can also be coupled with microresistivity logs to study stratification, bedding and lamination in shales. To evaluate shale heterogeneity, it is convenient to establish the purest mudstone in the sequence or Maximum Flooding Surface (MFS) that can be identified at the end of a fining up interval, with high GR, density and sonic values, also in image logs, the MFS can be identified as intervals with high clay content. In addition, it is necessary to establish a threshold for shaly sands; having the MFS and shaly sand log bounds as a reference, it is possible to compare the rest of the shaly intervals and gain understanding of their variability. When shale subintervals are identified and correlated from well to well, it can be observed that the correlation of fining up intervals overlying sands is poor when compared to correlations of flooding surfaces, which are more regional events and can be recognized even at basin scale. One should also be aware that abrupt contacts between shales and overlying clean sands may be erosive, which makes the recognition and correlation of the uppermost shale facies in a sequence very difficult. The quantitative analysis of shale architecture can be performed using single or double clay (crossplots) indicators for volume of shale and net to gross estimations, as described in the next section. Establishing representative numerical values for the sand-silt to shale ratio derived from calculations at the reservoir

modelling scale is one of the most challenging procedures in shale characterization, as usual conventional reservoir layering scales are much larger than shale lamination, bedding thickness and vertical variability.

The study of elastic properties of shales and their variations within the reservoir is a valuable method to characterize shale internal architecture, particularly for shale seismic modelling. Plotting shale density from log versus depth, P-wave velocity versus depth or acoustic impedance versus depth can give a hint about the variation in shale the variation in shale properties such as porosity and composition with depth, as a consequence of increasing compaction. The normal tendency is for density and velocity to increase with depth, based on a roughly linear trend, with deviations potentially related to compositional or diagenetic changes, variations in environmental energy, faster shale deposition and hence overpressure development, different provenance, and a different burial history between two intervals and unconformities.

2.7 Vshale and NTG estimations

There is not universal definition of the net-to-gross (NTG) term, as it involves the definition of cutoffs, a simplified representation of reality [*Chen and Larson*, 2013]. In this work, the NTG will be assumed as the ratio of the net play to gross pay thickness [*Egbele et al.*, 2005; *Worthington*, 2010], a concept used to define hydrocarbon productive zones in the clastic reservoirs, and is expressed in fractions with values from 0 to 1. The NTG is usually calculated using volume of shale (Vsh) as shown in the equation 2.1. The NTG estimation is based on the petrophysical qualitative establishment of sand-shale end members (cleanest sand and purest shale). The defined cutoffs or baselines for the two lithotypes varies from reservoir to reservoir, and may also change vertically, in the case of multiple stacked reservoirs with changes in sedimentological environments. The pure shale baseline is used to define how shaly reservoir sands are (applying linear equations), but it is particularly curious that the clean sand baseline is not used to determine how sandy or silty shales are. In numerical simulation, modellers usually assign to shale a value of NTG = 0, regarding all shales as pure mudstones, when most of the reservoir shales (both intra- and inter-reservoir) contain some amount of silt and fine sand, and hence have a NTG > 0.

$$NTG = 1 - Vsh \tag{2.1}$$

Shale Volume (Vsh): is the ratio of shale volume content in a reservoir's productive zone expressed in fractions from 0 to 1. As the term shale is related to laminated argillaceous rocks [*Potter et al.*, 2005] and the fine-grained sediment distribution is not always laminated, in petrophysical evaluations the term Volume of clay (Vclay) is more commonly used. In this research, the term Vsh is adopted (despite academic discussions regarding differences between both of them). There are several methods to calculate Vsh: using core analysis, wireline well logs and drilling well logs (mud logs). Due to their relative lower cost, availability, continuous sampling and accuracy, the wireline well logs are the most widely used. Based on the physics involved in each wireline tool measurement (electrical, nuclear or acoustic) for discriminating shales, some logs can be used directly as single shale indicator, while others need to be coupled to differentiate shale from other lithologies.

Single shale indicator logs

Vsh calculations using single shale indicators are based on baseline definitions for cleanest sand and purest shale; those baselines should be picked within discrete zones, in the case that a field contains two or more reservoirs, and also in the case of changes in sedimentological environments and major stratigraphic events, such as discordances.

Spontaneous Potential (SP): this log measures the natural potential differences between an electrode in the borehole and a reference electrode at the surface. The electrical disequilibrium is created by connecting (in the electrical sense) formations vertically. The SP electric currents (Figure 2-5) arise from the difference in salinity between the borehole fluid (conductive mud filtrate) and the formation water (in the porous medium where diffusion of potential occurs), or by the contact of the borehole fluid with an impermeable surface, with these two scenarios creating responses with opposite polarities [*Rider and Kennedy*, 2013].

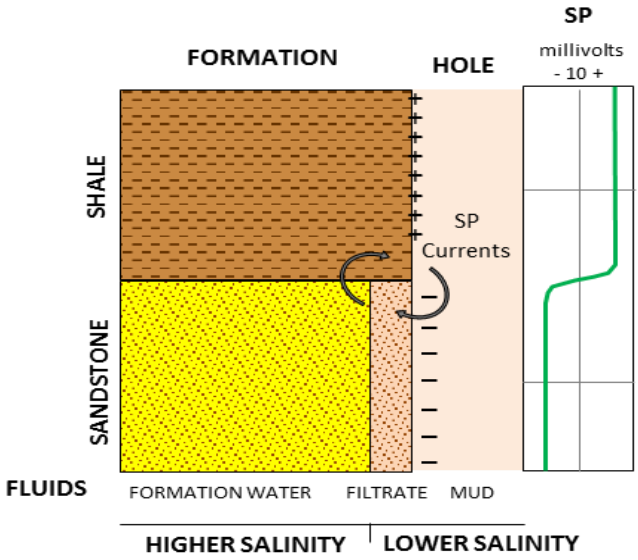

Figure 2-5 *Spontaneous Potential currents in the borehole, redrawn from Rider and Kennedy,* 2013.

As the SP does not have absolute values, this log is treated quantitatively and qualitatively, in terms of curve deflection. Due to the nature of the spontaneous potential contrast, the SP log works better for fresh water mud/saline formations borehole environments as the ion exchange is larger, conditions present in onshore fields. To calculate Vshale using SP, a shale baseline (SP_{shale}) has to be defined in the log value, where the interpreter considers that there is 100% of shale composition, and also a SP_{clean} value, where the shale content is 0%. The Vshale is given by the linear relationship shown in equation 2.2. The role of the mud salinity is very important in creating SP contrast between lithologies. Usually the SP deflections are weak and therefore the bed resolution is poor (lithological boundaries should not be drawn using SP). Minimum vertical resolution is above 3 metres and the penetration depth depends on the hole diameter and formation permeability (2-3 inches for highly permeable and 2-3 feet for very low permeability). The Vshale calculations derived from SP are usually over-estimated [*Rider and Kennedy,* 2013]. The VshSP can give shale trends, but usually needs the analysis of additional logs to define changes in fine-grained rocks, and only if those changes involve variations in the fluids' self-potential. For this reason, the VshSP can rarely be used to define bed structure and mineralogical changes in shales.

$$VshSP = \frac{SP - SPclean}{SPshale - SPclean} \quad (2.2)$$

Gamma Ray (GR): is a record of the formation's natural radioactivity. The GR tool measures the energy (photons with non-mass and no change) emitted by uranium, thorium and potassium particles contained in the rocks. The simple GR gives the radioactivity of the three elements combined, while the GR spectral log shows each element's contribution. Potassium is a very important component of the clay silicate structure of the shales, with an average of 2.7% of the total volume of this rock [*Serra*, 2008]. Uranium is a very soluble element that can be fixed and passed to sediments, and is also abundant in phosphates and bioclasts (uranium is absorbed by organic matter). Thorium is a very stable element found as a detrital component in shales, with more frequency in continental environments than in marine. Most rocks are radioactive to some degree, igneous and metamorphic rocks more than sedimentary ones, but sedimentary shales are by far the most radioactive, as GR is mainly used to identify the presence of this lithology and is also known as the "shale log". With a vertical resolution of 90 centimetres (~3 ft) and a penetration depth of 30 centimetres, the GR log is a very good tool to define bed boundaries, but not in thinly bedded intervals. The GR is the most frequent shale indicator used in petrophysical evaluations for Vshale estimations, and several linear and curvilinear equations have been developed using the GR Index

$$VshGR = IGR = \frac{GR - GRclean}{GRshale - GRclean} \tag{2.3}$$

where, *VshGR* is the Vshale derived from the GR log; I_{GR} is GR index; GR_{clean} is GR (API) value with 0% shale content (sand baseline); and GR_{shale} is GR API value with 100% shale content (shale baseline)

The average Gr_{shale} or pure shale baseline should range between 90 and 120 GR API units, with lower values indicating the presence of chlorite and higher values indicating dominance of illite-kaolinite mixtures in the clay fraction. The linearity of equation 2.3 may lead to overestimation of the volume of shale (Figure 2.6); to correct this, empirical calibrations have been developed [*Bhuyan and Passey*, 1994] using GR logs and laboratory compositional data (equations 2.4 and 2.5).

Curves for I_{GR} less than 0.55

$$VshGR = 0.0006078 \times (100 \times IGR)^{1.58527} \tag{2.4}$$

Curves for $0.55 \leq I_{GR} \geq 0.73$

$$VshGR = 2.1212 \times IGR - 0.81667 \tag{2.5}$$

Considering that clay's natural radioactivity may be affected by the geological time of deposition (burial history, more radioactive protolithic, diagenesis and the illitization process), some empirical corrections (equations 2.6 and 2.7) according to age have also been developed to compensate the effect of higher radioactivity in older shales as consequence of more igneous protolith [*Larionov*, 1969]:

$$VshGR = 0.083 \times (2^{3.7IGR} - 1) \qquad \text{For Tertiary rocks} \qquad (2.6)$$

$$VshGR = 0.33 \times (2^{2IGR} - 1) \qquad \text{For older rocks} \qquad (2.7)$$

Other relationships

$$VshGR = \frac{IGR}{3-2\times IGR} \qquad [\textit{Stieber}, 1970] \qquad (2.8)$$

$$VshGR = 1.7 - \sqrt{3.38 - (IGR + 0.7)^2} \qquad [\textit{Clavier et al.}, 1971] \qquad (2.9)$$

In the case of GR spectral logs, the thorium component is the best Vshale indicator, due to the linear mathematical relationship between the thorium (Th) content (ppm) and Vshale [*Rider M., and Kennedy M.*, 2013].

$$VshGRTh = \frac{Th\,(\log value) - Th\,(clean)}{Th(pure\ shale) - Th(clean)} \qquad \text{(Th in ppm)} \qquad (2.10)$$

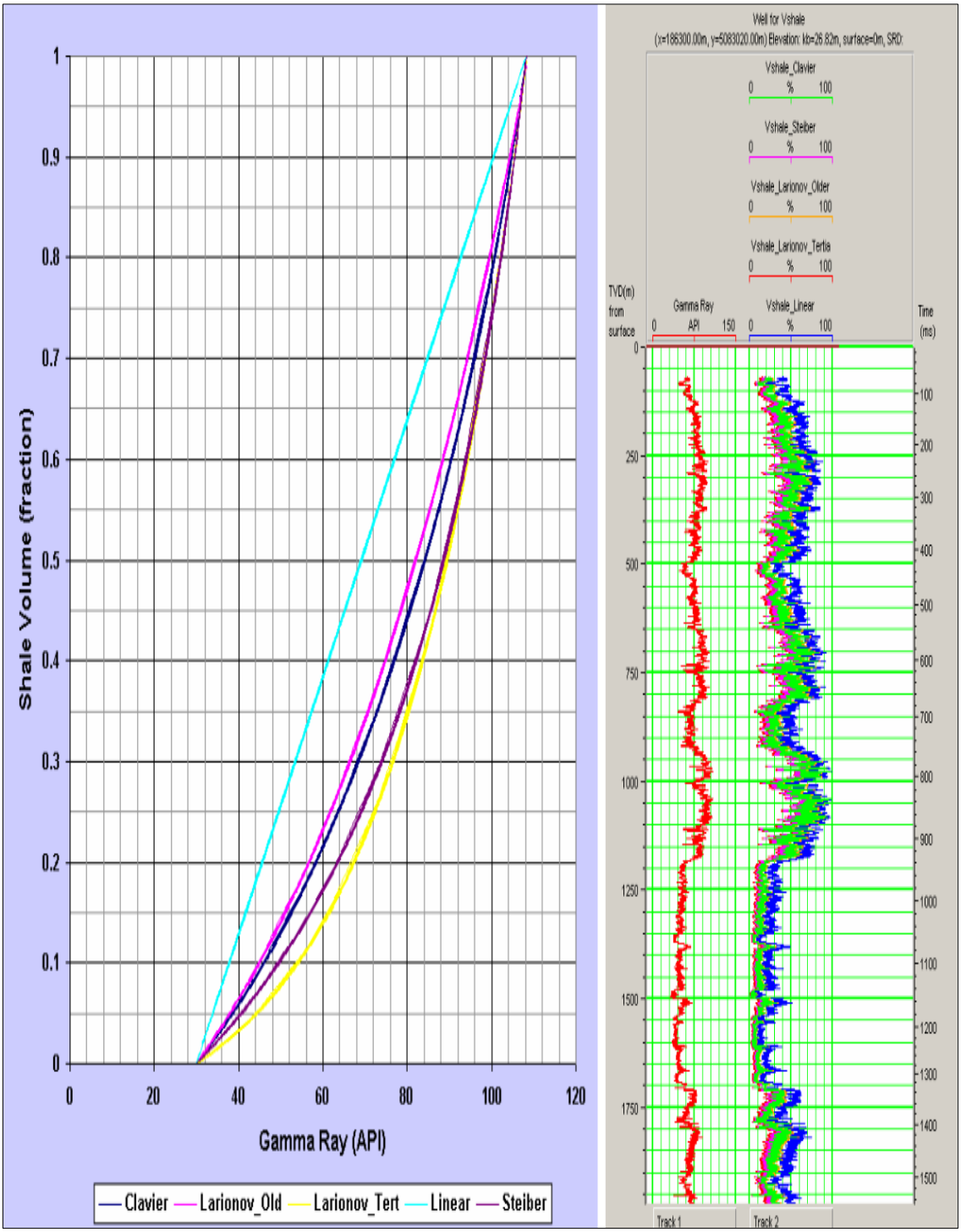

Figure 2-6 *Comparison between some VshGR methods, taken from published literature [Saputra, 2008]*

Neutron porosity (NPHI): this log records the formation's reaction to fast neutron bombardment, which involves subatomic particles travelling through matter and losing energy upon collision with equivalent mass particles such as hydrogen (which is present in both water and hydrocarbons). The Hydrogen Index is almost the same for water and oil, but is especially low for gas (NPHI is a very good gas indicator). In limestone and sandstones, the hydrogen is present in the fluids contained in the pores; for this reason

NPHI gives a measure of porosity. However, despite shales having low porosity (saturated with water), they contain clays that have a significant amount of surface absorbed (bound) water and their hydrogen index is higher than that of other lithologies. Shaly sandstones have higher NPHI values than clean sandstones and therefore an overestimated porosity measure. To study and differentiate this effect the Neutron log has to be coupled with the density or the acoustic logs (see the next section, with double shale indicators) and then calibrated. The natural expulsion of water in shales due to compaction causes a decrease in the NPHI values, and therefore unusually high values (which are out of the NPHI decreasing trends), in some shale intervals are indicative of overpressure. Increase in the organic matter content also produces an increment in the NPHI value of shales and can be used to identify the source rocks intervals [*Rider M., and Kennedy M.,* 2013].

According to the source-receiver spacing geometry of the tool, the neutron vertical resolution can vary from 0.5 metres for GNT (Gamma Ray/Neutron Tool) to 0.4 metres for SNP (Sidewall Neutron Porosity Tool) and 0.25 metres for CNL (Compensated Neutron Log); while the depth of penetration goes from 0.2 to 0.3 metres [*Asquith et al.*, 2004; *Rider and Kennedy* 2013]. Vshale estimation can be derived from the neutron log using equation 2.11. The average pure shale baseline definition should be between 0.40 and 0.50 NPHI units, with higher neutron porosity values related to smectite-rich intervals.

$$VshNeu = \sqrt{\frac{NPHIlog}{NPHIshale} \times \frac{NPHIlog - NPHIclean}{NPHIshale - NPHIclean}} \tag{2.11}$$

Resistivity (Rt): this log is a measure of the formation's inverse conductivity, expressed in ohm-m units. Even though the Microspherical Resistivity (MSFL) gives the highest vertical resolution (about 5 centimetres), for Vsh calculations, due to mud filtrate salinity, the recommended logs for computations are deep laterolog or induction logs, with a lower bed resolution of 60 centimetres [*Rider and Kennedy*, 2013] but higher penetration that gives true formation or uninvaded resistivity (Rt). The relationship with Vsh comes from the equations:

$$Z = \frac{Rshale}{Rt} \times \frac{(Rclean - Rt)}{(Rclean - Rshale)} \tag{2.12}$$

where *Rt* is deep laterolog or induction log reading; *Rshale* is resistivity of a pure mudstone interval (water saturated); and *Rclean* is resistivity of the cleanest sand. If *Rt* is greater than 2 x *Rshale*, then:

$$VshRes = 0.5 \times (2 \times Z)^{0.67 \times (Z+1)} \quad (2.13)$$

Otherwise *VshRes* = *Z*.

Double shale (crossplots) indicator logs

The estimation of volume of shale is based on crossplot analysis, where a clean sand line and pure shale point are defined in a two-shale-log indicators plot (variables plotted against each other), and then the Vsh is estimated according to the data position in the Vsh composition isolines.

Clean sand line: this is defined by two points (see Neutron/Density Crossplot, Figure 2-7).

Point 1: is the theoretical value for quartz monomineral sand (see Table 2-11)

Point 2: is determined by log data and depends on sand porosity, composition, diagenesis and saturation.

Pure Shale Point: is also log data defined and depends on shale composition, porosity and consolidation, with saturation assumed as 100% water.

Crossplot Value	Clean Sand line		Pure Shale Point
	Point 1	Point 2	
RHOB (gr/cm3)	2.65	2.65 – 2.0	3.1 – 2.0
NPHI (v/v)	0	0.0 – 0.30	0.25 – 0.75
DTC (µs/ft)	52.9	51 – 55.5 (Ø from 5 – 20%)	62.5 – 167
Vp (m/s)	5760	5029 – 3505 (Ø from 5 – 20%)	5180 - 2130

Table 2-11 *Common log values for clean sand line and pure shale point definition. With information from published literature [Mavko et al., 2009; Serra, 2008; Rider and Kennedy, 2013]*

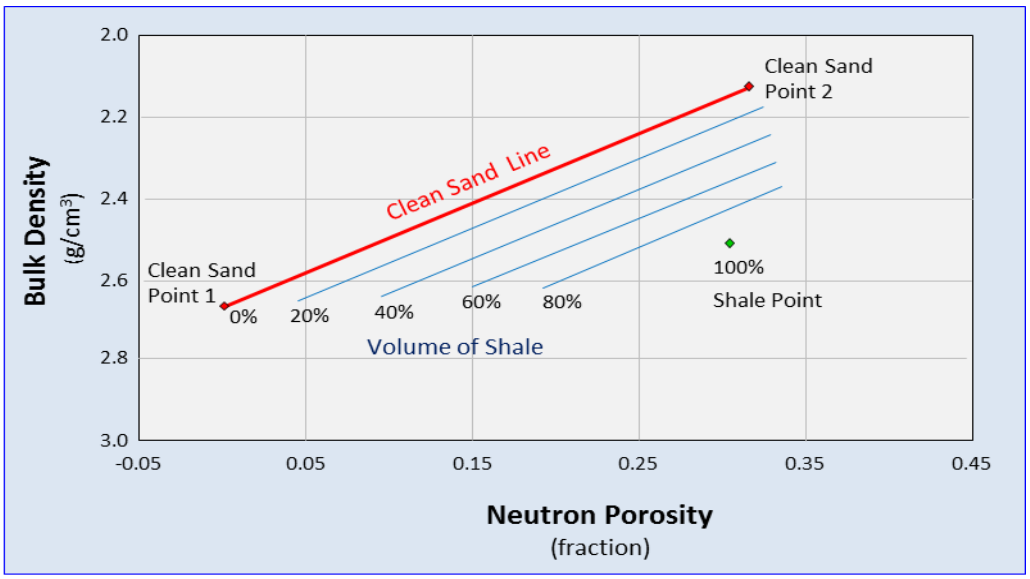

Figure 2-7 *Neutron Porosity & Bulk Density Crossplot for Volume of shale estimation*

Neutron / Density crossplot Vsh estimation

$$VshND = \frac{[(DenCl2-DenCls1)\times(Neu-NeuCl1)]-[(Den-DenCl1)\times(NeuCl2-NeuCl1)]}{[(Den\ Cl2-DenCl1)\times(NeuSh-NeuCl1)]-[(DenSh-DenCl1)\times(NeuCl2-NeuCl1)]} \quad (2.14)$$

Sonic / Density crossplot Vsh estimation

$$VshSD = \frac{[(DenCl2-DenCls1)\times(Son-SonCl1)]-[(Den-DenCl1)\times(SonCl2-SonCl1)]}{[(Den\ Cl2-DenCl1)\times(SonSh-SonCl1)]-[(DenSh-DenCl1)\times(SonCl2-SonCl1)]} \quad (2.15)$$

Neutron / Sonic crossplot Vsh estimation

$$VshNS = \frac{[(NeuCl2-NeuCls1)\times(Son-SonCl1)]-[(Neu-NeuCl1)\times(SonCl2-SonCl1)]}{[(NeuCl2-NeuCl1)\times(SonSh-SonCl1)]-[(NeuSh-NeuCl1)\times(SonCl2-SonCl1)]} \quad (2.16)$$

Saturation and fluid effect: Most petrophysical parameter estimations are done in water-saturated sand intervals, after the characterization (dependent of salinity, temperature and pressure) of the specific properties of the formation's water (density with a range from 0.95 to 1.15 g/cm^3, P-wave velocity between 1440 and 1550 m/s). To avoid the hydrocarbon effect (density and velocity reduction) in the clean sand line definition (point 2), some petrophysical workflows in commercial software (Interactive Petrophysics, Techlog) extend the clean sand line to the fluid point (100% water), and the interpreter only needs to define the pure shale point (Figure 2-8), thereby simplifying the *Vsh* equations.

$$Vsh = \frac{\emptyset Neu-\emptyset Den}{\emptyset NeuSh-\emptyset DenSh} \quad (2.17)$$

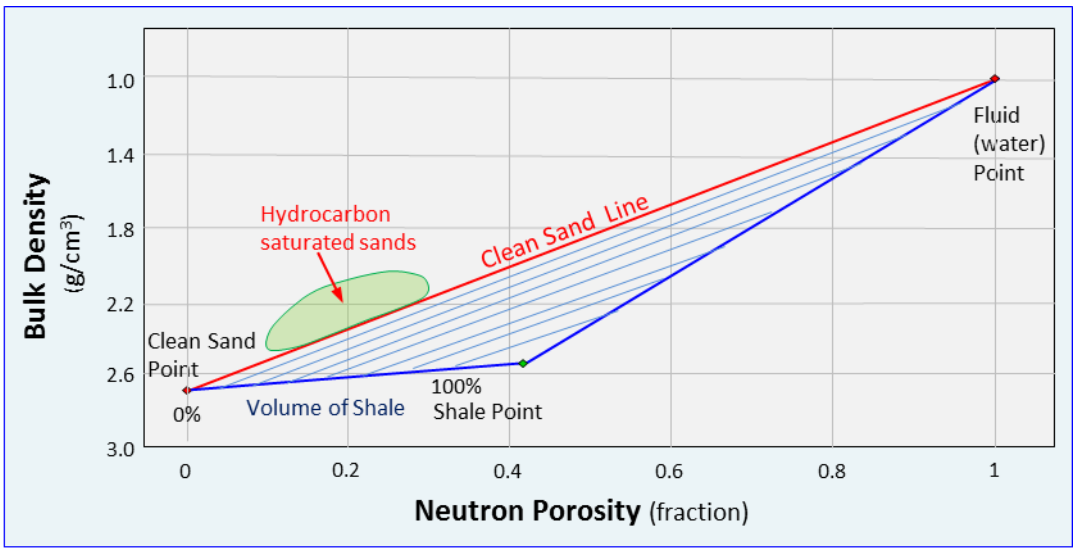

Figure 2-8 *Neutron Porosity and Bulk Density Crossplot for Volume of shale estimation (clean sand line defined with fluid point and quartz monomineralic response. In green, displaced data due to light hydrocarbon effect*

In the active shale workflow developed in this research, the key is to establish the shale baseline in the strictly purest mudstone, in order to then compare the rest of the shales with that scenario. It is important to clarify that Vsh estimation in this project was computed only for shale intervals that were inactive and not for sands: as the NTG may have a large impact on the reservoir reserves estimation, a decision was made to maintain the original hydrocarbon volumetrics of the provided simulation models, with the only exception being the Shearwater Field, where all the static and dynamic properties for sands and shale were modelled from wireline log.

2.8 Porosity estimation

Due to the planar phyllosilicate structure of the dominant component of shales (50% minimum percentage of clays), the porosity of this lithology is strongly dependent on compaction and related processes (water expulsion, precipitation of authigenic minerals – in short, diagenesis). Clays with charged surfaces repel each other, tend to aggregate under water salinity increase (free water ions neutralize surface charges) forming heavier floccules and settling faster. The aggregation between clays usually occurs in sub-perpendicular angles (due to charge attraction); this geometrical arrangement traps a considerable amount of water in the void space. Initial shale post-deposition porosity can be as high as 80% [*Ruud et al.*, 2003], but this decreases quickly with early compaction (Figure 2-9) and most unconsolidated shales have porosities between 15 and 25% [*Yang*

and Aplin, 2007]. Further compaction, water expulsion, illite transformation and other processes can reduce shale porosity to 5%.

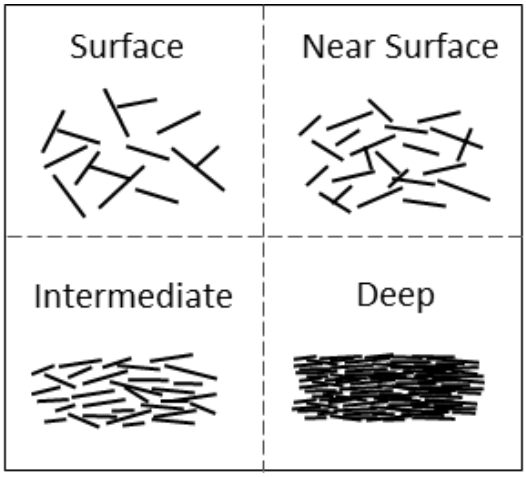

Figure 2-9 *Shale porosity reduction and fabric change with burial*

Shale porosity can even reach sand values, but it is still poorly connected. In fact porosity measures in the laboratory with mercury injection, nuclear magnetic resonance and helium expansion, show that only 60% of shale pore space is connected [*Keller*, 2014; *Mbia et al.*, 2014]. The pore throat diameter is in the range from 5 to 50 nanometres, pore tortuosity and capillary forces hinder fluid flow through shales. In this research I performed porosity estimation based on wireline log data and material balance equations, using as main input the shale component properties (density and velocity) whose proportion was already established in previous analysis. Assuming water-saturated shale intervals, the first step is to calculate the average density or velocity of the mineral components or shale rock frame in the following ways.

Using density:

$$\rho_{sat} = \rho_m(1-\phi) + \rho_w S_w \phi + \rho_g S_g \phi + \rho_o S_o \phi \tag{2.18}$$

As gas and oil saturations (S_o and S_g) are equal to 0, then

$$\rho_{sat} = \rho_m(1-\phi) + \rho_w \phi \tag{2.19}$$

$$\phi = \frac{\rho_m - \rho_{sat}}{\rho_m - \rho_w} \tag{2.20}$$

where ρ_{sat} is saturated density from the log; ϕ is porosity; ρ_m is mineral density; and ρ_w is water density

If the exact component proportions are known, ρ_m can be calculated averaging component densities:

$$\rho_{mineral\_Arithmetic} = \rho_{clay} Vol_{clay} + \rho_{quartz} Vol_{quartz} \quad (2.21)$$

$$\rho_{mineral\_Harmonic} = \frac{1}{\left(\frac{Vol_{clay}}{\rho_{clay}}\right)+\left(\frac{Vol_{quartz}}{\rho_{quartz}}\right)} \quad (2.22)$$

$$\rho_{mineral\_Average} = \frac{\rho_{mineral\_Arithmetic}+\rho_{mineral\_Harmonic}}{2} \quad (2.23)$$

Or being more accurate, by considering feldspar and organic matter:

$$\rho_m = (\rho_{\text{clay mixture}} \text{Vol}_{\text{clays}}) + (\rho_{\text{quartz}} \text{Vol}_{\text{quartz}}) + (\rho_{\text{feldspar}} \text{Vol}_{\text{feldspar}}) + (\rho_{\text{organic matter}} \text{Vol}_{\text{organic}}) \quad (2.24)$$

Using P-wave Velocity:

$$\phi = \frac{Vp_{log} - Vp_{matrix}}{Vp_{fluid} - Vp_{matrix}} \quad \text{(Wyllie equation)} \quad (2.25)$$

Or in the case of very unconsolidated shales,

$$\boldsymbol{\phi} = \frac{Vp_{log} - Vp_{matrix}}{Vp_{fluid} - Vp_{matrix}} \times \frac{1}{Cp} \quad (2.26)$$

where *Cp* corresponds to a compaction factor for shales, that usually ranges from 1.0 to 1.3 [*Dvorkin and Nur*, 1998].

P-wave velocities in equations 2.25 and 2.26 can be directly replaced by the inverse of sonic (transit time) values. The shale interval is considered 100% water saturated, and as the velocity of the water is well-known, the only parameter to estimate is the matrix P-wave velocity, which again can be derived from material balance equations, knowing the shale components and their proportion. Feldspar, organic matter, calcite and other components can also be included in this equation.

$$Vp_{matrix} = Vp_{clay\_mixture} Vol_{clay} + Vp_{quartz} Vol_{quartz} \quad (2.27)$$

For unconsolidated and thick reservoirs, shale porosity estimation needs to take into account the effect of compaction, so it is necessary perform the previous calculations at different datum depths in the reservoir (immediate overburden, middle reservoir and immediate underburden), in order to establish the ratio of shale porosity reduction to depth and introduce a compaction trend in the model.

2.9 Permeability estimation

Poorly connected porosity, extremely narrow pore throat geometry (diameter between 5 to 60 nanometres), tortuosity, small grain and pore size lead to the generalisation of shales being regarded as impermeable rocks. Certainly, fluid flow through pure shales is almost negligible during the hydrocarbon production time scale. However, shales in conventional reservoirs do have heterogeneity, in the form of fine sand and silt laminations that constitute preferential permeable paths. Shale's permeability depends on the clay-silt proportion, specific surface area, porosity, packing, sorting, pore size distribution, capillary forces and compaction (effective stress); autigenic clay mineralization associated with diagenetically mature shales also reduces drastically the already low shale permeability, but highly mature shales are not common in conventional reservoirs. Permeability in shales can be very unpredictable, with the controlling mechanisms not yet fully understood [*Yang and Aplin*, 2007; *MacBeth et al.*, 2011]. Reported permeabilities for shale with a range between 1μD to 1 nD (Figure 2-10), can coexist within shale samples of the same porosity. Shale permeability is strongly anisotropic, and is highly dependent on clay platelet alignment and material heterogeneity.

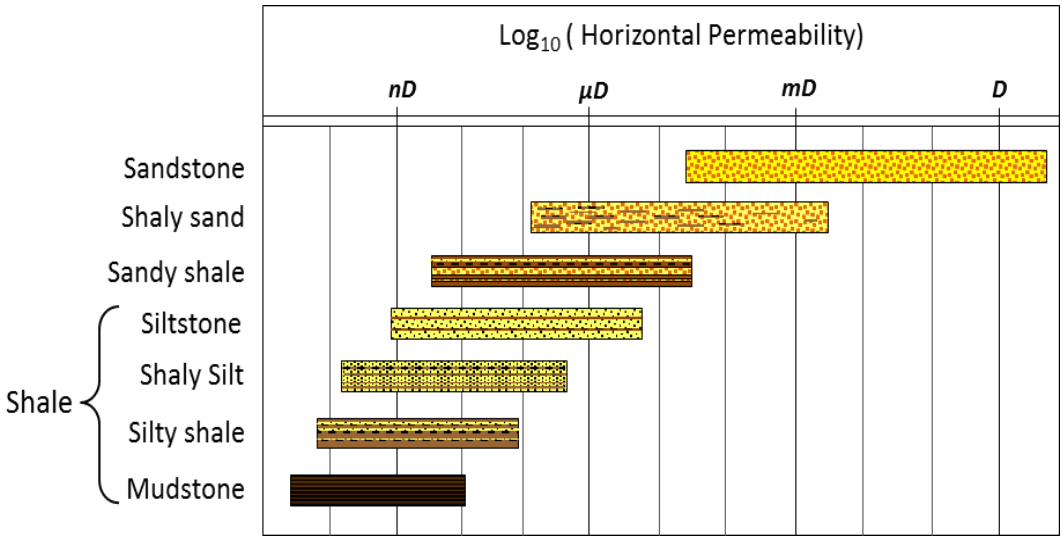

Figure 2-10 *Shale permeability range, redrawn from published literature [HajNasser, 2012]*

Laboratory measurements for shale permeability can be performed using constant flow, constant head, transient pulse decay and pore pressure oscillation. Due to the long time required to stablish steady state flow conditions, one of the most used techniques for shale permeability estimation is the transient pulse decay [*Brace et al.*, 1968]. As shale

permeability laboratory test data were not available for any of the studied fields, in this thesis the estimation of the vertical and horizontal permeability was conducted analytically, following equations and calibrated empirical models [*Yang and Aplin*, 2007], using as input the clay-silt proportion, porosity, pore throat size and pore alignment. Vertical and horizontal permeability are given by:

$$Kv = 10^{-19.21} {J_v}^{1.118} r^{1.074} \tag{2.28}$$

$$Kh = (\cot(\propto))^{2.236} Kv \tag{2.29}$$

where

$$J_v = \frac{9}{8} \emptyset (\sin(\propto))^2 \frac{{J_1}^3}{\left(1+J_1+{J_1}^2\right)^2} \tag{2.30}$$

$$J_1 = 2.371 - 1.62CF^2 + 153.8\emptyset^4 \tag{2.31}$$

J_1 is ratio of the largest radius of a pore to its throat radius; *CF* is clay fraction (from total volume of rock); $\emptyset$ is shale's porosity (fraction); α is the pore alignment; r is the pore throat ratio (nanometres). The pore throat is calculated using a pressure dependent empirical equation [*Lapierre et al.*, 1990].

$$r = \frac{746}{P} \qquad \text{(P is the reservoir pressure in MPa)} \tag{2.32}$$

$$\propto = 45° - 10.24°(e_{100} - e) \qquad \text{(for effective stress } \sigma > 100kPa\text{)} \tag{2.33}$$

$$\propto = 45° \qquad \text{(for effective stress } \sigma \leq 100kPa\text{)}$$

$$e = \frac{\emptyset}{(1-\emptyset)} \qquad \text{(void ratio)} \tag{2.34}$$

$$e_{100} = \frac{\emptyset_0}{(1-\emptyset_0)} \qquad \text{(void ratio at 0.1 MPa)} \tag{2.35}$$

To define $\emptyset_0$, which is the critical shale porosity or post-depositional porosity at 0.1 MPa of effective stress, I used the following relationship [*Ruud et al.*, 2003]:

$$\emptyset_0 = 0.8 \frac{Vol_{clay}}{Vol_{shale}} + 0.4 \frac{Vol_{quartz}}{Vol_{shale}} \tag{2.36}$$

The vertical and horizontal shale permeability estimated for the field applications of this project are in the order of few nanodarcys, but fluid flow, in most cases, is forbidden by capillary forces, modelled much higher than the pressure gradient induced by production or injection. So even when fluid flow should not happen in the modelled scenarios (except

maybe in induced fractures in shales around the wells), the low but finite shale permeability allows pore- pressure diffusion, a process that occurs much faster than the physical movement of the fluid and is not strongly limited by capillary forces [*MacBeth et al.*, 2011; *Thambynayagam*, 2011].

2.10 Shale modelling in simulation models

Once the static and dynamic properties of the shale have been estimated, the next step is their inclusion into the simulation model in order to evaluate pressure diffusion through shale and its implications in the reservoir saturation and induced elastic changes. The first step after changing the reservoir ACTUM (Eclipse keyword used to switch on or off a cell in the model) is considering if the model boundaries need to be changed; depending on the sand-shale geometries, reservoir structural and stratigraphic configuration, some extra sideburden, overburden and underburden cells or layers must be added to the initial 3D grid of the model. The advantage of adding these layers in the overburden and underburden to study the shales' response at top and bottom reservoir is that layer thickness can be reduced at more appropriate vertical scales (down to 1 metre or even less) to represent shale heterogeneity. The thickness of reservoir sandy cells is usually greater than 4-5 metres, even in fine scale models. As a result of this, intra and inter-reservoir shales (inactive cells in conventional modelling) are also represented at this coarse vertical scale, making it more difficult to honour shale variability, as property averaging and upscaling does not always capture shale anisotropy. Local grid refinement can be a solution, only applicable to 'layer cake' models with uniform vertical and horizontal distribution of shales, but these geometry modifications may bring problems during the synthetic seismic modelling, with the definition of the seismic gather corresponding to each cell centre.

With the model geometry established, populating inactive cells with shale static and dynamic properties is the next step, which strongly depends on the parameters used in the original model to represent reservoir heterogeneity, as the inclusion of shale must be compatible with the reservoir variability (inter-cell interaction is based on shared properties). The most obvious choice of parameters consists of variable NTG, porosity and permeabilities, but some companies only choose variable porosity and permeabilities, and use NTG as a switch on or off discriminator (1 for active and 0 to inactive). As the effective porosity (the multiplication of NTG by porosity) is very low for shales, the NTG

of shales has to be used as a variable input in the model and not as an on/off switch discriminator. In conventional reservoir dynamic modelling it is common to define rock types and saturation regions (under the Eclipse keyword SATNUM), which are mostly used to model transmissibility, connectivity and barriers between reservoir units. To some extent, this zone definition is also an expression of reservoir heterogeneity. Throughout this thesis, the sole constraints set on shale interaction were based on permeability values and capillary forces. Hence geobodies were not used to restrict shale transmissibility or connectivity with other facies; instead, they helped to define different types of shales and their corresponding spatial extents, which were thereafter populated with static and dynamic properties. Geobody definition was especially helpful in defining the regions of intra and inter-reservoir shales, as overburden and underburden shales are readily defined by additional layers. The next section describes the methodology used to model shale pore pressure, saturation, capillary pressure and relative permeabilities using the Eclipse software, but the principles can be applied to any available numerical simulator software.

2.10.1 Shale pore pressure and saturation

The definition of these two parameters is linked to the establishment of one (or the necessary number) of equilibrium zones (EQUILNUM keyword in Eclipse) for shale pre-production conditions, which can be done by either grouping all inactive cells, or using subgroups of a few layers, in the case of multiple shale zones. Once the spatial distribution of each equilibrium zone is established, its properties are defined in the SOLUTION section of the .DATA file using a pressure gradient (a pore pressure value associated with a specific depth datum), fluid contact depths (OWC and GOC) and capillary pressures at those contacts. If shales are not overpressured, the reservoir's pore pressure gradient (which is usually estimated in the field with RFT or production tests) can be used as guide to define the shale pressure, whereas in the case of overpressured intervals, higher values of pressure (extracted from drilling reports based on mud weight for those intervals) have to be used.

Shales in the case studies of this research were considered as 100% water saturated in pre-production conditions, to ensure that fictional oil-water and oil-gas contacts were created, defining their corresponding depths in the overburden at much shallower positions than the simulation model top, creating a water saturated column that goes from base to top in the model, only for the shales grouped under that equilibrium zone.

Capillary forces at those contacts are irrelevant but need to be numerically defined, or the simulation run will be compromised. In this work, shale water saturation is set at 100%, as during the hydrocarbon migration process the replacement of water by oil or gas in the shale pore space is a very unlike event, due to the high water-clay surface electrochemical affinity, poor pore connectivity, pore throat size and, finally, capillary forces. Shales modelled in this research are not considered as source rock, so oil or gas generated within them is discarded. Shale formation water was assumed to be similar to the reservoir water in all the field applications, so values for salinity, density and viscosity were taken from the PVT (pressure-volume and temperature test) reports.

2.10.2 Capillary pressure and relative permeabilities

The modelling of shale capillary pressure and relative permeabilities in this research was based on correlations of pore throat size (estimated with equation 2.32) between shales of the different case studies and samples of Barnett Shale and Louiseville Clay formation cores with laboratory measurements of mercury capillary pressure [*Lapierre et al.,* 1990; *Sigal,* 2013]. After looking at the results from the mercury injection test across different samples and the amount of pressure needed to change the shale saturation (the maximum pressure conditions during test were as high as 60.000 psi = 4136 bars), some patterns emerged, with the range in the incremental intrusion or fluid displacement depending strongly on pore throat, specifically ranging from 40% of the pore space in samples with pore throat ratio between 3 and 5 nanometres (Figure 2-11), up to a maximum of 60% for samples with pore throat ratio between 20 and 50 nanometres. The latter observed trends were very consistent with other laboratories' measurements of shale pore connectivity less than or equal to 60% [*Keller,* 2014; *Mbia et al.*, 2014].

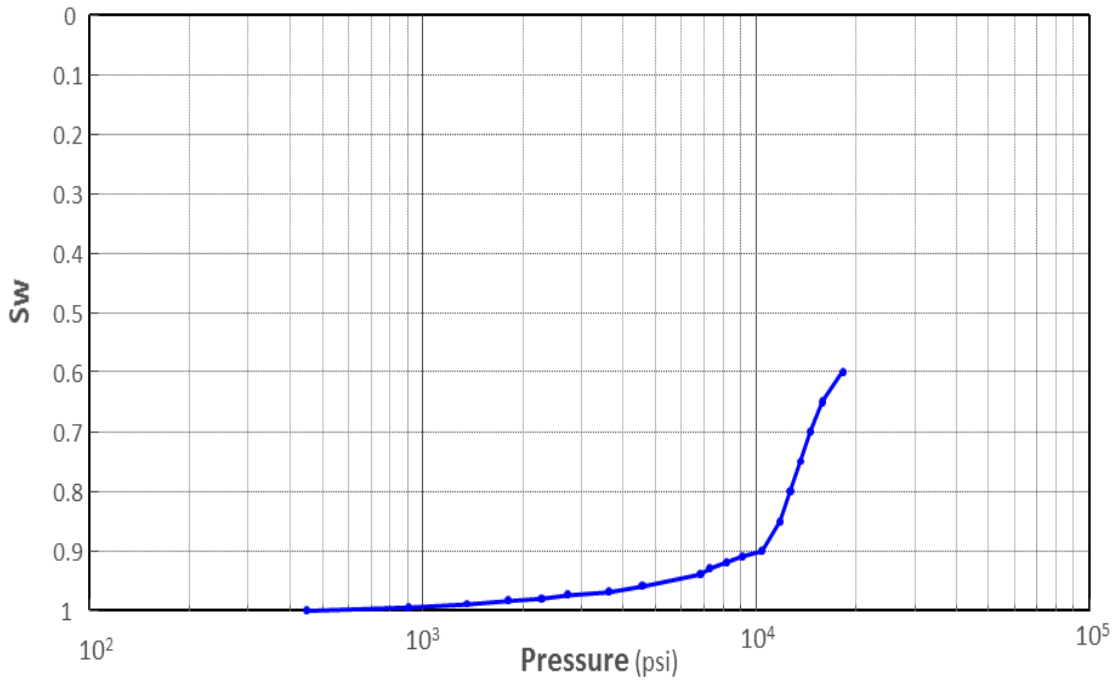

Figure 2-11 *Mercury incremental intrusion test on a Barnett Shale sample with a 3 nanometre pore throat, redrawn from published literature [Sigal, 2013].*

Relative permeability tables were built, taking as reference changes in water saturation with the pressure needed to produce the fluid displacement, see Table 2-12 and Figure 2-12.

Sw	Krw	Kro	P (bars)	P(psi)
0.6	0	1	1250	18180
0.7	0.001	0.92	1000	14545
0.8	0.03	0.6	877	12725
0.9	0.09	0.31	720	10450
0.92	0.17	0.17	560	8181
0.94	0.25	0.09	470	6815
0.96	0.31	0.06	313	4545
0.97	0.38	0.04	250	3630
0.975	0.47	0.02	187	2720
0.985	0.7	0.005	125	1810
0.995	0.9	0	62	909
1	1	0	0	0

Table 2-12 *Water Saturation (**Sw**), water relative permeability (**Krw**), oil relative permeability(**Kro**) and capillary pressure (P)in bars and psi for a shale sample with 3nm pore throat ratio size [Sigal, 2013].*

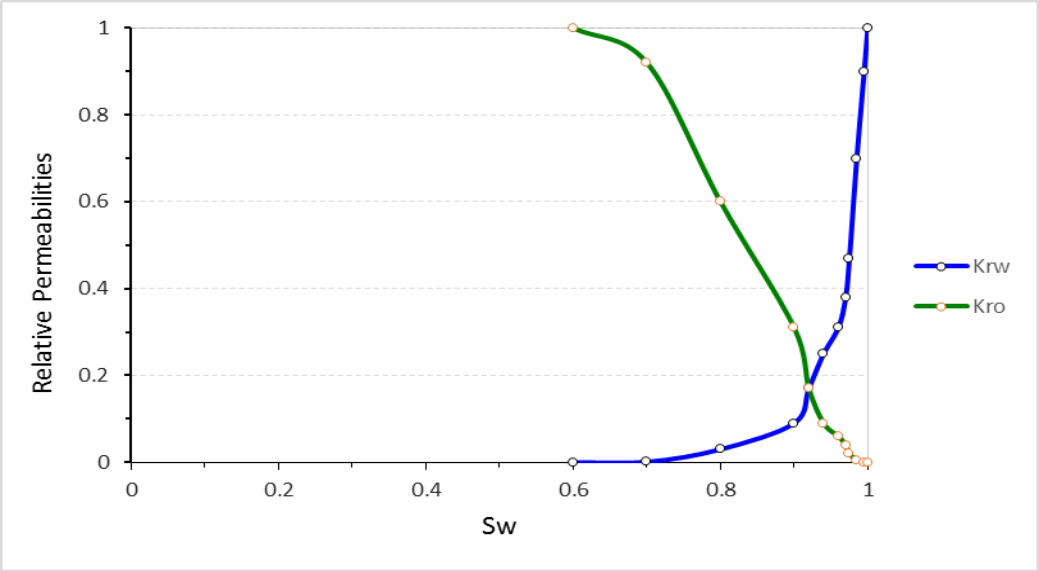

Figure 2-12 *Oil and water relative permeability curves for a shale sample with 3nm pore throat ratio size [Sigal, 2013]*

2.11 Shale elastic modelling

One of the ways to describe the elastic behaviour of a specific material under changing stress conditions is through its elastic moduli, which are relationships (fourth-rank tensors) describing the ratio of stress applied to a body to the resistance (strain) produced by the body. From the different elastic constants, the bulk (K) and shear (G) moduli are the most used in seismic modelling, as they relate material density to seismic wave propagation velocities, which are all parameters measured in wireline log data. As saturated bulk and shear moduli (natural rock state in the subsurface) are dependent on fluid properties, and those can change during the reservoir production lifetime, the modelling of the elastic properties is performed based on rock matrix properties, and as in the modelled scenarios changes in shale saturation are forbidden by the modelled capillary forces, there is no need to perform fluid substitution equations to find the saturated moduli for any period during production. The bulk and shear moduli of the rocks are given by:

$$G_{matrix} = {Vs_{matrix}}^2 x \rho_{matrix} \tag{2.37}$$

$$K_{matrix} = {Vp_{matrix}}^2 x \rho_{matrix} - \frac{4}{3} G_{matrix} \tag{2.38}$$

where G_{matrix} is the static shear moduli of the matrix; K_{matrix} = static bulk moduli of the matrix; ρ_{matrix} is the matrix density; Vs_{matrix} is the matrix S-wave velocity, which is the

same as $Vs_{saturated}$, as the shear moduli does not sense fluids, and Vp_{matrix} is the matrix P-wave velocity.

Shale matrix density can be calculated from equations 2.21 to 2.24 using density library values (Table 2-5) for mineral components and proportions; or, since porosity, saturated density and fluid properties (water) are known, a material balance analysis can be applied. Similarly, matrix P-wave velocity can be calculated from library P-wave velocities for the shale's mineral components proportions (Table 2-6, equation 2.39), or from basic material balance equations (2.41), assuming that compressional acoustic waves propagate isotropically (non-fabric dependent) in the shale mineral frame and fluid, and that P-wave velocity of the components can be averaged based on their proportions. The assumption of shale isotropy, in terms of velocity propagation, can be valid for some particular scenarios and types of shale [*Sayers*, 2010] and has been used as a simplification in this thesis, but it is widely recognized that shale velocity anisotropy can go up to 25%, depending on compaction [*Hornby*, 1998; *Sayers and Dewhurst*, 2008; *Sondergeld and Rai*, 2011], organic matter content [*Vernik and Nur*, 1992; *Sondergeld and Rai*, 2011] and maturity [*Prasad et al.*, 2009].

$$Vp_{matrix} = \left(Vp_{clay\ mixture} \times Vol_{clay}\right) + \left(Vp_{silt} \times Vol_{silt}\right) \tag{2.39}$$

$$Vp_{saturated} = [(1 - \emptyset) \times Vp_{matrix}] + \left(\emptyset \times Vp_{fluid}\right) \tag{2.40}$$

$$Vp_{matrix} = \frac{Vp_{saturated} - \left(\emptyset \times Vp_{fluid}\right)}{1 - \emptyset} \tag{2.41}$$

If the sonic log was not acquired with dipolar tools, Vs can be computed using the empirical equations for water saturated mudstones [*Castagna et al.*, 1985], or using a Vp/Vs ratio >1.8 for water saturated shales.

$$Vp = 1.16 \times Vs + 1.36 \qquad \text{(Velocities in Km/s)} \tag{2.42}$$

Depending on how the reservoir heterogeneity was represented in the simulation model, the Bulk and Shear matrix moduli had to be defined for each saturation region (SATNUM) or for the end members (cleanest sand and purest shale) and then estimated for each cell using the sand-shale mixing average (Backus average method). Bulk and shear moduli are dependent not only on fluid saturation, but also on changes in the effective stress, which may affect the mineral fabric (porosity and clay platelet alignment). Effective stress depends largely on induced pore pressure variations in the reservoir. Unfortunately, this research lacks geomechanical laboratory data to test the

shale rock frame's response to pressure changes. The only available pressure-dependent relationships to model stress sensitivity were the equations from *MacBeth*, 2004, so in this work, shales are regarded as equally stress sensitive as sands [*HajNasser*, 2012]. Changes with pressure in the elastic moduli are given by:

$$Kdry_{(P)} = \frac{K_\infty}{1+E_K e^{-P/P_k}} \tag{2.43}$$

$$Gdry_{(P)} = \frac{G_\infty}{1+E_\mu e^{-P/P_\mu}} \tag{2.44}$$

where K∞ and G∞ are high pressure bulk and shear moduli asymptotes; P_k and Pμ are the characteristic pressure constants that determine the rollover point beyond which the rock frame attains its state of relative insensitivity; E_k and Eμ are constants calibrated from isotropic loading and P is pressure in MPa.

With the cell elastic parameters defined (after the sands had been modelled similarly), the synthetic seismic modelling of different scenarios of shale activation for each field application was performed using the ETLP Reservoir Geophysics group's in-house Simulation to Seismic (Sim2Seis) code [*Amini*, 2014], which converts simulation data into impedances and then into synthetic seismic volumes, following the below workflow (Figure 2-13).

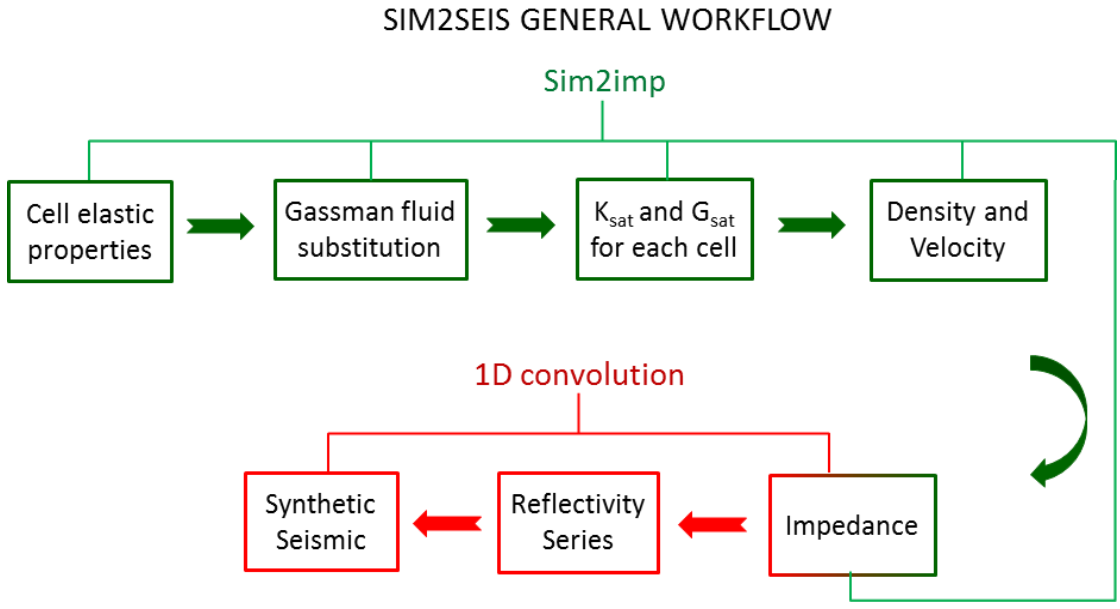

Figure 2-13 *Simulation to Seismic general workflow*

2.12 The 3D and 4D seismic interpretation

With the availability of the observed and synthetic seismic volumes corresponding to the different monitored stages of the reservoir, the first step in the interpretation of the obtained results is the static comparison of the predicted seismic volumes with the observed seismic data, a comparison usually performed between pre-production seismic volumes. The parameters to compare in this 3D data quality assessment are: top reservoir-overburden contrast (i.e., did the amplitudes of the synthetic data capture properly the elastic interface between the two media?); concordance in the geometry of the reservoir (are faults, the lateral reservoir extension and the shape of the horizons following those from the static seismic interpretation?); reservoir internal reflections (i.e., is the synthetic data showing lower scale events than those recorded in the observed seismic, or some events were missed?); reservoir thickness: this parameter is an excellent indicator of how accurate was the velocity and density modelling of the field lithology, as a faster or harder modelled interval will show a thinner reservoir and a or slower or softer modelled interval will lead to reservoir thickness overestimation.

If the results are satisfactory, the next step is the 4D signal estimation and interpretation; otherwise, the elastic modelling of the reservoir may need to be repeated or even the grid geometry and cell properties modified. As, by definition, all models are wrong but some can be useful [*Box et al.*, 2005], a reasonable match between the observed and the synthetic data is acceptable.

The 4D seismic signal can be extracted by using volumetric or surface attributes and computing the differences between the base and a specific monitor. As shale pressure diffusion is a process with dependence on time, the 4D seismic signal was computed only between long production periods (several years between the acquisition of the base and the monitor) and when the pressure profile of the reservoir showed a trend change (depletion or build up stages). The volumetric 4D differences are usually estimated by just performing the mathematical subtraction between the monitor and the base seismic volume (Equation 2.45), the operation is performed trace by trace and sample by sample; for this reason the geometry (Inline, Xline and Z range) of the seismic volumes must be exactly the same. The interpretation of the results is done on the base of the softening and hardening distribution (areas where the seismic amplitude decreased or increased as consequence of elastic contrast changes induced by production / injection), and the

visualisation is displayed in vertical intersections (Inline, X line and random direction) or, with less frequency, in horizontal ones (time slices).

Vol4Ddif= Monitor survey – Base survey (2.45)

The 4D seismic signal extracted from surface attributes (the most used method) consists in computing the differences between extracted attributes (amplitude based, most of the time) from the involved seismic volumes. The selection of the particular attribute to extract depends on the section of the reservoir to be highlighted and its seismic expression, the type and polarity of the recorded contrasts within the reservoir and the vertical and lateral variability of seismic reflections inside the interval being studied. At this point, it is paramount to have a properly calibrated well tie, to analyse the lithological and saturation correspondence of the seismic events and to make the appropriate selection of the intervals to evaluate. As amplitude polarity tends to cancel out in computations between intervals with internal reflections, RMS amplitude (Root Mean Square, Equation 2.46) is probably the most used attribute to study the amount of energy (contrast) within an interval, but also, only positive or negative amplitude events can be selected inside the reservoir to perform different arithmetic operations. For the selection of the interval, one or two interpreted surfaces are used to define a vertical and areal search window to apply the corresponding attribute algorithm trace by trace and sample by sample. The result is a surface with a spatial distribution of the numerical attribute computed. The 4D seismic differences are computed by carrying out the subtraction of the attribute from the monitor survey from the attribute extracted from the base seismic volume. The result will show on a map the distribution of positive and negative areas where the amplitude changed between surveys, the interpretation of the polarity is related to increase or decrease in the impedance or elastic contrast in a specific area, as consequence of the production induced changes

$$RMS = \sqrt{\frac{\sum_{base}^{top} {a_t}^2}{N}} \quad (2.46)$$

where a_t is the amplitude at a particular TWT sampling position and N is the number of samples.

3 Chapter:

Case study: Heidrun Field

This chapter addresses the implications of the activation of Not, Ile and Ror Formations, the shaly intervals of the Heidrun Field, and their influence on the 4D signature of the reservoir's dynamic and elastic behaviour. The inclusion of shale properties during static and dynamic reservoir modelling improves pressure and saturation predictability, because sand (reservoir) and shale interaction is allowed in numerical simulations to express the effect of pressure diffusion in this field. Comparison of synthetic to observed seismic data reveals an improved fit when shales are activated. However, the contribution of the added reservoir pressure connectivity through shales to the analysis and interpretation of the Heidrun Field behaviour and prediction of the 4D seismic response is limited by the poor understanding (in the current available model for the field) of the complex fault transmissivity, which produces an intricate compartmentalization in the reservoir.

3.1 Field generalities

The Heidrun Field is an oil & gas reservoir located 190 kilometres offshore in the Halten Bank region (blocks 6507/7 and 6507/8) of the Norwegian Sea, in water depths of 350 metres, covering an area of approximately 40 km^2 (Figure 3-1). Discovered by Conoco and partners in 1985 and on-stream since October 1995, the Heidrun Field contains estimated recovery reserves of 186 million cubic metres of oil and 46.5 billion cubic metres of gas. The field is operated by Statoil (12.41%) on behalf of its licence partners Petoro (58.16%), ConocoPhillips (24.31%) and Eni (5.11). Reserves are developed using a floating concrete tension leg platform (TLP), which was the first ever to be installed in the world.

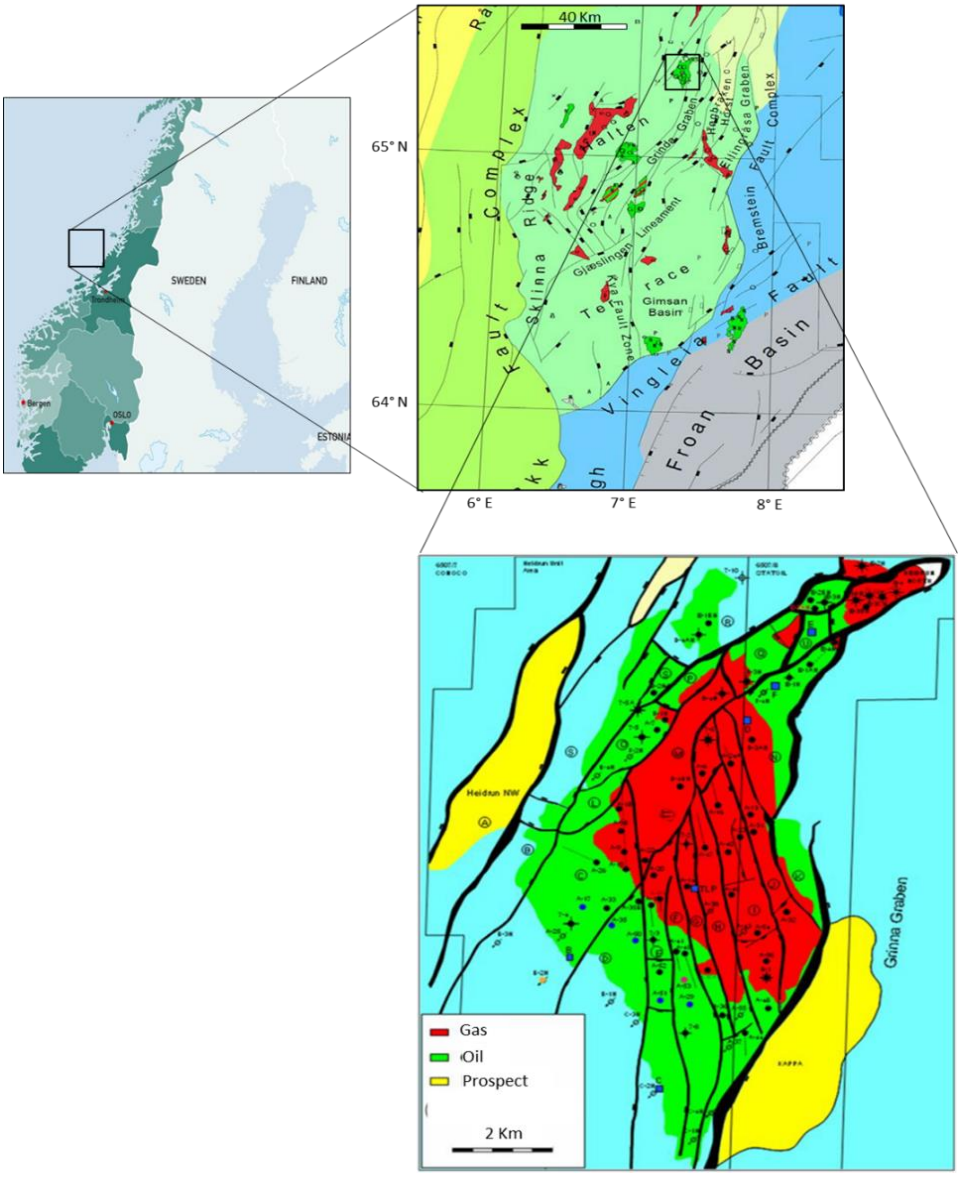

Figure 3-1 *Heidrun field (fluid distribution map) and Haltenbanken location. Modified from Statoil internal report.*

Located between 2175 and 2475 metres TVD, the reservoir is highly compartmentalized, due to its typical Jurassic fault-tilted block configuration. Reserves consist of live oil (28° API) and primary gas cap accumulations in the very good quality sandstones of the Fangst and Bat Groups (porosities up to 35% and permeabilities up to 5000 mD). To maintain reservoir pressure (260 bars at top reservoir) and drain the oil column up to 190 metres, the primary production strategy has been up-flank gas and down-flank water injection, together with gas cap expansion. During several campaigns, an intense infill drilling (77 wells until 2011) has been conducted to accomplish an effective oil sweep; however due to the complexity of the field, the prediction of drainage pattern, fluid saturations and contact movements has proven to be difficult. This may be tracked better through time-lapse seismic monitoring. For the study and shale activation workflow in this reservoir, the available data comprises wireline well data, the geological model, the reservoir simulation model with history matched production from October 1995 to July 2011 and six seismic surveys 1986/1991, 2001, 2004, 2006, 2008 and 2011. The seismic data used in this study are all full stack.

3.2 Geological context

The stratigraphic and structural configuration of the Halten Terrace or Haltenbanken is the consequence of the extensional tectonic evolution between the northwest margin of the Eurasian Plate (Scandinavian block) and the northeast margin of the North American Plate (specifically the Greenland microplate). Prior to the opening of the northeast North Atlantic in the Paleogene [*Morton et al.*, 2009], this area underwent a number of rift events, from the Late Paleozoic to Early Cretaceous, which are evident in the Halten Terrace from the Toarcian (Early Jurassic) and onwards [*Pedersen et al.*, 1989]. The tectonic activity of this period produced a large influx of clastics into the Vøring Basin and Halten Terrace area, developing very prospective deposits of sands in fluvial and shallow marine environments [*Marsh et al.*, 2010]. The deposition (from Late Triassic to Bathonian, Middle Jurassic) of the Fangst and Bat Groups (which can be correlated with the North Sea Brent Group) occurred over a series of rotational-normal faulted blocks, which were configured during previous rift events (Figure 3-2). In addition, strike-slip regimes [*Harris,* 1989] created localized depocentres (pull-apart basin type) in the area and stratigraphic variations in the syntectonic deposits.

As consequence of the increment of energy, the Early-Middle Jurassic interval shows a coarsening up profile in the sedimentation and occasionally erosive events (Base Callovian Unconformity [*Harris*, 1989]) even when the subsidence makes sedimentological environments more marine towards the top of the sequence, starting from fluvial and deltaic settings at the base, to shoreface and shallow marine at the top. The predominant sandy sediments of this period are interrupted by interbedded shales (flooding surfaces) deposited by transgressive pulses that by the Late Jurassic dominated and established platform and open marine conditions in the Halten Terrace, as evidenced in the deposition of the shaley Viking Group. Intense Late Jurassic-Early Cretaceous rifting with strong subsidence [*Bell et al.*, 2014] resulted in the distinctive partitioning configuration of the area, with listric or growth faults, tilted blocks, rollover structures, grabens and horsts being very common. During maximum extension, the accommodation of underlying Triassic salt deposits produced locally inverted structures, with elevated blocks and highs partially eroded by the Base Cretaceous Unconformity (BCU) in a regressive pulse.

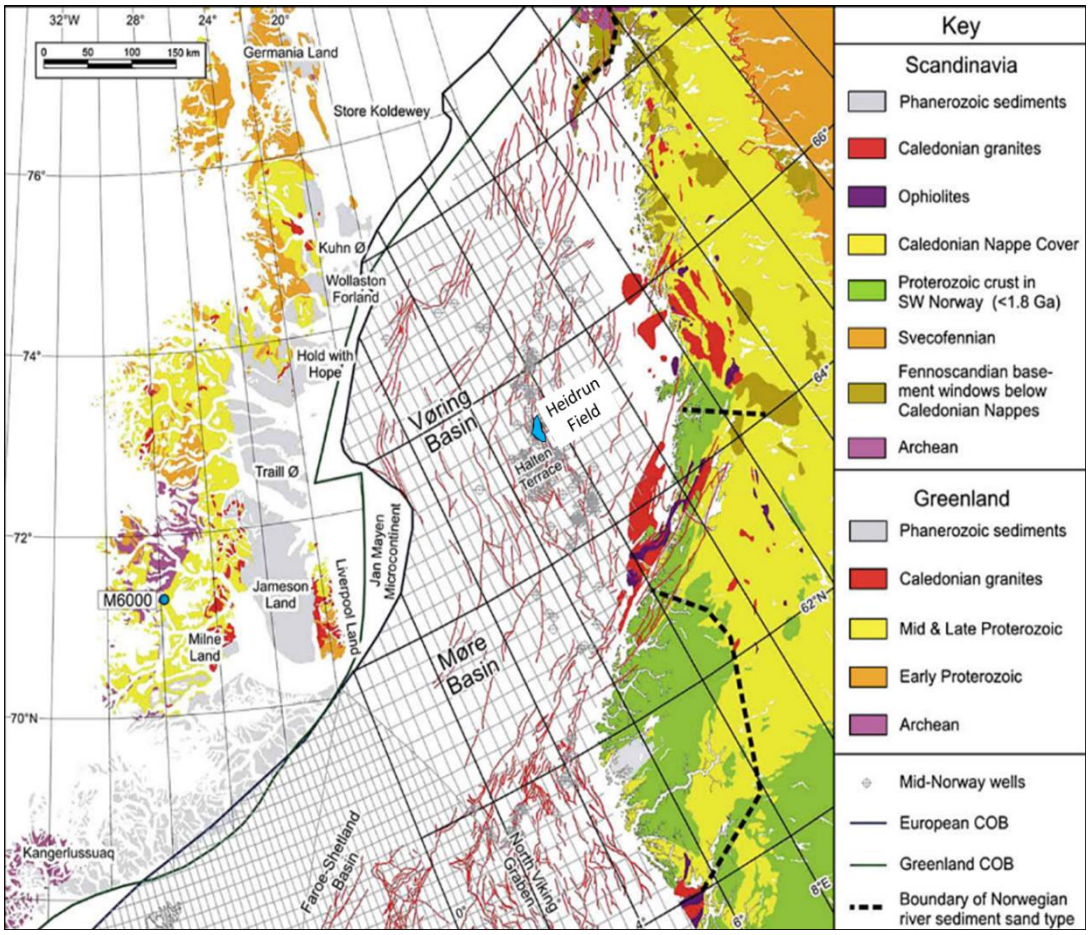

Figure 3-2 *Norwegian Sea reconstruction prior to Northeast Atlantic opening, taken from published literature [Morton et al., 2009]*

The structural configuration of the Heidrun Field consists of a triangular shaped south-dipping (5°) horst block, constrained in the east by a normal fault system of sinistral-slip component and in the west by listric faults. The strike of the main fault system is northeast-southwest with vertical displacement of up to a few hundred metres. A secondary fault system, with a predominant north- south/southeast direction (Figure 3-1 and Figure 3-3), clearly developed after the reservoir deposition but before BCU, and is antithetic to the west listric fault, with throws in the range of 30 metres, reaching values up to 80 metres. The coupled effect of this faulting pattern together with the stratigraphic configuration makes the reservoir highly compartmentalized.

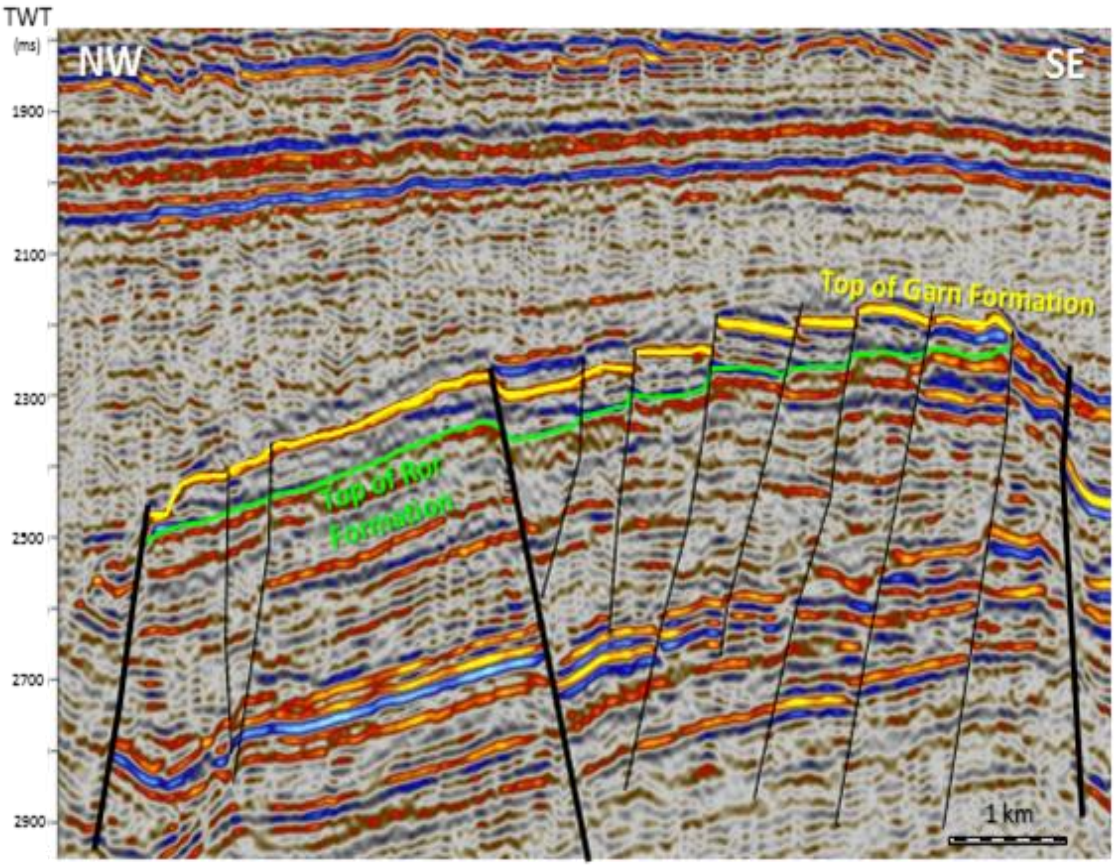

Figure 3-3 *Heidrun Field structural configuration, main faults are highlighted in black bold lines*

The Heidrun Field is comprised of two reservoirs: at the bottom the Early Jurassic fluvial sandstones of the Bat Group with an intricate configuration of sand geobodies and at the top the more prospective and uniform shallow marine and shoreface sands of the Fangst Group, which were deposited in the Middle Jurassic. The two reservoirs are separated by the thick, shaley Ror Formation (Figure 3-4). The next section describes the detailed stratigraphy of the reservoir units.

Fangst Group

Garn Formation: deposited from Bajocian to Bathonian (Middle Jurassic), this unit consist of medium to coarse-grained, moderate to well-sorted sandstones, with some mica rich intervals, cross-bedded laminations, and occasionally carbonate cemented. The deposition of this unit represents the mixture of wave-dominated upper to middle shoreface sediments with progradations of braided delta lobes [*Harris,* 1989]. The thickness of the Garn Formation in the Heidrun Field ranges from 22 – 40 metres.

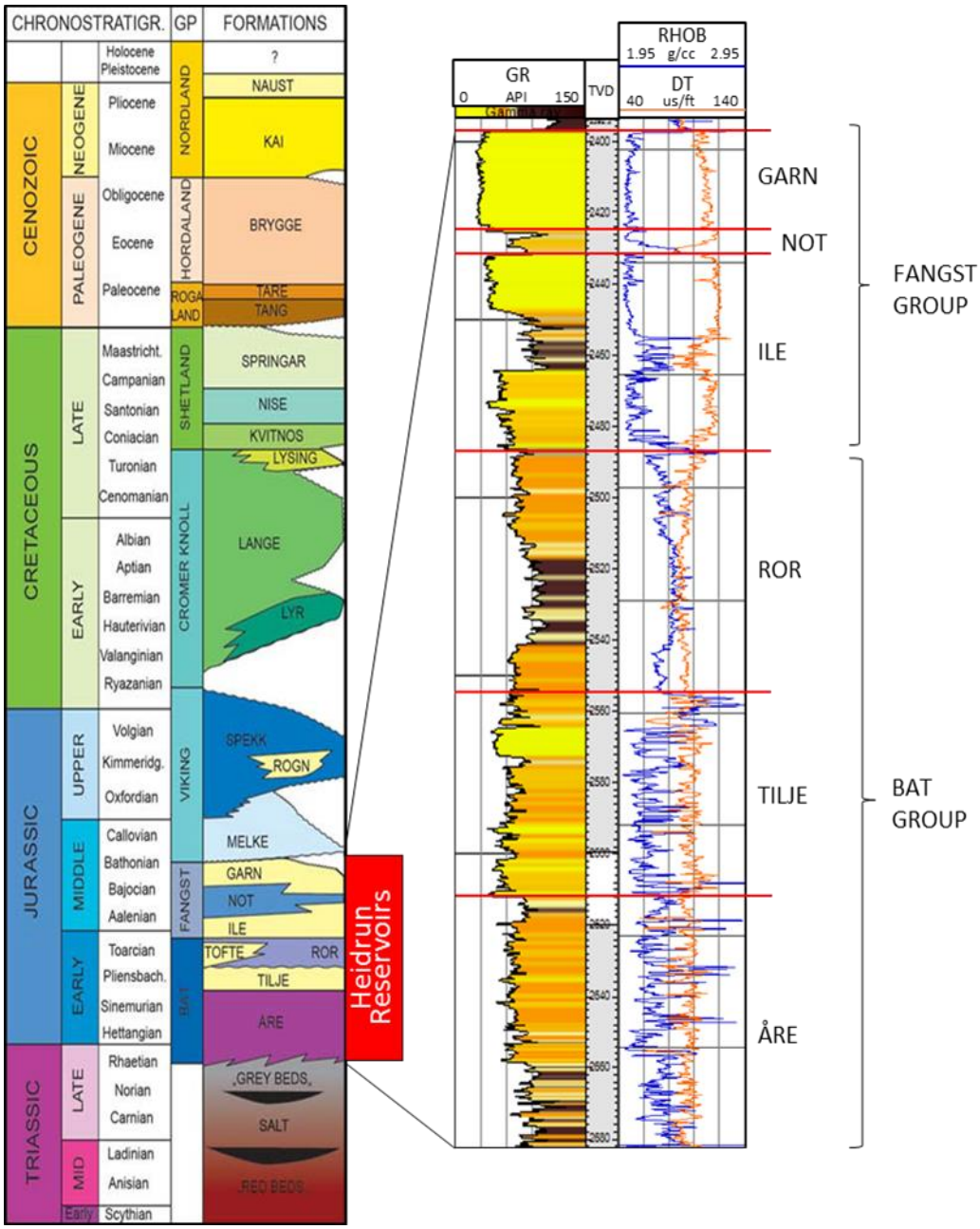

Figure 3-4 *Halten Terrace Local Stratigraphy Column, taken from published literature [Dalland and Ofstad, 1988]. On the right, wireline logs showing lithology response of Fangst and Bat Groups*

The basal contact of the Garn Formation with the Not Formation is erosive (thin basal conglomerate), while the upper contact is non-transitional with the shales of the Melke Formation. In the centre and northeast areas of the Heidrun Field, the Garn Formation is partially or totally eroded by the Base Callovian Unconformity.

Not Formation: deposited from the Aalenian to Bajocian (Middle Jurassic), this formation consists of a shallowing upward succession of offshore shales with micropyrite, siltstones and fine-grained bioturbated sandstones. The depositional environment is a prograding delta front, developed over a very flat platform highly influenced by tides. The basal section of the formation (Statoil internal reports divide this formation into two units in the Heidrun Field) reflects a semi-regional transgression which led to the development of sheltered bays. The thickness of the Not Formation varies from 4 to 10 metres, with the upper contact showing ravinement surfaces by erosion of the Garn Formation.

Ile Formation: deposited from late Toarcian to Aalenian (Early-Middle Jurassic), this formation consists of medium and occasionally coarse-grained sandstones with variable sorting, interbedded with thinly laminated siltstones and shales. Statoil divides the Ile Formation into 4 units, from base to top: a) a carbonate cemented interval, b) a sandstone sequence coarsening upwards, c) a thin laminated interval (Ile Shale Member) composed of shales, siltstones and fine-grained bioturbated sandstones, and d) a transitional prograding coarse-grained sandstone sequence (Upper Ile sands). The Ile Formation was deposited in a delta influenced by tides. The thickness of this unit in the Heidrun Field ranges from 50 to 70 metres.

Bat Group

Ror Formation: deposited from Pliensbachian to Toarcian (Early Jurassic), The Ror Formation consist of dominant grey to dark grey shales with interbedded silty and sandy sequences, coarsening upward, commonly a few metres thick. These sequences become more frequent towards the top of the Ror Formation, with the depositional environment for this unit being open shelf below the wave base. The coarsening upwards trend reflects ongoing shallowing and storm-generated sands. Sand input from the west indicates synsedimentary tectonic uplift along the western margins of the basin. The top of Ror

Formation is transitional to the basal sandstones of the Ile Formation. The thickness of this unit in the Heidrun Field ranges from 70 to 100 metres.

Tilje Formation: deposited from Sinemurian to Pliensbachian (Early Jurassic), this formation consists of very fine- to coarse-grained sandstones interbedded with shales and siltstones. The sandstones are commonly moderately sorted with high clay content, with most of the beds being bioturbated. Mudstone beds are rare; most of the fine-grained interbedded layers are silty or sandy. The Tilje Formation was deposited in a nearshore marine to intertidal environment. Statoil divides the Tilje Formation into 4 units, based mainly on the limits of the internal coarsening upwards cycles. The thickness of Tilje ranges from 80 to 100 metres in the area of study.

Åre Formation: deposited from Rhaetian to Pliensbachian (Late Triassic to Early Jurassic), this unit is a sequence of interbedded very fine- to coarse-grained greyish sandstones with claystones, coals and coaly claystones. The Åre Formation was deposited in coastal plain to delta plain environments, with swamps and channels passing upwards into marginal marine facies [*Harris*, 1989]. Statoil divides this formation into 7 units; the thickness of the Åre Formation in the Heidrun Field ranges from 300 to 500 metres.

3.3 Shale characterization

Production in the Heidrun Field has mainly focussed on the sandstones of Garn and Ile Formations. Due to their stratigraphic positioning, geometrical relationships with the depleted units and potential for pressure diffusion, the activated shales in this study were Not Formation (inter-reservoir shale), the shaly member of the Ile Formation (intra-reservoir shale) and the Ror Formation, treated in this project as underburden shale (Bat group reservoirs were not taken into account). All these shales were deposited in shallow marine environments under the influence of transgressive pulses and general basin subsidence.

3.3.1 Composition

Unlike other case studies in this research, the Heidrun Field database includes laboratory reports with valuable information for the characterization of shales, with most tests conducted in shale samples of the Melke Formation in the overburden (to determine

geomechanical properties). In addition, core analysis was available for the Ile, Not and Ror Formation, with only the last unit containing compositional data. The mineral content and proportions of the Ile shale Member and Not Formation were inferred by coupling well log data analysis and basin evolution to the composition of the underburden and overburden shales. With a marked increase in smectite content towards the top of the sequence, due to higher intensity in the rifting process (more volcanic rocks exposed to weathering), the composition of shales in the Heidrun Field (Table 3-1) also varies in the silt/clay fraction ratio, ranging from higher (45%) average content of silt in the Ror Formation to 30% in the Not Formation (even lower at the maximum flooding surface deposited at the base of Not Formation). Fine sand and silt layers interbedded with shales are very common in this field, especially in the Ror Formation and the Ile Shale Member.

Formation	Silt Fraction		Clay Fraction			Calcite
	Quartz	Feldspar	Illite	Smectite	Kaolinite	
Not	0.2	0.1	0.3	0.35	0.05	0.0
Ile Shale Member	0.25	0.15	0.25	0.3	0.05	0.0
Ror	0.25	0.2	0.25	0.15	0.1	0.05

Table 3-1 *Composition of shales in the Heidrun Field, with information from Statoil internal reports and well logs.*

3.3.2 Shale internal architecture

As shales in the Heidrun Field were deposited mostly during transgressive pulses (base of Not and Ror Formations) or under the influence of tides (Ile Shaly Member), their lateral continuity is good and is captured at seismic scale with very continuous reflectors only interrupted by the normal faults (figures 3-1 and 3-5). Indeed, as sands of the Fangst Group in this area have also a uniform distribution and good lateral extension, the Heidrun Field geological and simulation models resemble a “layer cake” geometry of interbedded sands and shales, and, as highly porous and light hydrocarbon saturated sands are elastically softer than shales and the contrast between those lithologies is pronounced, visually, the seismic reflects the clear elastic signatures of the distinct layers.

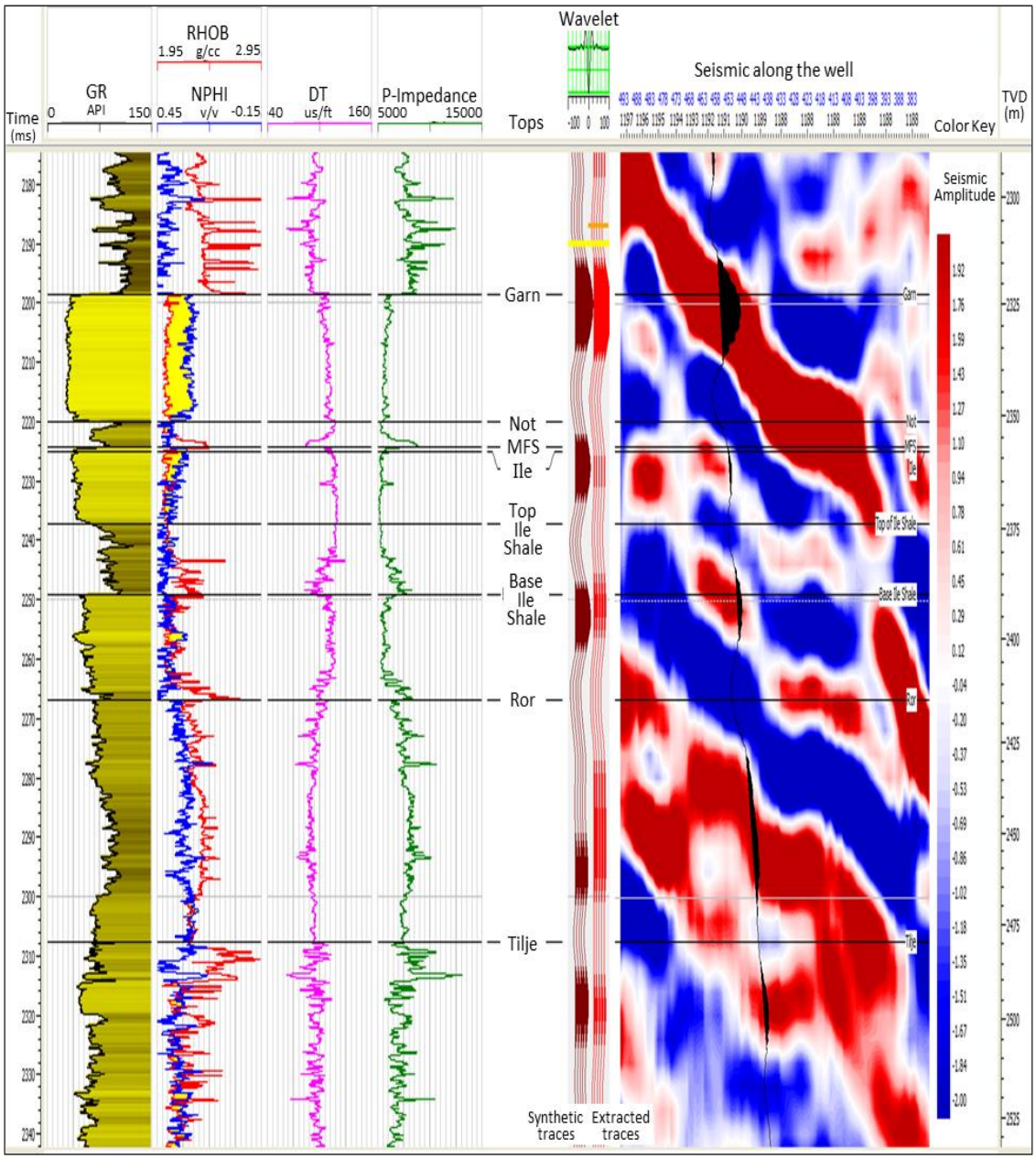

Figure 3-5 *Well tie in the Heidrun Field for the Fangst Group. Strongest seismic reflectors correspond to Top of Garn Formation (also the top reservoir, positive according to North Sea polarity) and to the Ile-Ror Formation interface (calcite-cemented sandstones and water-saturated shaley sequence, negative).*

Shales in this field have good lateral extension, their thickness distribution is also very uniform, and correlation between formations, members and even intervals is easy and straightforward. Only the Not Formation presents thickness variations, due to partial erosion at the top by the high energy deposits (basal conglomerate) of the Garn Formation (Figure 3-6). According to the analysis of several stratigraphic correlations across the field and volume of shale computations, in some delimited areas the Ror Formation and Ile Shale Member show less heterogeneity, becoming shalier, as shown in wells W6 and W7 of figure 3-6. The extent and distribution of this behaviour appears to be controlled

by the occurrence of faults, which were active during the deposition of these intervals, creating locally deeper depocentres with more restricted conditions, favouring higher clay deposition. Mud properties during the drilling of the wells W6 and W7 were similar to those applied for the other wells displayed in the stratigraphic section

From a detailed analysis of the well log electrofacies, unit by unit, the Ror Formation architecture can be subdivided into two main sections: at the base, a fining up interval that goes from shaly sands to interbedded silt and shale and finally to mudstones, which corresponds to a flooding surface; the thickness of this interval is between 20 and 30 metres. The upper section consists of a 40- to 50-metre coarsening up sequence that ranges from shale to shaly sands, with some occasional intervals rich in calcite. The Ile Shale Member is an interbedded interval, the periodic alternation of shale, silt and fine sand clearly evidence the influence of tides as the dominant mechanism during the deposition in a deltaic environment. Globally, the Ile Formation is a coarsening up unit, but that character is not always evident in the Ile Shale Member, but most of the time the contact with the upper Ile sand unit is transitional. The thickness of this interval ranges between 10 to 20 metres. Similarly to Ror, the Not Formation can be divided in two units: a basal fining up interval of 1 - 2 metres thick that ends with the deposition of a Maximum Flooding Surface, followed by a coarsening up section that goes from mudstones to fine shaly sands. The thickness of this interval ranges between 2 and 7 metres and depends on the erosion caused by the basal conglomerates of the Garn Formation. Overburden shales of Melke Formation were not included in this study.

At the smaller petrologic analysis scale, looking at core plug samples of these three shales (Figure 3-7) the architecture is defined mainly by the hydraulic sedimentary structures. The influence of the shallow marine open-shelf conditions in the Ror Formation is reflected by the predominance of horizontal plane thin bedding and laminations of fine sand, silt and shale. Higher energy stages during deposition result in the occurrence of wavy bedding and laminations (image C in Figure 3-7). Rare bioturbation is reported in the Ror Formation.

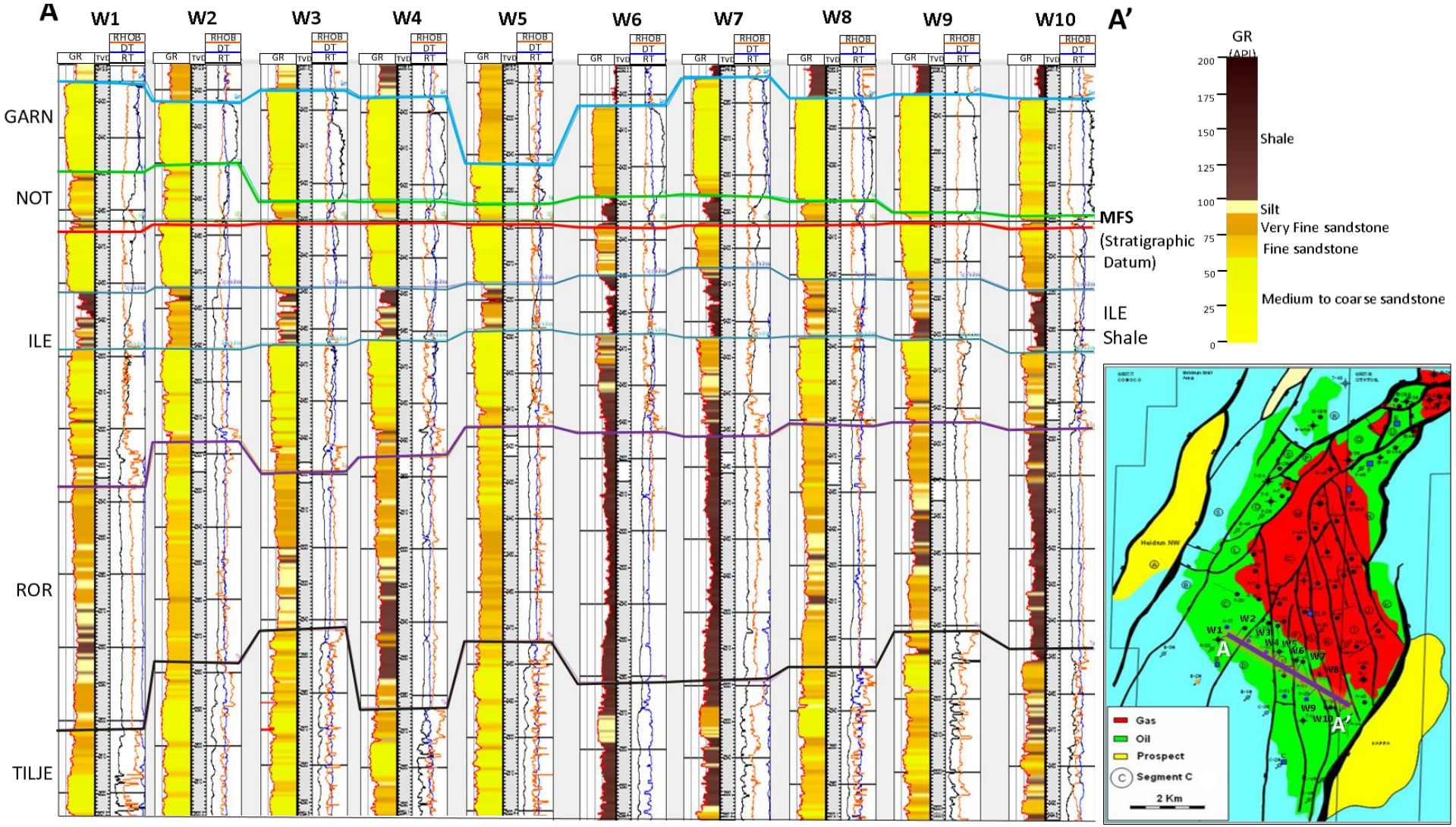

Figure 3-6 *Stratigraphic correlation for the upper reservoir at the Heidrun Field. Datum set at the Maximum Flooding Surface in the Base of Not Formation*

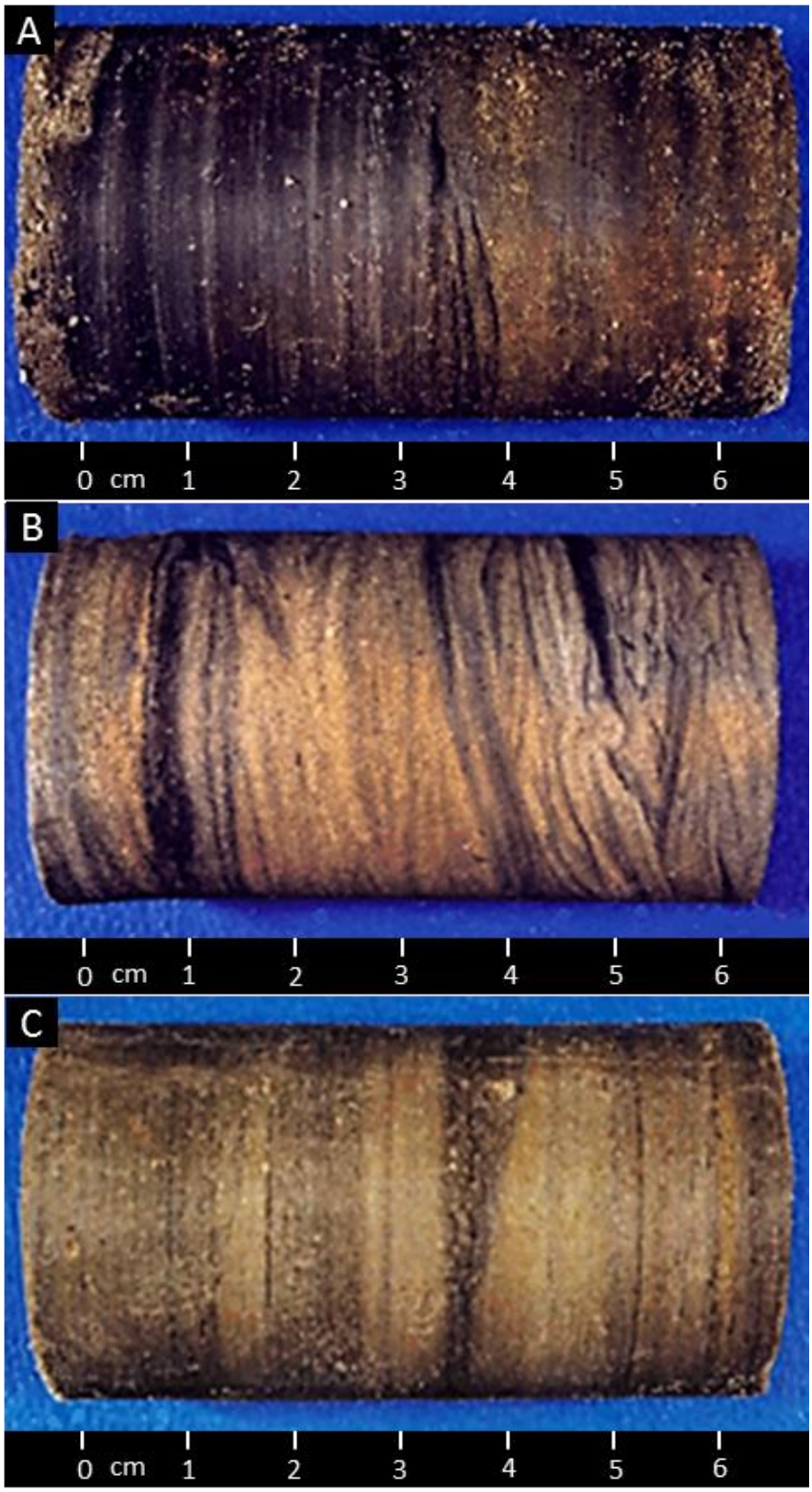

Figure 3-7 *Core plugs of Heidrun Field Shales. A) Not Formation; B) Ile Shale Member, and C) Ror Formation*

The Ile Shale Member (image B in Figure 3-7), presents a higher level of anisotropy, due to the combined effects of fluvial mechanisms, tide influence and reworked clasts, which

results in the occurrence of ripples, lenticular, wavy, flaser and cross-lamination sedimentary structures. The partial or total destruction of these hydraulic features by bioturbation is very frequent. This interval is the siltiest of the Heidrun Field shales. The deeper marine conditions for the deposition of the lower Not Formation interval (image A in the Figure 3-7) are expressed through the occurrence of very fine plane horizontal laminations of shale and silt; shallower conditions in the upper section of this formation produce thicker laminations, and eventually bedding, with the occurrence of fine shaly sands, rare bioturbation is reported for this formation.

3.4 Reservoir model and shales

The initial reservoir model for the Heidrun Field, has the particularity that it regards Not and Ror Formations as inactive, but the Ile Shale Member as an active interval of the reservoir, saturated with hydrocarbon above the OWC and represented in the simulation model as a decrease (not substantial) in porosity and permeability within the Ile Formation. However, the wireline well log analysis suggests that this interval should be considered as shale, although its interbedded layers of sands can play an active role in the reservoir fluid flow. The vertical communication through this shale member must certainly be limited. For these reasons, the Ile Shale Member was remodelled during the process of shale activation for Not and Ror Formations, changing its static and dynamic properties to represent heterogeneous shale behaviour.

As the influence of the Base Callovian Unconformity is stronger northwards in the field (higher up the dip position in the structure) and the Fangst Group units are partial or totally eroded, the shale activation workflow was applied to a smaller area of approximately 3.5 x 6.5 km in the southwest Heidrun Field, where the stratigraphy and structure is more uniform. The boundaries (a purple rectangle, Figure 3-8) were arbitrarily defined, and as Tilje and Åre Formations in this area are below the OWC, their respective layers were also removed from the simulation model, leaving a grid geometry for the model of 77 x 69 x 18 cells (i, j and k directions), with a X and Y cell size of 100 x 100 metres and vertical thickness between 1 and 10 metres

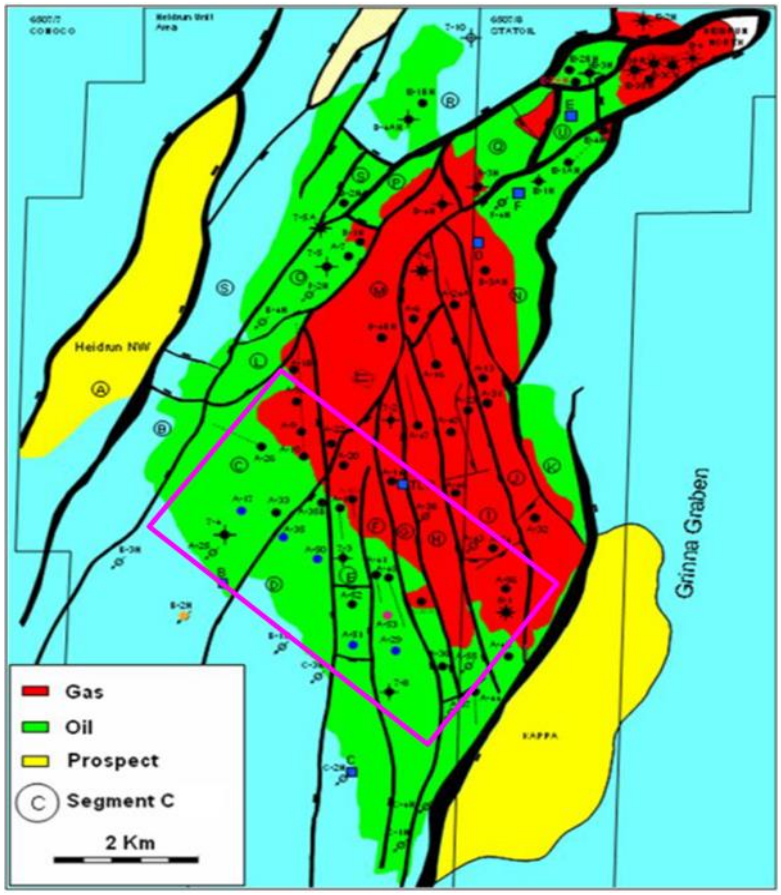

Figure 3-8 *Heidrun Field model showing study area (purple rectangle) and distribution of Garn Formation (in blue). Inner map areas in black show the erosion of this unit.*

3.5 Shale activation and modelling

As the Ile Shale Member was already active in the model as part of the reservoir, the first step was to modify the ACNUM (Eclipse keyword to switch cells on/off) for the cells corresponding to Not and Ror Formation. The distribution of units in the Heidrun Field model is defined by layers, which facilitates the process of population or modification of cell properties. With shale compositions established, and using wireline well log data, the static and dynamic properties of each interval were estimated and upscaled to the reservoir simulation model grid scale. In order to evaluate different scenarios or degrees of shale activation, the population of shale properties followed two modelling approaches: one model corresponding to a conservative shale properties from typical library values and the other model based on the estimation of properties from well log data. Due to Heidrun Field shales being thin, no compaction trend was modelled for shale properties varying with depth; so, in this case, only composition determined the variations between the different modelled shales. Moreover, as modelled shales were laterally continuous, grid refinement to represent heterogeneity was discarded.

3.5.1 Static properties

In the existing simulation model for the Heidrun Field, the reservoir heterogeneity was expressed directly in terms of effective porosity, using NTG as an on/off switch to discriminate reservoir from non-reservoir layers (NTG=1 for active and NTG=0 for inactive), which was not changed for the reservoir sands. Shale intervals were populated with variable NTG, based on Vshale estimations computed using GR as a shale indicator (equations 2.1, 2.3 and 2.7); high smectite content in shales of the Heidrun Field reduce the reliability of Vshale computations based neutron/density logs methods. Regarding Not, Ile Shale and Ror Formation porosities, the estimation was performed using density and p-wave velocity wireline log data and material balance equations (2.20 and 2.25). The modelled static properties used for simulated predictions are shown in Table 3-2, for the conservative (low scenario, Model 1) and computed properties (Model 2).

Shale	Conservative (Model 1)		Estimated (Model2)	
	NTG	Porosity (%)	NTG	Porosity (%)
Not Formation	0.1	8	0.2	12
Ile Shale Member	0.1	8	0.25	15
Ror Formation	0.2	10	0.35	17

Table 3-2 *Static properties modelled for Heidrun Field shales*

3.5.2 Dynamic properties

3.5.2.1 Shale permeability

The permeabilities for Not, Ile Shale and Ror Formations, were computed applying the model of *Yang and Aplin* (2007), which consists of empirical equations (2.28 and 2.29) using reservoir pressure, shale porosity, clay fraction and pore throat geometry to estimate horizontal and vertical permeability. Taking into account that the direction of source provenance and deposition is the same as that of the X-axis of the simulation model grid, clay platelet alignment suppose larger connectivity in that direction too, so, the horizontal permeability in that direction was modelled 1.5 higher than the horizontal permeability in the Y-axis direction, especially for the Ile Shale Member and Ror Formation, where the fluvial influence is stronger, while the more marine conditions in the Not Formation reduce that directional anisotropy. The estimated permeabilities and those corresponding to the conservative shale activation scenario are shown in Table 3-3.

Shale	Conservative parameters (Model 1)			Estimated properties (Model 2)		
	Kh		Kv	Kh		Kv
	X	Y		X	Y	
Not Formation	20 nD	15 nD	1 nD	60 nD	50 nD	10 nD
Ile Shale Member	20 nD	15 nD	1 nD	150 nD	100 nD	17nD
Ror Formation	500 nD	500 nD	10 nD	4.5 µD	3 µD	50 nD

Table 3-3 *Heidrun Field shale permeabilities; Kh=horizontal permeability and Kv=vertical permeability*

3.5.2.2 Pressure, saturation, capillary forces and relative permeabilities of the shales

As there was no evidence of overpressure development in the modelled shales of the Heidrun Field, the pore pressure of Not, Ile Shale Member and Ror Formations was modelled similarly to the reservoir units. To accomplish this, an extra equilibrium region (in SOLUTION section of the Eclipse .DATA file) was defined in the simulation model for Not, Ile Shale and Ror Formation with the same pressure gradient (267.17 bars) and depth datum (2550 m TVD) as that of the reservoir units of the Fangst Group. In the same shale equilibrium zone, the oil-water and gas-oil contacts were fictionally defined at 2250 and 2200 metres, respectively, at shallower positions than the Fangst Group reservoir, with OWC at 2451 metres and GOC at 2293 metres, in order to make shales 100% water saturated above and below the reservoir hydrocarbon contacts.

Regarding shale capillary pressure and relative permeabilities; the modelling was based on pore throat diameter correlation between the Heidrun Field shales and literature references of mercury injection test results of Barnett Shale and Louiseville Clay formations [*Lapierre et al.*, 1990; *Sigal*, 2013] and some assumptions about the degree of shale pore connectivity, in the way that higher silt fraction content is proportional to lower irreducible water saturation (Table 3-4). As the induced depletion is lower in most cases (Ror Formation is the exception) than the necessary pressure gradient to change shale's saturation, fluid flow from and into shale cells in the model is very unlike to occur. Pressure, saturation, capillary forces and relative permeabilities were modelled as the same for the two active shale models (conservative activation and estimated properties).

Not Formation				Ile Shale Member				Ror Formation			
Sw	**Kwr**	**Kor**	**CP**	**Sw**	**Kwr**	**Kor**	**CP**	**Sw**	**Kwr**	**Kor**	**CP**
0.6	0	1	4000	0.5	0	1	3500	0.4	0	1	3000
0.65	0.05	0.95	3200	0.6	0.05	0.95	2810	0.5	0.05	0.95	2650
0.7	0.1	0.9	2500	0.7	0.15	0.85	2050	0.6	0.15	0.85	1900
0.75	0.2	0.8	1700	0.75	0.25	0.75	1450	0.7	0.3	0.7	1100
0.8	0.4	0.6	790	0.8	0.45	0.55	920	0.8	0.45	0.55	780
0.85	0.6	0.4	650	0.85	0.65	0.45	530	0.85	0.6	0.4	470
0.95	0.8	0.2	300	0.95	0.8	0.2	250	0.95	0.75	0.25	215
0.99	0.9	0.1	75	0.99	0.9	0.1	60	0.99	0.9	0.1	50
1	1	0	0	1	1	0	0	1	1	0	0

Table 3-4 *Relative permeabilities and capillary pressure modelled for Heidrun Field shales. Sw= water saturation, Kwr=relative permeability to water, Kro= relative permeability to oil, Cp=capillary pressure*

3.6 Simulation Results

To understand the impact of shale activation in this field, apart from the conservative modelled parameters and estimated properties models, a base case scenario with all shales inactive (original Heidrun Field simulation, Model 0) was included in the results analysis as reference, to compare changes in pressure and saturation. According to the Heidrun Field pressure profile (Figure 3-9) and the availability of seismic survey monitors, the results for the three simulated scenarios will be analysed only for the predicted July 2006 and July 2011 time steps, which match the end of pressure depletion and build up periods respectively, and also coincide with the acquired 4D seismic. All simulations were carried out using the Eclipse numerical simulator, keeping the same run parameters, model boundaries, and history matched production data.

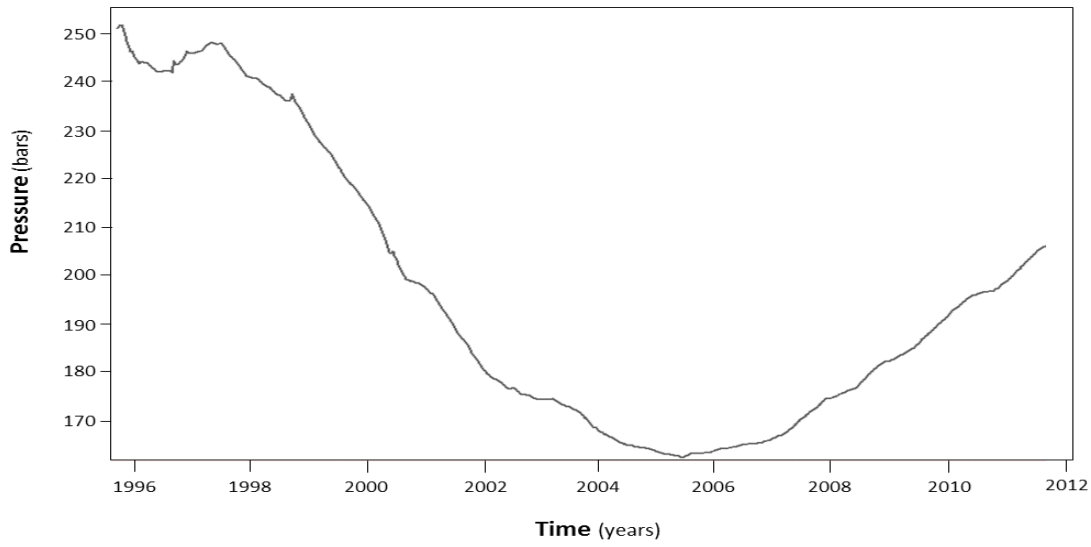

Figure 3-9 *Heidrun Field pressure profile; showing an initial depletion stage (injection was not effective as a consequence of poor understanding of fault transmissivity) and then a build-up stage.*

3.6.1 Pressure diffusion

Looking at the pressure results for the three modelled scenarios (Figure 3-10), we firstly observe that the Ror Formation only shows pressure diffusion in the smaller compartments, where the depletion is higher in the reservoir units (maybe linked to fault transmissivity), but in most cases (Models 1 and 2) pressure changes are absent. The second observation is that the Not Formation shows more pressure diffusion (in some blocks, even pressure equilibrium with Garn and Ile sands for Model 2) than Ile Shale Member, even when Not Formation was modelled with lower permeability values. These results clearly establish the strong dependence between shale thickness and pressure diffusion, reaffirming previously published results [*MacBeth et al.*, 2011; *HajNasser*, 2012]. The Not Formation, being the thinnest unit, reaches pressure equilibrium with the reservoir pore pressure faster than the Ile Shale Member (Table 3-5). The Ror Formation does not show any pressure response, due to several factors, the first one being that the base of the Ile Formation consists of a calcite-cemented interval, modelled with very low permeability, which limits connectivity between the Ror Formation and the reservoir; another parameter is the thickness of the Ror Formation layers (two layers each 30 – 35 metres in the model), a vertical refinement in the grid down to 1 or 2 metres may show some pressure diffusion in the upper layers of this unit. Inactive shale (Model 0) shows higher depletion or pressure imbalance, while in active shale models the response is smoother, as consequence of the connectivity through shales.

Shale	Thickness (metres)	Number of layers	Time to reach pressure equilibrium with the reservoir
Not Formation	3-6	2	9 years
Ile Shale Member	7-16	2	13 years (in some blocks)
Ror Formation	60-70	2	Not found

Table 3-5 *Timing of pressure diffusion for Heidrun Field shales.*

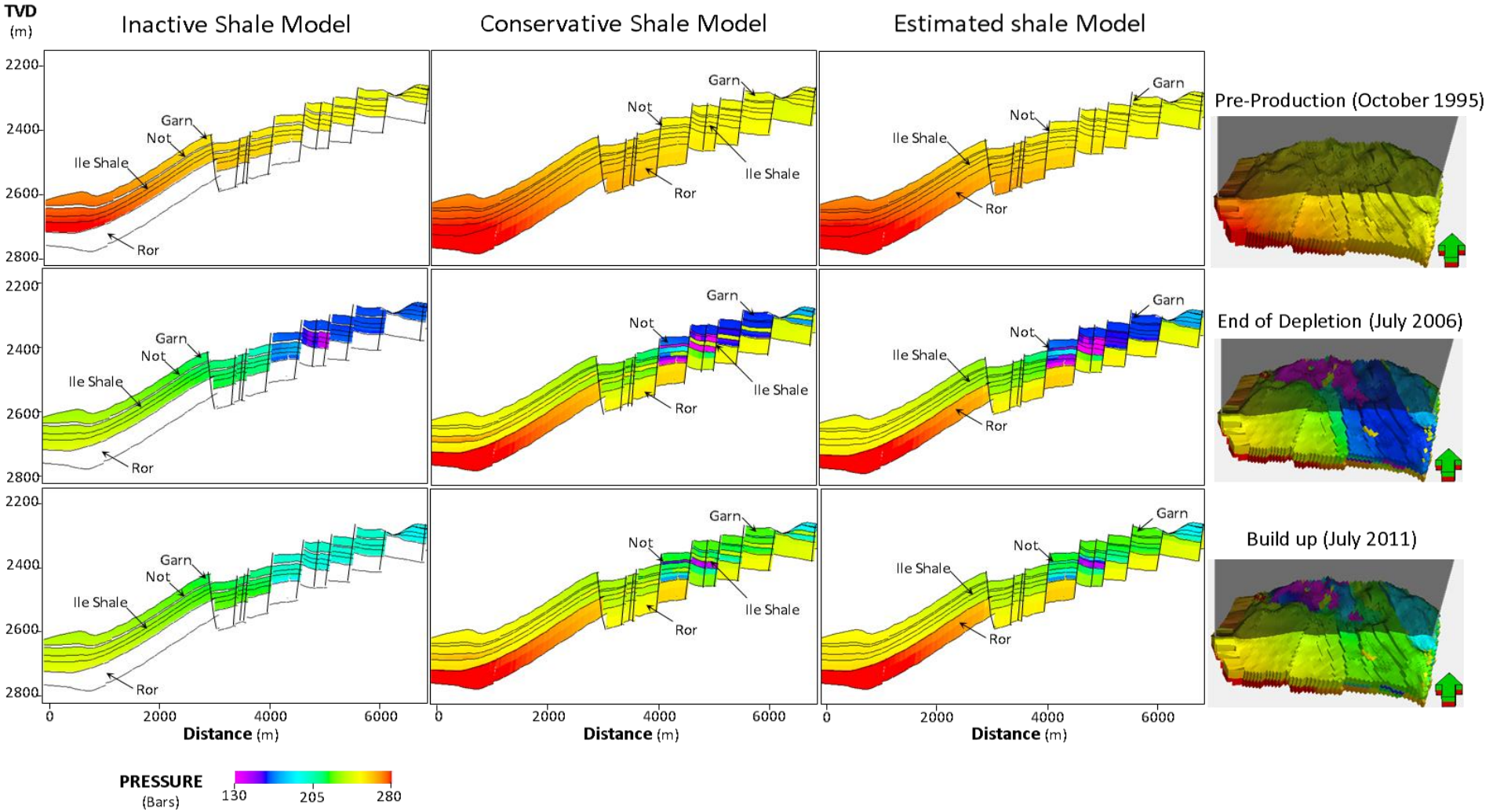

Figure 3-10 *Predicted Heidrun Field pressure for pre-production, end of depletion and end of build-up stages in inactive and activated shales models*

3.6.2 Saturation and volumetric production results

Due to the very limited variability in terms of saturation changes within the active shale scenarios considered (Model 1 and 2), the results are only compared between the inactive and active shale models. The observed variations in saturation (Figure 3-11) are related to gas exsolution in small compartments corresponding to the inactive shale models, as the depletion and compartmentalization is higher for this case (less pore space to equilibrate induced pressure imbalance). As the Ile Shale Member was considered part of the reservoir in the base scenario (inactive shale model), the results show oil saturation for that interval, but in the active shale scenarios the same interval is water-saturated.

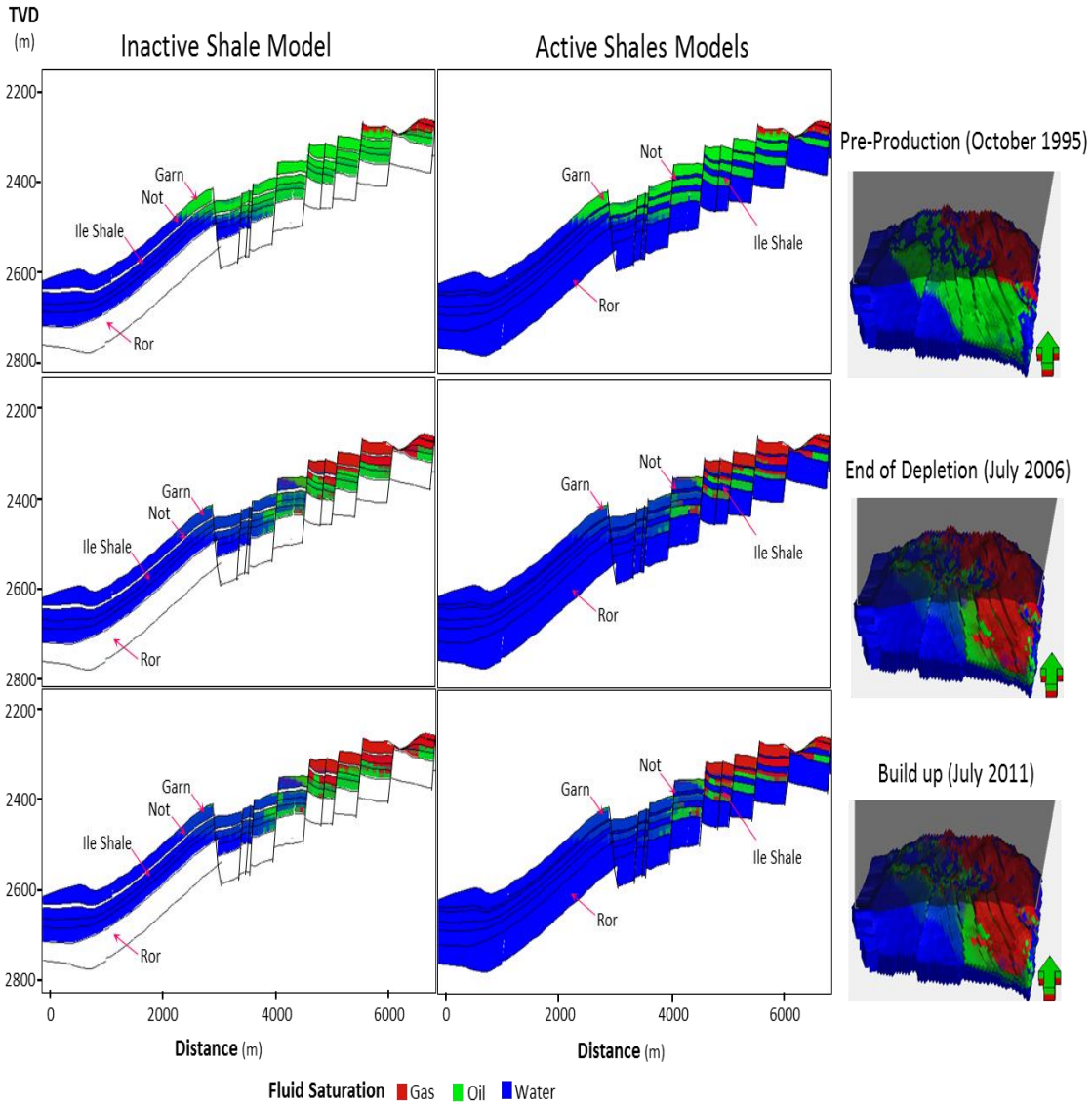

Figure 3-11 *Predicted saturation for Heidrun Field modelled inactive and active shales scenarios.*

Regarding the predicted volumetrics for the modelled scenarios, the normalized total production of oil, gas and water (Table 3-6) compared against the historic data (100%) shows that the pressure diffusion in shales clearly does not affect field oil production, with variations from low pressure diffusion (Model 1) and pressure equilibrated (Model 2) scenarios being less than 0.5% of the produced volume. Gas production also shows very small volume variations between shale active models, but when they are compared with the inactive shale models, the match with the historic data is better for active shale models, as the volume of produced gas decreases with pressure diffusion in shales and higher compartmentalization allows more gas come out of solution. Water production volumes show a very low variation between the inactive and active shale models. Predicted oil production for the inactive shale model shows a higher volume than that for the active shale models, due the inclusion of the Ile Shale Member as part of the reservoir (extra hydrocarbon volume included in this model).

Case scenario	Model ID	Total Oil Production (%)	Total Gas Production (%)	Total Water Production (%)
Historic data		100	100	100
Inactive shales	0	68.96	121.80	81.00
Conservative parameters	1	61.91	115.99	81.85
Estimated properties	2	61.95	115.79	82.13

Table 3-6 *Normalized total oil, gas and water production for the modelled scenarios of the Heidrun Field*

3.7 Synthetic seismic modelling

With small differences in saturation between active shale models, the synthetic elastic modelling was performed only for the inactive and estimated properties scenarios (Models 0 and 2) to compare and contrast the effect of shale activation. As changes in pressure and saturation were more pronounced during the depletion stage, the synthetic seismic volumes for 4D analysis were computed for the October 1995 and July 2006 time steps. The modelling of the Heidrun Field elastic parameters was performed by rock physics analysis (Equations 2.37 and 2.38) to well log data to determine the matrix moduli for clean sand and pure shale (Table 3-7); the definitive elastic value for each cell is determined by its porosity and NTG, applying a sand-shale mixing average method [*Backus*, 1962]. Shales were regarded as equally stress-sensitive as sandstones [*HajNasser*, 2012], with the pressure dependent stress sensitivity relationships of *Macbeth* (2004) for elastic moduli (Equations 2.43 and 2.44).

	Sandstone	Shale
K_{matrix}	31.56 GPa	17.76 GPa
G_{matrix}	15.06 GPa	12.55 GPa
ρ_{matrix}	2630 kg/m^3	2597 kg/m^3

Table 3-7 *Sandstone and shale matrix elastic properties for the Heidrun Field*

To complete the reservoir characterization, fluid properties were included as inputs in the Sim2Seis (Simulator to Seismic in-house code), to calculate their elastic moduli and contribution based on the cell's saturation. Also an earth model (overburden and underburden characteristics) (Table 3-8). Applying Sim2Seis the predicted pressure and saturation for the different reservoir stages studied (time steps) were coupled with the static reservoir properties (rock matrix properties) to perform fluid substitution (not in shales, where saturation remains the same) and to estimate the changes in the reservoir elastic response and their correspondent impedances and reflectivity series. With the application of a convolutional model and a representative wavelet (Figure 3-12), statistically extracted using the Hampson & Russel application Geoview, from a 200 millisecond window around the reservoir (Appendix C), the computed impedances were transformed into amplitudes for synthetic traces placed in the centre of each cell (position of the correspondent gather), and the responses were stacked covering an offset angle between 5 and 30° (which is the range of the full stack angle for the acquired seismic in the Heidrun Field) and then, synthetic seismic volumes were generated for each modelled scenario

Reservoir temperature	85 °C
Water salinity	65,000 ppm.
Oil gravity	28° API
Gas gravity	0.7683
Overburden properties (outside the model)	P-wave velocity= 3,270 m/s; S-wave velocity=1,470 m/s; Density=2.32 gr/cm^3
Underburden properties (outside the model)	P-wave velocity= 3,450 m/s; S-wave velocity=1,570 m/s; Density=2.38 gr/cm^3

Table 3-8 *Reservoir parameters (fluid properties, temperature and earth model) used for synthetic seismic modelling in Heidrun Field*

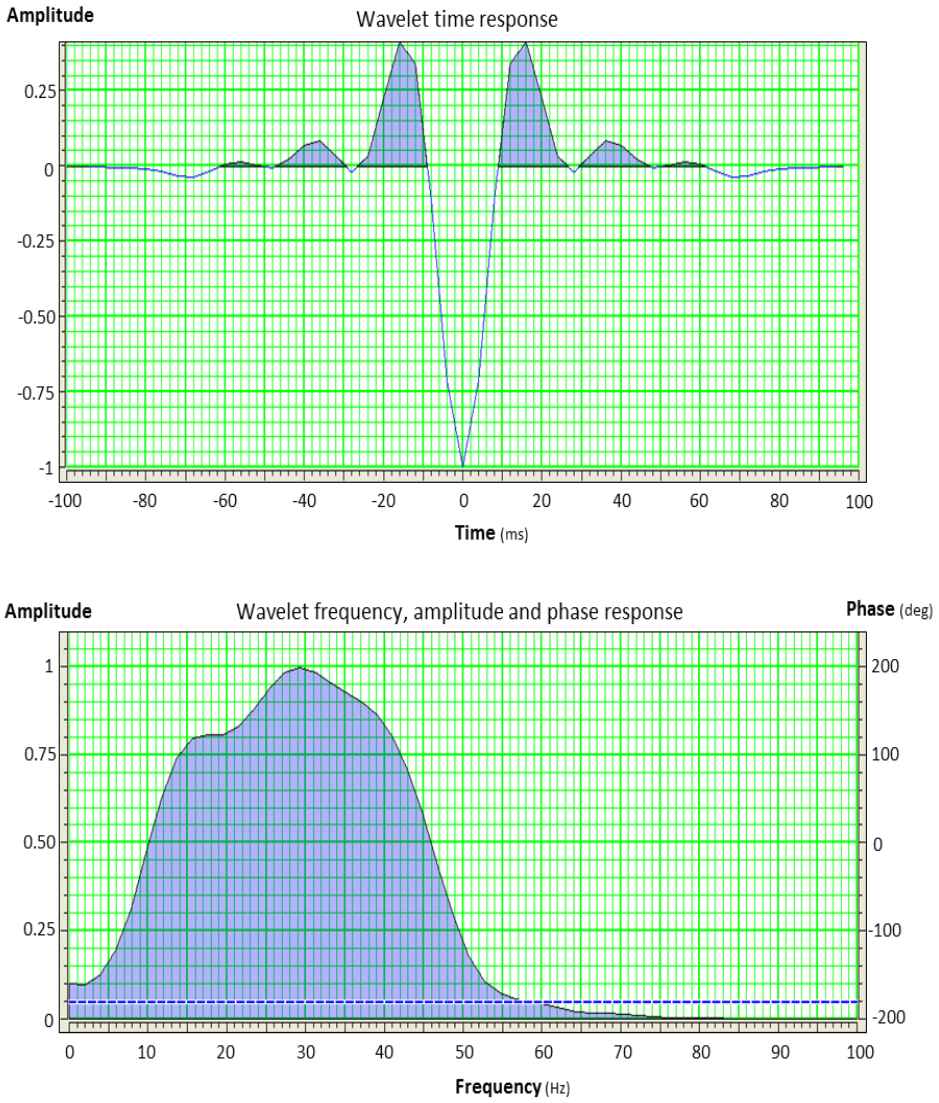

Figure 3-12 *Statistically extracted wavelet used for seismic convolution for the synthetic seismic modelling of the Heidrun Field. With a maximum frequency around 29 Hz and a typical North Sea reverse polarity.*

When comparing the observed to the generated synthetic seismic volumes for the active and inactive shale pre-production models (Figure 3-13) and the end of depletion (Figure 3-14), the results show a higher amplitude contrast within the reservoir (brighter negative reflections, blue) in the inactive shale model, while the active shale model seismic volume exhibit lower amplitude contrast in the reservoir, closer to the recorded in the observed seismic (86/91 vintage). Inactive shale model seismic volume also exhibit more continuity in the reflectors showing more internal reflections in the reservoir, even in the areas where the fault density is higher. Active shale model have less continuity in the internal reflector in the faulted areas. Inactive shale seismic also shows strong reflections in the immediate overburden, feature that in the active seismic volume has a lower amplitude.

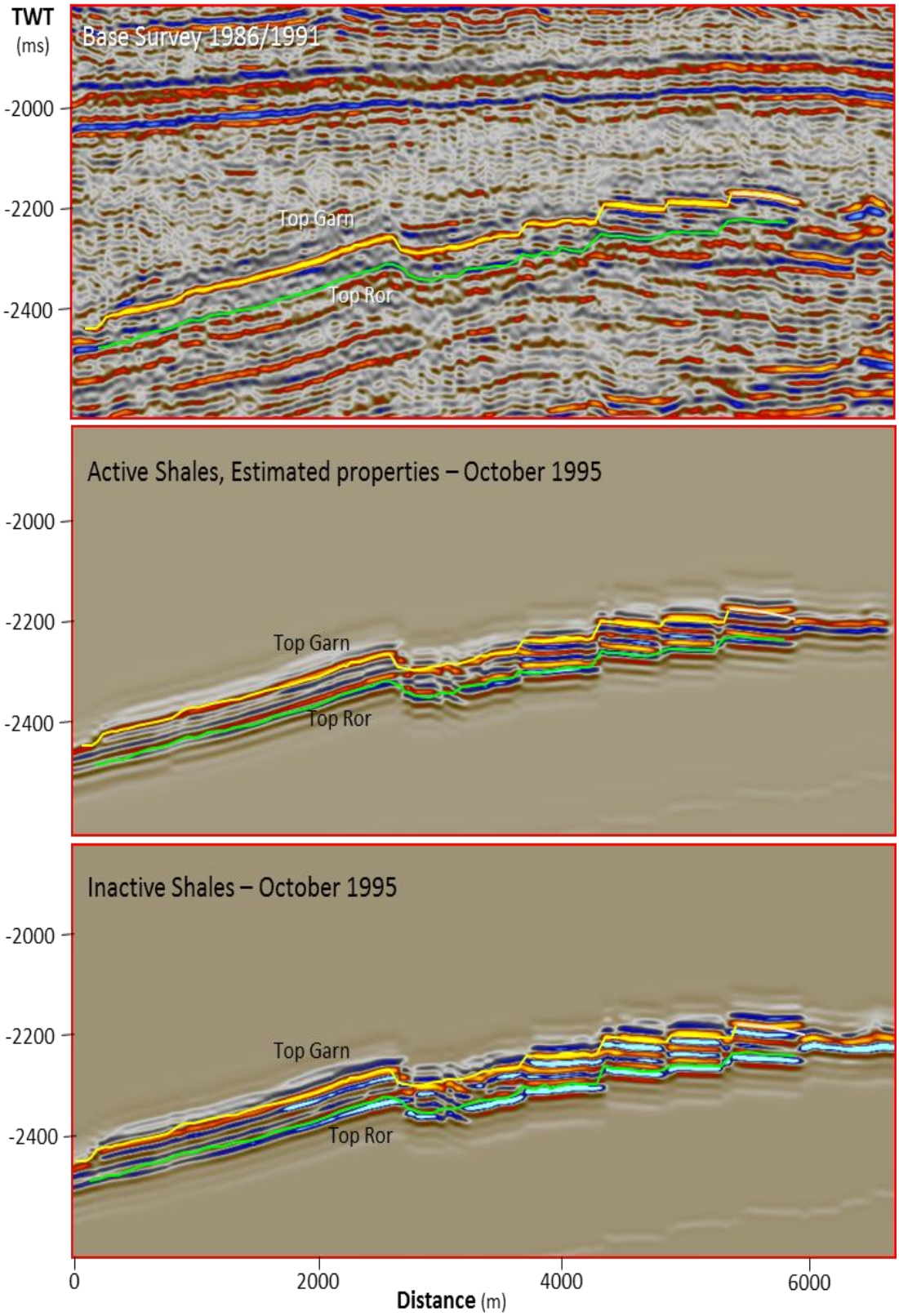

Figure 3-13 *Pre-production seismic. At the top, Seismic survey 1986/1991; in the middle synthetic seismic volume for active shale, estimated properties model at October 1995 time-step; at the bottom, synthetic seismic for inactive shales model at October 1995 time-step.*

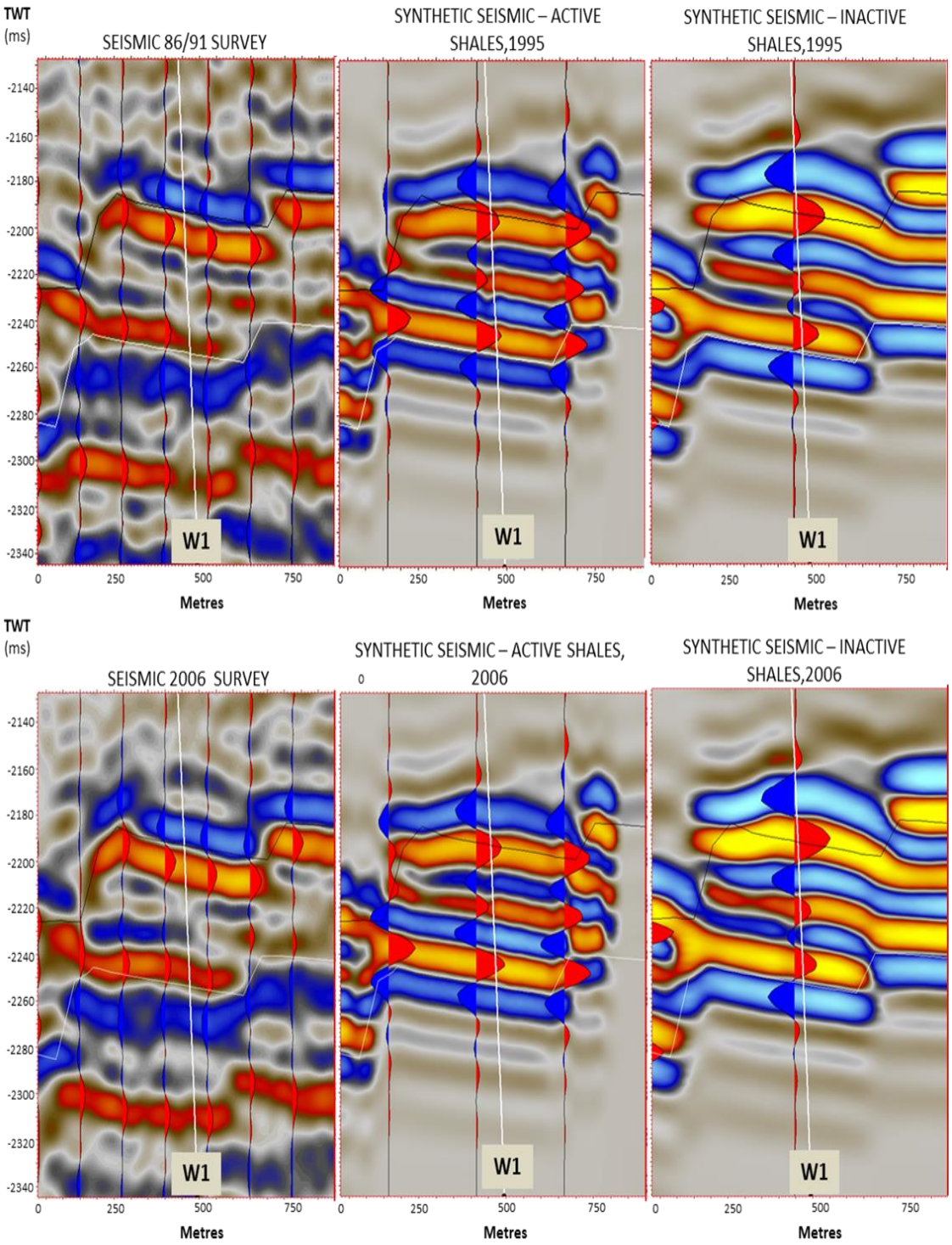

Figure 3-14: *Detail of synthetic seismic volumes for inactive and active shale models for pre-production and the end of depletion stage. At the left observed seismic.*

As the shale intervals are better modelled, shale active seismic models have a more accurate elastic response, velocity modelling and reservoir thickness estimations, and hence vertical placement of the seismic reflections associated with specific geological features. Figure 3-15 shows how the synthetic seismic for the active shale model matches

better the observed seismic in terms of events positioning, but also in terms of the amplitude.

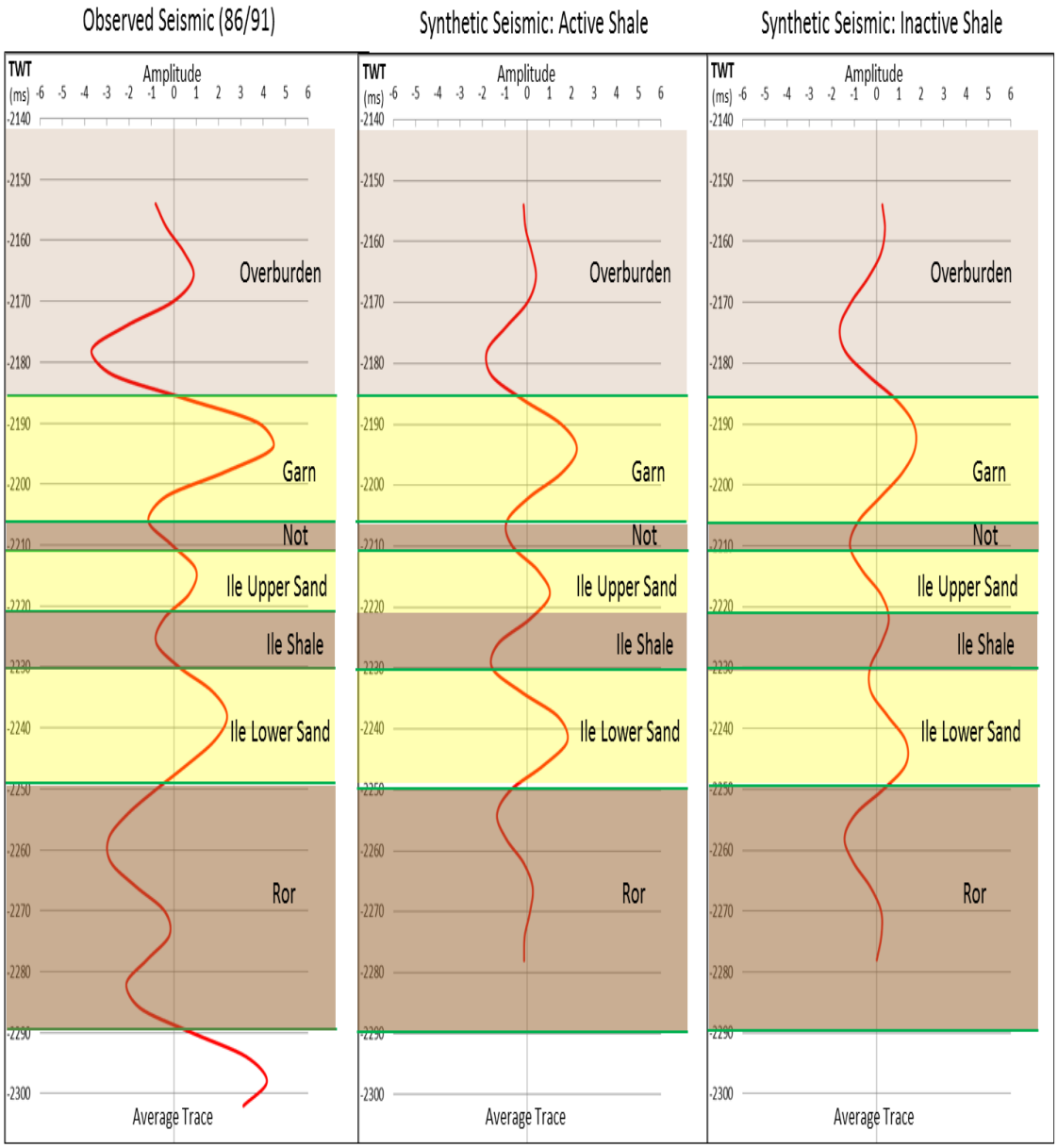

Figure 3-15 *Average extracted seismic traces around a Heidrun Field well (5 Inlines and 5 Xlines), for observed and synthetic (active and inactive shales) pre-production seismic volumes. Traces were 90° phase-rotated to obtain a better correspondence with the geological interval boundaries (a process also known in seismic interpretation as the application of pseudo impedance volumetric attribute). Stratigraphic positioning of tops (TWT) extracted from the well.*

3.8 4D seismic response and interpretation

The time lapse responses were calculated for the 2006-86/91 and 2011-89/91 differences. The three seismic volumes (86/91, 2006 and 2011) were pre-stack and post-stack parallel reprocessed in 2011 by WesternGeco (processing contractor) with a repeatability estimated (200 ms time window 200 ms above top reservoir) in 25% NRMS (Normalized Root Mean Square). The 4D seismic analysis and interpretation to evaluate the effect of shale activation in this dataset was performed at two scales: the initial one considers that pressure diffusion may generate its own 4D seismic response within shales, while in the second, the analysis is performed at the scale of the overall reservoir elastic response (including shales and sands). Due to the good lateral continuity of Heidrun Field shales and their relatively consistent thickness, the analysis was performed by applying surface-based amplitude seismic attributes (RMS) for carefully selected time windows associated with the horizons corresponding to top and base of the studied shales in the observed seismic. The extracted static and dynamic seismic amplitude response for the Not Formation (calculated with the RMS amplitude algorithm applied to a 15-millisecond time window) for the depletion and build up stages (Figure 3-16) shows the strong influence of the reservoir signature, as saturation changes in the adjacent sands (oil-water contact fluid movement and gas exsolution) are easy to recognize in the response extracted for the Not Formation interval. With no changes in the Not Formation saturation (which remains 100% water-saturated, due to capillary forces), and with no correspondence between the predicted shale pressure and the observed elastic response (Figure 3-16), the reservoir sand's elastic response (static and dynamic) was imprinted in the extracted signal corresponding to the shale intervals, making impossible to determine if the response of the shale pressure diffusion creates a measurable seismic signature within the shale interval.

Similar observations were made for the Ile Shale Member (Figure 3-17), where the extracted 4D response for this shale (RMS Amplitude for a 20-millisecond interval) shows similarity with the 4D signal of the adjacent Ile Formation sands and discrepancy with the predicted pressure for this interval in the simulated scenario with shales activated. The same results for the Ror Formation confirm the strong influence of the reservoir sands' response in the studied time window intervals corresponding to Heidrun Field shales, even when the Ror Formation' 45 milliseconds seismic thickness rules out any mistake during the time window selection or cycle skipping effect in the estimated 4D seismic response.

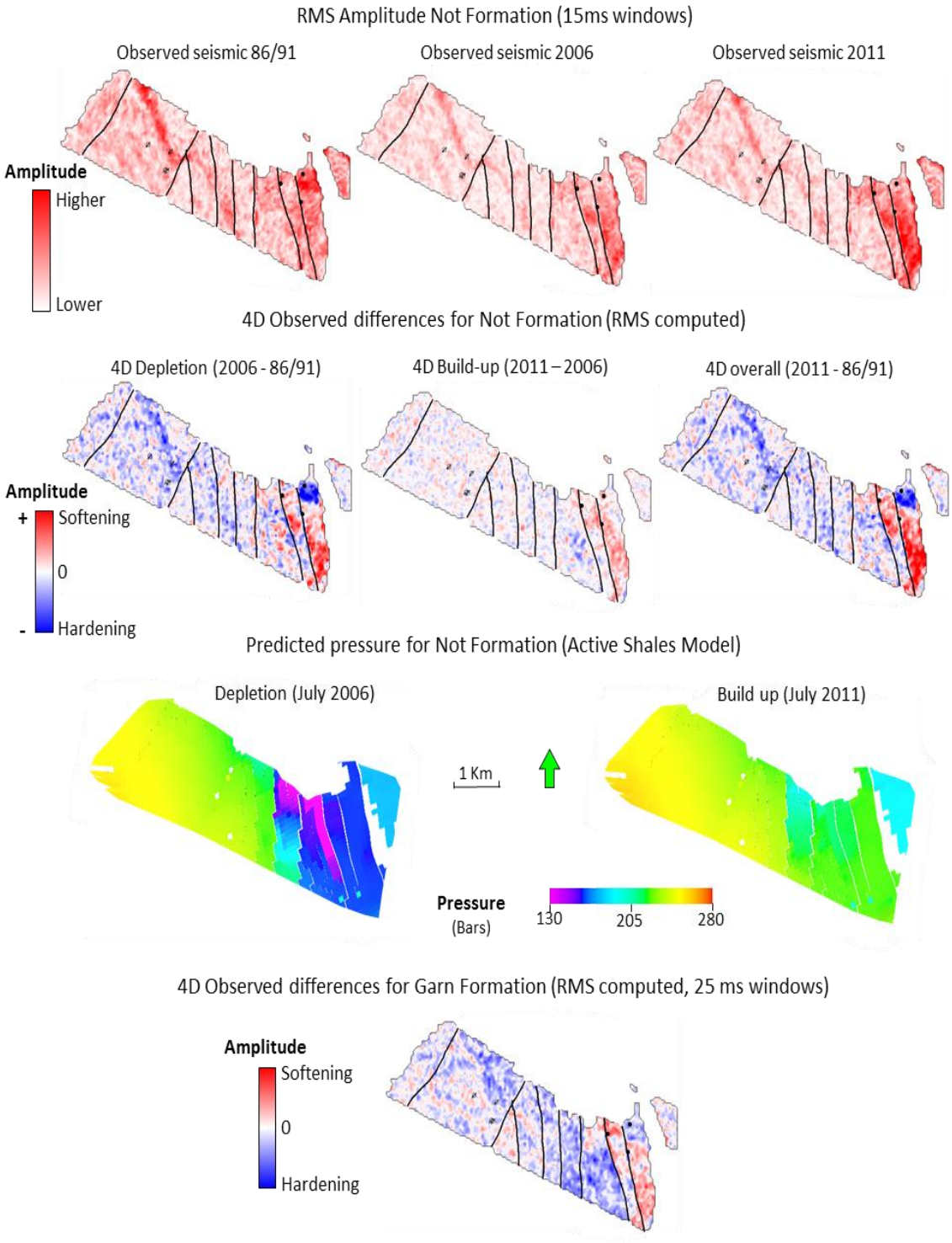

Figure 3-16 *Comparison between static and dynamic (4D response) of the seismic observed data and the predicted pressure changes for the Not Formation at different stages. At the bottom, the 4D seismic response of the Garn Formation, to compare and show its concordance with the Not Formation 4D seismic signal.*

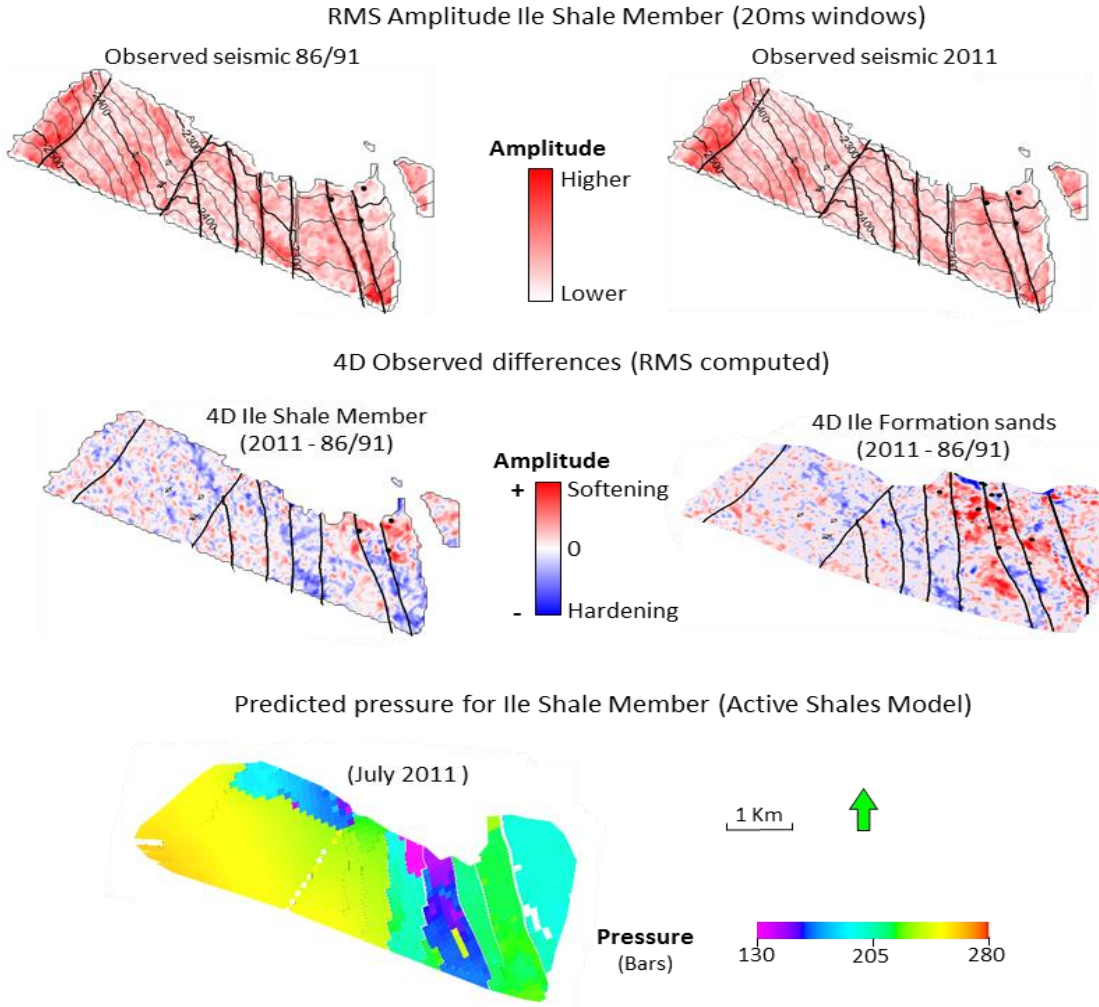

Figure 3-17 *Comparison between static and dynamic (4D response) of the seismic observed data with the predicted pressure changes for the Ile Shale Member and 4D response of Ile Formation sands.*

Since it was established that the 4D analysis of the observed seismic data for the intervals corresponding to the Heidrun Field shales was not enough to evaluate if they were active or not (as no correspondence was found between the shale pressure diffusion and the recorded elastic changes), the 4D seismic analysis and interpretation was carried throughout the entire reservoir. The idea is that shale pressure diffusion may have some effect on the sand's response, by reducing vertical compartmentalization and pressure imbalance in the reservoir, which further impacts the process of gas exsolution and its related elastic implications. For this analysis was used the generated synthetic seismic volumes for active and inactive shale models based on their predicted changes in saturation and pressure, and applied surface and volumetric based seismic attributes to study the predicted 4D responses and their correlation with the observed 4D. Results from the computed RMS amplitude 4D differences between 2006 and pre-production seismic surveys between the top Garn Formation and the base of Ror Formation horizons are

shown in m show in the (Figure 3-18). The 4D response comparison between the synthetics and observed scenarios shows a relatively good match between observed and synthetic seismic scenarios (around 55.46 % match for active shale model and 51.75% for inactive shale model, Figure 3-19), being the hardening signal corresponding to the effect of water being swept and OWC displacement the area where the highest match is achieved. The active shale synthetic seismic model has a smoother 4D response than the response for the model with inactive shales. The softening distribution, which is mostly attributed to gas exsolution, is not very accurate for the predicted scenarios, but in general, the intensity of the 4D signal for the inactive shale model is stronger than that for the active shale model, indicating higher volumes of gas for the inactive shale scenario.

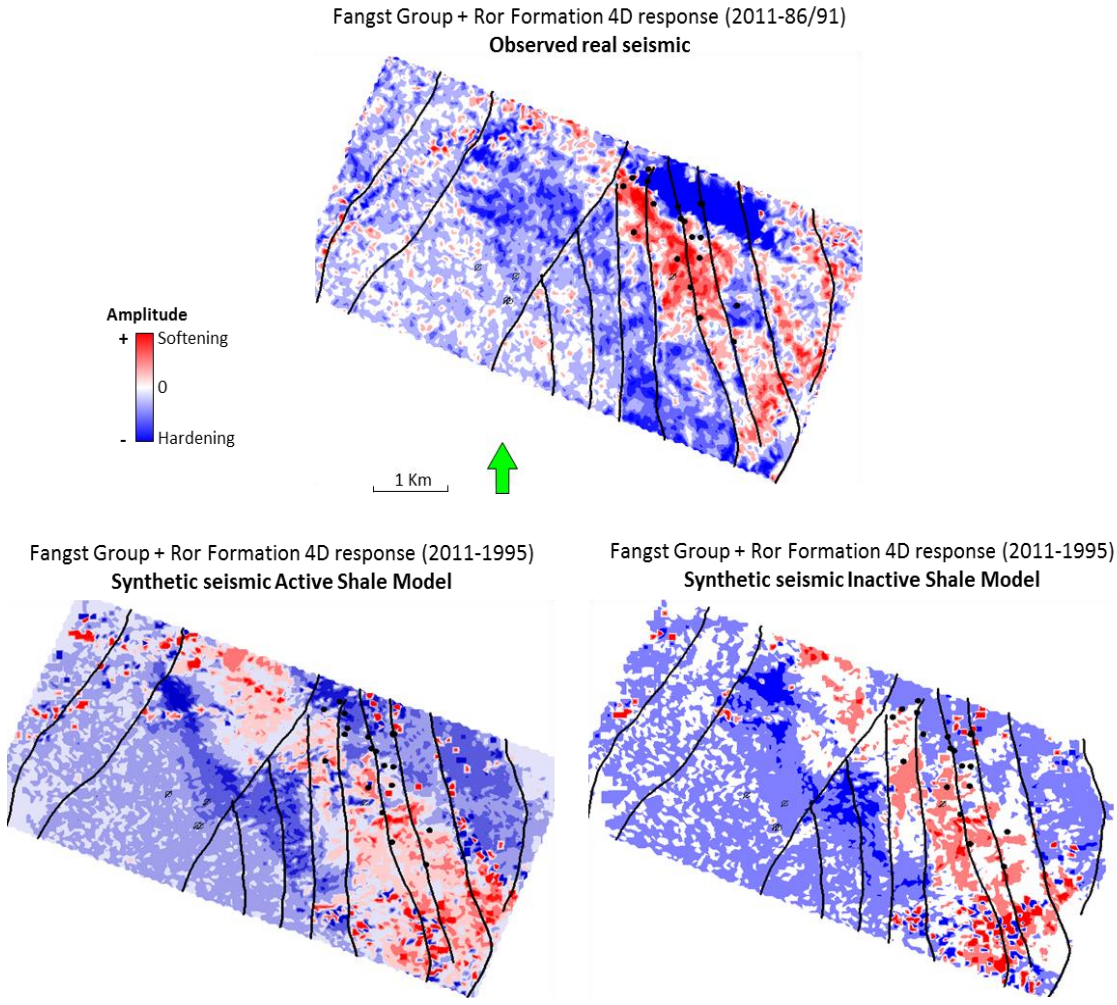

Figure 3-18 *RMS Amplitude 4D seismic differences calculated for the Fangst Group and Ror Formation for observed and synthetic seismic volumes, to analyse the effect of production and injection between October 1995 and July 2011.The strong hardening response in the northeast of the observed 4D corresponds to absence of seismic data due to platform positioning in one of the surveys.*

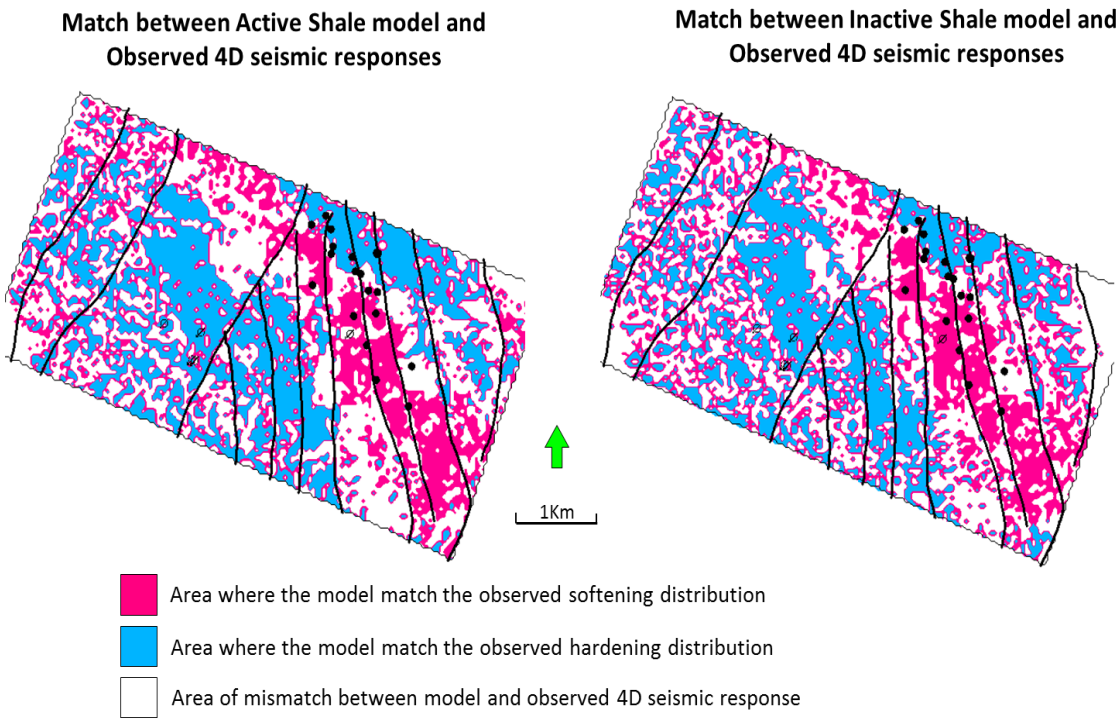

Model	Softening (%)	Hardening (%)	Without 4D changes (%)	Mismatch (%)
Observed seismic	40.54	59.46	0	
Active Shale	18.14	36.33	3.78	44.54
Inactive Shale	18.19	33.53	2.62	48.25

Figure 3-19 *Statistics for the 4D response match distribution between observed seismic and synthetic differences for active and inactive shale models. Active Shale model showed a better fit to observed seismic data. Very similar responses for both models, even when the signal and distribution of the hardening and softening are different.*

With different distribution, but similar statistics related to the softening match with the observed 4D seismic response between active and inactive shale 4D seismic synthetic response (Figure 3-19), it's difficult to establish is shale activation in this RMS Amplitude map based analysis is improving the interpretation of the observed 4D seismic in the Heidrun Field related to gas exsolution. The active shale model shows better fit to the observed seismic data regarding the distribution of the hardening signal corresponding to the water swept, characteristic also evidenced in the volumetrics for total water production (Table 3-6). The areas where the mismatch between the observed and predicted 4D responses are larger corresponds to fault compartmentalized blocks. Fault transmissivity in the Heidrun Field has high variability along each fault segment, affecting the reservoir connectivity and compartmentalization, and constraining the analysis of the shale activation and the evaluation of the shale pressure diffusion effect in

the 4D seismic. The complicated fault transmissivity is the consequence of the transferred transtensive component of the main fault system that causes a "scissor effect" in the secondary normal faults, altering the behaviour of the fault from sealing to transmissive and vice versa, in the same segment.

The 4D response of the Heidrun field was also studied through the 4D differences of the modelled seismic volumes (subtraction trace by trace and sample by sample of the monitor minus the base). The results for the Heidrun Field depletion stage (2006 pre-production survey) for the inactive shale models show a strong 4D synthetic seismic response in the upper blocks of the reservoir (highlighted with a green oval in Figure 3-20).

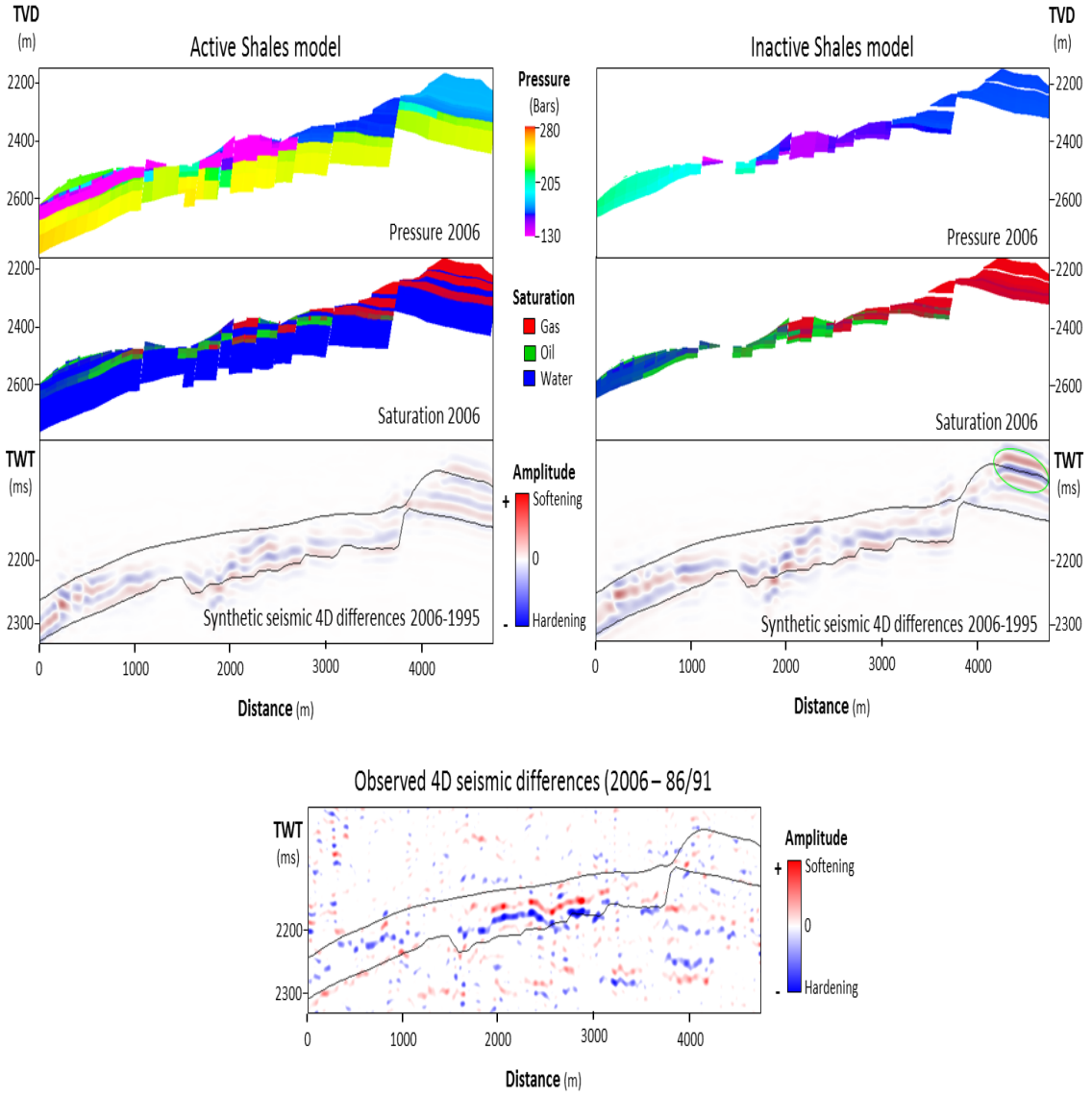

Figure 3-20 *Comparison between active shales, inactive shales model and observed volumetrically computed 4D differences for the depletion stage (2006 pre-production survey) of the Heidrun Field; for the synthetic scenarios predicted pressure and saturation are shown for the 2006 time-step.*

The response is generated by pressure drop; saturation changes in that area were not very different from those predicted by the active shale model. As pressure compartmentalization is higher in some particular blocks in the inactive shale model, the predicted depletion is higher as well, creating its own 4D signature on, a signal that is absent in the active shale model and the observed seismic, which suggest that pressure diffusion into shales is indeed an active process in some areas of the field, especially in the Not Formation and Ile Shale Member. The 4D volumetric response (Figure 3-20) also show areas where the inactive shale model response fits better in terms of amplitude the observed seismic data.

3.9 Conclusions

The Heidrun Field stratigraphic and structural configuration has proved to be a good scenario to test the occurrence of pressure diffusion into shales. In this case, the layer-cake distribution of interbedded sand and shale and the lateral continuity of these lithologies, coupled with the compartmentalization of the fault-generated blocks, creates the necessary boundaries that force induced depletion in reservoir sands to interact with the over- and underlying shales, placing shales in the middle of two opposite pressure diffusion fronts. The modelling of different magnitudes of shale permeability showed significant pressure diffusion in shales and pressure equilibrium with the reservoir sands, even for low permeability scenarios. The predicted pressure results suggest a strong dependence on time and shale thickness for the occurrence of sizeable pressure diffusion within this lithology, with the Not Formation (the thinner shale) first reaching depletion of pressure build-up and in the Ror Formation (the thicker), the interval showing very small or null pressure diffusion.

The inclusion of the internal architecture of these shales in the reservoir numerical simulations enhances the pressure and saturation prediction, as better volumetric fit with the history matched production data, in terms of total gas produced for predicted volumes of active shale models, reveals the influence of the shale pressure diffusion on the gas exsolution process in this field. The high heterogeneity inside the Heidrun Field shales observed at core sample scale (Figure 3-7) makes it a valid point to think that fluid flow interaction between shaly intervals and reservoir sands is very likely to occur. The production of trapped hydrocarbon saturation in fine laminations of sands within shaly intervals may close the volumetric gap between the observed and predicted total oil

production. However, in this research I consider that the inclusion of fluid flow through shale makes the analysis of the impact of shale pressure diffusion more complicated.

The synthetic seismic modelling of the reservoir taking into account shale heterogeneity helps to capture better the elastic contrast within the reservoir; it also allows a more accurate seismic thickness estimation and vertical positioning of events. As no observed 4D seismic signal was correlatable with the predicted shale pressure diffusion, one can assume that the effect of active shales in a reservoir may more easily generate an elastic response related to the saturation in the adjacent sands, especially if the reservoir pore pressure and the bubble point are relatively close. The activation of shales in the 3D and 4D seismic modelling of the Heidrun Field case, improved the predictability of the model as higher fit to the observed 4D seismic was achieved, particularly with the hardening signal corresponding to the effect of OWC movement and water swept. Also, in particular blocks, the absence of 4D seismic signal for the active shale models (matching the observed 4D), proves the validity of the assumption that shale pressure diffusion is active in this dataset, while the inactive shale scenario creates an artificial 4D seismic signal, as a result of a higher level of vertical compartmentalization and, hence, higher depletion.

Pressure diffusion through the Ile Shale Member, Not and For Formation shales is an active process in this field, the statistic but as the statistical analysis of the 4D response showed (Figure 3-19), certainly is not the dominant process in the modelling and interpretation of the Heidrun Field 4D seismic response, in which fault transmissivity modelling takes first place. However, shale has a valuable contribution in the understanding of the reservoir compartmentalization and its elastic implications.

4 Chapter:

Case study: Girassol Field

This chapter, explore the implications of shale activation in the 4D seismic response of a West African turbidite reservoir, where shale compaction and mineral composition play a paramount role in the reservoir elastic response. The inclusion of shale internal architecture in this dataset improves the synthetic seismic modelling and in general the static reservoir characterization. The shale pressure diffusion process is strongly affected by the high connectivity between the stacked and coalescent sands from the channel complex, reducing the pressure imbalance and delaying the diffusion towards shale. This limits the role of shale in the reservoir dynamic behaviour and consequently in the 4D seismic response.

4.1 Field generalities

The Girassol Field, one of the first giant discoveries in West Africa Offshore, is located in Angola, Block 17, 150 km offshore in waters under 1350 metres deep in the Atlantic Ocean (Figure 4-1). Discovered in 1996 and on-stream since December 2001, this light oil (32° API) accumulation has estimated recoverable reserves of between 630 and 700 million barrels. The field is owned by Sonangol (Angola's state oil company) and is operated by TotalFinaElf E&P Angola (40%) on behalf of Girassol partners (Esso Exploration Angola 20%, BP 16.7%, Statoil 13.3% and Norsk Hydro 10%. The reserves have been developed using a subsea facility tied back to an FPSO (Floating Production Storage and Offloading) vessel, the largest of its type ever built, that serves also to provide subsea facilities and production for the neighbouring fields Rosa and Jasmin.

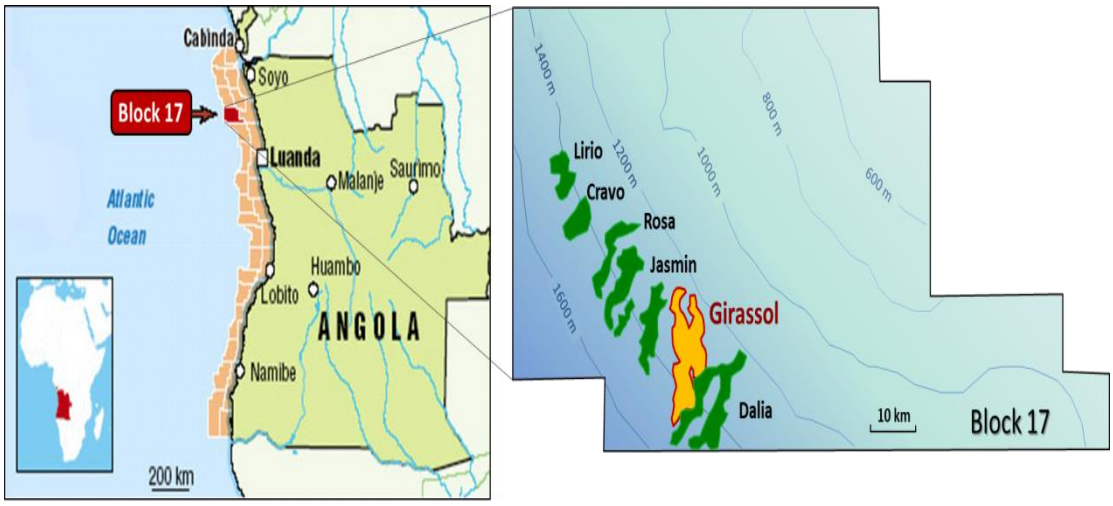

Figure 4-1 *Girassol Field location*

The reservoir is a Tertiary live black oil accumulation with high gas-oil ratio (560 scf/bbl). The reservoir pressure is 268 bars at 2450 metres TVD (top reservoir), which is very close to the oil bubble point (257 bars). In order to support field pressure and avoid gas exsolution, production was developed under water (down-dip) and gas (top structure) injection plan. Due to the large reservoir potential and ideal seismic conditions (deep water, homogeneous overburden and relatively shallow reservoir), the Girassol Field was planned to be developed under 4D seismic surveillance prior to production starting, with the first monitor acquired in 2002, a few months after the first barrel was produced and then several monitor surveys has been shot. For the application of my shale activation

workflow in this field, the database available consisted of well data (14 wells with wireline logs), a simulation model with history matched production data and 3 seismic volumes (a base pre-production survey from 1999, and monitors from 2002 and 2004).

4.2 Geological context

The West African continental margin has undergone a complex history of gravity-driven deformation, beginning with the extensive rift regime from Triassic to Late Jurassic that led to the separation of Africa and South America, followed by a long process of thermal subsidence and then the uplift of the African continent [*Séranne*, 1999]. The interaction of actively evolving structures and depositional systems constitutes the primary control on the Oligocene–Miocene stratigraphic sequences [*Anderson et al.*, 2012]. Velocity variations in the spreading of the Atlantic ridge sea-floor drove structural changes in the basin that led to rapid changes in the sedimentary record. In the area of this study, the offshore Congo Basin (a segment of the West African margin), the subsidence/extension favoured the intrusion of early Cretaceous salt deposits into the late Cretaceous and Tertiary sequences (Figure 4-2), a structural control that conditioned the lateral distribution and geometry of the extensive turbidite fan system deposited in the Oligocene, during a period of high sediment influx caused by the uplift of the African continent.

The Girassol Field corresponds to the mid-distal deposits of an unconsolidated turbidite reservoir, part of the fan system of the Lower Paleo Congo River, deposited during the Upper Oligocene. The turbidite reservoir consists of a stacked complex of several sinuous meandering channel-levee and sheet complexes [*Roggero et al.*, 2012]. The presence of "turtle back" structures in the Oligocene -Miocene pelagic sequence generated by the remigration of Aptian salt deposits [*Gonzalez-Carballo et al.*, 2006] created sea-floor highs that favoured convergence and control in the deposition of the turbidite flows, limiting the lateral spreading of overbank and levee sediments at the mid-section of the turbidite complex and thus creating the stacking and coalescence of sand channel facies. In the distal section of the turbidite (towards the South-West in deeper marine conditions) the structural control of salt-related structures disappears, allowing the deposition of dispersed and digitated sheet complex sediments (Figure 4-2).

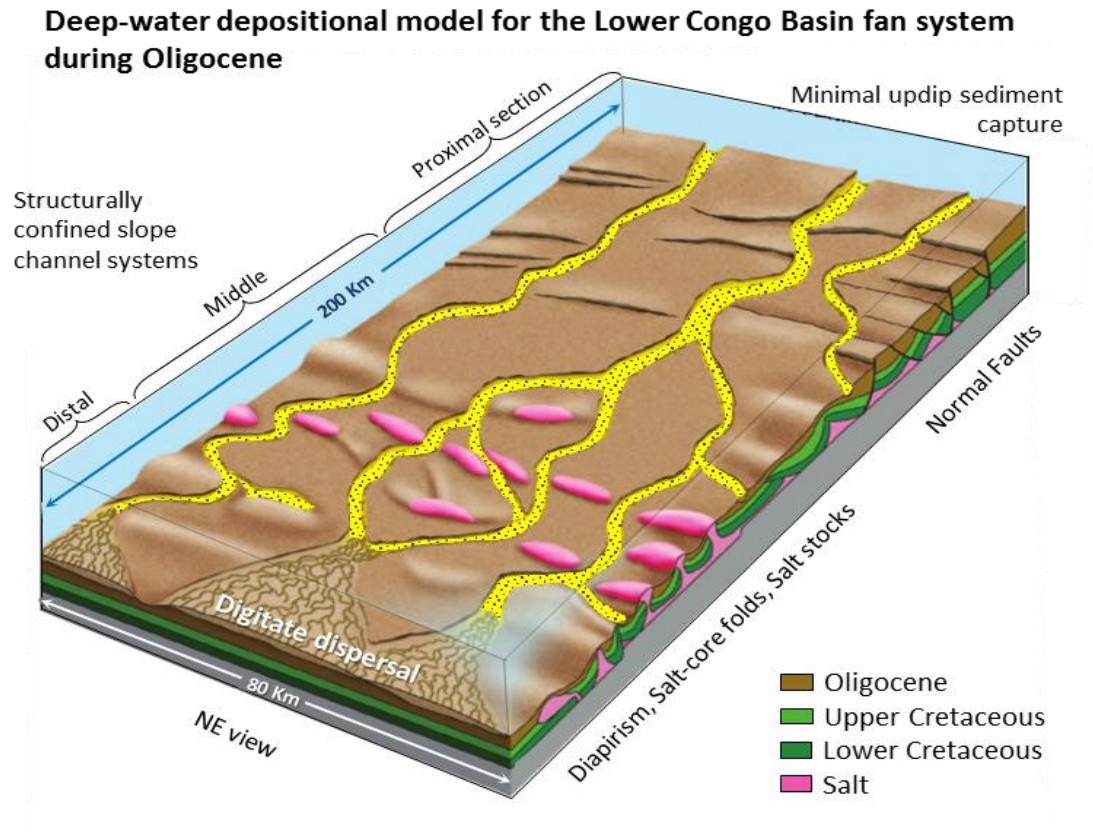

Figure 4-2 *Deep-water depositional model for the Lower Congo Basin fan system during Oligocene. Modified from published literature [Anderson et al., 2012].*

The channel complexes, with general NE-SW and N-S orientations, extend over an area 18 kilometres long and 10 kilometres wide (narrower at the upper and middle section of the turbidite and wider at the distal section). Three stratigraphic sequences corresponding to genetically associated turbidite flows have been identified in Girassol field [*Bouchet et al.*, 2004]; the sequences B1, B2 and B3 (Total's internal operational nomenclature), which are part of the Malembo Formation (Figure 4-3), have a combined thickness of 250 to 270 metres in the central area of the reservoir, B3 being the most recent (Figure 4-4), thicker and more prospective because of the higher sand-shale ratio. The field's structural configuration also includes some normal faults at both flanks of the turtle back structure, caused by gravity and differential compaction between the turbidite deposits and the pelagic deep marine shaly background; the vertical throw of these faults is not large enough to seal and create compartmentalization in the reservoir.

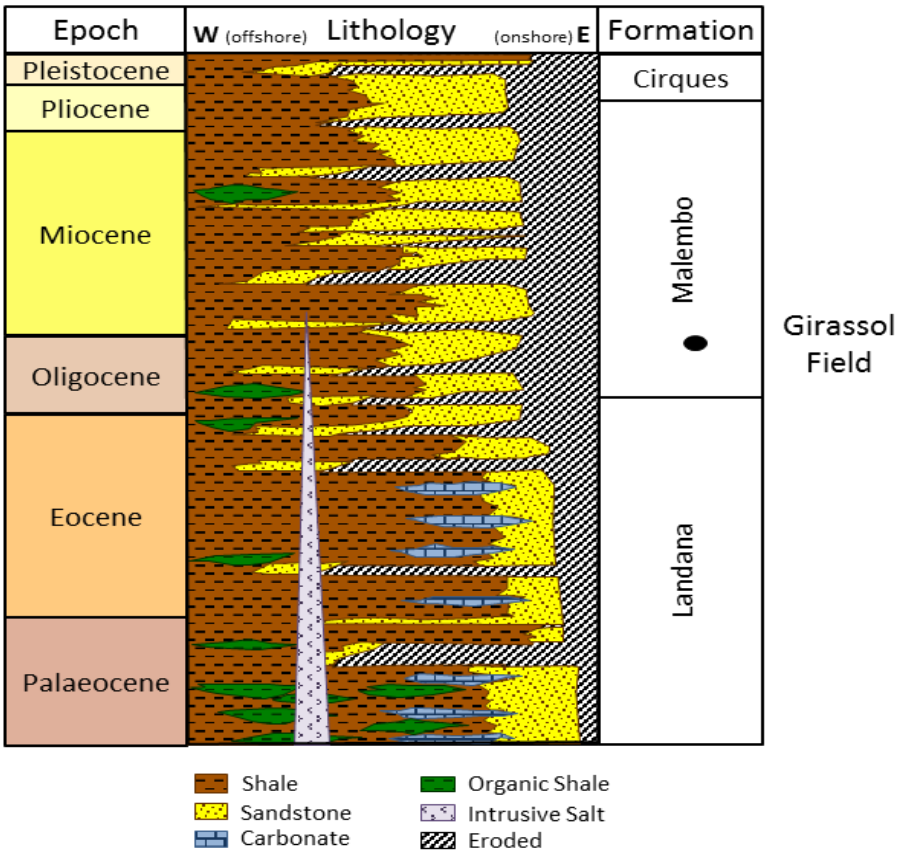

Figure 4-3 *Lithostratigraphic Chart for Angola Offshore (Lower Congo Basin) for the Cenozoic. Redrawn and modified from published literature [Anderson et al., 2012].*

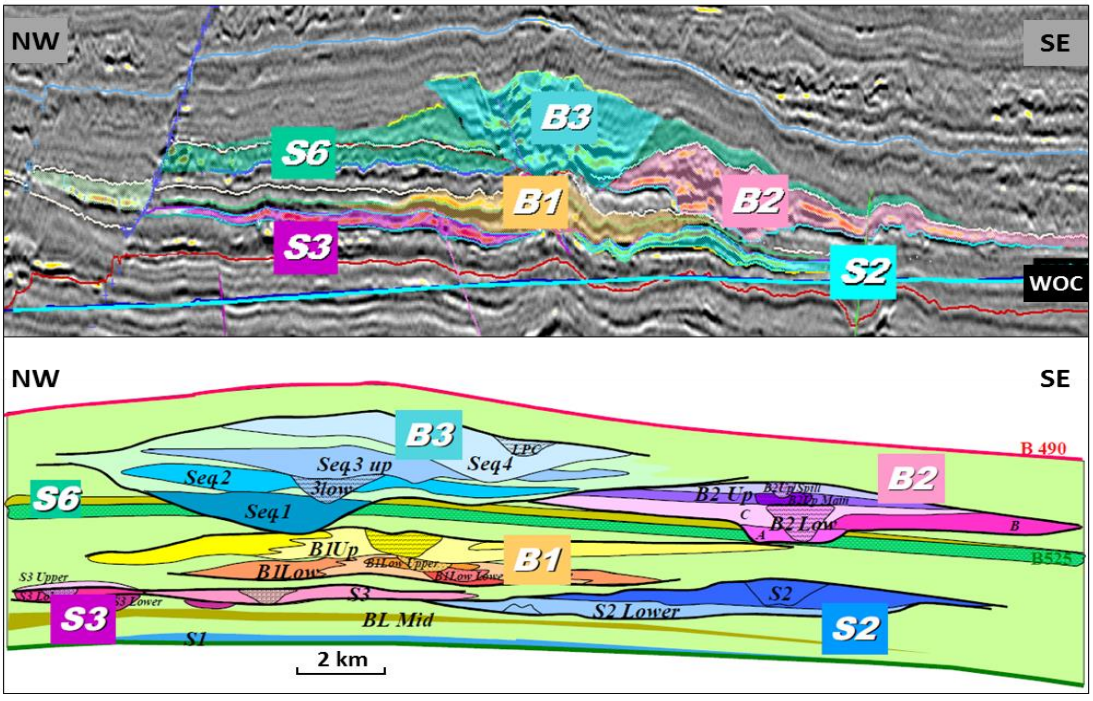

Figure 4-4 *Seismic cross-section and sketch of the middle area of the Girassol Field, showing the stratigraphic structure of the reservoir. Taken from published literature [Bouchet et al., 2004].*

As in any turbidite reservoir, the architecture is the combination of deposits corresponding to a low energy deep marine environment, with the occasional high energy influx of sediments carried by the turbidite flows from the platform edge and slope into the deep marine plain, with the particularity in this case that sea-floor paleo-highs create structural control in the turbidite flow direction. Globally the stratigraphy of the sequences in the Girassol Field can be defined as coarsening upwards, going from interbedded fine sand, silt and shale at the base to coarse and very clean channel sands at the top, with high porosities between 27 and 30% and permeabilities as high as 5 Darcy. With no relevant eustatic changes recorded for this period to define a strong regression (the Atlantic sea-floor was still expanding), the increase in the energy of the deposits corresponds to the beginning of the African continental uplift, which accentuated inland erosion and a major sediment influx into the Palaeo Congo River, increasing the rate of deposition on the platform and quickly creating a thick and unstable column of sediments, very prone to generate turbidite flows.

The base of the sequence B1 corresponds to a heterolithic sheet complex with thin turbidite channels, shaly sands and silt-rich levee deposits with interbedded shales; towards the top, channel facies become more frequent and thicker but still with an important shale content. The high lateral continuity and vertical heterogeneity of the facies, correlated between wells, suggest that the deposits of this sequence in the Girassol Field corresponds to the mid-distal deposits of an association of turbidite flows. Most of the channels are vertically separated by shales deposited by the resettling of clay particles that were suspended and re-transported by the turbidite flow, coupled with the uninterrupted flocculation and pelagic clay deposition inherent in the deep marine environment. Overlying the channel facies there is usually a fining-up interval, correlatable with Bouma's sequence [*Bouma et al.*, 1962], with a shale interval at the top. The preservation of these deposits, only sometimes eroded by the subsequent turbidite flow, suggests a wide area for sediment accommodation, characteristic of a more horizontal and uniform seafloor topography, where deposits create a digitate dispersal pattern. The thickness of B1 goes from 40 – 65 metres in the central area of the reservoir and becomes gradually thinner towards the flanks of the structure, with an almost gradual transition to the pelagic shale deposits.

The B2 sequence consists of higher energy deposits from a series of turbidite flows that migrated towards the east and south-east (in comparison with the B1 distribution) and only overlies B1 in that area of the reservoir. It is a thicker sequence (around 120 metres

in the area where the channels stack) and its cross-section geometry suggests a classical turbidite channel-leveed sequence, with a higher proportion of overbank sediments deposited towards the east, a probable indicator of the direction of maximum slope during the deposition. In the central and western area of the reservoir, the overbank and levee facies of B2 were eroded by the turbidite flows corresponding to the B3 sequence (Figure 4-4). The channel sands of B2 are much cleaner than those corresponding to B1, and, with a higher energy and frequency of turbidite flow, coalescence is very common between them. Due the massive size of the Girassol Field, I focused my study only on the central area of the reservoir, where the sequence B2 is missing, and for this reason I omit a deeper characterization of this sequence.

The sequence B3, is the most prospective unit of the Girassol Field: the high quality clean sands from the channels' facies can have a thickness up to 30 – 40 metres (the sequence thickness is about 200 metres in the central area of the reservoir); the elevated energy and erosive character of the flow creates vertical and lateral coalescence (channels have a meandering shape) producing a very high connectivity between the facies of the reservoir. Fining-up intervals overlying channels and overbank/levee deposits are frequently eroded; the distribution of intra-reservoir shales in the central area corresponds to patches, but are more continuous toward the sides of the main deposition axis.

As the stacking of channel units in this sequence is higher than for the previous B2 and B1 sequences, apart from an increase in the sediment influx from the African continent, it is also assumed that the structural control during the deposition B3 was stronger, increasing the confinement and convergence of the turbidite flows. At the base, in the central and west area of the field, the contact is erosive and non-transitional with the inter-reservoir shales that overlie the B1sequence, while toward the east the contact is also erosive but more transitional with the overbank deposits of the sequence B2. In the distal section of the Girassol turbidite fan system, the lateral migration of the B2 and B3 sequences separate their fan lobes (B3 deposits pretty much overlie the B1 sequence). The top of the B3 sequence marks a very gradual transition between the resettled silt and clay particles of the turbidite flow and the deep marine deposition of pelagic shale.

Looking into a profile of the seismic expression of the reservoir's architecture (Figure 4-5), one of the main noticeable features is the inversion in the polarity of the elastic contrast between shale and sand from a positive amplitude in the B3 sequence to a negative amplitude in the B1 sequence. The behaviour of the shale-sand elastic contrast suggests a strong compaction effect in shales; those at the top are slower and less dense (softer)

than even high porous and hydrocarbon-saturated sands, but at the base of the reservoir, because of the increment in the effective stress, compacted shales become harder than the sands. Properties such as the reservoir thickness (up to 270 metres) and the unconsolidated nature of the deposits can easily explain the effect of shale compaction in the reservoir's elastic behaviour, but part of this response corresponds as well to the particular shale mineralogy in this area and its contrast with the sand components.

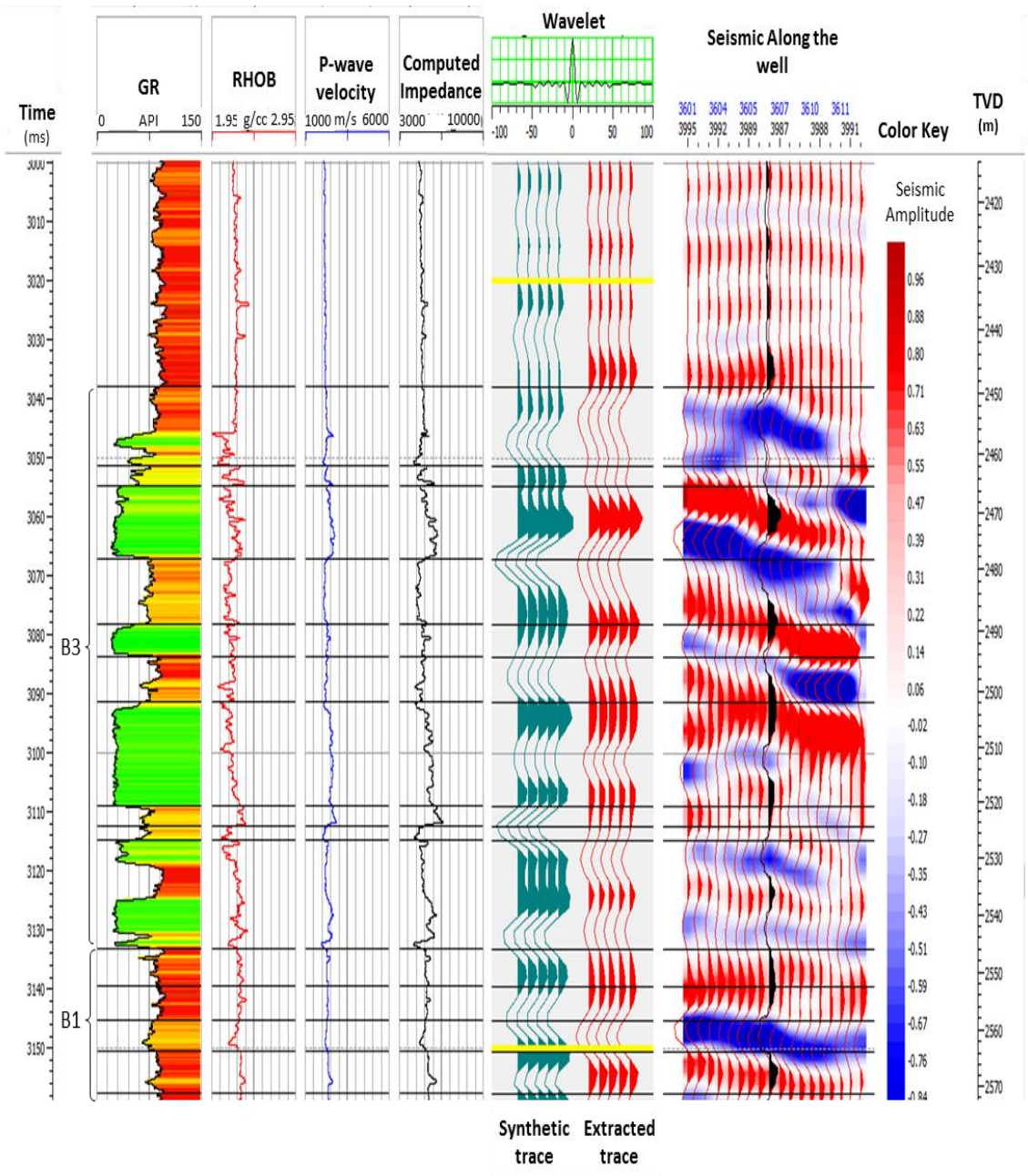

Figure 4-5 *Seismic well-tie for the Girassol Field. Observe the inversion of the elastic contrast corresponding to B3 sequence sands (positive amplitude) and B1 sands (negative amplitude).*

4.3 Shale characterization

Girassol Field shales correspond to deep marine pelagic sediments deposited in an environment normally with low energy conditions, so that only very small particles (clays) travel in suspension to then settle, which assures a very homogeneous lateral lithologic continuity, with only vertical alternance created by stationary periods of high energy (rainy season) that bring some silt and fine sand influx from the continent into the deep marine basin. As the turbidite flow re-transports and resettles the platform fine sediments towards the slope and deep marine plain, shales in turbidite deposits have a fraction with more proximal (or continental) provenance of clays, compared with the strictly pelagic sediments that can have a wider provenance, depending on the marine currents and clay flocculation mechanisms [*Potter et al.*, 2005].

4.3.1 Composition

As there were no available laboratory reports to define shale mineralogy in the Girassol Field, the composition of this shale lithology was established by applying rock physics, a clay provenance study and well log analysis, The heterogeneity of the shales (Figure 4-7), was established on the comparison of any shaly interval with a defined pure mudstone reference (maximum flooding surface), to determine the average fractions of silt and clays, proportions verified in the rock physics analysis when the density of the components (mineral and fluids) were averaged to match the recorded value in the bulk density from the well log (equations 2.19 and 2.24). The notoriously low density (between 2 and 2.2 g/cc) of the shaly intervals in this field (especially in the upper more uncompact section of the reservoir) suggests the presence of a mineral component with a density much lower than the typical quartz-feldspar-illite range (between 2.65 and 2.6 g/cc), which is fairly common in most clastic reservoirs around the world. The lighter material corresponds to kaolinite, a clay mineral of considerably less density (see Table 2-5) than other clays. The abundance of this mineral is particularly high in areas under tropical weather, where the process of denudation and weathering of pre-existing rocks generates a larger proportion of kaolinite over illite and other types of clay (Figure 4-6). This chemo-mechanic process is further accentuated if the eroded substratum is igneous, which is the case of the continental area that is under the erosive influence of the Congo River. As the position of Angola and this segment of the West African continental margin had been in an equatorial location at least since the Middle Jurassic, it is reasonable to also

assume that during the deposition of turbidites from the Girassol Field (Upper Oligocene) the dominant clay being generated was kaolinite.

The clay fraction composition of shales in this reservoir was defined as 40% kaolinite - 60% illite for pelagic shales (with a broader marine provenance), and 60% kaolinite - 40% illite for intra-reservoir shales. This change in the proportions for intra-reservoir shales is due to a larger volume of kaolinite transported from proximal marine locations by the turbidite flow into the deep marine conditions. The proportion between silt (quartz and feldspar mixture) and clays varies depending on the energy of deposition, so for overburden, sideburden, underburden and inter-reservoir shales (pelagic conditions), the clay fraction represents 70 % of the rock mineral volume while for the intra-reservoir shales (turbidite flow resettle), clay fraction and silt represented 60% and 40% respectively.

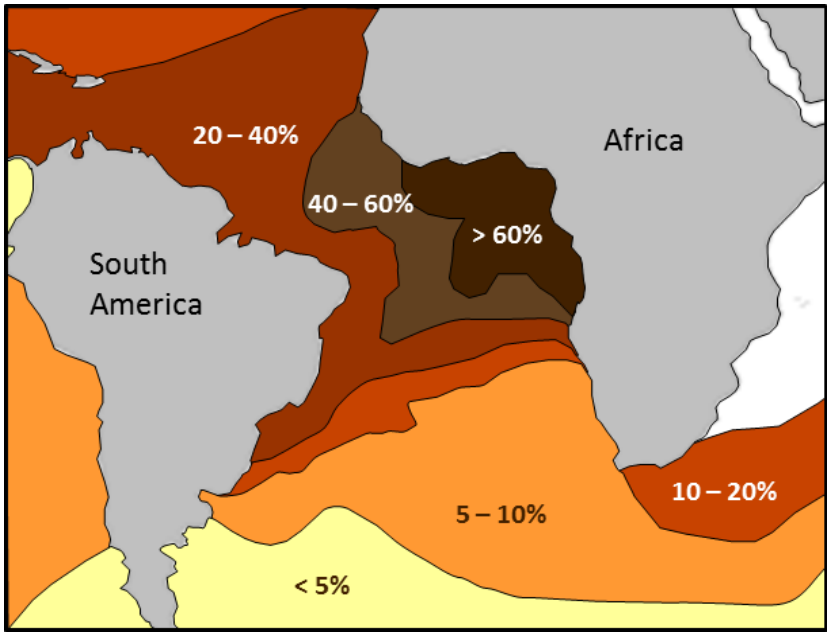

Figure 4-6 *Present day kaolinite clay distribution in the Atlantic Ocean. Redrawn from publish literature [Petschick et al., 1996].*

4.3.2 Shale internal architecture

The architecture of the Girassol Field shales depends on the dominant regime of sediment deposition. Where pelagic, deep marine, low energy conditions prevail, shales are laterally and vertically homogeneous, with only some thin interbedded laminations of silt and fine sands, corresponding to the higher energy deposits associated with the rainy

season. Overburden, sideburden, underburden and inter-reservoir shales were deposited under pelagic conditions where the settling of fine particles is a low and continuous process. As a consequence, the grains are very well sorted; clay platelets are orientated with their longer axis parallel to the prevailing marine current and the horizontal alignment between platelets increases with the effect of compaction that is quite important in this reservoir. So it is expected that more porous and anisotropic shales will be found in the overburden, and denser shales of lower porosity with increasing depth (Figure 4-7). The continuity of shales is very good, with almost no noticeable lateral facies changes, it is only interrupted by abrupt erosive contacts with the turbidite channels. In the sideburden there is lateral transition between distal levee/overbank deposits and pelagic shales.

The intra-reservoir shales were deposited during high energy turbidite flow, which eroded, re-transported and resettled fine particles previously deposited in the marine platform. As these particles had already undergone a flocculation process, their size and weight was higher and their re-sedimentation is faster. Intra-reservoir shale deposits have a more chaotic fabric, with higher angularity between clay platelets preserving a larger porosity and volume of water. With even lower density, the acoustic impedance and compaction trend of the inter-reservoir shales is displaced from the normal pelagic compaction trend (Figure 4-7). This group of shales have a higher sand and silt/clay ratio (fine sand and silt layers are frequent, especially at the base of the intervals) and their electrofacies correspond to fining up intervals, deposited over the channel facies. Due to confinement and stacking of turbidite flow deposits created by structural control during the sedimentation of the Girassol turbidite system, inter-reservoir shales are commonly eroded by the subsequent flow, so the spatial distribution of this facies is very irregular and patchy.

One of the very interesting features of this reservoir is the elastic response of dispersed and laminar shale inside the sand bodies. As the elastic properties of kaolinite in this area are much lower than those of quartz (main component of sands), any content of clay (or shale if it is a lamination) inside the sands will make the sandy interval softer (less dense and slower in terms of acoustic wave transmission) lowering its acoustic impedance, which would otherwise be caused by an increase in porosity or a lighter fluid saturation (Figure 4-7). Due to the evolution of the energy in the sequences, this phenomenon is more common in the B1 sequence, where sands have a higher volume of shale (lower NTG), and less frequent in the B3 sequence, where the very clean sands are harder than

the poorly compacted shale background (overburden and sideburden), thereby increasing the elastic contrast and the seismic response between these two facies.

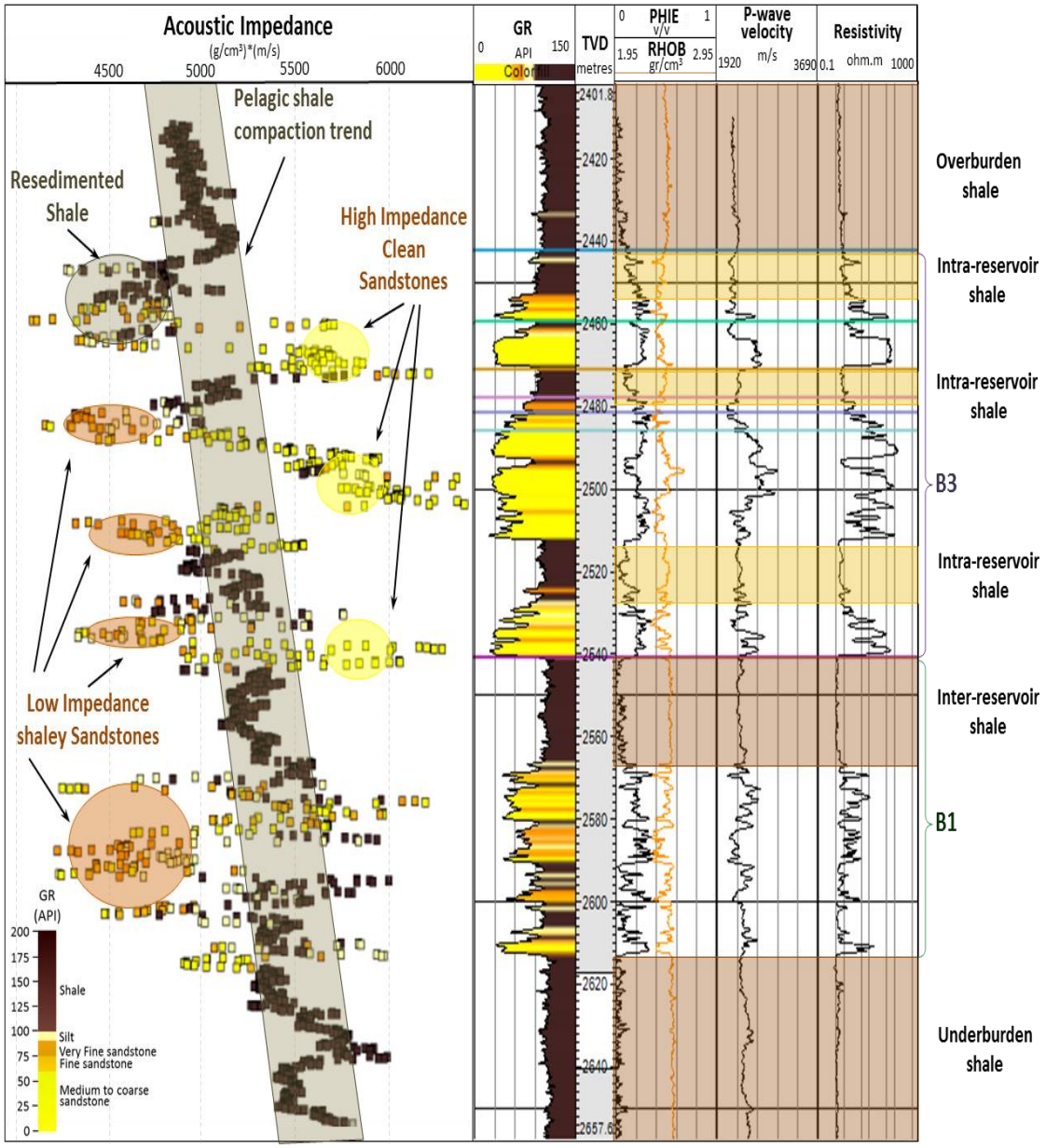

Figure 4-7 *Reservoir architecture of Girassol Field and acoustic impedance variations with depth, showing (dark brown band) the shale compaction trend.*

4.4 Reservoir model and shales

Even when shales were regarded as inactive in the initial reservoir model for the Girassol Field, the NTG value used as the shale cut-off was quite low (0.1) and some of the intra-reservoir shales were included in the model to represent the heterolithic sheet-layered complex of the B1 sequence. Shales in this field were defined with a range of net to gross

between 0.07 and 0.1, to guarantee that the activated cells were below the initial cut-off considerations. In order to activate shales and study their effect in this reservoir, the geometry of the model had to be modified, with an extra layer added at the bottom of the model to consider underburden shales as part of the model. Conveniently, the initial model had an overburden layer (initially inactive) that was used to model the overburden shales. Due the large size of the model, which includes part of Jasmin Field, I defined a smaller study area corresponding to the central section of the Girassol Field, which includes the reservoir section corresponding to the sequences B1 and B3. The boundaries (Figure 4-8) are defined arbitrarily but following the main axis of the turbidite system and wide enough to include some shale sideburden in the model. The geometry of the study area consists of a grid of 238 x 192 x 103 cells (i, j and k directions) with X and Y cell size of 100 x 100 metres, and 50 x 50 metres in some areas with local grid refinement, cell thickness goes from 1 to 10 metres.

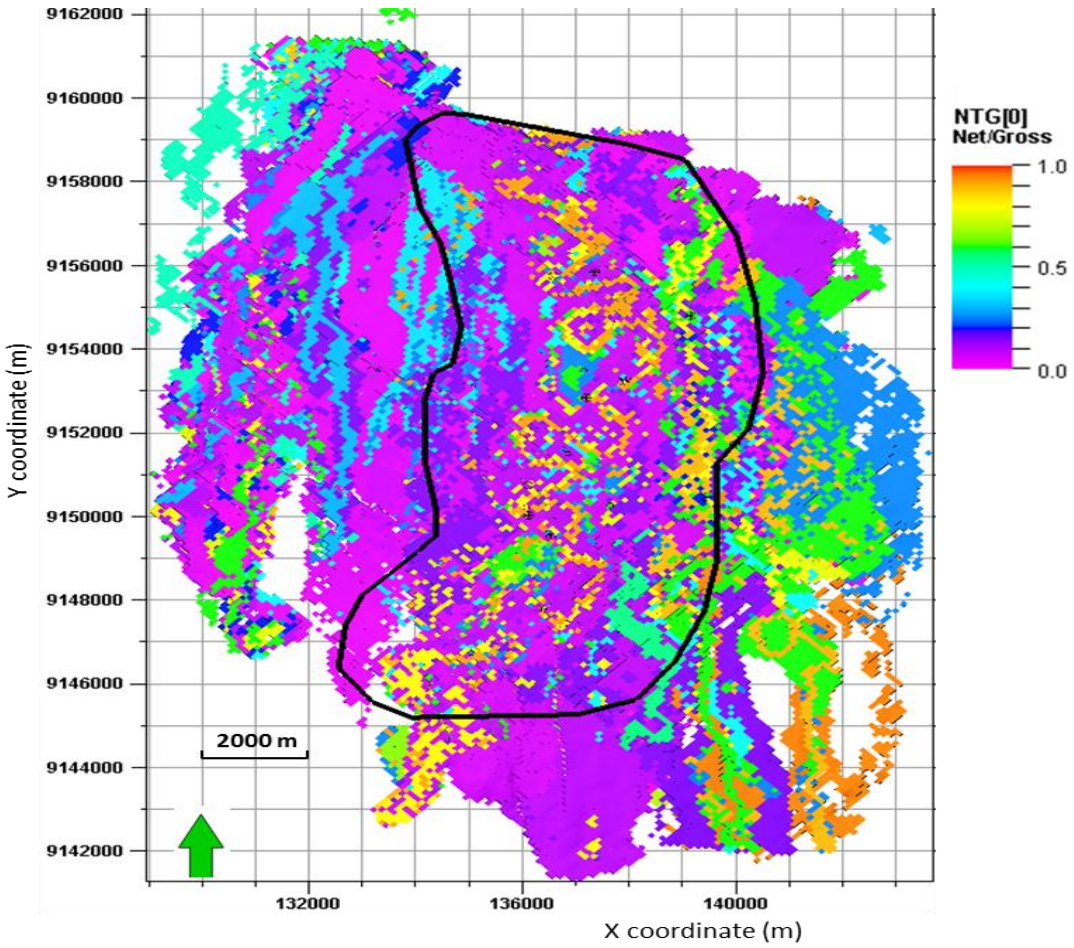

Figure 4-8 *Girassol and Jasmin fields' NTG distribution (TotalFinaElf E&P Angola model). Within black line, the polygon that defines the study area of this project, defined on base of the distribution of the B3 sequence.*

The geological model (static properties distribution) of the Girassol Field was built using 3D seismic data and wireline well logs as main input. The exceptional conditions for seismic acquisition (deep offshore and relatively shallow reservoir) allow the recovery of a dominant frequency of 60 Hz, seismic signal with very good quality and resolution, at the scale to enable identification of geobodies and facies mapping (obviating any shale-related architecture, with the exception of the overburden). The reservoir's heterogeneity in the model was expressed using a highly detailed characterization of NTG and saturation regions (SATNUM keyword in Eclipse numerical simulation) (see Table 4-1 and Figure 4-8). The ETLP database for the Girassol Field includes a simulation model with history matched production data from December 2001 to August 2004.

4.5 Shale activation and properties modelling

To activate shales in this reservoir, first I had to estimate and model static (porosity and NTG) and dynamic (horizontal and vertical permeabilities) properties for shales in order to populate the inactive cells of the model. The subsequent stage of shale activation consisted of the reservoir engineering modelling of the activated shales as transmissivities, pressure gradient, capillary pressure and relative permeabilities, saturation, equilibrium zone definition and finally the dominant compaction trend and stress sensitivity, which in this reservoir play an important role in the elastic imaging of the reservoir.

4.5.1 Static Properties

In the Girassol Field simulation model, the reservoir heterogeneity was expressed in terms of saturation regions; to be consistent, two additional SATNUMs were created to represent shale variability in the field (Table 4-1 and Figure 4-10): one saturation region (number 10) was defined for the overburden, sideburden, inter-reservoir and underburden shale, which share the same sand-silt/clay ratio (or NTG) and compaction trend (gradual reduction in porosity with depth increment). Another SATNUM (number 9) was defined to represent the intra-reservoir shales, defined laterally by a closed polygon around the main stacked turbidite channel system. From the gamma ray linear relationships (equations 2.3 and 2.6) for the volume of shale computations to averaged well log data around the field, the estimated NTG is 0.07 (SATNUM 9) for intra-reservoir shales and

0.05 (SATNUM 10) for overburden, inter-reservoir, sideburden and underburden shales (Figure 4-9)

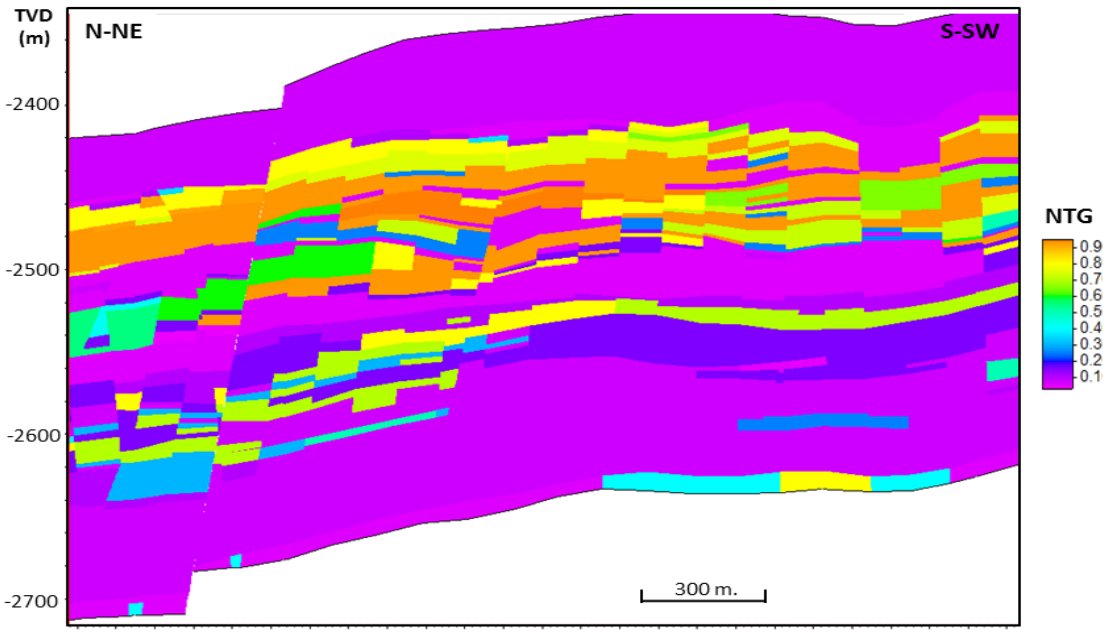

Figure 4-9 *Girassol Field NTG distribution in study area with shales activated, longitudinal section along main tubidite channels*

As shale porosity varies with depth, it was essential to define a depth datum for the compaction trend, where correlations and average overburden shale properties from well logs can be used as inputs for the rock physics analysis (equations 2.20 and 2.26). This depth datum was selected at 2410m TVD, with corresponding porosity around 12%. The next reference depth to define the linear trend for pelagic shales was selected at 2620m TVD, resulting in Equation 4.1. For intra-reservoir shales the depth datum was defined at 2450m TVD, with a computed porosity of 16%, and a compaction trend defined by Equation 4.2.

$$\emptyset_{\boldsymbol{pelagic\ shales}} = 0.12 - 0.00014 \times (Depth - 2410) \quad (4.1)$$

$$\emptyset_{\boldsymbol{intra-reservoir\ shales}} = 0.16 - 0.00023 \times (Depth - 2450) \quad (4.2)$$

As can be appreciated in the above equations, due the differences in the deposition mechanism and fabric between the pelagic and intra-reservoir shales, the porosity is higher for the resettled shales, but the compaction gradient is faster too. The porosity for overburden, sideburden, underburden and inter-reservoir shales ranges from 12 to 9%;

while for intra-reservoir shales it is between 16 and 10%. In both types of shales, no lateral variability was taken into account for porosity, only vertical variability.

Neither NTG nor porosity of sandstones were modified in the geological model, with shale activation conducted only in the previously inactive cells of the model, and the volume of shale inside the sandy cells (dispersed or laminar shale within sands) was considered as inactive.

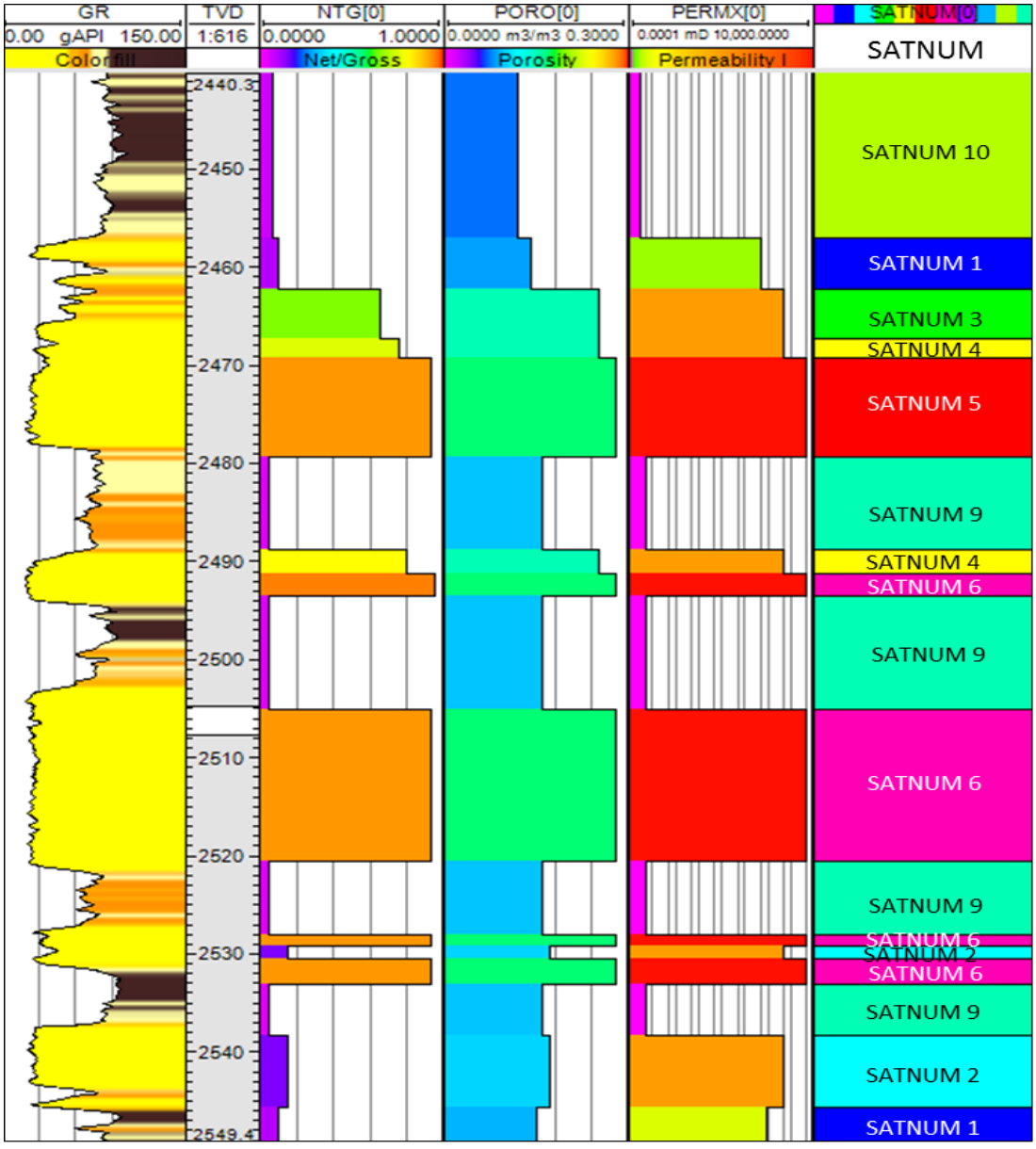

Figure 4-10 *Gamma Ray well log in the Girassol Field, showing the lithological variation in the reservoir and the corresponding modelled NTG, porosity, permeability and SATNUM distribution.*

SATNUM	Lithology, NTG and Porosity
1	Predominant silty and shaly intervals, turbidite lateral lobes, NTG of 0.1 – 0.15. Used to define sequence limits. Porosity = 0.12
2	Fining up interval (high shale and silt content) usually the top of a turbidite flow event. NTG= 0.15. Porosity = 0.14
3	Interbedded sequence of thin fine sands with silt. NTG can go from 0.3 to 0.6. Sandy deposition outside of the main turbidite channel. Porosity = 0.23
4	Fining up sequence just on top of main channels. NTG can go from 0.7 – 0.8. Porosity 0.24
5	Main turbidite sand channel (Jasmine Field) with some silt and shale layers. NTG is 0.93. Porosity = 0.27
6	Clean medium sands, main turbidite channel (Girassol Field). NTG is 0.93. Porosity = 0.30
7	Sand channels in lateral lobes (mainly B2 sequence). NTG = 0.9. Porosity = 0.26
8	Clean medium turbidite main channel (B3 sequence). NTG = 0.95. Porosity = 0.25
9	Intra- reservoir shales NTG = 0.07. Porosity = 0.16
10	Overburden, sideburden, underburden and inter-reservoir shales. NTG = 0.05. Porosity = 0.12

Table 4-1. *SATNUM description (lithology, NTG and porosity) for the Girassol Field geomodelling. In light blue, added SATNUMs used for shale representation.*

4.5.2 Dynamic properties

4.5.2.1 Permeability

The lack of core laboratory data for shales in the Girassol Field means that no poro-perm relationship was available to model the shale dynamic properties. So vertical and horizontal permeability for the pelagic and resettled shales were estimated applying the empirical equations of *Yang and Aplin* (2007) (equations 2.28 and 2.29), using clay fraction content, shale porosity and pressure as inputs. The values obtained for horizontal permeability were between 27 and 32 nanodarcys for inter-reservoir, over, side and underburden shales; and values between 31 and 40 nanodarcys were estimated for intra-reservoir shale. Directional variation in horizontal permeability was discarded for pelagic shales, because deep marine particle settlement is dominated by the flocculation process, showing very poor alignment. However, for intra-reservoir shales, permeability in the Y axis direction was modelled 1.5 higher than the X-axis, because the Y-axis direction is

subparallel to the turbidite flow deposition and pore connectivity, and hence, permeability along this direction should be higher, due to clay platelet alignment.

Vertical permeability for pelagic shales was estimated as 5 nanodarcys, and 8 nanodarcys for resettled shales. To maintain consistency and correlation between the static and dynamic models, NTG and porosity distributions were used as inputs and trends for permeability computations. Neither horizontal nor vertical permeability were modified in the sandy reservoir cells, as the idea was to test the contribution of the external shales, so once again shale embedded in the sands as Vshale was considered as inactive with respect to cell permeability (Figure 4-11). Regarding transmissivities, multipliers equal to 1 were created between the two new shale SATNUMs and the other reservoir (sands) saturation regions, to ensure full interaction in terms of pressure, with fluid flow not allowed, due to constraints from capillary forces.

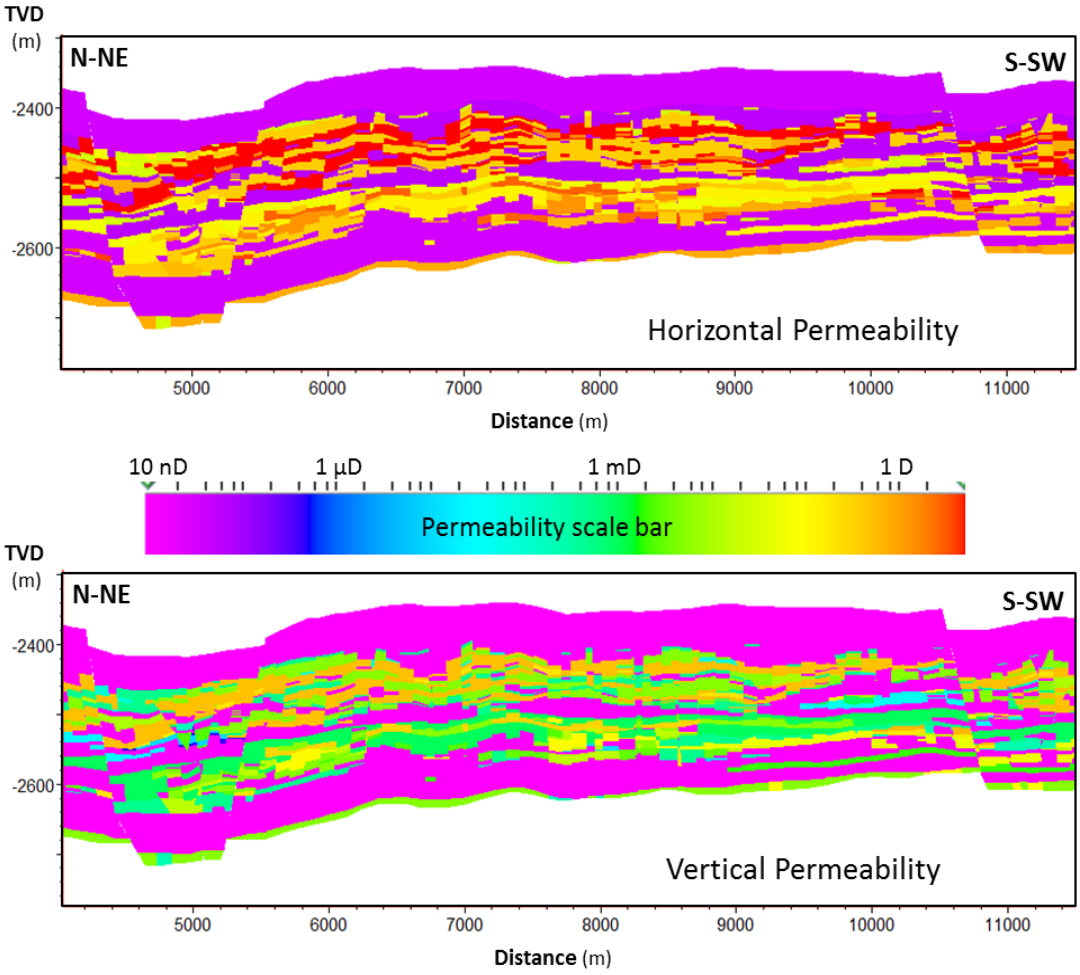

Figure 4-11 *Horizontal and vertical permeabilities for shale active model of Girassol Field: longitudinal section along the main turbidite channel complex.*

4.5.2.2 Shale pressure

Log analysis (sonic, density, calliper curves) of the pelagic shale intervals (inter-reservoir, over, side and underburden) indicates a uniform compaction trend with no evidence of overpressure; this is also corroborated by drilling reports in the area, where complications related to the presence of overpressured shales had not been reported. Fast deposition of intra-reservoir shales suggests a slightly higher pore pressure for these intervals, due to more chaotic fabric, and higher porosity and water content, but the unconsolidated nature of the reservoir deposits and the stronger compaction trend of the resettled shales quickly equilibrates any differences in the pore pressure. For this reason, the modelling of the initial pressure conditions for all shales in the Girassol Field (pelagic and resettled), was modelled with the same pressure gradient, using the definition of an extra equilibrium zone in the simulation model for the formerly inactive cells (shales now activated). The pressure datum for that shale equilibrium zone was modelled similar to the reservoir (263 bars), defined at 2470.8 metres TVD.

4.5.2.3 Shale saturation, capillary pressure and relative permeability

Shale capillary forces, and the very high electrochemical affinity between water and clay platelets, makes it difficult for hydrocarbons to displace depositional water from the shale pore space. For this reason, shales are regarded as an excellent seal, and in conventional reservoir modelling and characterization shales are assumed as water saturated. To model this condition in Girassol field shales, an artificial OWC was created (oil-water contact at 2000 metres TVD) in the simulation model for the shale equilibrium zone; this contact was positioned in the overburden outside the model, much shallower than the respective reservoir contact (OWC at 2621 metres TVD), to guarantee that shales in the simulation model were 100% saturated with water.

Shale capillary pressure was modelled using a pore throat geometry correlation between Girassol shales and some shale gas samples under laboratory mercury and CO_2 injection tests [*Sigal*, 2013]. This is used because unconventional reservoir characterization is one of the very few research lines that is currently working on shale dynamic properties estimation. The shale pore throat ratio for the Girassol Field was established as 25 nanometres for over, side and underburden shales, and as 30 nanometres for intra-reservoir shales, applying pressure dependent empirical equations calibrated for shales [*Lapierre et al.*, 1990]. The correlated capillary pressures needed to induce changes in

shale saturation (Table 4-2) are far higher than the pressure depletion induced by production, acting as a constraint to avoid fluid flow through shales.

Sw	Kwr	Kor	CP
0.4	0	1	3510
0.5	0.0001	0.97	3000
0.6	0.0007	0.95	2457
0.65	0.001	0.92	2213
0.7	0.008	0.88	2006
0.75	0.01	0.8	1968
0.8	0.03	0.6	1830
0.85	0.06	0.45	1692
0.9	0.09	0.31	1485
0.91	0.13	0.23	1278
0.92	0.17	0.17	1110
0.93	0.21	0.12	985
0.94	0.25	0.09	810
0.96	0.31	0.06	579
0.97	0.38	0.04	405
0.975	0.47	0.02	315
0.98	0.59	0.008	200
0.985	0.7	0.005	126
0.99	0.8	0.001	78
0.995	0.9	0.0001	48
1	1	0	0

Table 4-2 *Relative permeabilities and capillary pressure for shales in Girassol Field. Water saturation (Sw), water relative permeability (Kwr) and oil relative permeability (Kor) are expressed in fractions; capillary pressure (CP) is in bars.*

Looking into the behaviour of the relative permeabilities and the changes in water saturation, draws attention the lower water saturation, which is 0.4 in the relative permeability, Table 4.2, but in many laboratory tests documented in the bibliography, it had been revealed that, due poor pore connectivity and bound water content, only 60 % of shale pore space can be replaced with the injected fluid.

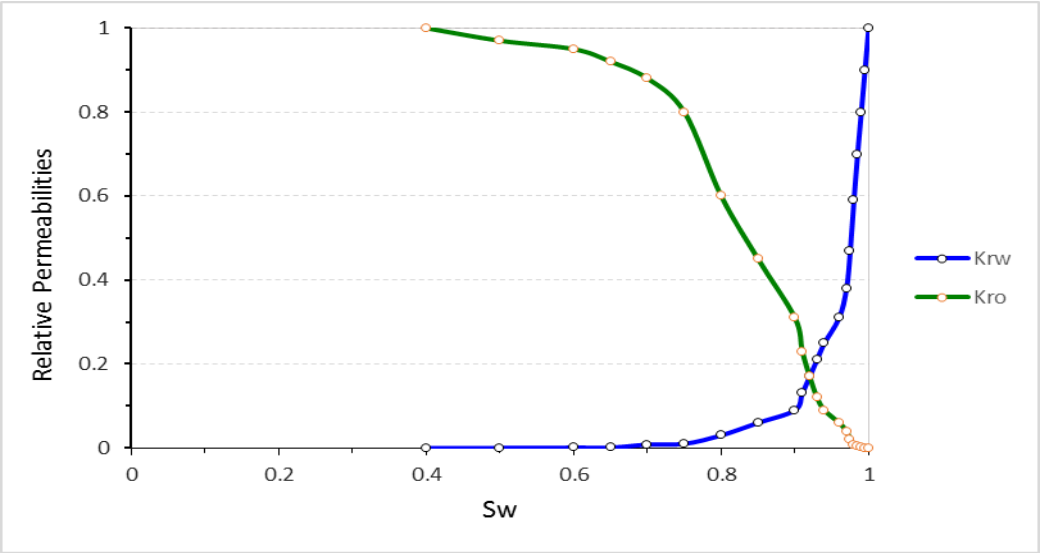

Figure 4-12 *Oil (kro) and water (krw) relative permeabilities modelled for Girassol shales.*

4.6 Simulation Results

All simulation results for active shales were compared to the conventional model with shales inactive. The simulation model for Girassol that was available within the ETLP database contained history matched production data from December 2001 to August 2004 (2.7 years), and conveniently, by the end of that period, we also had available the last seismic monitor in our database. However, as the pressure diffusion in shales is a time dependent process [*HajNasser*, 2012], the length of the simulated period was extended until August 2009 (even when there was no seismic volume to compare the 4D response for this period) maintaining the same production rates, well configuration and production/injection mechanisms in the simulation model. Due to the volumetric control used as the constraint for production, time steps further than August 2009, caused the simulation to crash. Active and inactive models were simulated using the Eclipse application from Schlumberger; predicted simulation outputs were analysed only for August 2004 and August 2009 time steps, and then compared to the initial December 2001 pre-production conditions.

4.6.1 Pressure diffusion

The analysis of the predicted changes in pressure after 2.7 years (August 2004 time-step) shows no difference between active and inactive shale models: depletion in the sands for both scenarios is pretty much the same and in the activated shales the pressure in the cells remains as it was established in the initial pre-production conditions. For the August 2009

time-step, some differences between the active and inactive shale models can be discerned, specifically depletion in the sands is slightly lower and some pressure diffusion occurs in the shales around the main channels. These changes only occurred within the intra-reservoir shale cells that were nearby sand cells (almost only in direct contact) creating a ring-like shape of depletion around the reservoir channels (Figure 4-13). The amount of pressure diffusion is very low, only in the range of 5-10 bars (0.5-1 MPa), with maximum vertical penetration of 20 metres and horizontal of 100 metres (one cell). Higher pressure changes in the shales are positioned at the reservoir top, close to the sand intervals opened to production.

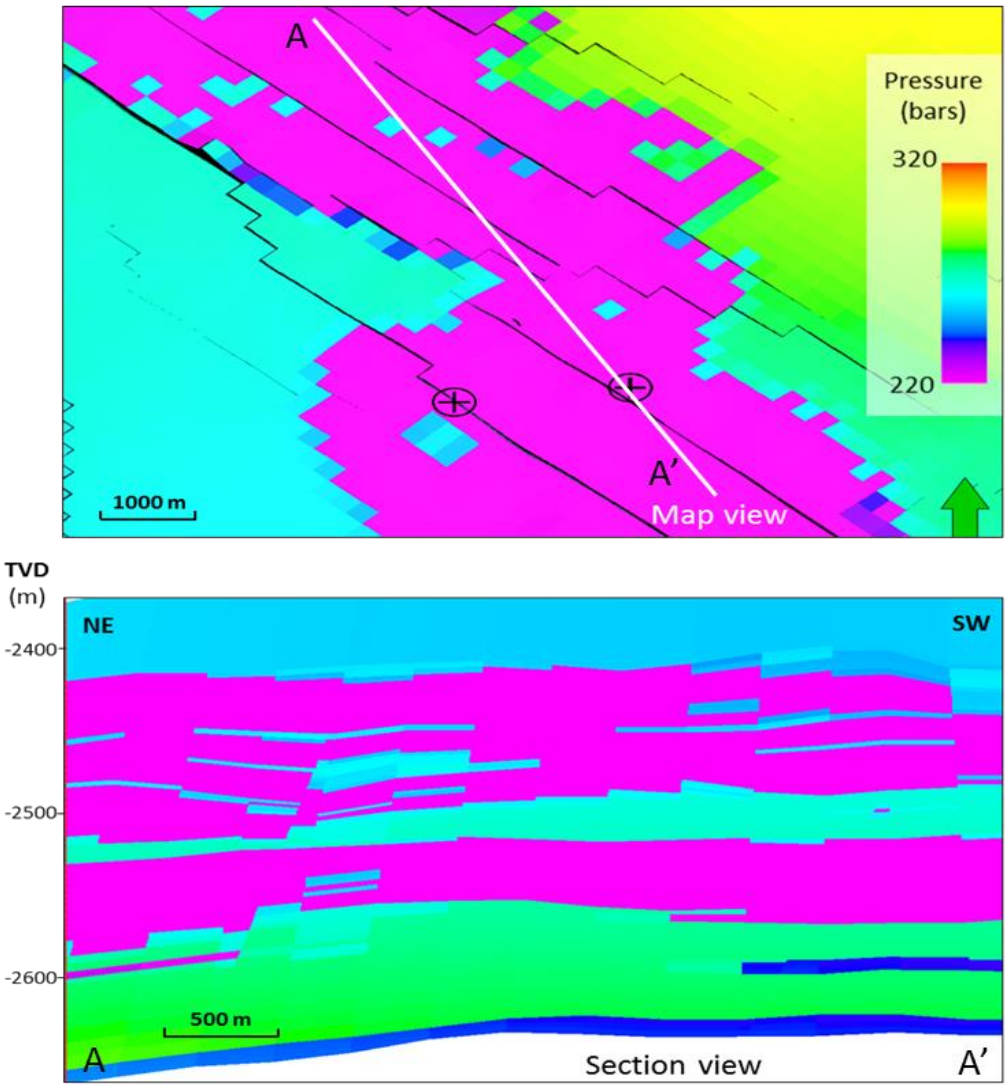

Figure 4-13 *August 2009 time-step pressure for active shales: at the top, 2D map view section and at the base longitudinal section along the main channel. Depletion in channels is below the colour bar range, but in order to see shale pressure diffusion the scale of pressure was saturated inside of the reservoir.*

4.6.2 Saturation

In accordance with the pressure results, inactive and active shale models did not show any difference in terms of reservoir predicted saturation for the August 2004 time-step. In the extended scenario (August 2009) very small variations were detected in the predicted saturation between the two models (Figure 4-14). Most of the time these changes occur in isolated reservoir cells, where the depletion induced by production is less, due to the effect of small shale pressure diffusion, causing less gas exsolution in the reservoir for the active shales model.

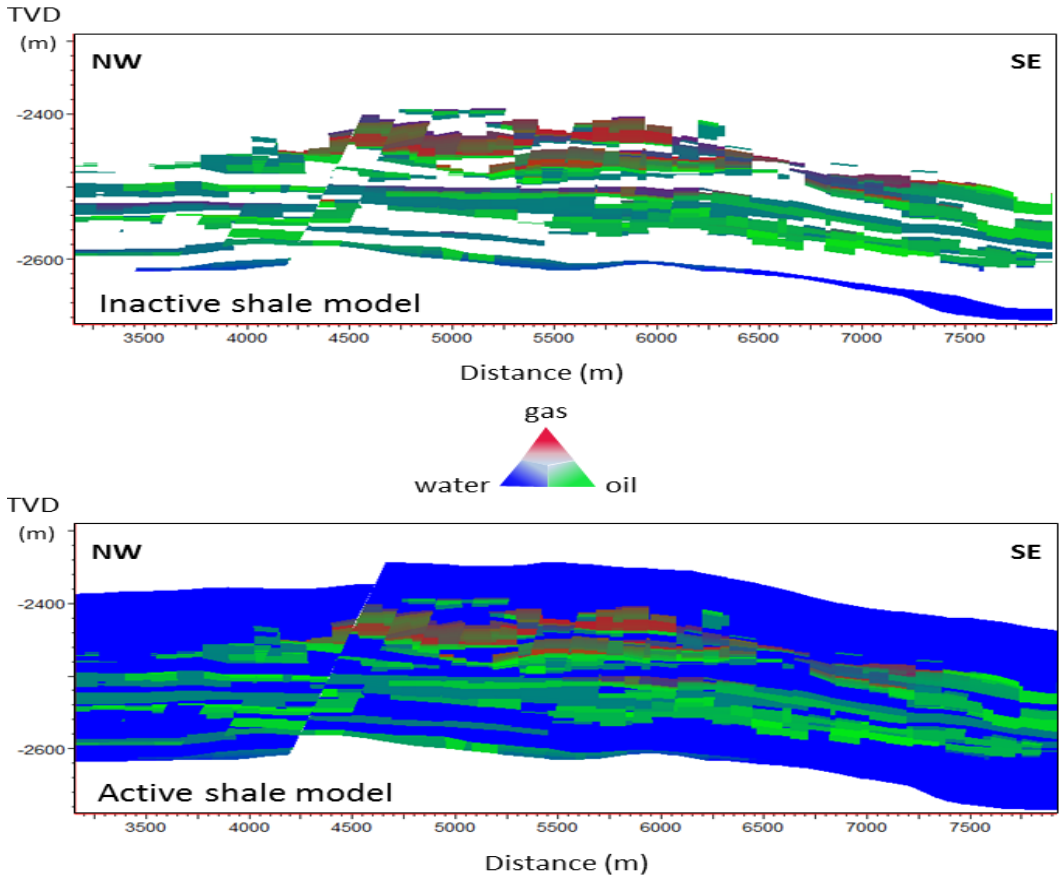

Figure 4-14 *Reservoir transversal sections, showing predicted saturation for August 2009 time-step: at the top, inactive shale model, at bottom, active shale model.*

4.7 Synthetic seismic modelling

To evaluate how changes in pressure and saturation due to shale activation impact the 4D seismic interpretation, synthetic seismic modelling was performed for both models (active and inactive shales) for three different times: December 2001 (pre- production),

August 2004 (last seismic monitor available) and August 2009 (extended simulation to see pressure diffusion in shales). Using predicted pressure and saturation of time steps, and the elastic properties of the reservoir rock frame as inputs, the simulator to seismic code (in house Sim2Seis program) converted reservoir static and dynamic cell properties into impedance, then into seismic traces (after the application of a convolutional model) and stacked in gathers with angles between 4 and 30° to match the observed 1999 full stack seismic (static comparison) and in middle angle stacks from 10 to 20° to match the time lapse data, and be converted finally in 3D seismic volumes. These are later used to estimate and interpret the predicted 4D seismic signature and its validity after comparison with the observed 4D of the Girassol Field. In order to determine the elastic parameters of the rock matrix, using the well log database, I applied rock physics analysis (see Chapter 2, equations 2.37 and 2.38), to representative intervals of each saturation region (Table 4-3) in order to determine the elastic parameters (density, velocity, bulk moduli and shear moduli) and their spatial distribution and variations (shale properties corresponding to SATNUM 9 and 10).

SATNUM	ρ ma (g/cm3)	Vp ma (m/s)	Vs ma (m/s)	G ma GPa	K ma GPa
1	2.29	2351	1030	2.43	9.42
2	2.37	2436	1090	2.83	10.34
3	2.43	2654	1110	3	13.14
4	2.55	2758	1290	4.25	13.74
5	2.62	3099	1410	5.21	18.22
6	2.62	3217	1570	6.46	18.52
7	2.61	3044	1490	5.80	16.46
8	2.63	3105	1590	6.65	16.49
9	2.27	2236	940	2.01	9.24
10	2.33	2290	985	2.26	9.38

Table 4-3 *Elastic parameters estimated for rock matrix properties of Girassol Field SATNUM.* ***ρ*** *ma= matrix density, Vp ma= matrix P-wave velocity, Vs ma= matrix S-wave velocity, G ma= matrix shear moduli and K ma= matrix bulk moduli.*

For the elastic modelling of the fluids, in addition to the PVT functions, temperature and salinity of the reservoir were defined (Table 4-4), and for the accurate alignment of the

synthetic seismic, the seismic horizon of the top B3 sequence was used as guide to tie the synthetic volume in TWT (two-way-time). The characteristics of the wavelet used in the convolutional model can be seen in Figure 4-15 and the procedure of wavelet extraction in the Appendix C.

Reservoir temperature	65 °C
Water salinity	117,800 ppm.
Oil gravity	32° API
Gas gravity	0.857
Overburden properties (outside the model)	P-wave velocity= 2190 m/s; S-wave velocity=810 m/s; Density=2.2 gr/cm^3
Underburden properties (outside the model)	P-wave velocity= 2450 m/s; S-wave velocity=1080 m/s; Density=2.35 gr/cm^3

Table 4-4 *Reservoir parameters (fluid properties, temperature and earth model) used for synthetic seismic modelling in Girassol Field.*

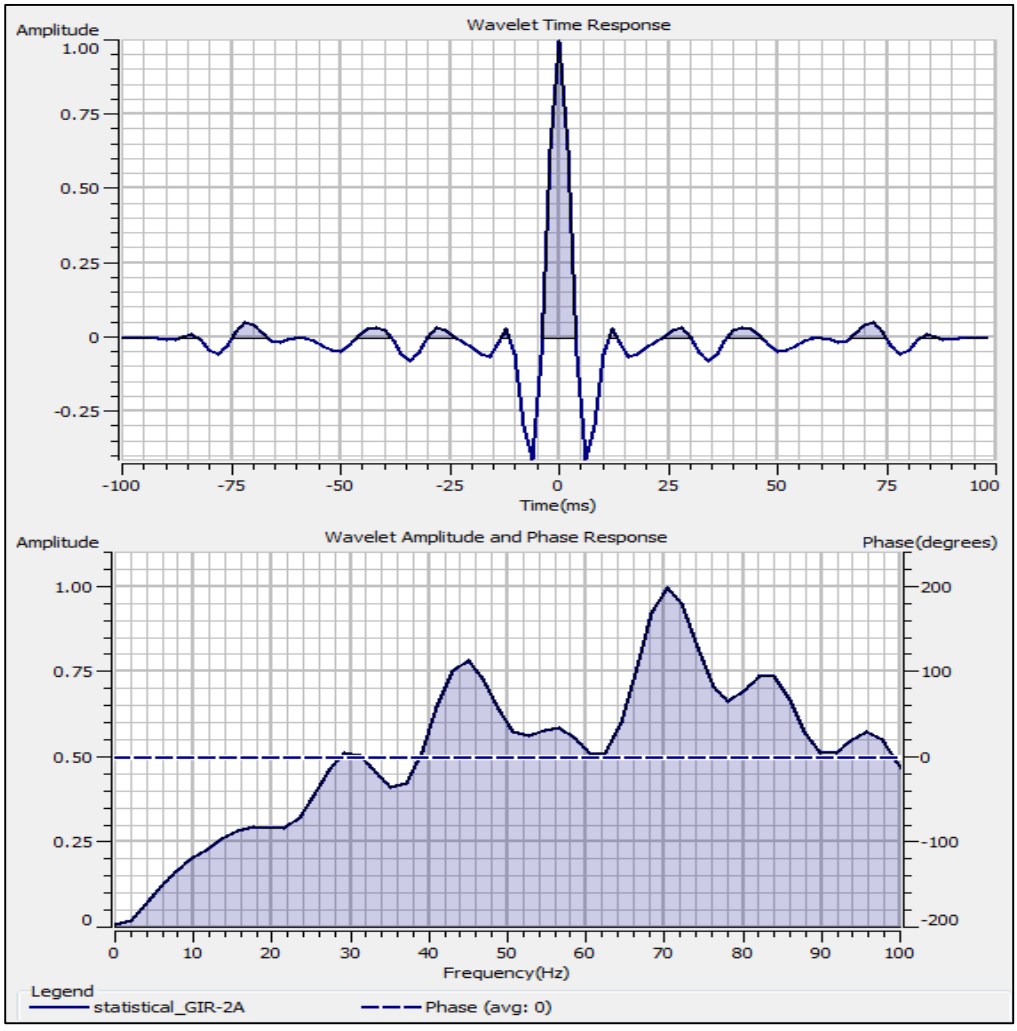

Figure 4-15 *Well base extracted Wavelet for the Girassol Field. (Roy White method)*

The rock frame stress sensitivity for Girassol Field sandstones and shales was modelled as effective pressure dependent, using the equations and lower bound coefficients established for the West of Shetland Palaeocene sandstones [*MacBeth*, 2004], due to lack of data for the West Africa area. So even when the sandstones and shales are modelled with equal stress frame sensitivity, it is obvious that the stress sensitivity of shales is changing with depth (Figure 4-16) and pressure diffusion (Figure 4-17).

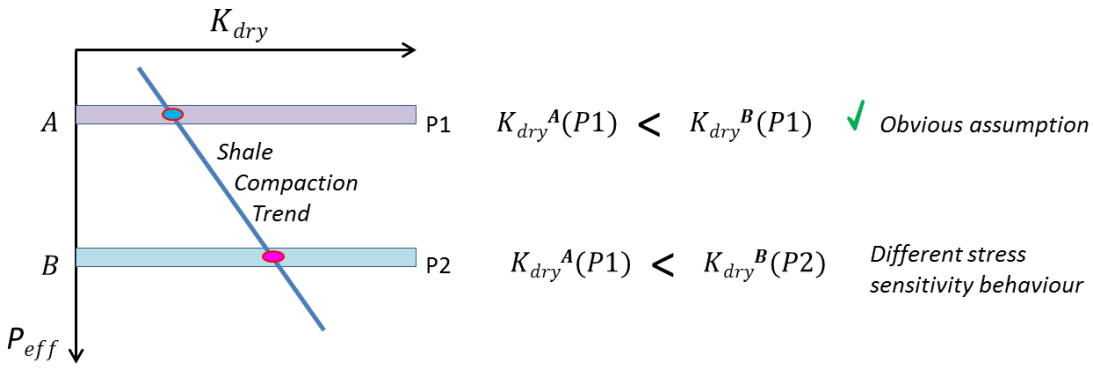

Figure 4-16 *Scheme for dry bulk moduli (K_{dry}) variations for two different intervals of shales A and B (with B more compacted than A) under P1 and P2 effective pressure conditions (with P1< P2). As density and velocity due to compaction are higher in the B shales, it is logical to assume that under the same effective pressure conditions (P1) the dry bulk moduli of A will be lower than B, but if is under higher effective pressure condition (P2) B shale dry bulk moduli is higher than A shales in P1 conditions, that means that the stress sensitivity behaviour of the shales is also changing with the depth and compaction.*

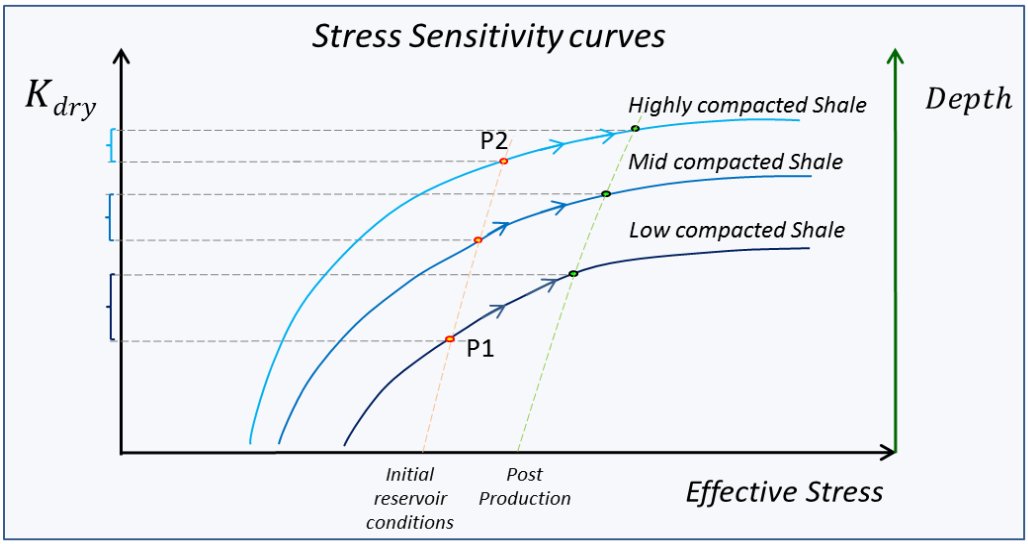

Figure 4-17 *Stress sensitivity evolution for shales under compaction and pressure diffusion.*

To model these variations into the stress sensitivity relationships used (equations 2.43 and 2.44) I had to introduce a depth-dependent pressure trend and an elastic moduli trend (also depth-dependent). From *MacBeth* (2004), we know that

$$K\infty = K_{dry}(P) * (1 + Ek * e^{-P/Pk}) \quad (4.3)$$

$$G\infty = G_{dry}(P) * (1 + E\mu * e^{-P/P\mu}) \quad (4.4)$$

Replacing K∞ and G∞ into the equations 2.43 and 2.44, we have

$$Kdry(P) = \frac{Kdry(1)*\left(1+Ek*e^{-P1/Pk}\right)}{1+Ek*e^{-P/Pk}} \quad (4.5)$$

$$Gdry(P) = \frac{Gdry(1)*\left(1+E\mu*e^{-P1/P\mu}\right)}{1+E\mu*e^{-P/P\mu}} \quad (4.6)$$

where *P1 is* P_{trend} for the initial pressure conditions and is defined by equation 4.7 (pressure in MPa and depth in metres). Now for inter-reservoir, over, side and underburden shales (SATNUM 10), if we substitute the bulk and shear moduli calculated from well log and rock physics analysis for the depth datum (2410 metres) in the initial conditions Kdry(1) and Gdry(1), we obtain equations 4.8 and 4.9.

$$P_{trend} = 25.57 + 0.009112 * (depth - 2410) \quad (4.7)$$

$$K_{dry}(P) = \frac{[Kdry(SATNUM_{10})+0.01864*(depth-2410)]*\left(1+Ek*e^{-Ptrend/Pk}\right)}{1+Ek*e^{-P/Pk}} \quad (4.8)$$

$$G_{dry}(P) = \frac{[Gdry(SATNUM_{10})+0.0019685*(depth-2410)]*\left(1+E\mu*e^{-Ptrend/P\mu}\right)}{1+E\mu*e^{-P/P\mu}} \quad (4.9)$$

and finally for changes in density

$$\rho_{matrix\ shale\ trend} = \rho_m(SATNUM_{10}) + 0.56*(depth - 2410) \quad (4.10)$$

These equations describe the stress sensitivity of overburden, sideburden and underburden and inter-reservoir shales. For the intra-reservoir shales (SATNUM 9) the depth datum was established at 2450 metres TVD, and, as was mentioned before (in the porosity modelling section) the compaction trend for this group of shales increases faster than for the pelagic ones. Looking into the static (pre-production) synthetic seismic for active and inactive shale models and comparing them to the observed real seismic (figures 4-18 and 4-19), shale activation and detailed elastic modelling of this lithology improves the synthetic seismic image, with higher amplitude events and contrast at the reservoir bottom being better captured, as well as the positioning of the horizon corresponding to the reservoir base (more accurate thickness estimation). As the effect of the compaction is at its minimum in the upper reservoir, inactive and active shale synthetic seismic volumes are quite similar, but from the middle to the reservoir base, the shales'

compaction trend creates some important differences (Figure 4-19). The bright reflectors in the central lower section of the active shale model synthetic seismic (B in Figure 4-18) correspond to erroneous amplitude contrast due to problems with the grid. As a local refinement was applied in that area, the geometry of the inactive cells (after being populated as shales and activated) was not taken into account, creating some corner point inconsistency and negative thickness, thus hindering the elastic modelling of that area. In general, for active and inactive shale synthetic seismic, the elastic modelling of the different saturation regions captured very well the true seismic expression of the intervals: the amplitude mismatch is low when compared with the observed seismic response. Variations between other time-steps' computed 3D synthetic seismic volumes will not be displayed, due to their poor contribution to the analysis (small elastic variation). Instead, I show the 4D seismic differences between the modelled scenarios in the next section.

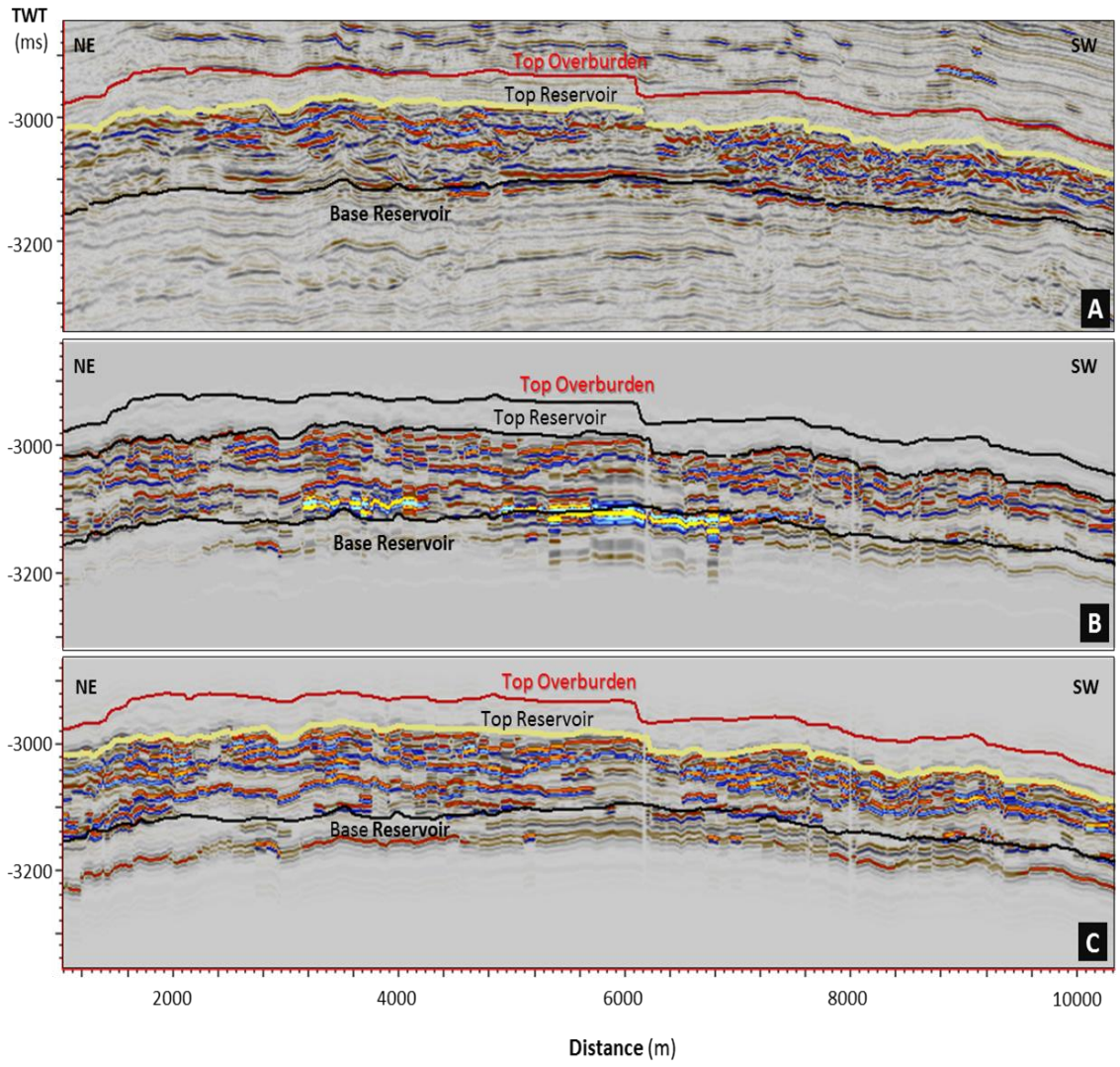

Figure 4-18 *Girassol Field seismic (section along the main turbidite channel complex): in A, Observed 1999 full stack seismic; in B, synthetic seismic Active shale model, December 2001 time-step; C synthetic seismic for inactive shales model, December 2001 time-step.*

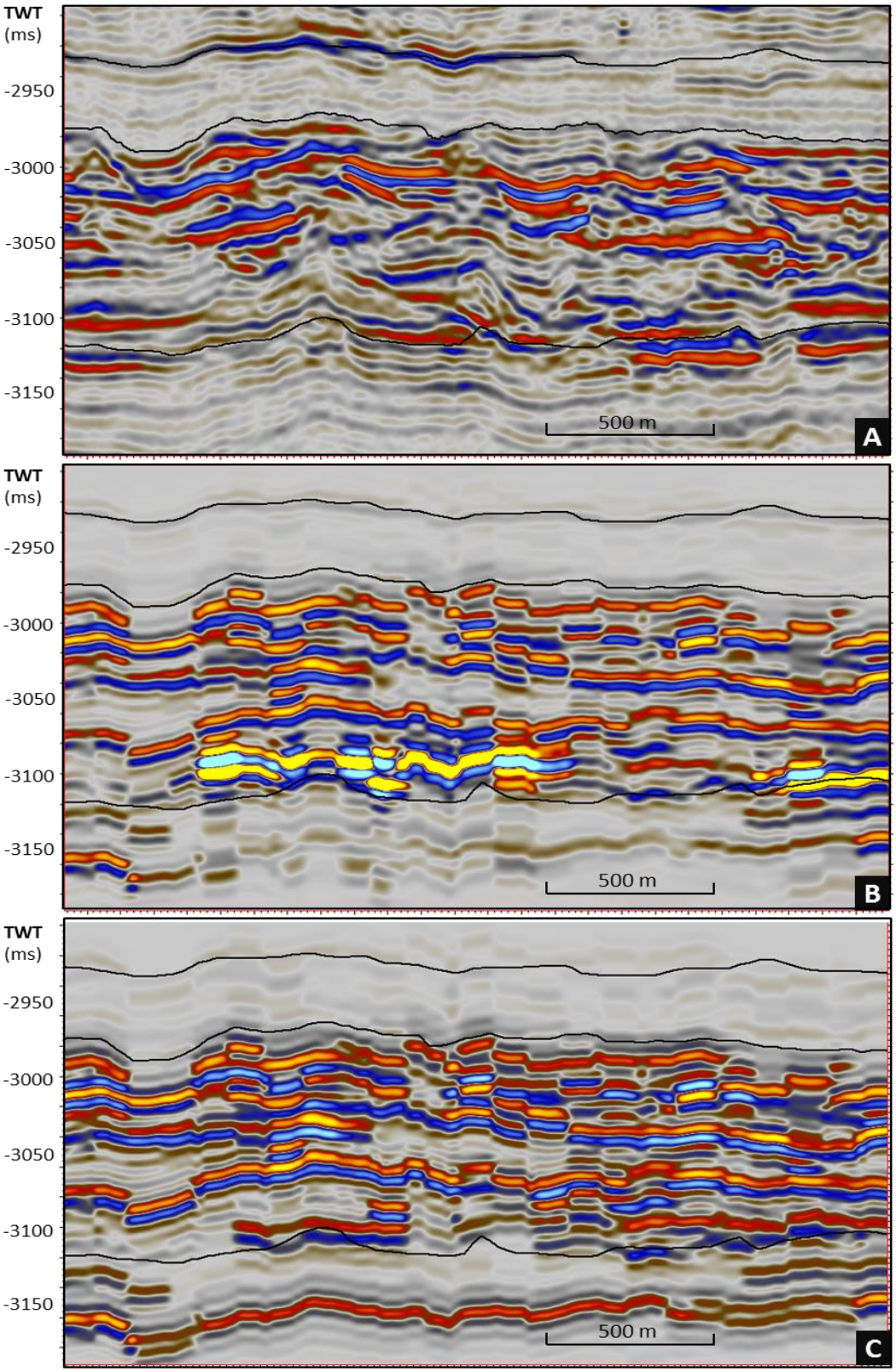

Figure 4-19 *Girassol Field seismic detail (section along the main turbidite channel): in A, Observed 1999 full stack seismic; in B, synthetic seismic Active shale model, December 2001 time-step; C synthetic seismic for inactive shales model, December 2001 time-step. High amplitude events observed in the mid-lower section of the reservoir in the active shale model in this capture (B) corresponds to cell geometry issues (minimum thickness) during the process of convolution.*

4.8 4D seismic response and interpretation

The computation of the observed 4D seismic response for the 2004-1999 was done using the Middle Angle Stack data (1999 is available in full stack, near, middle and far stacks, but the 2004 its only in angle stacks, being the middle range (10 to 20° angle stack) the data selected to compute de 4D response. Both surveys (1999 and 2004) were re-processed in parallel in 2004 using Very Fast Track (VFT) processing sequence [*Walia*, 2004; *Gonzalez-C., et al.*, 2006;], with a repeatability estimated in 23% NRMS. The 4D seismic response corresponding to the RMS Amplitude maps differences extracted for the 2004 and pre-production surveys for observed and predicted scenarios for active and inactive shales (Figure 4-20) shows similar distribution and polarity for the predicted scenarios, and poor correspondence with the observed 4D seismic response (mismatch around 65.5%, Figure 4-21).

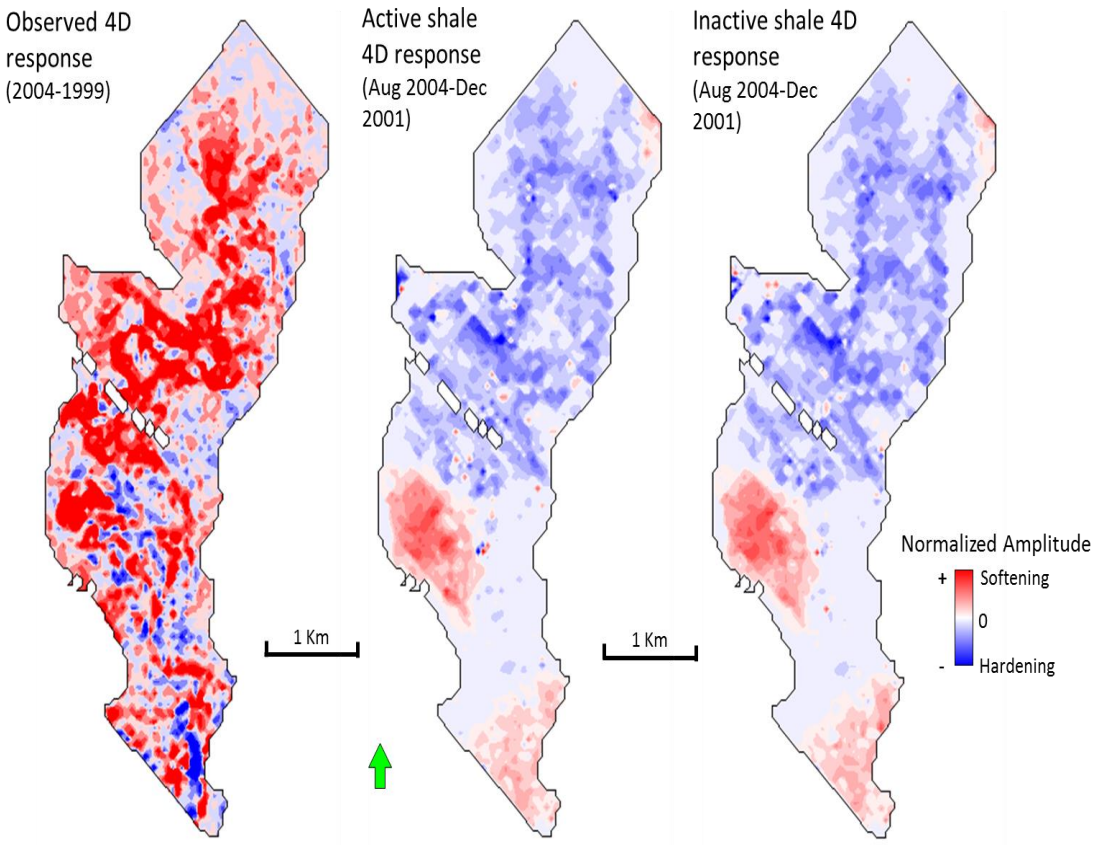

Figure 4-20 *Time lapse response based on RMS Amplitude maps differences extracted for a time window between the overburden and base reservoir horizons for the 2004 and pre-production surveys for observed and predicted scenarios for active and inactive shales.*

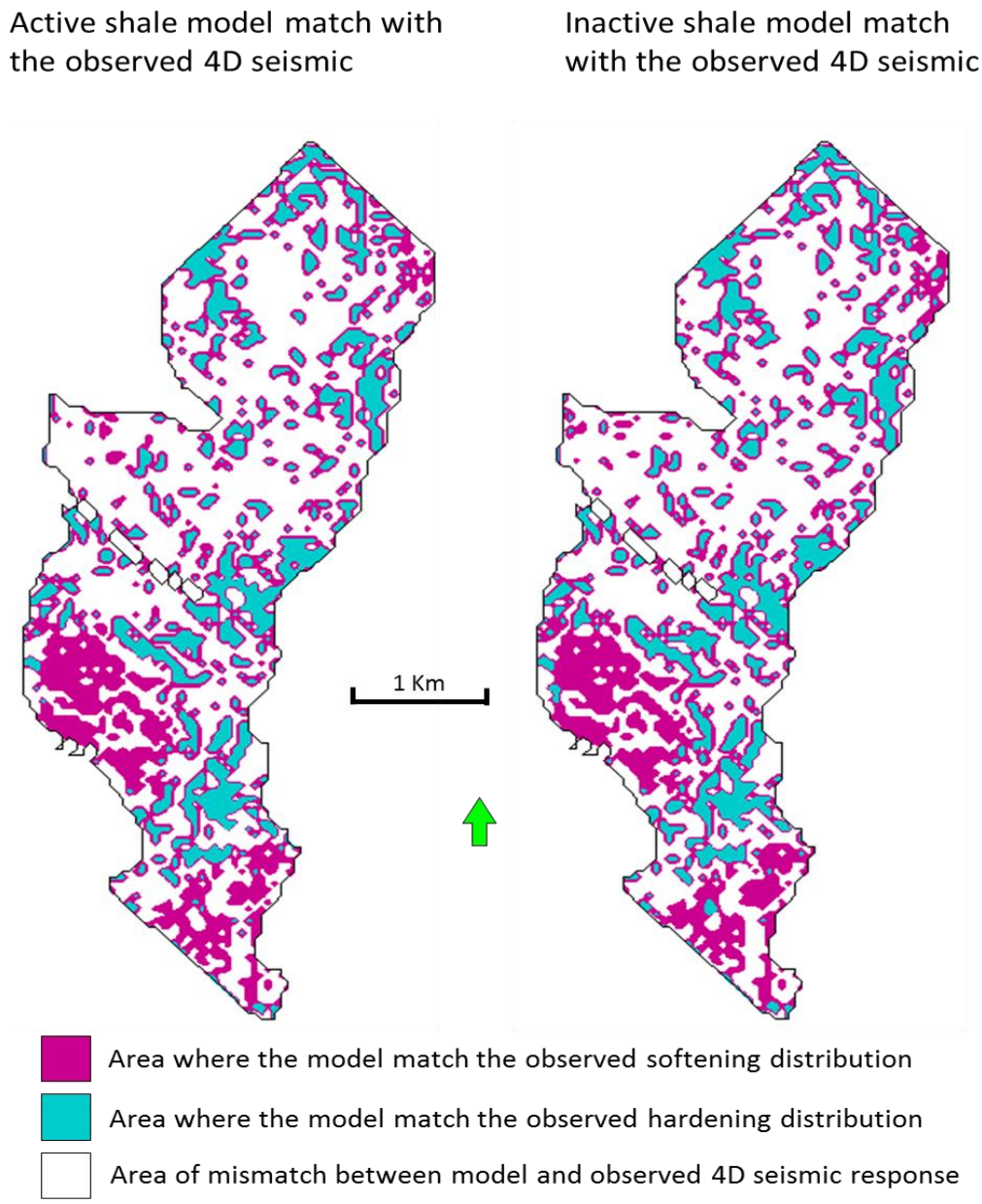

Model	Softening (%)	Hardening (%)	Without 4D (%)	Mismatch (%)
Observed seismic	69.58	30.17	0.25	
Active Shale	12.19	22.28	0	65.45
Inactive Shale	11.94	21.96	0	66.01

Figure 4-21 *Statistics for the 4D response match distribution between observed seismic and synthetic differences for active and inactive shale models. Active shale model showed a slightly lower mismatch (65.45%) with the observed 4D seismic, while the inactive shale model had a 66.01% of mismatch.*

The 4D seismic analysis in the Girassol Field was also carried out using the volumetric computed differences between monitor and base seismic surveys. Due to the availability of the observed data, the time lapse volumetric differences were computed for the Middle Stack (10 -20°) synthetic seismic volumes corresponding to the time steps August 2004 and December 2001 (to be compared with 2004-1999 4D differences of the Middle Stack observed data) and for August 2009-December 2001 (without real seismic data to compare).

For the first period, after 2.7 years of production/injection (Figure 4-22), the larger differences between active and inactive shale 4D responses correspond to the cell geometry problems reported at the base of the activated shale model grid (very bright events in that area, figures 4-18, 4-19 and 4-20). In the upper section of the reservoir, were most production/injection induced changes occur, the 4D seismic response for active and inactive shale synthetic models is very similar, which makes sense, as no large pressure diffusion (and hence non-elastic changes between the active and inactive shale model responses) was reported for that short period of time in the predicted simulation results.

Looking into the mismatch between observed and synthetic 4D seismic data, it is clear that static modelling of the reservoir is acceptable (the comparison between pre-production synthetic volumes and observed data good, figures 4-18 and 4-19), but the parameters that influence the dynamic behaviour were not properly captured by the simulation model, as the differences between predicted (both active and inactive shale synthetic scenarios) and observed 4D are substantial, especially towards the south-west (Figure 4-22).

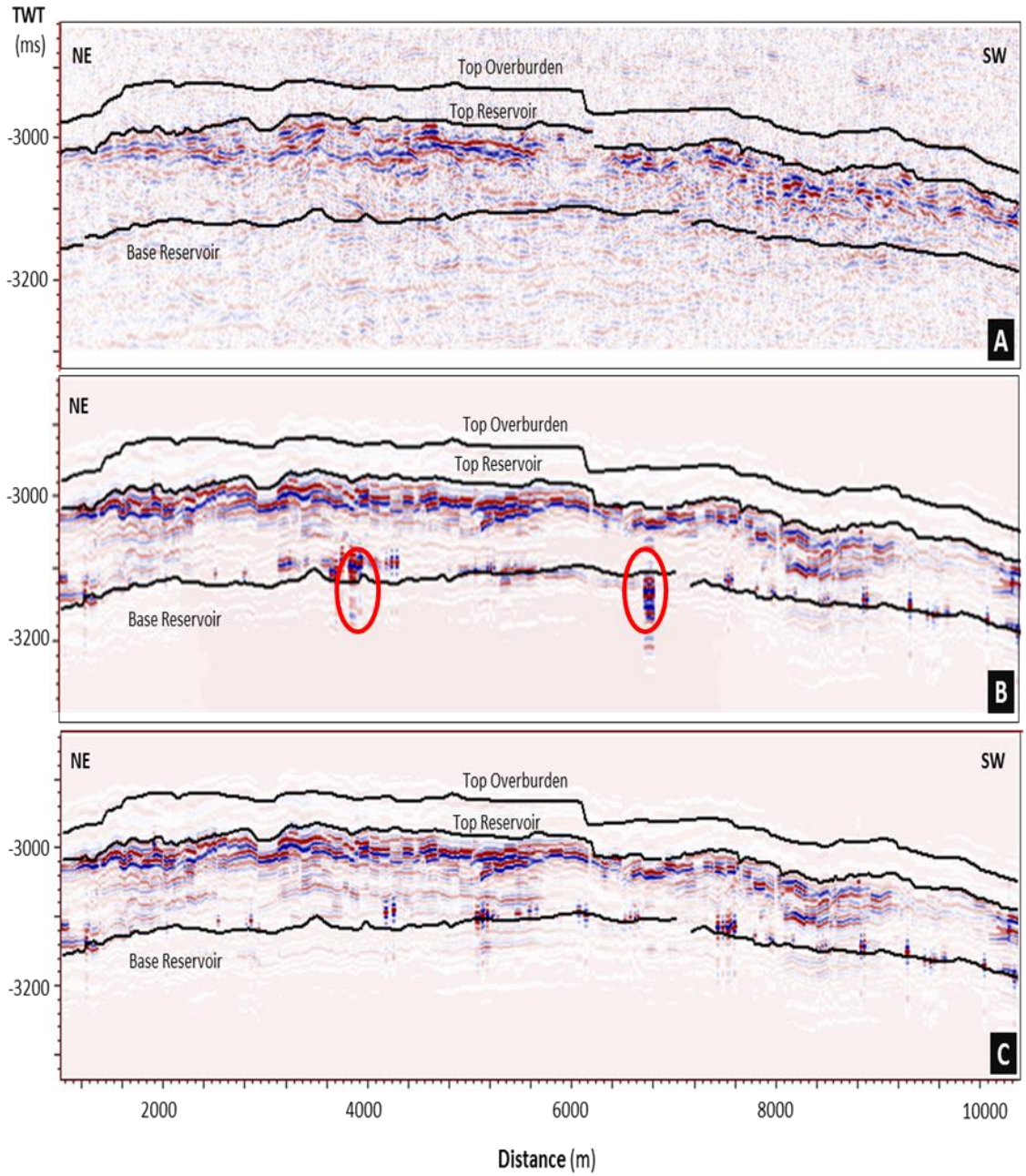

Figure 4-22 *Girassol Field 4D seismic differences: 2004 – base seismic, displayed in longitudinal section along the main turbidite channel complex. A) Observed 4D (2004-1999 seismic volumes); B) Active shale 4D differences (Aug 2004-Dec 2001 synthetic seismic volumes): C) Inactive shale 4D (Aug 2004- Dec 2001 synthetic seismic volumes).In red ovals areas for the active shale model were the synthetic 4D seismic response is showing cell geometry issues during the process of convolution, so that signal do not corresponds to induced elastic changes.*

The second period analysed (8.7 years), where the predicted synthetic volumetric differences cannot be compared with observed data, was computed using full stack (0 to 30°) angle range for the synthetic volumes between the pre-production (December 2001) and extended production (August 2009) time steps. This period shows variations between the two modelled scenarios (active and inactive shales), especially at the base of the reservoir, where inactive shale models have a slightly stronger 4D seismic signal,

suggesting that without active shales, the higher induced pressure imbalance is responsible for those changes, and is more evident at the base of the reservoir (B1 sequence) where the reservoir connectivity and channel facies coalescence is lower. In the upper reservoir section, the 4D seismic signal is similar (Figure 4-21) for both models, showing the direct relationship between reservoir's connectivity and pressure diffusion in the surrounding shales. The validity of these findings is obviously subjected to the assumptions that I made regarding the fixed field conditions used to extend the simulated period (constant production and injection rates and same well number and completions) from August 2004 to August 2009.

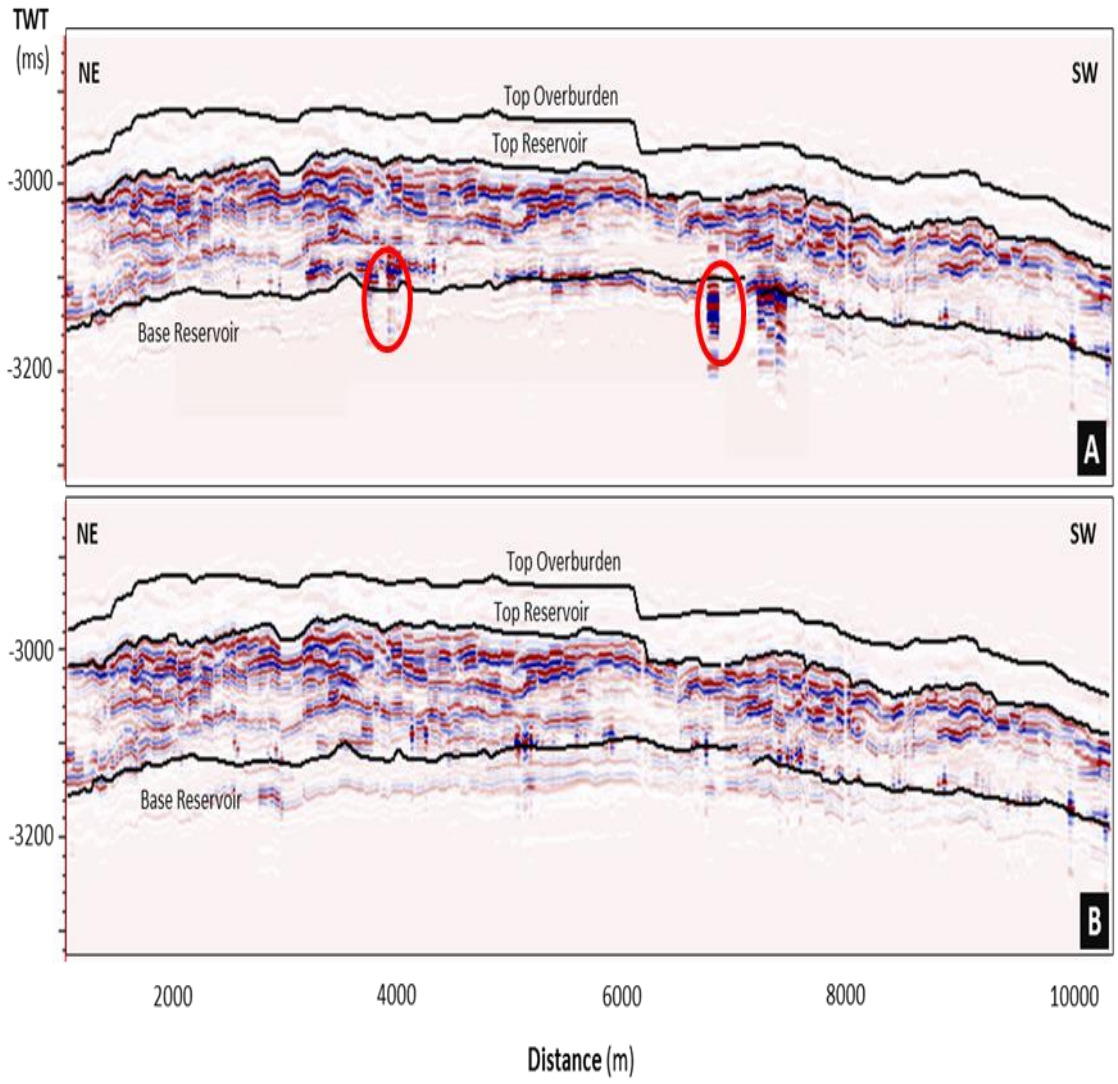

Figure 4-21 *August 2009-December2001 synthetic 4D volumetric seismic response for Active (A) and Inactive (B) shale models, shown in a longitudinal section along the main turbidite channel complex. In red oval, response linked to cell geometry problems in the simulation model of the shale active scenario.*

4.9 Conclusions

Taking into account results from the previous shale activation workflow application (Heidrun Field), it was expected to see substantial pressure diffusion in shales of the Girassol Field, due the more varied and convenient sand -shale contact geometry (lateral contact between sand and shale implies a higher pressure interaction, due to larger shale permeability in the horizontal direction). The reservoir characteristics created by the structural control during deposition, such as coalescence and very high connectivity between the channel units, plays a dominant role in the shale pressure diffusion process. For instance, the connectivity within the reservoir helps to quickly equilibrate the production-induced depletion. Having a large volume of complex connected channels' facies, which resembles an open system, contributes to the reduction of the pressure imbalance between sands and shales, delaying the pressure diffusion in shales until a more mature production and depleted stage is reached in the reservoir. Another factor influencing this process is the directionality of the pressure diffusion. In the particular case of the Girasol Field, the front of pressure diffusion goes from the reservoir outwards, but with shales constituting a background of almost infinite extent, in modelling terms, an opposite front of diffusion is created from the external shales towards shales in contact with reservoir sands. This opposite front is fighting depletion back, trying to equilibrate the pressure imbalance generated from the depleted sands towards the shales, thus, reducing the net pressure drop in the shales. Under those conditions, only isolated patchy intra-reservoir shales have conditions to experiment with sizeable depletion.

Changes in the reservoir saturation associated with the shales' activation were not significant, and although the reservoir pore pressure was very close to the bubble point, the magnitude of pressure diffusion in shales did not affect the process of gas exsolution in the reservoir and its related elastic implications in a significant manner.

As changes in the shales' pressure were small (1 bar or less for the 2004 time step and between 5 to 10 bars for the 2009 time step) and only in the immediate shale cells around the reservoir it is logical to expect little influence from this process in the overall reservoir elastic behaviour and 4D seismic signal, so the response for active and inactive shale models showed similar distribution and less than 1% of improvement in the fit to the observed seismic data. The absence of longer history matched production data and corresponding extra seismic monitors limited the scope of this study, due the strong

dependence of the shale pressure diffusion process on time, but the validity of the findings is reasonable, if the extended conditions for simulation are deemed reasonable.

Due to the relatively unconsolidated nature of the reservoir I believe that Girassol Field shales are not utterly inert in the reservoir dynamic behaviour and 4D seismic interpretation (even when for the studied period they look as if they are almost so); a more mature production stage in the reservoir, probably derived from an induced geomechanical response due to the compaction of the reservoir sands by the effect of depletion, can trigger a more active participation of shales in this reservoir.

In any case, the inclusion of the shale's internal architecture into the static and elastic modelling of the Girassol Field clearly enhanced the synthetic seismic modelling of this area, and the reason is simple: the compaction trends of the pelagic (inter-reservoir, over, side and underburden) and resettled (intra-reservoir) shales dominate the seismic contrast and the expression of the reservoir sands.

5 Chapter:

Case study: Schiehallion Field

This chapter focuses on the shale activation workflow for the 3D and 4D seismic modelling of the Schiehallion field, Segment 1. To evaluate shale implications in the 4D seismic response, a series of models were created to explore different shale activation scenarios and their contribution to the reservoir dynamic properties. To isolate the effect of pressure diffusion inside shales and to assess its implication in reservoir connectivity, transmissivity multipliers were removed from the simulation models. Dynamic results from simulation and synthetic seismic modelling for active shale scenarios showed better modelling prediction and more accurate 4D seismic matching, especially in the case of gas exsolution. Shale activation also improved the understanding of the sandy facies' behaviour, providing valuable insights for updating the static and dynamic models.

5.1 Field generalities

The Schiehallion Field is a deepwater (350-450 metres) offshore oil and gas field, located in the quadrants 204/205 of the United Kingdom Continental Shelf, approximately 130 kilometres west of the Shetland Islands in the North Atlantic Ocean (Figure 5-1). Discovered in 1993 and on-stream since 1998, this field has estimated recoverable reserves between 425 and 600 million barrels (2 billion barrels on site) and is operated by BP on behalf of the Schiehallion field partners (Shell - 55%, BP - 33.5% and OMV - 11.8%). The Schiehallion Field and the adjacent Loyal Field reserves are developed using a Floating Production Storage and Offloading (FPSO) vessel.

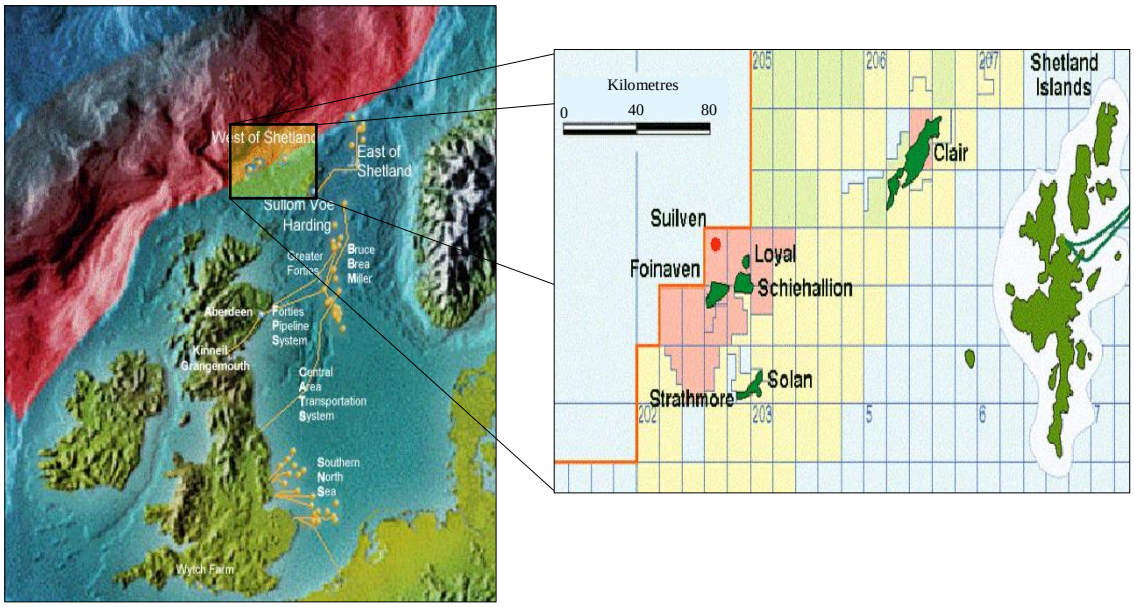

Figure 5-1 *Schiehallion Field location.*

The reservoir is a Tertiary live black oil accumulation (25° API) with small local gas caps. As the reservoir's pressure, 200 bars at 1940 metres TVD (top reservoir), is very close to the oil bubble point (194 bars), the field production was developed under a down-dip water injection plan. The Schiehallion Field has been under 4D seismic monitoring since 1999, (base line survey was shot in 1996) and up to this time 8 monitors have been acquired over the field. For the shale activation workflow in the Schiehallion Field, the dataset available for this study consisted of well log data (35 wells), the simulation models (coarse and fine scale models), and the seismic surveys, namely the 1996 base seismic survey and 2004, 2006 and 2008 seismic monitor surveys.

5.2 Geological context

During the Late Cretaceous - Palaeocene, as part of the Alpine tectonic megacycle, the North Atlantic sea-floor spreading axis propagated northward into the Norwegian-Greenland Sea, creating rifting regimes [*Ziegler*, 1988]. In the West of Shetland Basin, the induced extension generated NE-SW normal faults and the associated subsidence created deep marine conditions during the Palaeocene. The generated depocentre (elongated and parallel to the normal faults) received clastic sediments (mostly sands) from the deltaic-shallow marine environments located in the East, pelagic sedimentation (clays) from marine circulation in the North and volcanic sediments from the West (Figure 5-2). The turbidites deposited in this deep marine environment constitute the reservoir facies for the fields Schiehallion, Foinaven and Loyal.

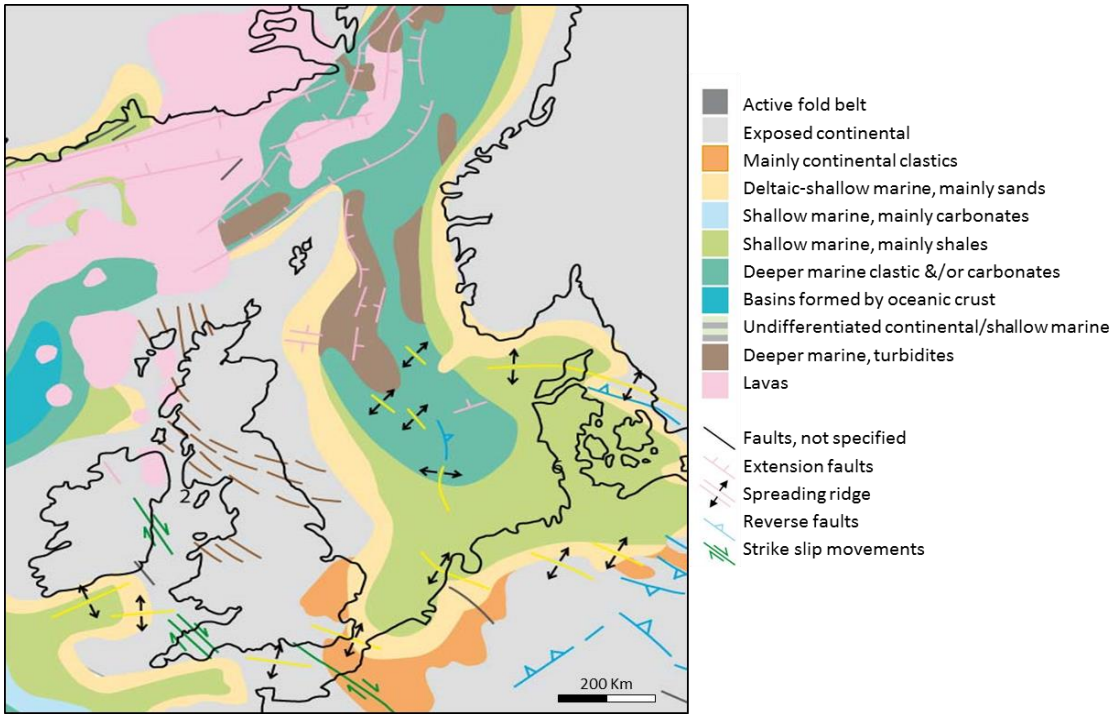

Figure 5-2 *North Atlantic and North Sea Palaeocene configuration. Modified from published literature [Ziegler, 1988].*

The Schiehallion Field consists of stacked turbidite channels with good reservoir quality (porosities between 25 -30% and permeabilities between 200-1000 mD). The sequence, which is sedimented from North to South, is cross-cut by several W-E normal faults (south dipping) that divide the reservoir into 4 compartmentalized segments (Figure 5-3). In this case study, shales were activated only for segment 1.

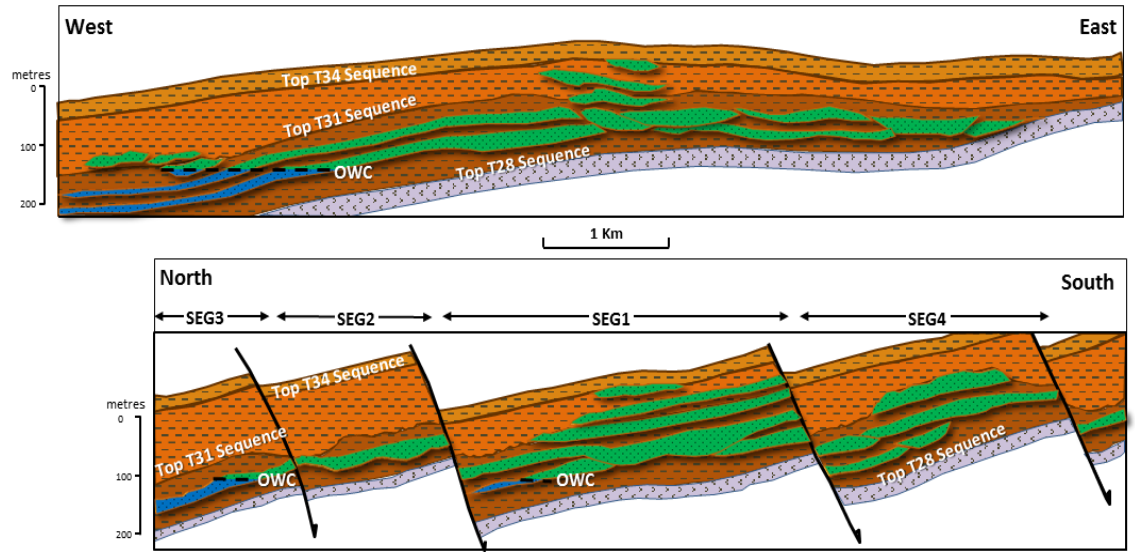

Figure 5-3 *Schiehallion Field structural configuration. Redrawn from published literature [Leach et al., 1999]*

The reservoir comprises deposits from four turbidite sequences, which are lateral equivalents of the Lista Formation (North Sea Middle Palaeocene lithostratigraphy), starting from bottom to top, these are the T31B, T31A, T34 and T35 sequences (nomenclature based on the BP operational Tertiary nomenclature for the West Shetland Basin), as shown in Figure 5-4. These four sequences, which overlie the volcanic sediments of the T28 sequence (Figure 5-3), were deposited by high energy turbidite flows, with events T31B and T31A separated by the deposition of a thin shale interval (Figure 5-5). The spatial distribution of the T31B sequence suggests the development of two turbidite lobes, connected in the proximal section of the sequence but separated in the distal section. The subsequent T31A deposits are more extensive, covering the whole area of segment 1, which suggests coalescence between channels and overbank deposits from different flows. Both sequences (T31A and T31B) have a high ratio of overbank (levee)/channel sediments, evidencing a low angle marine floor plain in the turbidite sedimentation process. Overlying T31A, the deep marine shale succession is eroded in the central area of the reservoir by the turbidite channel facies of the T34 and T35 sequences (Figure 5-5). The incisive, narrow and erosive character of these two sequences in Segment 1 of the reservoir, suggest a different geometry of the marine floor plane (more tilted) during turbidite deposition. The lower ratio of overbank/channel sediments also indicates less sediment load in the turbidite flow, with probable conditions corresponding to a terraced turbidite system. The hydrocarbon saturation column in the Schiehallion Field makes T34 and T35 not very prospective for production (at least in

Segment 1), because of the narrower pressure window between the reservoir pore pressure and the oil bubble point, which usually results in the development of local gas caps in these sequences. The most prospective sequence is the T31A, due its lateral extension, volume and higher quality sand facies. The overall thickness of the reservoir in Segment 1 is approximately 150 metres (where all the sequences overlie each other).

Epoch	BP T-Sequence	North Sea Lithostratigraphy
Lower Eocene	T50	Balder Fm
Upper Palaeocene	T40	Sele Fm / Forties Mbr
	T30 (T35, T34, T31)	Balmoral Mbr; Glamis Mbr; Andrew Mbr (Lista Fm)
Middle Palaeocene		
Lower Palaeocene	T20	Maureen Fm
	T10	Ekofisk Fm

Figure 5-4 *Comparison between BP West of Shetland Tertiary nomenclature and the North Sea lithostratigraphy. Redrawn from published literature [Leach et al., 1999].*

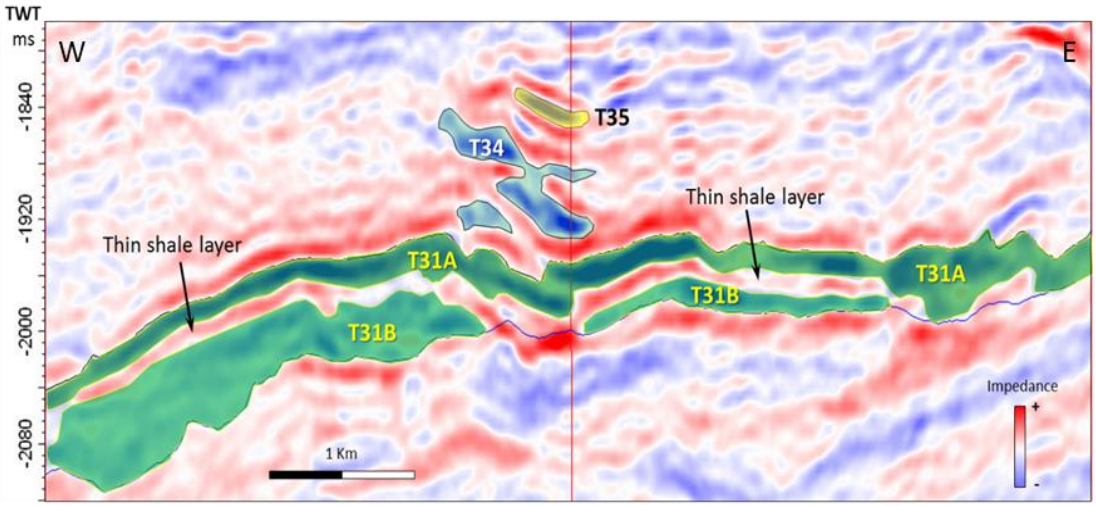

Figure 5-5 *Pseudo-acoustic impedance seismic cube (90°phase rotation) of Schiehallion Field, Segment 1, showing (inline direction) the distribution of the turbidite channels' sequences T31B, T31A, T34 and T35. Modified from ETLP published literature [Amini, 2014]*

Looking into the seismic expression of the reservoir's architecture (Figure 5-6), the elastic contrast between sands and shales in this field is influenced mostly by saturation. On the other hand, there exist thin intervals inside the channel facies of all sequences, which correspond to cemented sandstone intervals having high density and velocity, which may give rise to internal seismic reflections. These sandstone intervals are expressed as spikes in the logs and have important implications in the reservoir's connectivity, due to their spatial distribution. Also one can observe a gentle compaction trend for the pelagic shales (corresponding to an increase in density and velocity with depth, Figure 5-7).

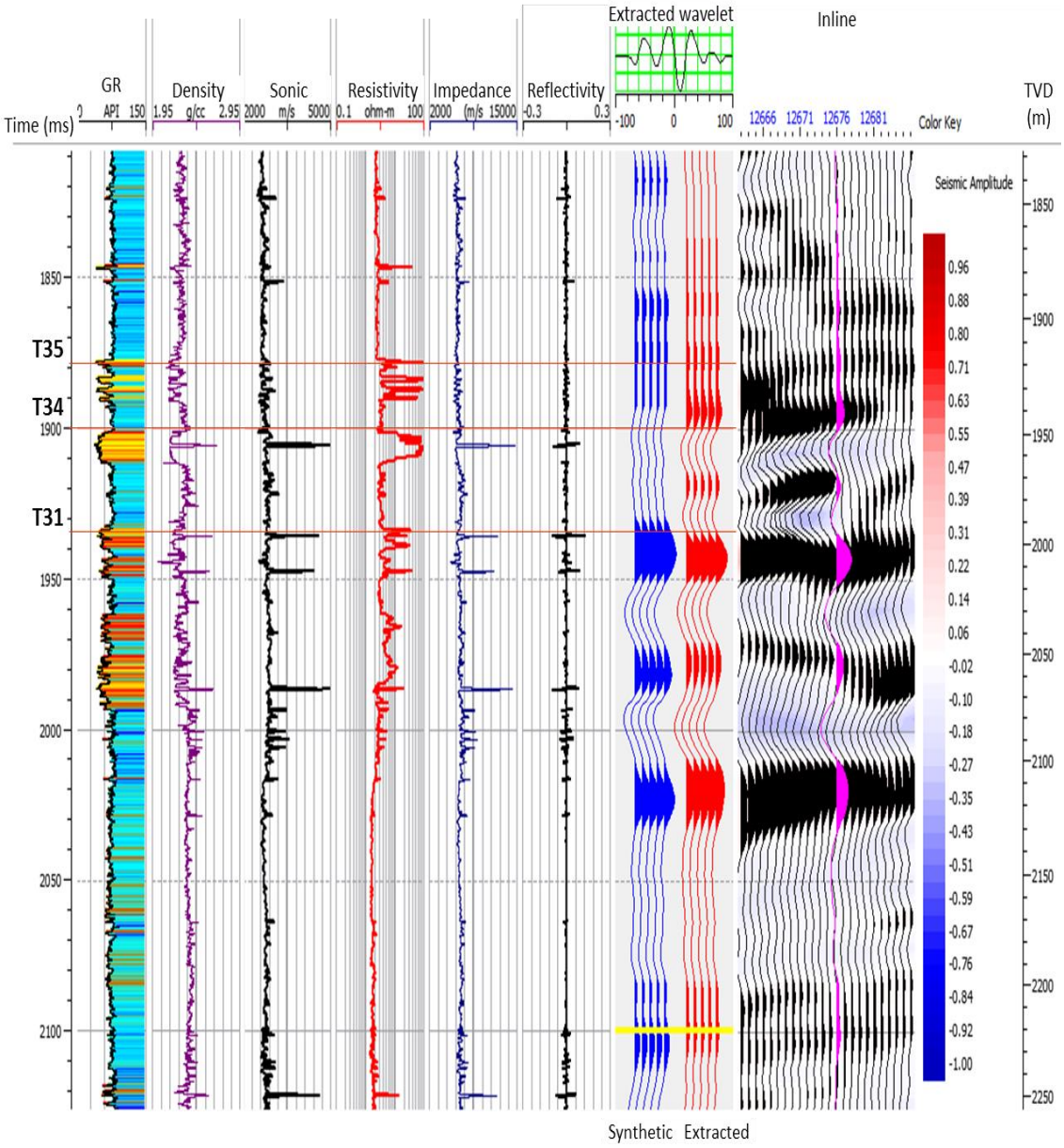

Figure 5-6 *Well tie in the central area of Segment 1 showing (inline direction) the seismic expression of the reservoir's architecture and T31, T34 and T35 sequences*

5.3 Shale characterization

Shales in the Schiehallion Field were deposited in a deep marine environment under normally low energy conditions, which implies that clays travelled most of the time in suspension and settled through gravity in a flocculated structure, which incorporated electrochemical characteristics of marine water [*Potter et al.*, 2005]. Stationary periods of high energy tend to bring some silt and sand influx into the deep marine basin, creating vertical alternations between the different types of sediments. Fast sedimentation (high porosity and water content in shale intervals) and slope changes create instability and subsequent turbidite flows that produce erosion, transport and rearrangement of the sediments. Poorly consolidated shale intervals rich in clays usually go back to suspension and are thereafter resettled, whereas more consolidated shale intervals travel and are deposited as clasts, together with the heavier sand particles, creating dispersed shales in the turbidite channel facies. After the deposition of the turbidite flow, normal low energy deep marine conditions deposit pelagic clay sediments. As a result of this dynamic sequence of events, a distinct geometric pattern is created, with reservoir sandy facies surrounded by shales in the overburden, sideburden and underburden, as well as intra and inter-reservoir shale layers deposited in the resettlement process of lighter material in the turbidite flow.

5.3.1 Composition

To establish the properties of shales, the first step is to know the clay content and its provenance. As there was no availability of compositional laboratory data for shales for this study, the characterization was performed using lithological well log data from the Schiehallion Field. Observed heterogeneity in density and gamma ray logs, coupled with volume of shale computations were used to establish the average shale composition of this field, estimated as 65% clay fraction and 35% of silt (this proportion changes a little, vertically). For the clay fraction, the mineral density of the shale (equation 2.19) suggests a mixture of clays, due the geographical location (high latitude) of the West Shetland Basin (which has not changed much since the Late Cretaceous), the dominant clay generation process corresponding to illite and chlorite. The illite and chlorite provenance came from the weathering of the exposed continental material in the east (Figure 5-2) and from marine circulation at the north of the basin. In addition to these two types of clays, shales from the Schiehallion Field also contain montmorillonite originating from the

weathering of volcanic material exposed in the northwest direction, with the content of this clay type varying vertically. The average composition for the clay fraction of the shales in this field was established as 60% illite, 20% chlorite and 20% montmorillonite.

5.3.2 Shale internal architecture

The internal architecture of shales associated with turbidite reservoirs is the consequence of the mixture of energy regimes between the permanent pelagic conditions (continuous clay flocculation and settlement process) and episodic turbidite flows. To analyse the internal architecture of shales in the Schiehallion Field, I used the gamma ray well logs and computed volume of shale to establish lithological heterogeneity, and the density and P-wave velocity well logs to determinate acoustic properties that were useful in identifying sedimentation settlement patterns and compaction trends.

According to the observed variations explained below, shales in this field can be categorized from top to base in the following groups: overburden, inter-reservoir, intra-reservoir and underburden shales. The overburden interval is dominated by pelagic deposition conditions with some episodic clastic influx, which results in shales that are moderately uniform, with some thin layers of fine sandstones and siltstone (Figure 5-7). Compared with the other shales of this field, the clay fraction in this interval has a lower montmorillonite content. At the base, the contact of this interval with the top of the sequence T35 is abrupt (strong clean sand-mud shale contrast) evidencing the localized and fast deposition of the channel facies corresponding to the turbidite event of T35. The elastic properties of the overburden (Crossplot of Figure 5-7) show a clear compaction trend behaviour (density and velocity increasing with depth), which is quite common for fine-grained deep marine sediments, and is associated with a reduction in shale pore space and water expulsion with burial (an increase in the lithostatic column). From the reservoir configuration point of view, Schiehallion overburden shales constitute an excellent cap rock interval.

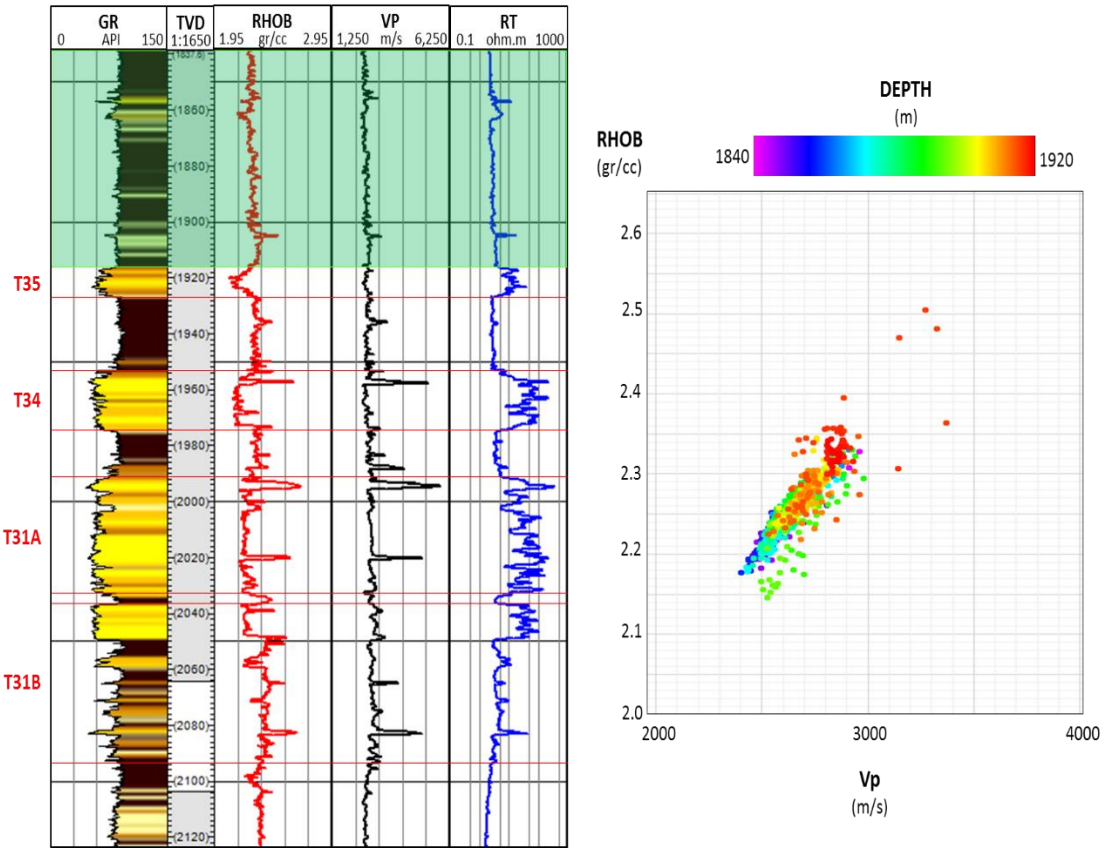

Figure 5-7 *Overburden shales in the Schiehallion Field. Well logs and Vp vs RHOB cross-plot. Depth color code shows compaction trend.*

The inter-reservoir shales (Figure 5-8) separate the reservoirs corresponding to the channel facies of T35, T34 and T31A sequences in the central area of Segment 1; these shales also constitute the overburden cap rock for the reservoirs of the sequence T31A outside the central area (Figure 5-5) and the sideburden for the sequences T35 and T34. As seen in well logs, the inter-reservoir shales are very uniform, with just a few interbedded silt layers. The homogeneous lithology shows evidence of stable conditions during deposition, specifically low energy and absence of sand influx, with the exception of the turbidite flows corresponding to the T34 and T35 events. The abrupt and erosive contact of the inter-reservoir shales with the T34 and T35 sequences, coupled with the absence of turbidite overbank deposits, suggest a gradual change in the slope of the marine plain (more tilted), which is consistent with deeper marine conditions in the basin (subsidence), low energy, and thus, more stable conditions for the pelagic deposition of clays. The elastic behaviour (shown in the acoustic impedance crossplot in Figure 5-8) of this type of shale shows a pronounced compaction trend (black arrow), with a considerable increase in P-wave velocity with depth. The clay fraction of the inter-

reservoir shales is assumed to be higher, around 70 % of the whole rock volume, with an increased content of montmorillonite, compared to that of overburden shales.

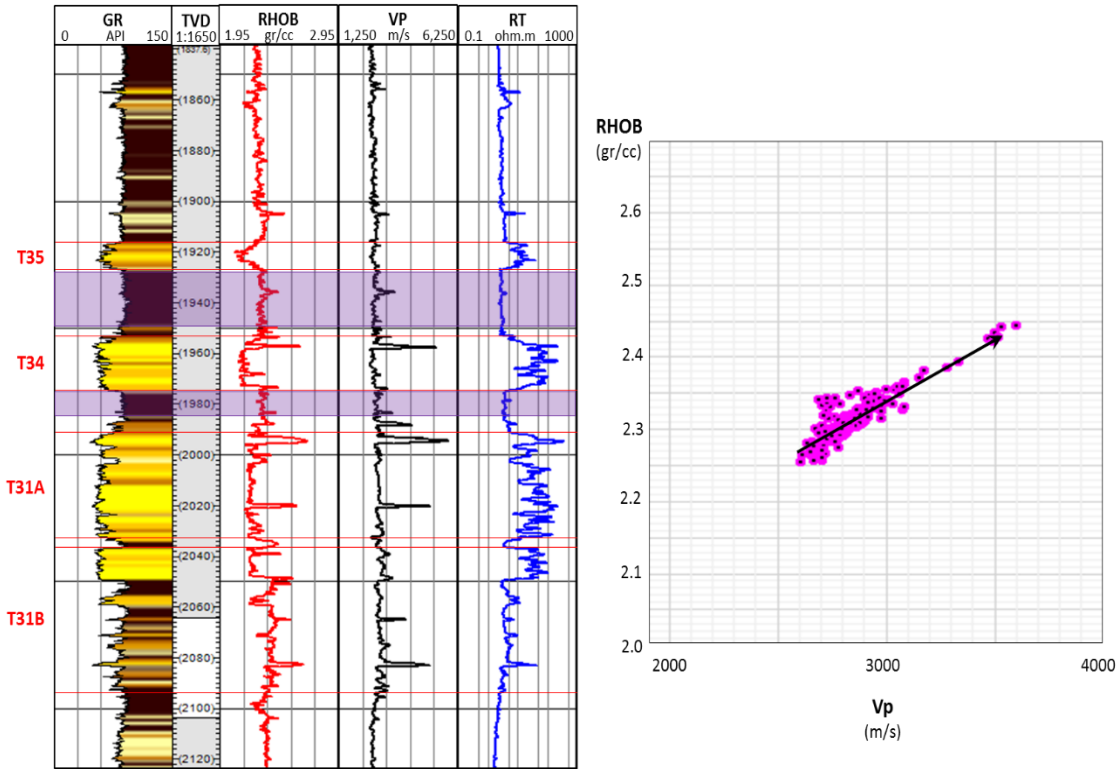

Figure 5-8 *Inter-reservoir shales of Schiehallion Field. Well log displays and acoustic impedance cross-plot. Black arrow shows compaction trend.*

The intra-reservoir shales of the Schiehallion Field are fine particle deposits retransported and resettled by the turbidite flows of the sequences T31B and T31A, with their distribution corresponding to fining up intervals deposited over channel facies (sometimes partially eroded by the subsequent flows) and inter-turbidite lobe deposits, all mixed with pelagic sediments (Figure 5-9). This group of shales has a higher sand and silt/clay ratio when compared to the overlying shales of this field (fine sandstone and siltstone layers are frequent, especially at the base of the intervals). The contacts with the rest of turbidite deposits are mostly transitional (vertically with the channel facies and laterally with the overbank – levee facies). The increase in quartz mineral content in the form of silt and sand results in increased density values; in addition, the absence of a compaction trend is indicative of a faster sedimentation, where the shale fabric and porosity are not dependent on the burial.

The underburden shales (Figure 5-10) correspond to the marine deposits between the top of T28 and the base of the T31B sequences. The internal architecture of this interval consists of a shale, siltstone and very fine sandstone interbedded sequence deposited in shallower marine conditions than the previously described shales. With the highest content of montmorillonite, due the dominant influence of volcanic events at the end of the Lower Palaeocene, these shales exhibit lower density (the swelling properties of montmorillonite cause an increase in the water content of shales), lower P-wave velocities and lower resistivity.

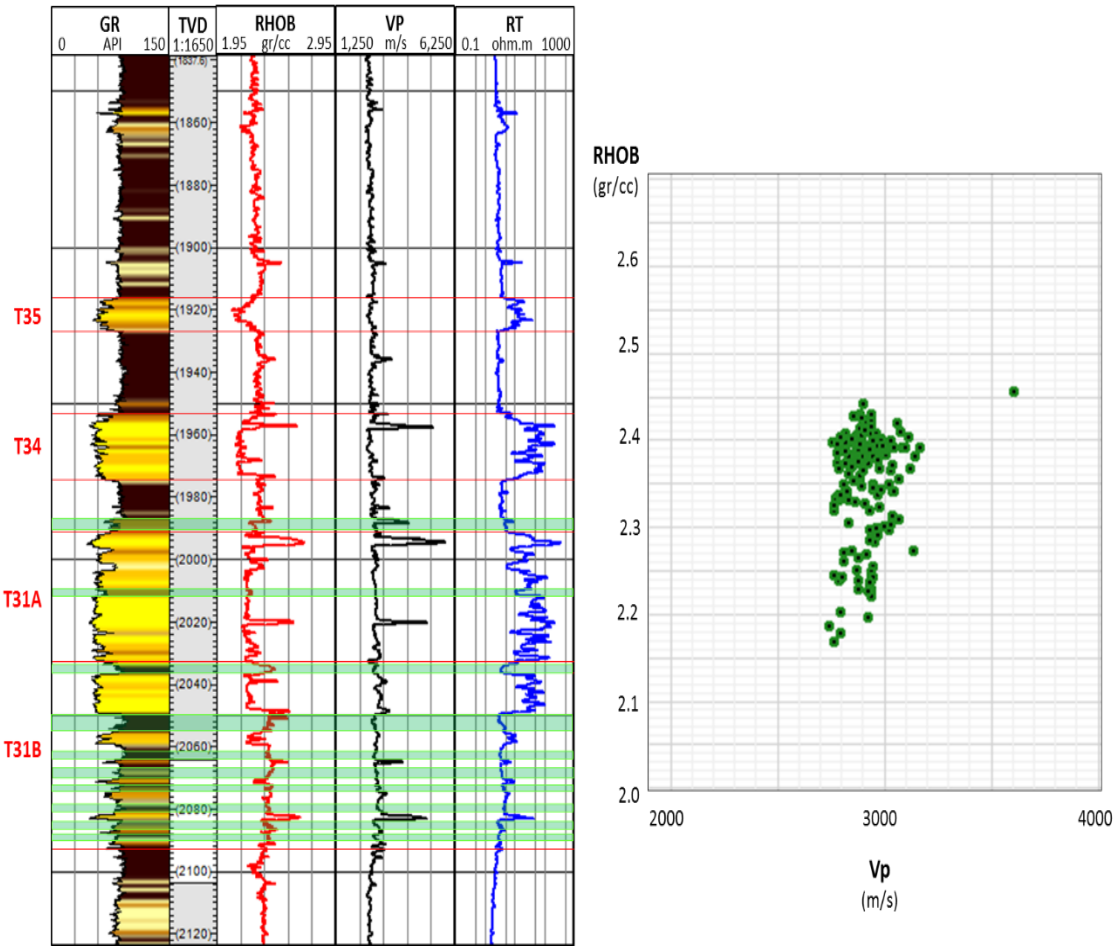

Figure 5-9 *Intra-reservoir shales of Schiehallion Field. Well log displays and acoustic impedance cross-plot.*

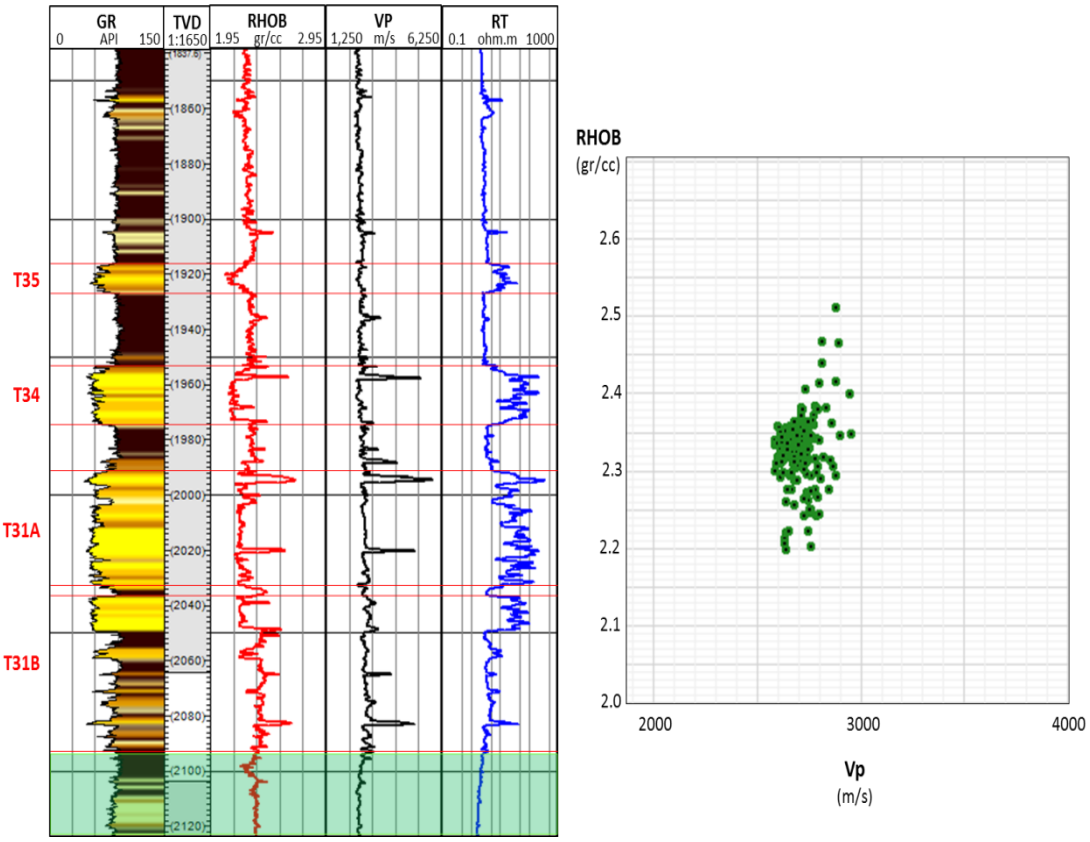

Figure 5-10 *Underburden shales of Schiehallion Field (lower section of Lista Formation). Well logs and acoustic impedance cross-plot.*

5.4 Reservoir model and shales

Following conventional reservoir characterization, and specifically, reservoir simulation modelling, shales in the available models for the Schiehallion Field were inactive; The top and base of the reservoir model correspond to the top of the T35 channel facies and the base of the T31B channels respectively (overburden and underburden layers were not included in the dynamic model). The ETLP database for Segment 1 of Schiehallion included well logs, time-lapse seismic volumes shot in 1996, 2004, 2006 and 2008, and fine and coarse simulation models with history matched production data from August 1998 to January 2009. For this study case was used the coarse scale simulation model of Segment 1, with a geometry of 128 x 53 x 35 cells (i, j and k directions) and a cell size of 75 x 75 metres. The lithologic heterogeneity in the available model (provided by BP) for the Schiehallion Field is expressed by a highly detailed geobody characterization (Figure 5-11), with 360 geobodies defined through the 4D seismic response and NTG distribution criteria. These geobodies are also linked with the reservoir's connectivity, and modelled multipliers between them are included in the simulation model, to history match the

reservoir response, thereby increasing or decreasing the permeability and transmissivity between geobodies.

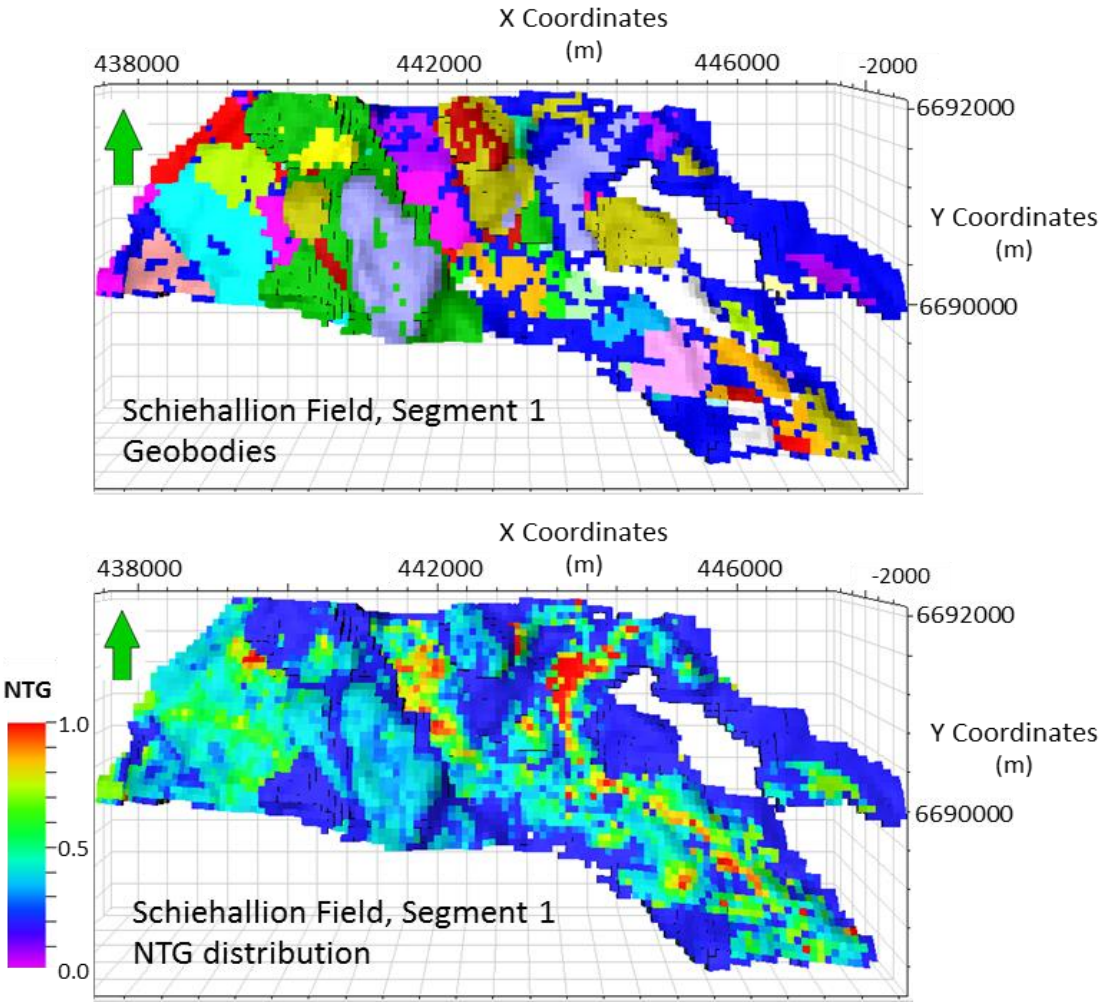

Figure 5-11 *Schiehallion Field Coarse Simulation Model Segment 1: on the topt, geobodies; on the bottom, NTG distribution (view from above).*

The volume of shale used as the reservoir rock cut off is 0.8, and it is used to represent the lowest NTG (0.2), corresponding to distal overbank (levee) deposits. Any cell with a higher volume of shale is turned off (without any static or dynamic property assigned) and regarded as shale in the simulation model, without any influence in the fluid flow and pressure dynamic behaviour of the reservoir. So, technically, in the Schiehallion Field models shales were defined as intervals with a NTG lower than 0.2 and that value corresponds to the upper bound used during the static properties definition for shale activation in this field. In order to evaluate the effect of pressure diffusion in the shales of this dataset, the geometry of the simulation model was also modified, with 20 layers

of constant one metre thickness added at the top of the reservoir as overburden, and 20 more layers were added at the base as the reservoir's underburden. The lateral geometry and reservoir boundaries were conserved and well completions were updated with the new positions of open intervals.

5.5 Shale activation and properties modelling

The process of shale activation in this dataset is carried out in two stages: the initial one corresponds to the geomodelling and assignment of static (generation of geobodies, NTG and porosity) and dynamic (horizontal and vertical permeability) properties for shale in the inactive cells, while the second process consists of modelling the reservoir engineering parameters of shales, including their transmissivities, capillary pressure and relative permeabilities, saturation, equilibrium zone definition, compaction tables and stress sensitivity.

5.5.1 Static properties

To be consistent with the criteria used to represent the geologic heterogeneity in the Schiehallion Field simulation model, three additional geobodies were created, one corresponding to the overburden shales, another corresponding to the inter- and intra-reservoir shales (inactive cells) and finally, one for the underburden shales. To perform the NTG computation was used the Vsh generated from GR curve as a single clay indicator (equations 2.3 and 2.6). It should be noted that other Vsh methods such as Neutron-Density were not appropriate, due to the vertical variability of montmorillonite, which implies changes in the clay-bound water and therefore uncertainty in defining the shale endpoint for neutron-porosity log readings. The NTG values obtained ranged from 0.07 to 0.16, which were used as upper and lower bounds to populate the shale cells with a uniform distribution of random values (Figure 5-12), applying the Geometrical Modelling tool of Petrel software.

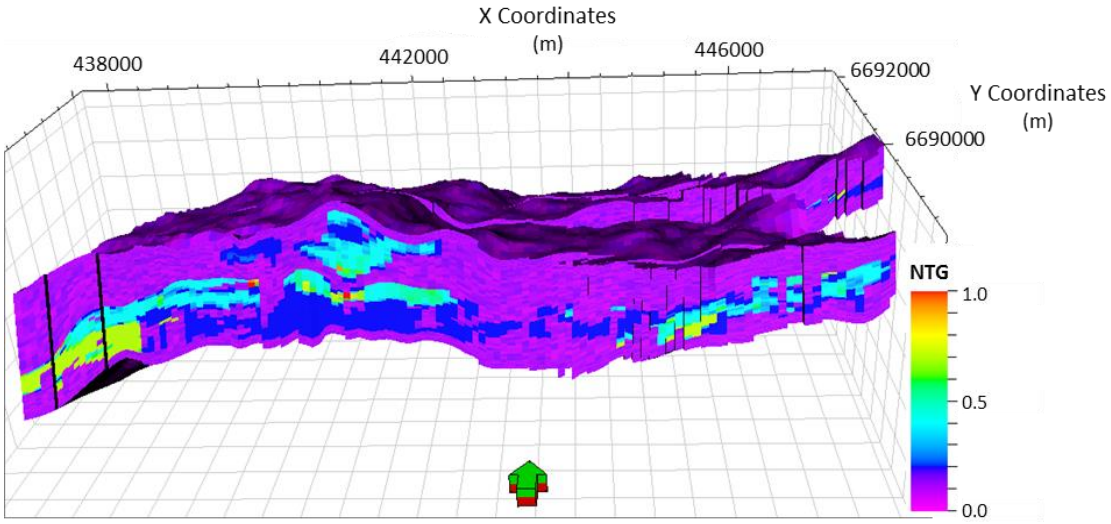

Figure 5-12 *NTG distribution for shale active simulation model of Segment 1, Schiehallion Field (view from south).*

To estimate shale porosity, I used the density method (equation 2.20) to derive porosity, based on the density of the rock matrix, the fluid and saturated rock; results from this method were checked against the Wyllie equation method (equation 2.25). With the clay fraction composition and the silt content established, I used library density parameters (Table 2-5) to calculate the density of the rock matrix. Shales in this case study are assumed as 100% water-saturated and the density of the water is corrected for salinity (18.000 ppm), reservoir pressure (200 bars) and temperature (57.8 °C) conditions. For the rock saturated density values, the RHOB well logs were used and upscaled to the simulation model layering vertical resolution. The estimated porosity in the modelling was assumed as laterally uniform, varying vertically from 0.16 in the overburden shales, to 0.15 in the intra and inter-reservoir shales and 0.14 for the underburden shales (Figure 5-13).

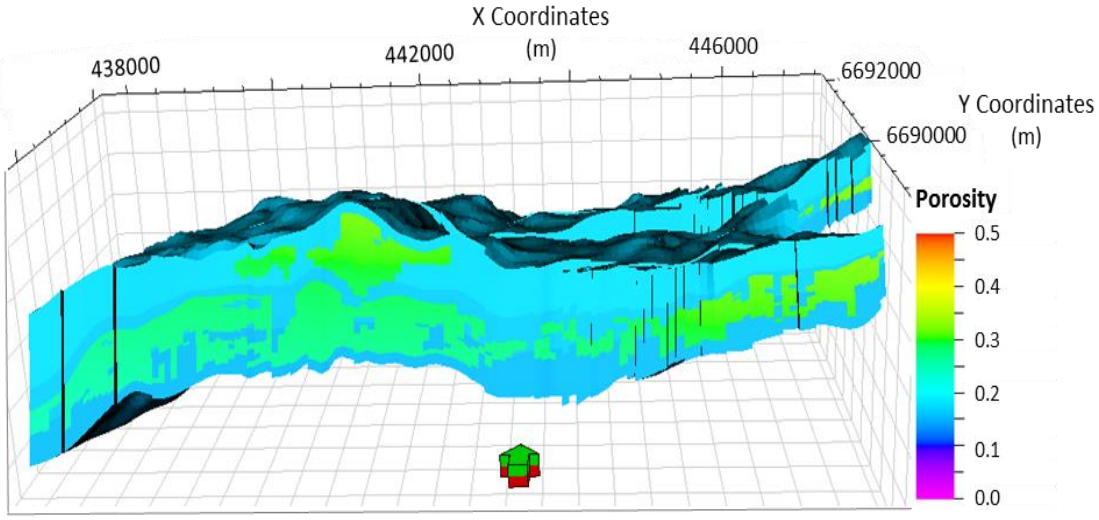

Figure 5-13 *Porosity distribution for Shale Active simulation model, Segment 1, Schiehallion Field (view from south).*

Neither NTG nor porosity of sandstones were modified in the geological model, in order to avoid additional pore space, which would imply extra hydrocarbon reserves (sandstone cells above the OWC are saturated with hydrocarbon). Thus, even when the shale volume embedded in the sandstones does have a NTG $\neq 0$ and a pore space $\neq 0$, the fluid included in that shale fraction is not allowed to flow, due to the capillary pressure and pore throat size conditions. However, in the next section I show how to consider the dynamic contribution of that shale fraction, in terms of its pressure behaviour.

5.5.2 Dynamic properties

5.5.2.1 Permeability

The permeability modelling of the shales is performed in two steps, starting with the estimation of shale horizontal and vertical permeability and population of inactive cells in the model, and followed by the second stage, where I explore several scenarios in which the contribution of shale fraction permeability embedded in the sandstones is taken into account and added in different degrees to the overall permeability of the reservoir.

Due to the lack of conventional laboratory core analysis routines (porosity and permeability tests) for shales in the Schiehallion Field, the vertical and horizontal permeability are once again estimated by applying the empirical equations of *Yang and Aplin* (2007) (equations 2.28 and 2.29), which use as inputs the clay fraction content,

shale porosity and pressure. The values obtained for horizontal shale permeability are between 30 and 100 nanodarcys, lower and upper limits used to populate shale cells in the model with a uniform distribution of random values. For vertical shale permeability the corresponding range is found to be between 7 and 14 nanodarcys (Figure 5-14). Directional variation in horizontal shale permeability is discarded for overburden and underburden shale layers (deep marine and pelagic conditions prevail in those intervals), so permeability is modelled with the same values in both the X-axis and Y-axis. For intra- and inter-reservoir permeability, shale permeability in the Y-axis direction (the same direction as deposition of turbidite flows, north to south) is modelled as 1.5 times higher than the X-axis permeability as Y axis match the deposition direction and pore connectivity is higher in that direction due to clay platelet alignment. In order to have consistency between the modelling of the static and dynamic properties, NTG and porosity distribution are used as trends during the modelling of shale permeability.

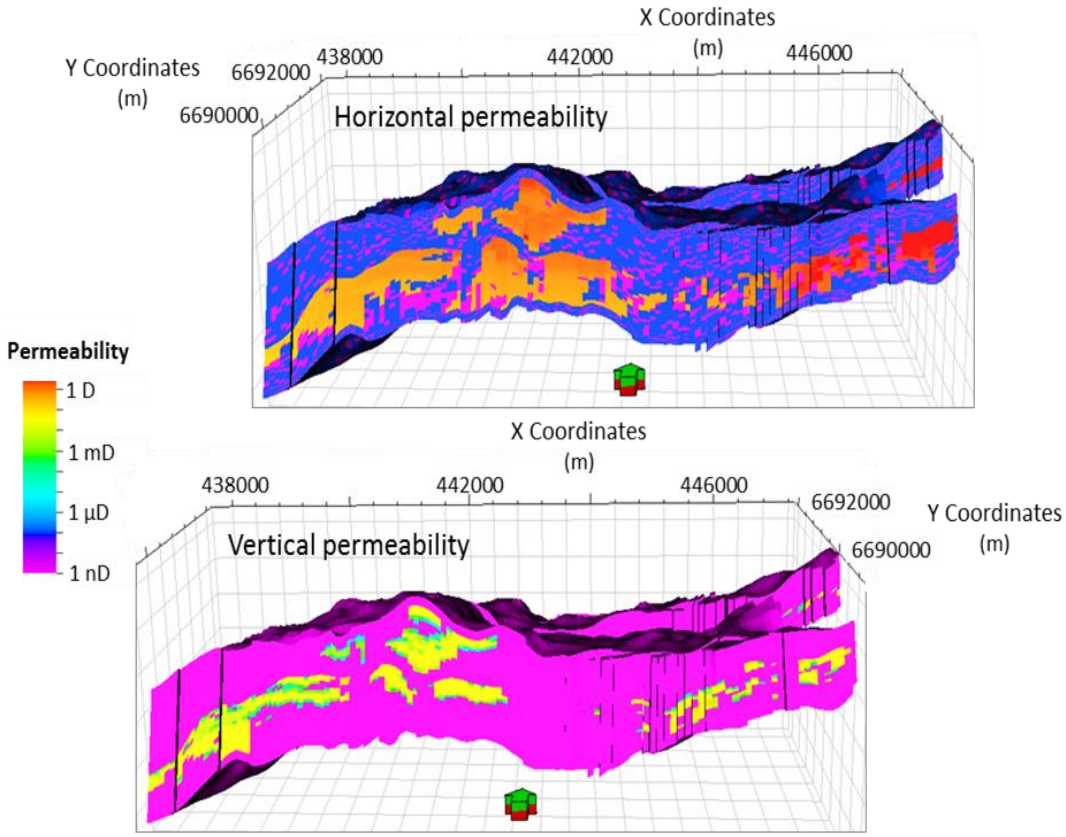

Figure 5-14 *Schiehallion Field active shale modelling. On top image, horizontal permeability in the X-axis direction. On the lower image, vertical permeability.*

With the horizontal and vertical values for shale permeability established, in addition to the active and inactive shale models two extra scenarios were included, where the permeability of shale volume embedded in sandstones is taken into account. The approach consists of exploring a low and a high permeability scenario for the contribution of the shales to the reservoir's pressure evolution. For the low permeability case, shale horizontal and vertical permeability is added to every single reservoir cell, with the contribution of those extra nanodarcys being negligible for high permeability clean sand (200-2000 mD for Kh and 0.05-80 mD for Kv) and even for lower NTG and permeability reservoir units, such as levee and overbank facies. However, with the inclusion of the shale fraction permeability, the zero permeability cells used to model some geological intra- reservoir features such as cemented zones are removed, also allowing external shales (overburden, underburden, inter- and intra-reservoir) to be activated. For the high intra-reservoir permeability contribution scenario, the effective porosity of the shale fraction is added to the reservoir's porosity and taken into account to model reservoir permeability, using a poro-perm relationship, deduced from reverse engineering trendlines between effective porosity and permeability of the initial model.

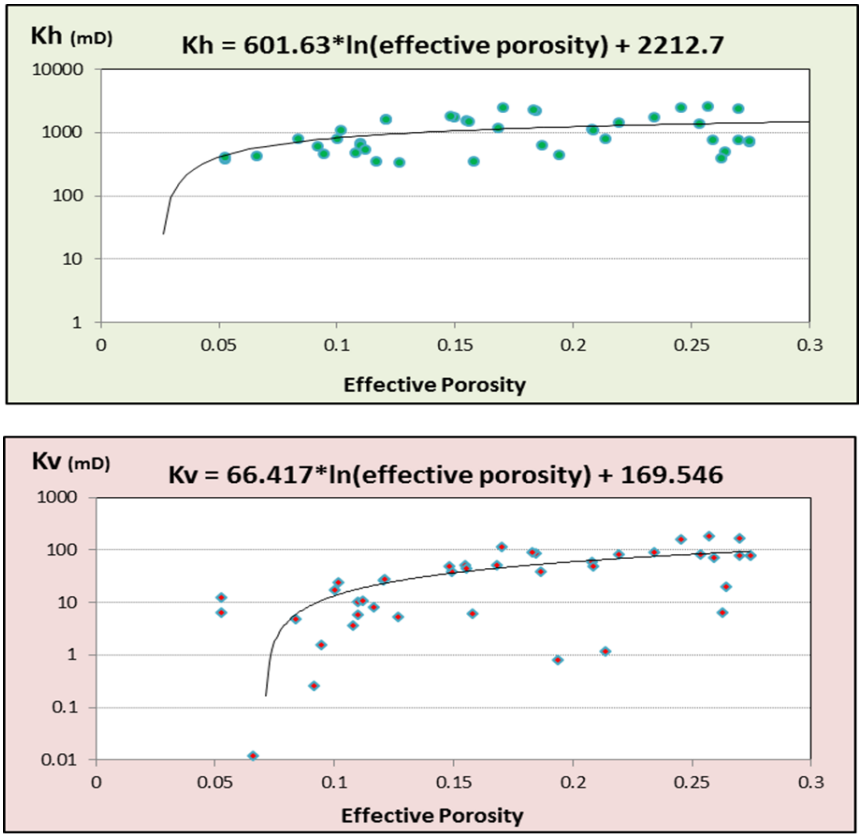

Figure 5-15 *Porosity -permeability relationship for reservoir cells in the Schiehallion Field original simulation model; on top horizontal permeability; vertical on the bottom.*

The logarithmic functions (Figure 5-15) are applied to model new permeabilities using the reservoir porosity with the inclusion of shale fraction porosity. This porosity modification is only used in the computation of permeability, and to avoid volumetric addition of reserves to the reservoir. The initial porosity is used for the simulation flow modelling (assuming that even if the shale fraction was hydrocarbon saturated, the pressure gradient was not enough to change shale saturation and capillary pressure). As in the previous cases, all the external shales (overburden, underburden, inter- and intra-reservoir) are also activated. In order to evaluate the shale contribution in reservoir connectivity, in addition to the previously described four dynamic scenarios, were created an equal number of simulation cases (duplicates), where the transmissivity multipliers used for model reservoir connectivity (between geobodies) are removed.

5.5.2.2 Pressure in shales

The first step in pressure modelling of shales is the analysis of well logs, with emphasis on those that can indicate overpressure (sonic, density, caliper), sometimes showing an anomalous compaction trend. Petrophysical evaluation of overburden and underburden shales of the Schiehallion Field (Figure 5-7 and Figure 5-10) shows no evidence of overpressure; this is also corroborated by drilling reports from this area, and because of this, shale pressure initial conditions are modelled with the same pressure gradient as that of the reservoir, with a datum of 200 bars at 1940 metres TVD. An extra equilibrium zone is created in the simulation model for all external shales, in order to model pressure and other dynamic properties.

5.5.2.3 Shale saturation, capillary pressure and relative permeability

In this study, all shales are regarded as 100% water-saturated; to model that, fictional OWC (oil-water contact) and GOC (gas-oil contact) are created for the shale equilibrium zone; those contacts are positioned at a much shallower depth that the respective reservoir contacts. In order to have shale cells 100% saturated with water, capillary pressure and relative permeabilities (Table 5-1) are modelled correlating laboratory results from shale gas injection tests with similar pore throat geometry [*Sigal*, 2013], based on pressure conditions [*Lapierre et al.*, 1990]. The lower water saturation in shale is 0.6, because of clay-bound water and pore throat diameter. In Table 5-1 can be observed that the modelled capillary pressure for the Schiehallion Field shales establish a minimum

pressure gradient of 52 bars needed to produce any change in shale 100% water saturation (pressure depletion is not high enough to defeat shale capillary pressure); this value acts as a constraint to fluid flow into or from shales, as the water injection plan of the Schiehallion Field to maintain pressure the reservoir in order to avoid gas exsolution keep the pressure gradient bellow the point of shale capillary pressure.

Sw	Kwr	Kor	CP
0.6	0	1	1204
0.65	0.0001	0.97	1100
0.7	0.001	0.92	1034
0.75	0.008	0.85	964
0.8	0.03	0.6	895
0.85	0.06	0.45	792
0.9	0.09	0.31	687
0.91	0.13	0.23	616
0.92	0.17	0.17	550
0.93	0.21	0.12	517
0.94	0.25	0.09	471
0.96	0.31	0.06	344
0.97	0.38	0.04	275
0.975	0.47	0.02	205
0.98	0.59	0.008	137
0.985	0.7	0.005	115
0.99	0.8	0.001	81
0.995	0.9	0	52
1	1	0	0

Table 5-1 *Relative permeabilities and capillary pressure for shales in Schiehallion Field: Water saturation (Sw), water relative permeability (Kwr) and oil relative permeability (Kor) are expressed in fractions; capillary pressure (CP) is in bars.*

5.6 Simulation Results

Due to the strong time dependence of pressure diffusion processes in shales [*HajNasser*, 2012], simulation results are only analysed at the end of the simulated period (10 years of history matched production data, from August 1998 to August 2008). Case scenarios were simulated using the Eclipse application from Schlumberger. Due to the direct impact on the elastic changes in the reservoir, in this study, only pressure and saturation variations are showed (from all the simulation dynamic outputs); results that can be correlated to the observed 4D seismic signal.

5.6.1 Pressure diffusion

Depletion in absolute terms inside shales of the Schiehallion Field is not significant, only in the order of a few (1–3) bars in shale cells adjacent to wells located in channel reservoir units. However, reservoir simulation results show that pressure diffusion through shales impacts the reservoir connectivity and changes the pressure profile of the reservoir (Figure 5-16).

Regarding changes within the active shale models, the build-up signal corresponding to water injection is spatially more extended and production induced depletion is lower, due to the addition of extra volume to the reservoir. Comparing pressure results in the figure 5-16 between models with and without transmissivity multipliers (maps from left column with those at right), can be seen that the effect of multipliers in the pressure profile is reduced in the models where shales are active, which is logical, considering the additional connectivity that active shales add in the reservoir simulation model. The average pressure map shows much higher pressure, because of the averaging of pressure from thick shale intervals with depleted reservoir units, but in shale active models, depletion in sandstones causes some areas to be below the bubble point.

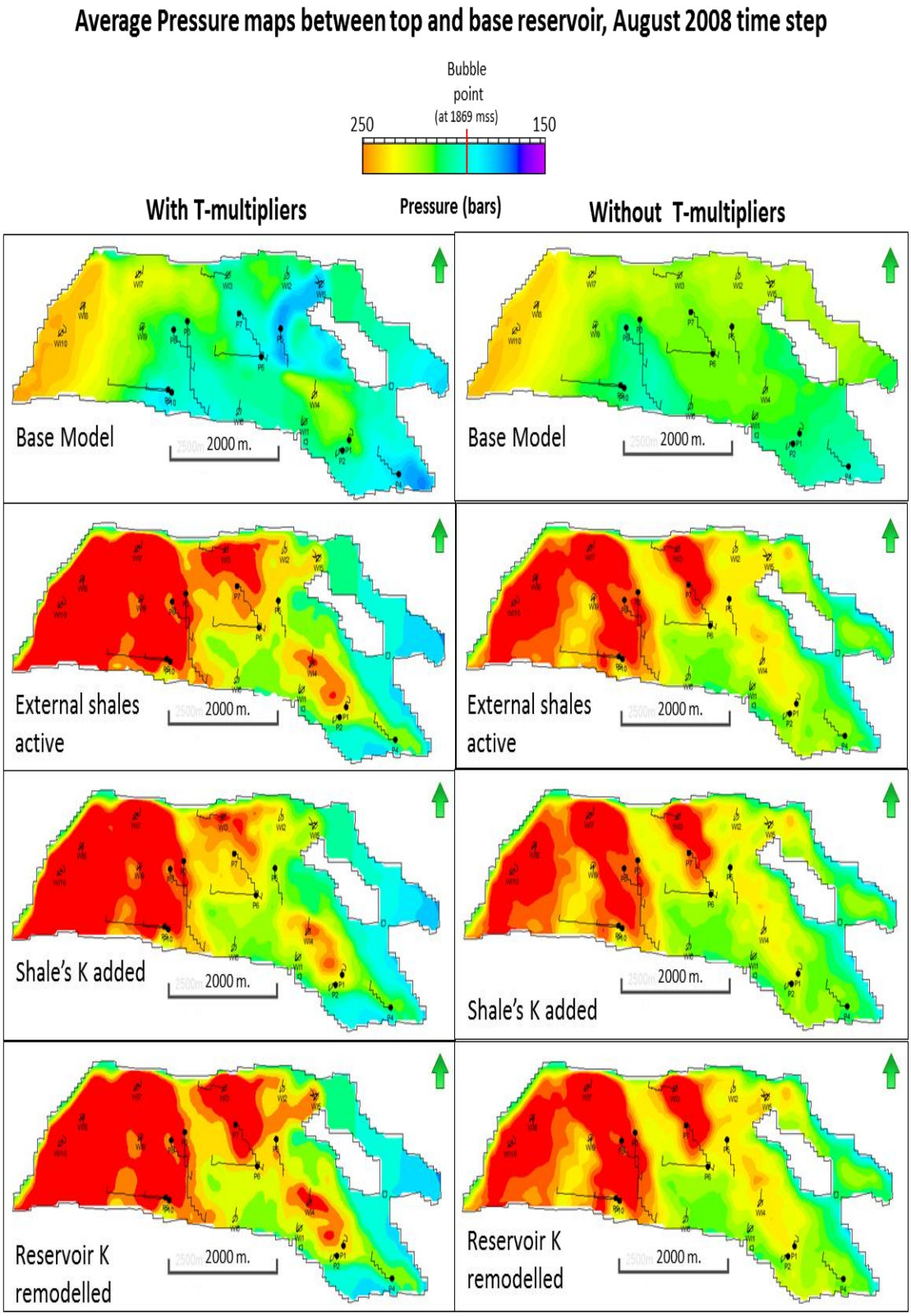

Figure 5-16 *August 2008 average pressure maps between top and base reservoir for study cases in Schiehallion Field, segment 1. In left column, scenarios with transmissivity multipliers included; on right, transmissivity multipliers were removed.*

5.6.2 Saturation and volumetric production results

As the pressure gradient induced by production / injection is not enough to defeat the modelled shale capillary forces, saturation in the activated shaly cell will remain unchanged (100% water), but pressure interaction between shale and reservoir facies impacts connectivity, water injection performance and the gas exsolution process, producing variations in the reservoir saturation (in channel sandstones and heterolithic overbank facies). The effects of shale activation on saturation (Figure 5-17) can be related to less gas coming out of solution in channel facies (because of the extra volume that is equilibrating pressure). At the same time, due to shale connectivity, depletion is also reaching levee and heterolithic overbank facies that previously were not connected to the main channel reservoir units. This depletion lowers the pressure below the bubble point and causes gas exsolution in these facies. Even though the volume of gas produced from the overbank facies is much smaller in comparison to the volume of gas produced in the main channel reservoir (especially for the inactive shales model), its spatial distribution is more widespread in the reservoir, with important consequences in the 4D seismic signal. Models without transmissivity multipliers included (right column in the Figure 5-17) display a more uniform (radial) distribution of fluids, especially in areas under water injection, where water sweep appears to be more 'efficient', while models with multipliers exhibit preferential paths where water injection moves further, according to the modelled connectivity and transmissivity values.

Looking at the total volumetric production of oil, gas and water for the Schiehallion Field Segment 1 during the studied period (Figure 5-18) for the 8 simulated scenarios and comparing them to the historic production data (black line in the graphs), it is obvious that the production history matching is strongly dependent on the reservoir's connectivity and transmissivity (left column of Figure 5-18); models with multipliers included and active shales show larger differences with the historic data, when the addition of shale fraction contribution to the reservoir's permeability. This initial finding confirms that, effectively, there are impermeable barriers inside Schiehallion that are restricting fluid flow- those barriers could correspond to sandstone cemented intervals, reported especially in the sequence T31 (Figure 5-6 and Figure 5-7).

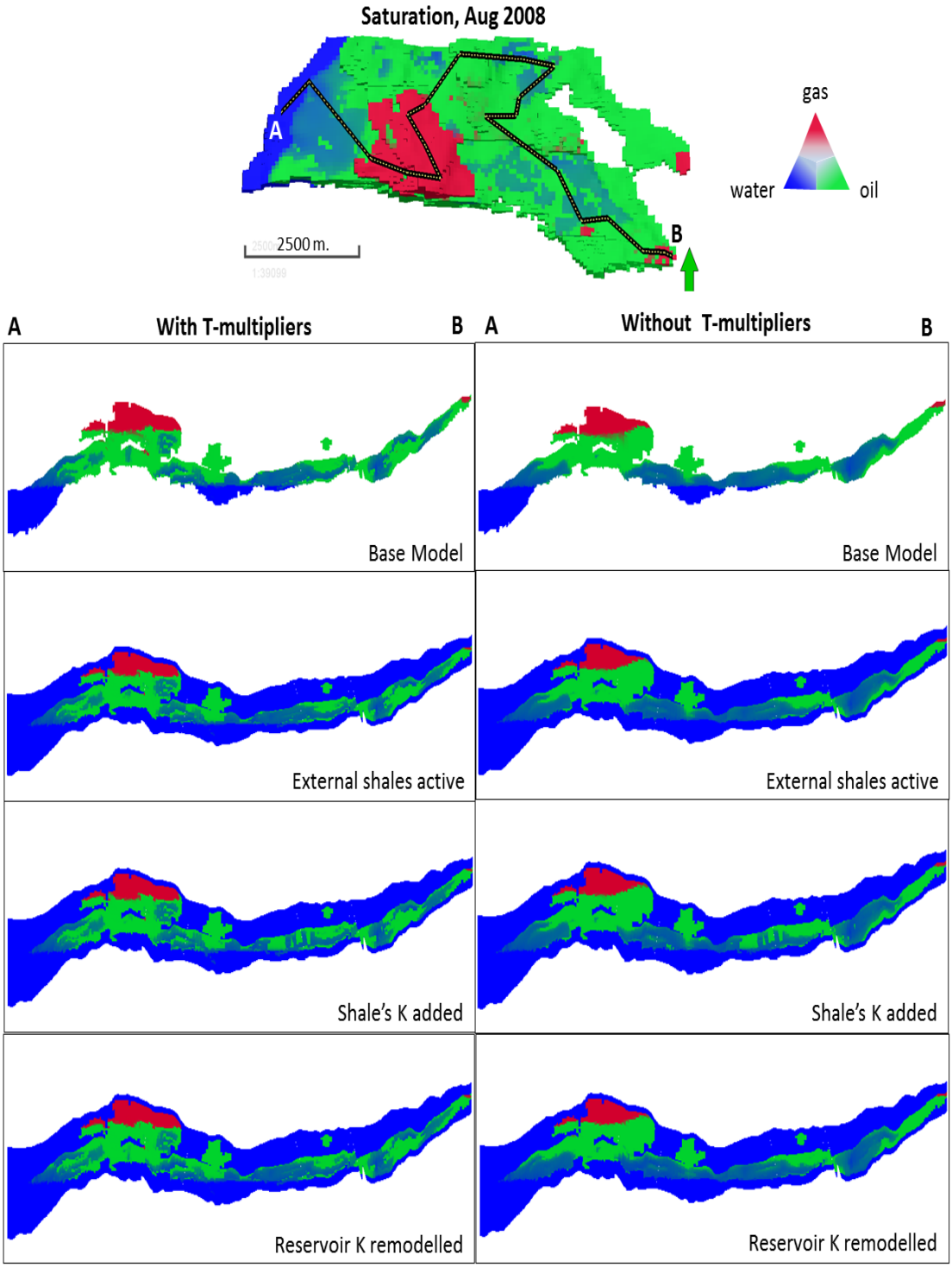

Figure 5-17 *Saturation changes for August 2008 time step in shale activation case scenarios of Schiehallion Field, Segment 1, sections displayed in a vertical intersection along the profile A -B. Left column shows models with the initially modelled transmissivity multipliers; on right same models but without transmissivity multipliers, just cell's permeability acting.*

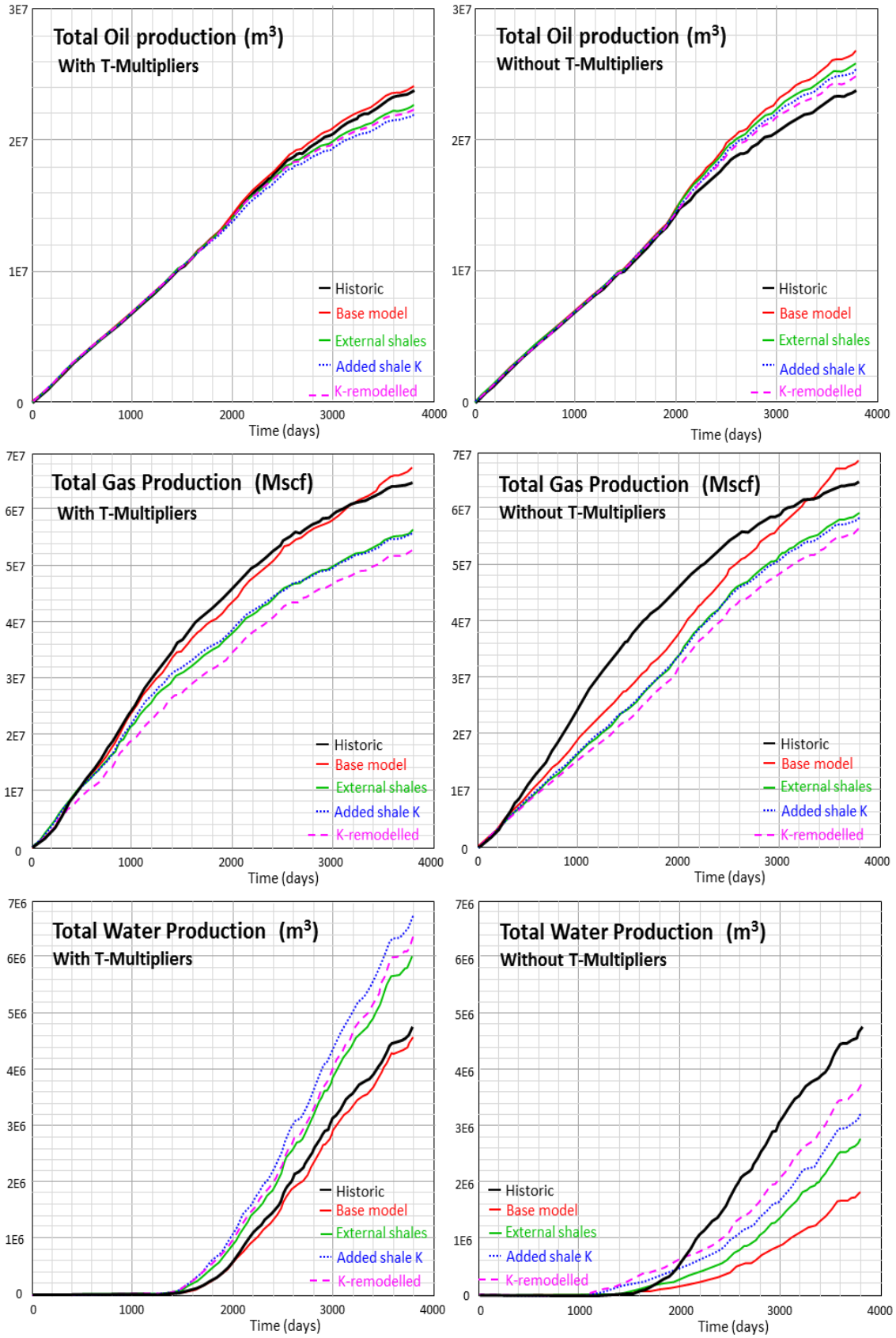

Figure 5-18 *Total oil, gas and water volumetric production for simulated scenarios in Schiehallion Field. Historic production data is represented by black line. In left column, models with transmissivity multipliers included, on right, without them.*

However, when the analysis in the predicted production for models is performed without transmissivity multipliers, the best match with the historic oil and water total production data is achieved by models with shales activated, the exception being total gas production, where volumetric results are considerably lower than those for the inactive shale case (Base model). This suggests that, to a certain degree, the use of transmissivity multipliers in the simulation model of this field is compensating part of the shale effect, but the implications of this are not only related to the produced volume: it is the provenance of that volume that is very important too, because it has direct consequences in the spatial distribution of the elastic changes recorded in the 4D seismic. For that reason, even when there is no discussion about the presence of geological features that act as flow barriers in the reservoir, and that their simplest representation is as multipliers, the application of these engineering modelling tools should be carried out after the evaluation of the role of shales in the dynamic behaviour of the reservoir.

5.7 Synthetic seismic modelling

To determine the effect of shale pressure diffusion, simulator to seismic modelling was performed for the eight model scenarios. To be consistent with in the initial model, where the reservoir lithologic heterogeneity was expressed in terms of NTG, all the lateral and vertical variations in the rock frame of the field were expressed as a sand-shale mixture (Backus average) based on the definition of two end members, the cleanest sand and the purest shale (mudstone), lithotypes that were established by petrophysical analysis and correlations along the field in water-saturated intervals (to avoid the effect of hydrocarbons in the elastic parameters). In the simulator to seismic process, static and dynamic cell properties are converted into impedance. The variations of cells' properties induced by production / injection are determined by changes in the rock frame and pore space (saturation and pressure), so each of the components of the saturated rock system (minerals and fluids) needs to be characterized in static and dynamic terms through the elastic moduli (relationship between density and velocity). Regarding fluids, once their properties have been defined (Table 5-3), the cell saturation changes are predicted for different time steps. For rock, to isolate the properties of the matrix I performed rock physics analysis (see Chapter 2, equations 2.24 and 2.41) on representative values extracted from well logs to compute bulk and shear moduli for the end members' matrix (Table 5-2), which will be averaged using the NTG distribution to then be used as inputs

for fluid substitution equations [*Gassmann*, 1951]. For the Schiehallion Field, the rock frame stress sensitivity (for sandstones and shales regarded as equally stress sensitive) was modelled as being dependent on the pressure using the equations and coefficients established for the West of Shetland Basin Palaeocene sandstones [*MacBeth*, 2004],

Property	Cleanest sand	Purest shale
Porosity (fraction)	0.26	0.14
NTG (fraction)	1.0	0.1
Bulk Moduli (GPa)$_{matrix}$	25.08	17.64
Shear Moduli (GPa) $_{matrix}$	7.23	4.83
Density (kg/m^3) $_{matrix}$	2623	2617

Table 5-2 *End members' (clean sand and pure shale) parameters for cell matrix moduli computation during Sim2Seis procedure.*

Apart from the static and dynamic properties of each scenario, Sim2Seis also requires additional inputs to represent the synthetic seismic correctly in two-way time, including the well based extracted wavelet (Figure 5-19 and Appendix C) overburden and underburden density and velocity (Table 5-3), a seismic horizon (top reservoir in TWT) to tie, and an extracted wavelet to perform convolution with the computed cell impedance and interface reflectivity. For the Schiehallion Field Segment 1, were computed sixteen 3D seismic cubes, two per shale activation scenario, one for the pre-production time step and another at the end of the simulated period (in order to compute the 4D seismic differences between base and monitor). The bin geometry used for the synthetic volumes is 25 metres x 25 metres (the real seismic has a bin of 12.5x12.5 metres), but considering the simulation model grid cell geometry (75 x 75 metres), reducing the bin to the real seismic size would not bring extra resolution.

Reservoir temperature	57.8 °C
Water salinity	18,000 ppm.
Oil gravity	25° API
Gas gravity	0.58639
Overburden properties	P-wave velocity= 2,699 m/s; S-wave velocity=1,260 m/s; Density=2.31 gr/cm^3
Underburden properties	P-wave velocity= 2,810 m/s; S-wave velocity=1,400 m/s; Density=2.41 gr/cm^3

Table 5-3 *Fluids: overburden and underburden properties.*

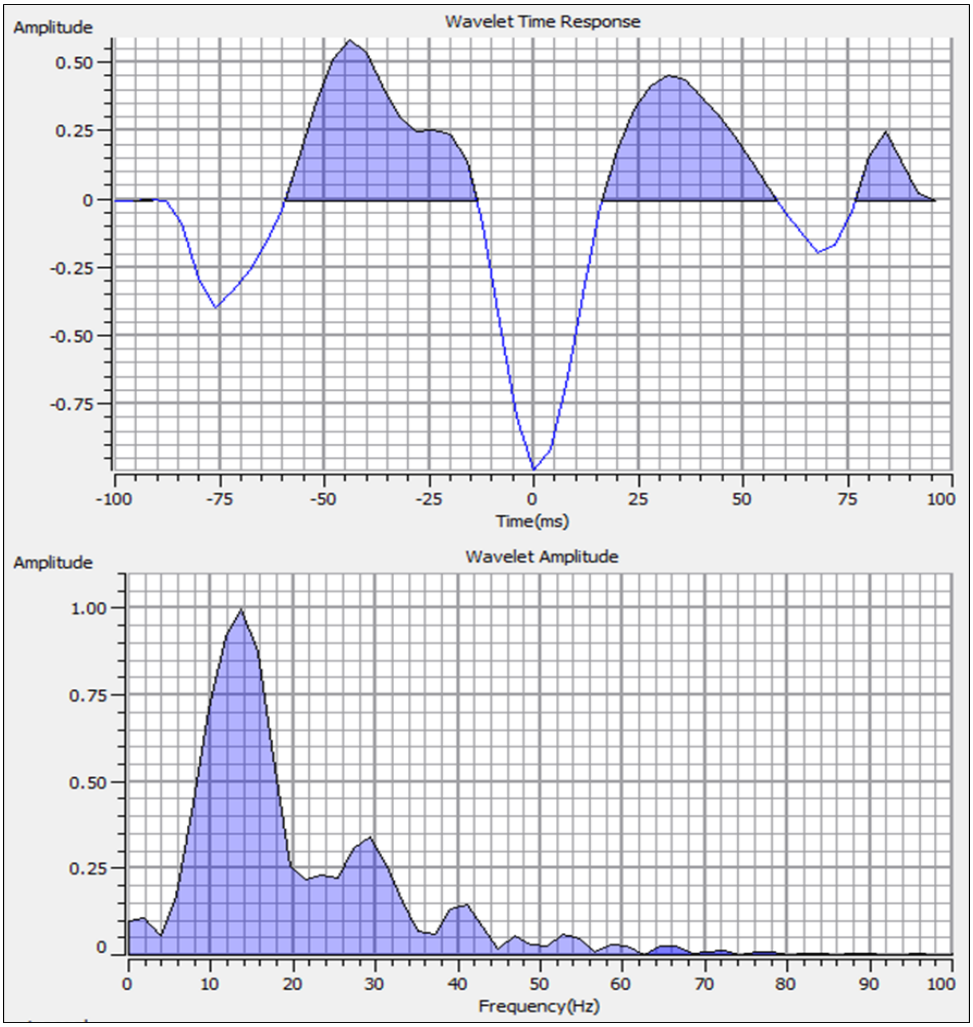

Figure 5-19*. Well base extracted wavelet for the Schiehallion Field (Roy White method).*

Comparison between results of synthetic seismic modelling and observed real seismic for the pre-production stage (Figure 5-20) shows only small differences between active and inactive shale models: in general, the amplitude contrast between the reservoir's internal reflections is stronger for the base model (inactive shale case), due to the poor definition of shale properties compared to reservoir sandstone units. On the other hand, shale active models show higher resolution at the base of the reservoir. This is because, even when the no compaction trend was modelled for this reservoir (because of its thickness), the vertical variations included in the shale properties modelling allow better reservoir thickness estimation and base reservoir horizon placement (the seismic was tied with the top reservoir horizon). In Figure 5-19 only one of the 3D synthetic models for activated shales is shown, because the similarity between them is very high for the pre-production volumes. For the 3D synthetic modelling corresponding to the August 2008 time step, variations between different seismic volumes are more accentuated, each scenario

producing different saturation and pressure outputs, consequently producing different elastic responses; however, to appreciate better those changes graphically, I show the results in the 4D seismic response and interpretation section, using maps and amplitude attributes.

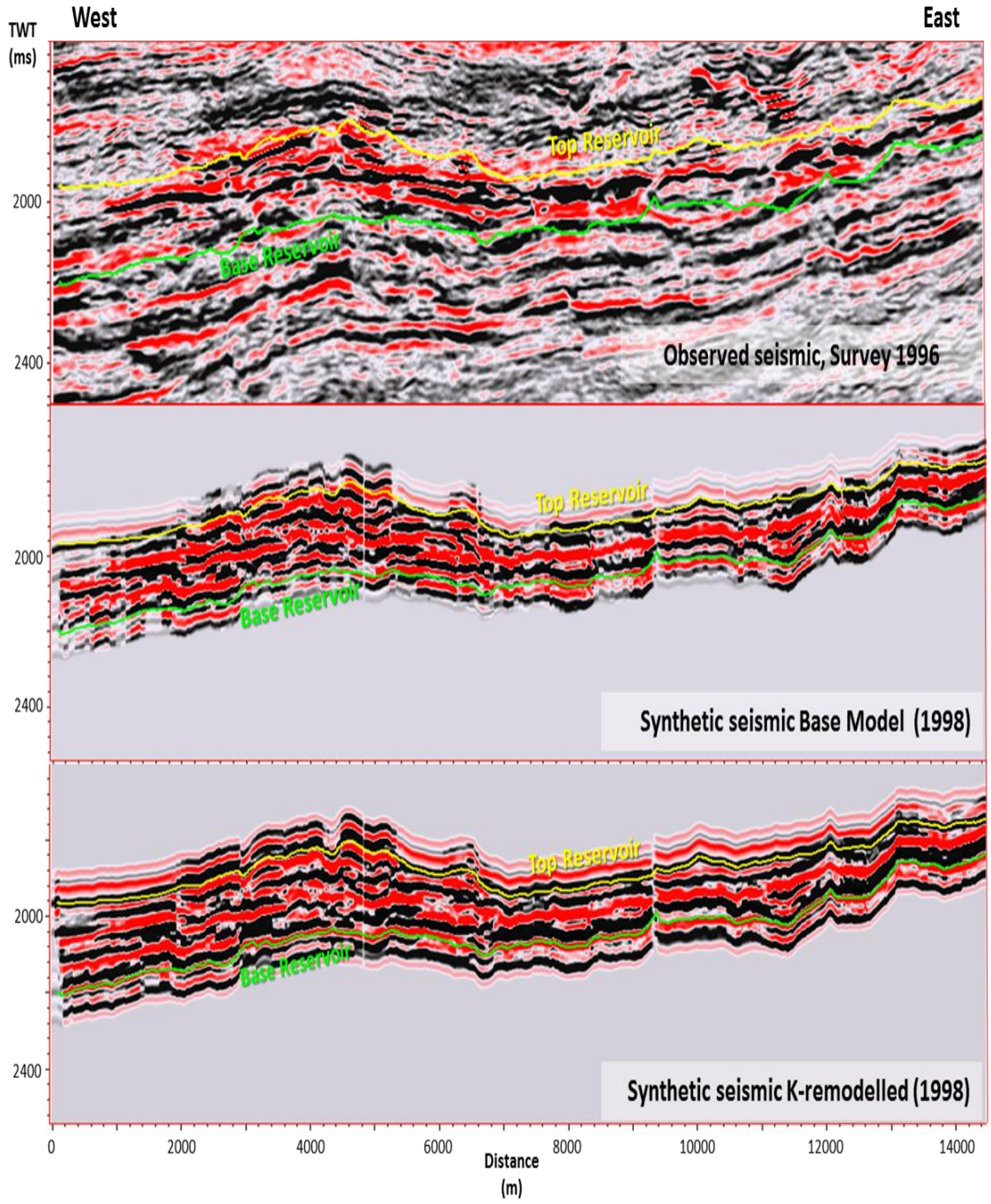

Figure 5-20 *Pre-production observed and synthetic 3D seismic volumes for Base and Remodelled permeability cases. Seismic displayed along a West-East vertical section.*

5.8 4D seismic response and interpretation

The 4D seismic response of the Schiehallion Field was computed between the base full stack (5 -30°) 1996 and the 2008 monitor surveys, after both seismic volumes were parallel pre and post stack reprocessed, with a repeatability estimated in 31% NRMS. The 4D analysis and interpretation was performed using the RMS amplitude attribute extracted from top and base reservoir (laterally restricted to Segment 1 area) for each seismic volume (pre-production 1998 and August 2008 for synthetic seismic, and 1996 and 2008 for the observed seismic). Then, the 4D differences were computed subtracting the attribute response of the monitor minus the base one for the same modelled scenario. In order to analyse the signal in terms of hardening (increase in the elastic moduli) or softening (decrease), the 4D seismic maps' results are adjusted to the same display range and colour code (normalized): positive changes (hardening) were plotted in blue, negative (softening) in red and non-elastic variations in white (Figure 5-21).

When comparing 4D responses of observed with synthetic models, the most obvious feature is that the use of transmissivity multipliers (left column in Figure 5-21) improves the match of the hardening response 4D synthetic models with respect to the observed 4D seismic. The signal around water injectors and well producers placed in main channel units is strong, suggesting that the hardening response is dominated by saturation changes (water sweep). This pattern confirms, to a certain degree, the existence of barriers (at fluid flow level) between the main channel (high quality sandstones) and the overbank facies. The second noticeable characteristic corresponds to the softening distribution that is considerably better (Figure 5-22 and Table 5-4) in predicted models with shales activated and in some cases with transmissivity multipliers removed (when compared to the observed data). The match between active shale models and observed 4D seismic decreases when intra-reservoir shale clay fraction permeability is taken into account, this finding advocates for the initial criteria for reservoir permeability modelling that may have included the effect of clay content in the poro-perm relationship. This also highlights the importance in the reservoirs connectivity of the cemented intervals that were modelled as zero permeability intervals, barriers that were removed when shale low permeability was added to the entire reservoir.

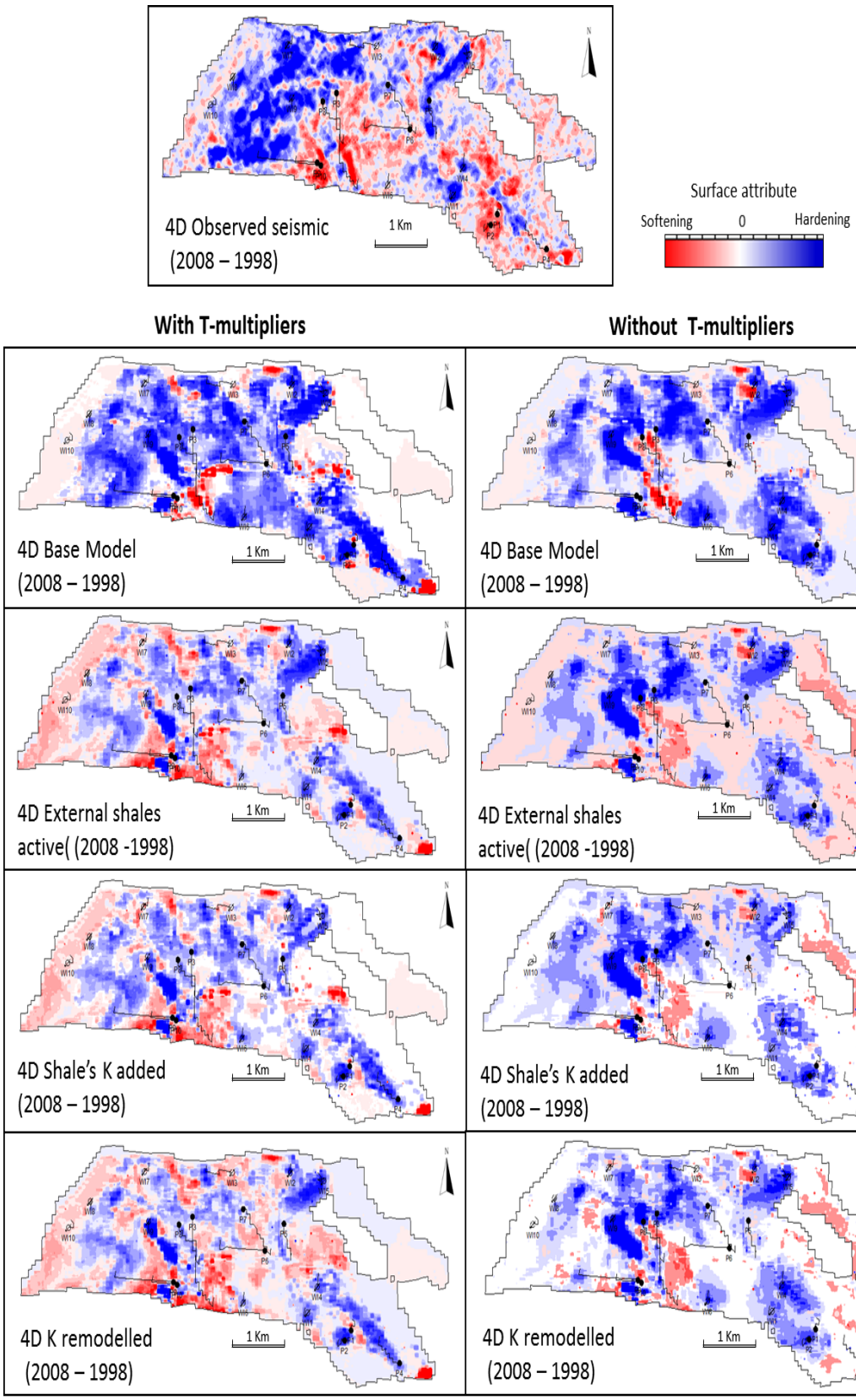

Figure 5-21 *4D seismic differences response for modelled shale activation scenarios: in left column, cases with transmissivity multipliers included, on right, without multipliers*

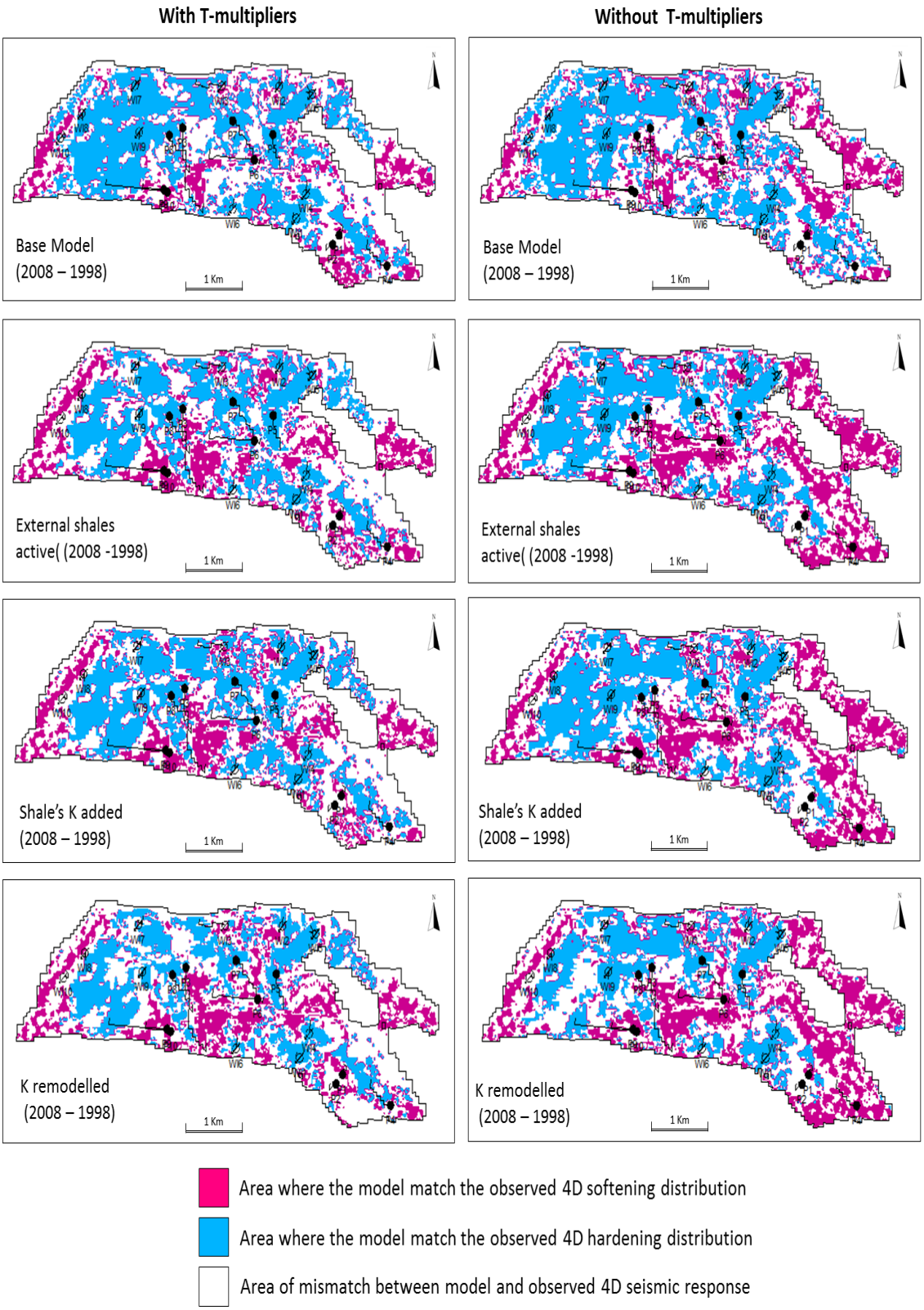

Figure 5-22 *Modelled shale activation scenarios fit to observed 4D seismic response: in left column, cases with transmissivity multipliers included, on right, without multipliers*

Model	Mismatch (%)	Softening (%)	Hardening (%)	Without 4D changes (%)
Observed seismic		44.66	55.34	0
Base model	46.17	12.54	41.29	5.46 (included in the mismatch)
Base model WTM	45.87	14.85	39.28	3.09 (included in the mismatch)
External shales	44.38	19.72	35.90	5.65 (included in the mismatch)
External shales WTM	40.61	26.36	33.03	2.65 (included in the mismatch)
Shale's K added	44.19	17.05	38.75	5.68 (included in the mismatch)
Shale's K added WTM	40.30	25.40	34.30	3.15 (included in the mismatch)
K remodelled	46.13	21.44	32.43	6.71 (included in the mismatch)
K remodelled WTM	43.94	27.08	28.98	3.05 (included in the mismatch)

Table 5-4 *Statistics of fit to observed 4D seismic data for predicted scenarios in the Schiehallion Field*

The best match between the predicted models and the observed 4D seismic is achieved for the active shale models without transmissivity multipliers included, with a reduction of the mismatch up to 6% when compared with the base model scenario. The removal of transmissivity multipliers reduce the hardening signal fit in the predicted models but increase the softening match, showing that the reservoir connectivity in terms of pressure is higher than it was initially modelled. The statistics proved clearly that in this dataset the pressure diffusion through external (overburden, underburden, intra- and inter-reservoir) shales is responsible for a series of dynamic changes in the reservoir during production, variations recorded in the 4D seismic signature.

Looking in more detail at the generated 4D seismic maps, specifically the softening occurrence, it is easy to spot that the spatial occurrence of the signal correlates very well with the distribution of the overbank and levee facies (Figure 5-23), which are modelled as one big geobody (dark blue in the Segment 1 Geobodies map) with a low NTG (between 0.2 and 0.3). These levee and overbank facies are not connected to the main channel units in the initial reservoir modelling, as they are represented with multipliers of '0' transmissivity. Certainly the 4D response related to water sweep and oil production shows very poor or null fluid flow connection between levee and channel units, but certainly at pressure level, the induced depletion in levee facies is going below the bubble point, creating gas exsolution and softening in the 4D seismic signal. Because of fluid

flow constraints between channel and levee units, the effect of gas exsolution and its 4D implications are not matched in the conventional modelling of this reservoir, only after the shale's activation is the occurrence of this dynamic process in the reservoir obvious.

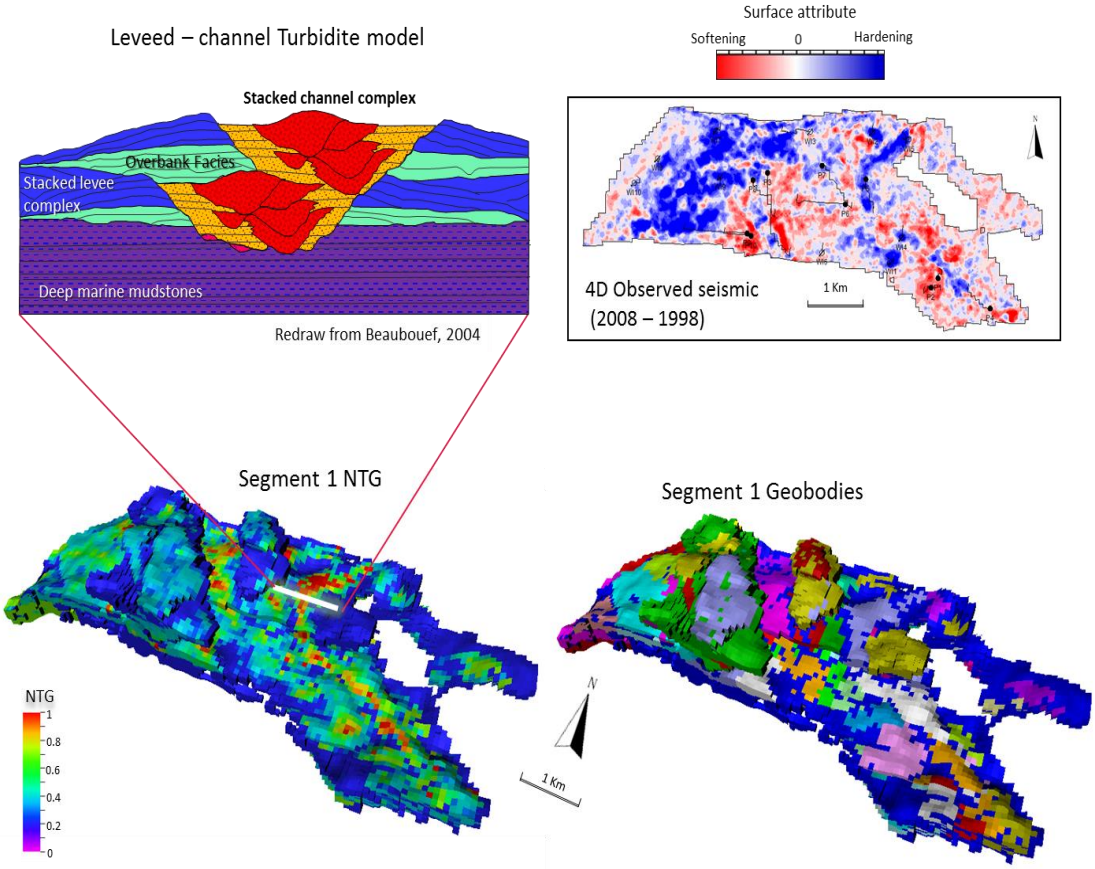

Figure 5-23 *Correlation between levee facies and softening distribution in the 4D seismic signal, some information from published literature [Beaubouef, 2004]*

5.9 Conclusions

The study of the reservoir-related shales in the Schiehallion Field, Segment 1, indicates a clear dynamic behaviour, with the results suggesting that pressure diffusion though shales is creating an important signature in the reservoir performance. Shale activation improves the model fit to the 4D seismic data (predicted responses reduces to 6% the mismatch with the observed seismic) and helps us to understand the reservoir connectivity by reducing the dependence on transmissivity multipliers inserted into the simulation model. Production / injection interaction between all reservoir facies was clearer, as was the case between main channel sandstone units and heterolithic levee facies. Shale

characterization provides more accurate modelling of the synthetic seismic data, in general, with the contrast between seismic reflectors corresponding to sandstones and shales better captured if variability in the elastic properties of shales is included in the model, which can translate into better reservoir time thickness estimation, as well better imaging of the top and base reservoir.

Considering the role of the levee connectivity and shale activation in the dynamic behaviour of Schiehallion Field and its impact on the 4D seismic signal, the results of this work suggest that the static and dynamic modelling of this field should initially test the implications of shale activation before exploring the use of transmissivity constraints, because multipliers cannot create at the same time fluid flow barriers and pressure bridges in order to explain the reservoir behaviour. Another consideration should be to address the levee and overbank characterization: currently, in the base model (provided by BP), there is poor variability in these facies; indeed, they are represented as a unique geobody in the entire area, when, in fact, each levee corresponds to a deposition of different turbidite flows.

The specific pressure conditions of the Schiehallion Field and the geometric relationships between the shale and sands in this turbidite-leveed reservoir mean that shale pressure diffusion has a strong impact and is immediately visible via the process of gas exsolution. Shales can therefore impact the distribution and polarity of the 4D seismic response and its consequent interpretation.

6 Chapter:

Case study: Shearwater Field

This chapter summarises the 4D effects of the Shearwater Field through the inclusion of its shale intervals in the numerical simulations. Heather and Kimmeridge Clay formations constitute the reservoir seal and immediate overburden of the Shearwater Field, and their inclusion into the reservoir model, allows us to explore the response of these shaley intervals to the large pressure changes registered in this HP/HT reservoir as a consequence of the gas and condensate production. Overburden time shift anomalies observed in the 4D seismic signature of the field may be explained by pressure diffusion through shale and its geomechanical implications. This final field application of my work, includes the geomodelling of this field, the inclusion of numerically predicted pressure variations in the overburden shales for the geomechanical estimations of the induced strain and the comparison of the different simulated scenarios with the observed time shift and time strains in the 4D seismic.

6.1 Introduction to the study case

Induced geomechanical effects due to production and injection can cause drastic variations in effective stress and lead to changes in the rock matrix frame, causing compaction or expansion and modifying completely the elastic properties and even the position of the reservoir and the surrounding rocks. These changes are seen in the 4D seismic changes as hardening / softening signals, but mostly as time shifts. The Shearwater Field, an HP/HT reservoir in the central graben of the North Sea has very particular conditions that make it prone to considerable geomechanical response. With depletion being the main production mechanism (due to the large pressure window between the initial conditions and the dew point), the pressure imbalance between reservoir and shale is guaranteed, and large changes in effective stress result in the shales being active geomechanically, conditions that constitute an excellent scenario to study if pressure diffusion into shales is affecting the 4D seismic signal. To understand better how this physical phenomenon operates in this reservoir, this study focuses on an integrated geomechanics analysis (Figure 6-1), using pressure and saturation results predicted for models with and without shales included, to estimate strain distributions in the reservoir and overburden. Comparison between the predicted and observed strains in the 4D seismic data was used to establish the validity of the modelled shale dynamic scenarios.

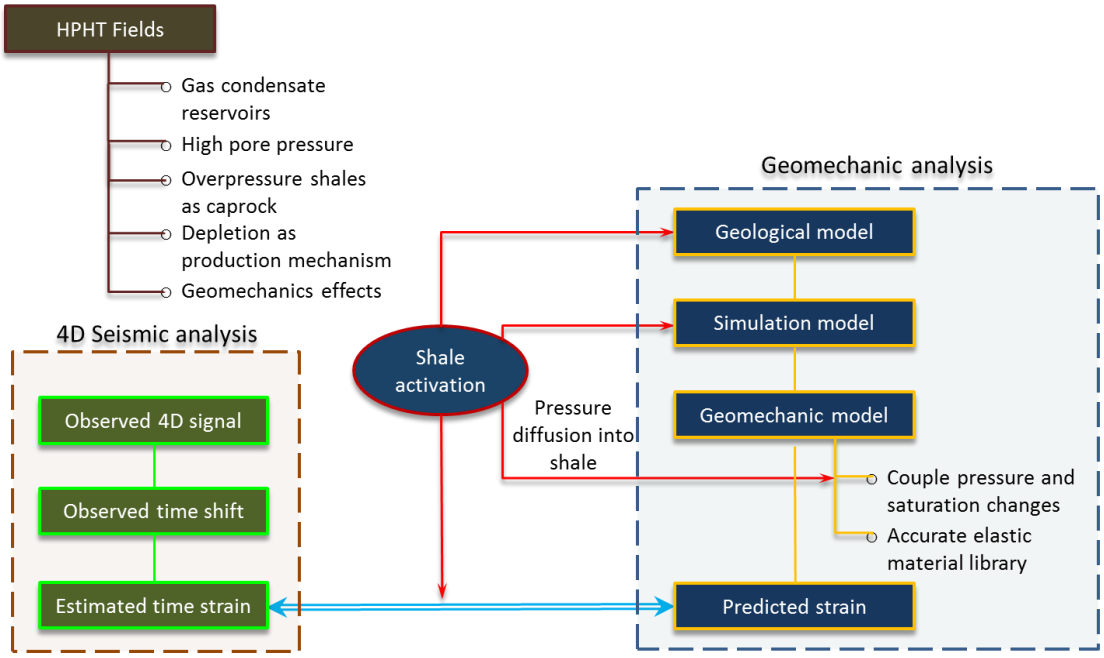

Figure 6-1 *Workflow applied to evaluate shale pressure diffusion implications in the strain behaviour of the Shearwater Field.*

6.2 Field general description

The Shearwater Field is an offshore high pressure, high temperature (HP/HT) gas and condensate reservoir, located 250 km east of Aberdeen in Block 22/30b of the United Kingdom Central North Sea (Figure 6-2). Discovered in 1991 under 90 metres of water and on-stream from July 2000 to December 2007, this field has estimated recoverable reserves of 159 million barrels of condensate and 844 billion cubic feet of gas. The licence holders of the Shearwater Field are Shell (28%), Esso (28%), Arco British (27.5%) and Mobil (16.5%), with Shell being the operator.

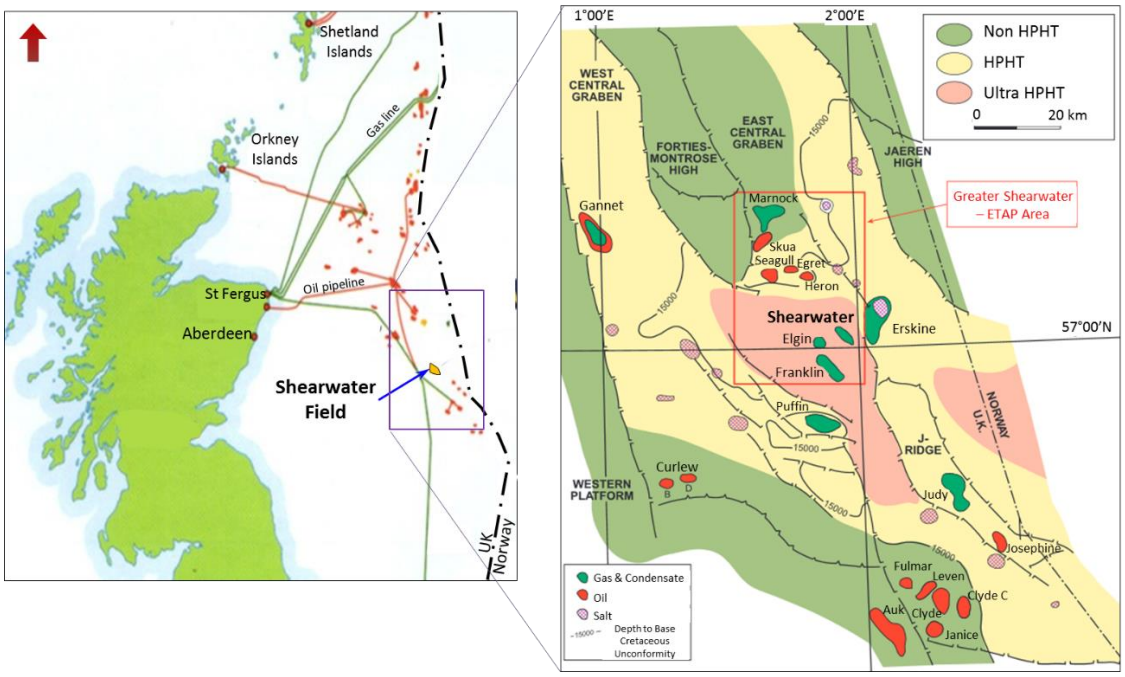

Figure 6-2 *Shearwater Field Location. Redrawn from published literature [Winefield et al., 2005].*

The reservoir consists of the prospective Fulmar Formation sandstones, with accumulations of condensate and gas with a ratio of 170 barrels of condensate per million cubic feet of gas. With the top reservoir located at 4800 metres TVDSS, pore pressures reported at 1050 bars, temperatures of around 180 °C (HP/HT) and a high salinity aquifer, these challenging reservoir conditions made the reservoir appraisal process longer, and it was only in October 2000 that production in the field started and when the platform installation was completed. After that, all production wells were drilled, with well stability being a major concern [*Gilham et al.*, 2005]. The mechanism to develop the Shearwater Field reserves was pressure depletion. A seismic monitoring program of the reservoir was planned, starting in 2001, with a seismic survey treated as base, with extra

survey monitors acquired in 2002 and 2004, previous to the well's geomechanical failure between the end of 2004 and 2007. With the purpose of field reactivation, a fourth seismic survey was acquired in 2013, to evaluate the geomechanical implications of the reservoir compaction.

6.3 Geological context

The geological evolution of the central North Sea Basin, its architecture and configuration is the result of several extensional phases associated with the failed North Sea rift system, starting in the Permian and climaxing in the Late Jurassic (the main trap-forming event), with minor, more localized reactivation in the Albian-Aptian [*Erratt et al.*, 2010]. The continental to marine transition from Triassic to Late Jurassic deposited reservoir-prone sandstone sequences and, with the cessation of the rifting, organic rich shale intervals covered the abandoned rift topography from the Late Jurassic Cretaceous. A regional thermal uplift associated with the Middle Cimmerian Orogenesis reported from Late Kimmeridgian in the Central Graben area [*Rattey and Hayward*, 1993], produced salt intrusion and diapirism. The structural inversion of some pre-rift extensional structures and the partial erosion of the Jurassic sequences (Figure 6-3), created a discordance associated with this event known as the Base Cretaceous Unconformity (BCU), which was the latest major tectonic and stratigraphic disturbance in the basin. After this event, the basin underwent very stable carbonatic conditions that led to the deposition of a thick chalk interval during the Cretaceous, followed by basin colmatation by shaly-dominated sequences during the Cenozoic.

The Central Graben of the North Sea has particular pressure development: while the Tertiary shaly interval is normally pressured (hydrostatic), the underlying Lower Cretaceous Chalk (Cromer Knoll Group) and Pre-Cretaceous Jurassic reservoir are highly overpressured, not only as a consequence of depth, but also due to fast sedimentation during deposition and rapid burial. Oil generation and migration started in the area in the Late Cretaceous, between 100 and 86 Ma, with peak activity between 70 – 60 Ma [*Winefield et al.*, 2005]. This relatively early reservoir hydrocarbon charge may have potentially preserved part of the primary intergranular porosity, preventing further compaction and possibly contributing to abnormally high pore pressures

The Shearwater Field is comprised of a rotated and tilted triangular-shaped fault block of Triassic, Middle Jurassic (Pentland Formation) and Late Jurassic stratigraphy (Fulmar,

Heather, and Kimmeridge Clay formations). The fault block is bounded to the north and east by two major almost vertical normal faults with variable throws that can be as high as 600 metres in the crest of the structure, which is underpinned by a Permian salt pillar (Figure 6-3) that pierces the sequence in the junction of the two major faults. As a consequence of the syntectonic deposition and the erosive effect of the thermal uplift, the thickness of the sequences in the block is variable, especially for sediments of the Late Jurassic that are thicker towards the southwest and finish in pinch-out, partially or totally eroded towards the northeast in the crest of the structure. The variable thickness makes the seismic interpretation difficult, as it may be impossible to track a specific reflection event, leading to reflection interference as a consequence of the 'tuning 'effect (Figure 6-4).

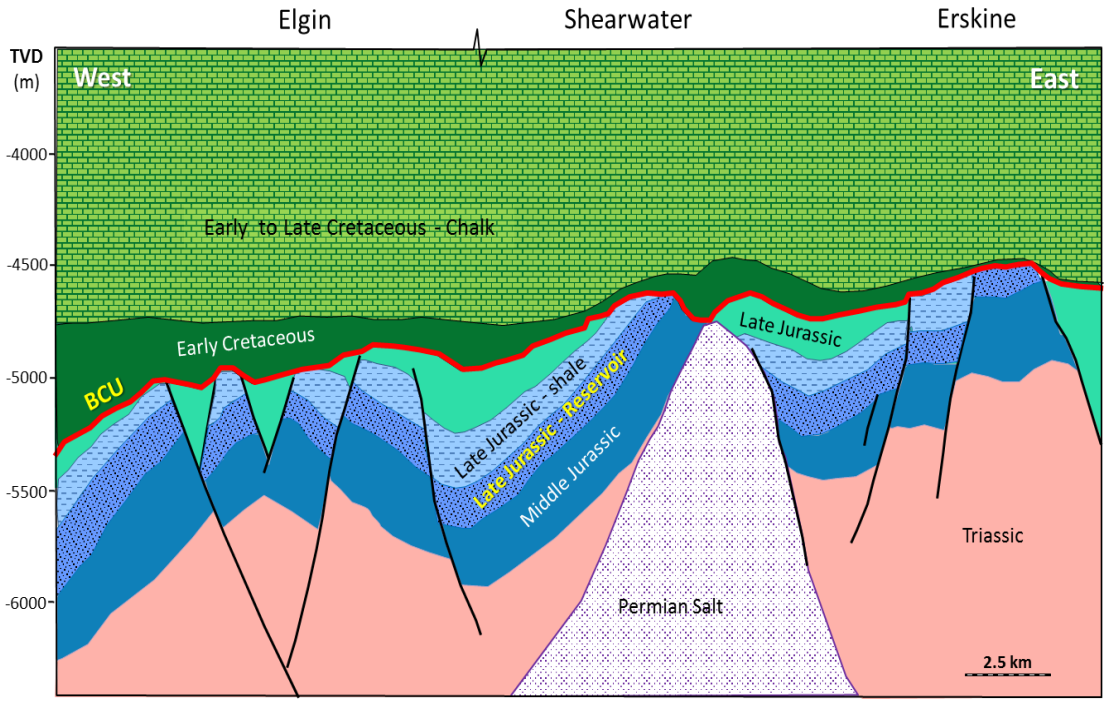

Figure 6-3 *Schematic model of the HP/HT fields in the central graben of the North Sea Basin, with information from Errat, et al. (2010).*

The reservoir architecture is dominated by the truncation and erosion caused by the Base Cretaceous Unconformity to the clastic units from the Late Jurassic. The seismostratigraphic analysis of the area (Figure 6-4) shows good parallelism and constant seismic thickness between reflectors corresponding to the Pentland and Fulmar formations (Middle to Late Jurassic), which shows a balance between the accommodation space, the amount of sediment and relatively stable tectonic conditions (aggradational stacking pattern, at least locally). The overlying seismic events corresponding to the

Heather and Kimmeridge Clay formations present downlap reflection terminations, suggesting a larger accommodation space during deposition (progradational stacking pattern towards the east-northeast), as a consequence of spreading and subsidence in the basin associated with an increase in the rifting activity, which also correlates with a rise in the sea level (transgression), and dominance of shale deposition. Finally, as a consequence of the thermal uplift, the Late Jurassic reflections are truncated by the strong reflection corresponding to the BCU. This geometrical analysis was used as a guide to model the layering of the different units of the Shearwater Field in the static and dynamic reservoir modelling.

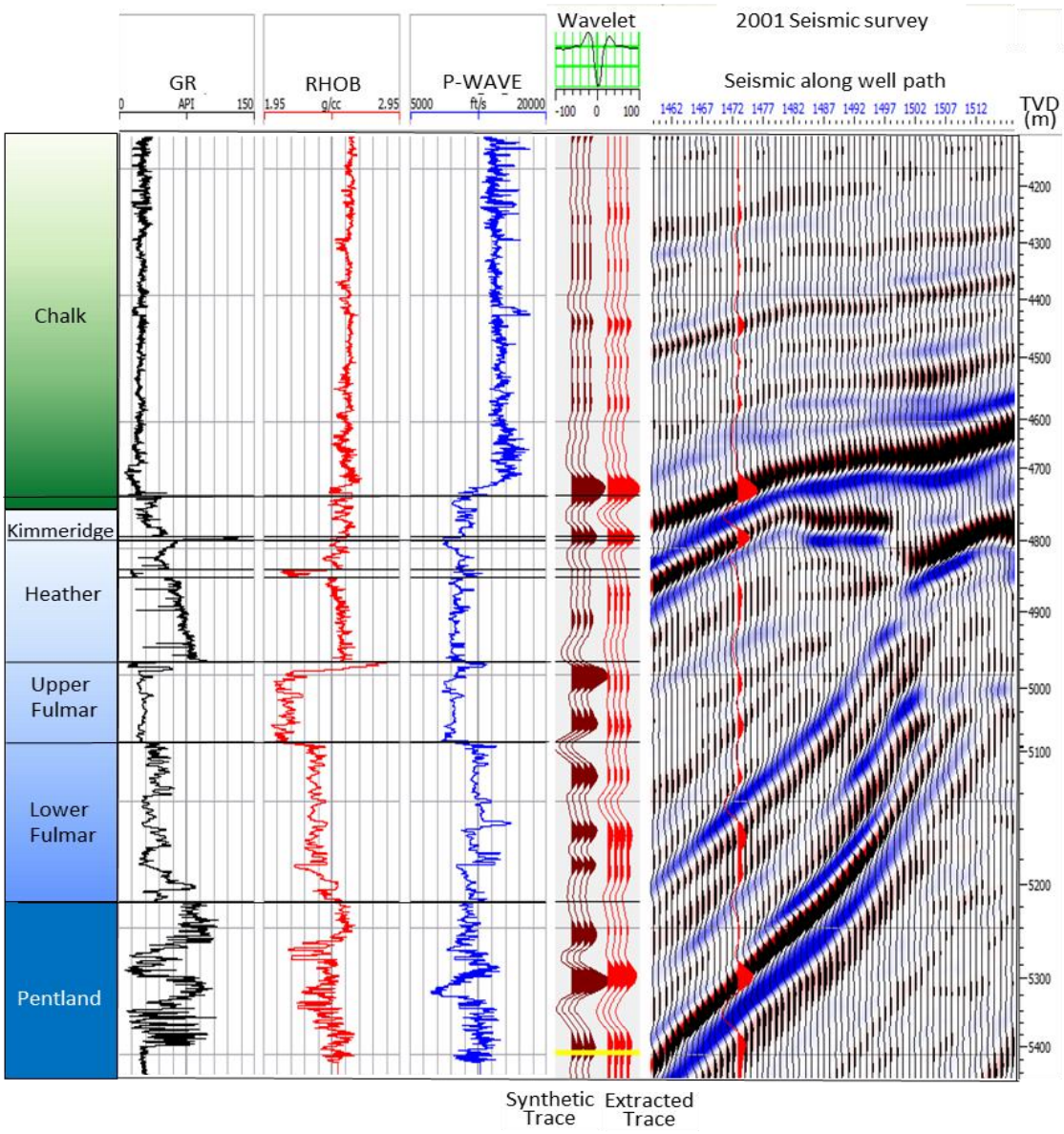

Figure 6-4 *Well tie showing part of the Shearwater Field architecture*

The reservoir stratigraphy in the Shearwater Field consists of two major intervals: at the base, a coarsening-up sequence, followed by a transgressive fining-up interval (Figure 6-5). The basal interval consists of the thick (up to 550 metres) stacked fluvial sand channels of the Pentland Formation, with frequent occurrence of crevasse splay, overbank shales and coals. Overlying this unit is the Fulmar Formation that consists of a clean stacked shoreface and shallow marine sandstones. The Fulmar Formation, whose overall thickness is around 210 metres, can be divided into two members: the upper one contains more prospective sands (high porosity and permeability), which constitute the main reservoir, while the lower member presents lower to moderate porosity, some dispersed shale and calcite cemented intervals. The coarsening-upwards interval composed by Pentland and Fulmar can be easily correlated with the Brent Group stratigraphy in other North Sea locations.

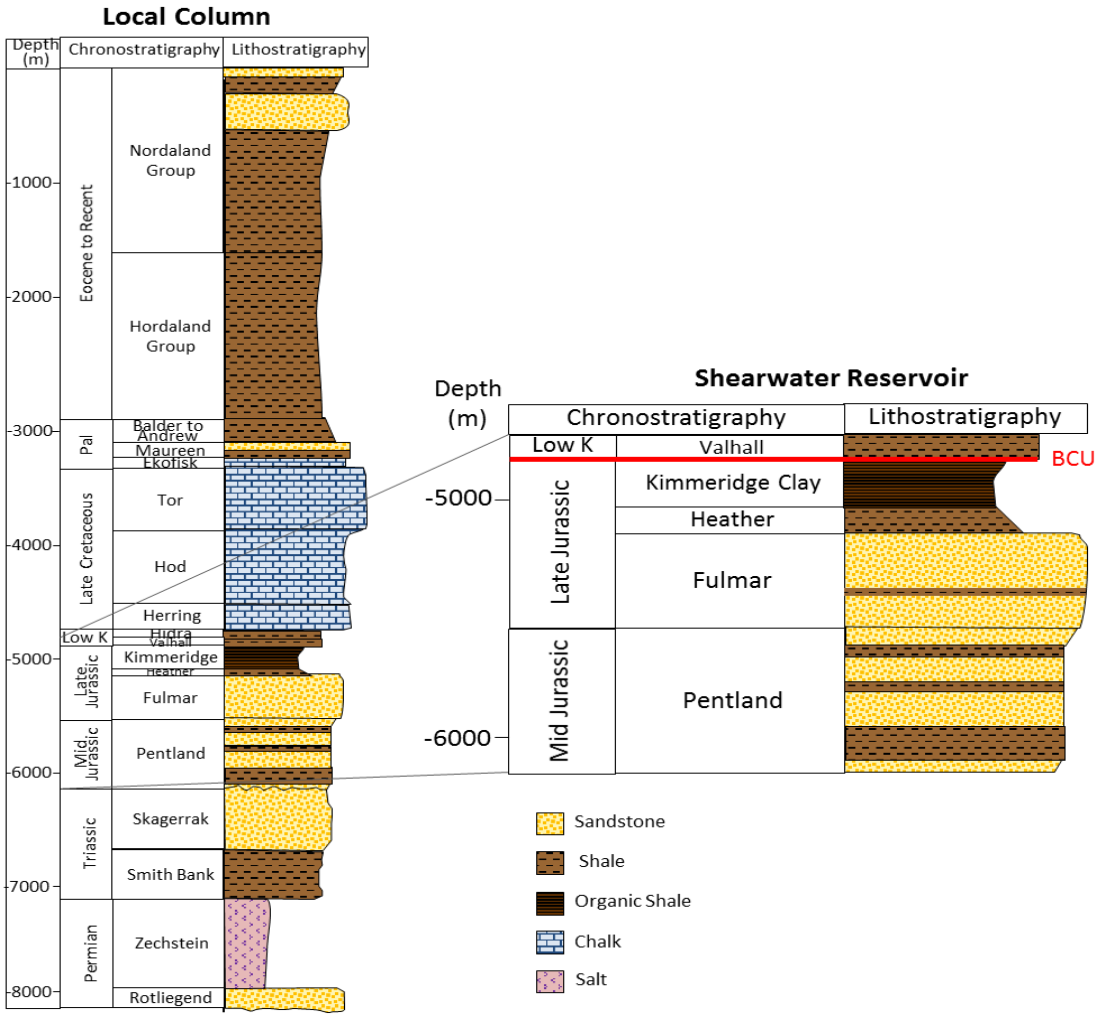

Figure 6-5 *Stratigraphic column for the Shearwater Field. Redrawn from published literature [Lasocki et al., 1999]*

Overlying this interval, the Heather Formation consists of a marine shale (between 30 and 200 metres thick), marking a locally non-transitional marine flooding event and back-stepping of the shoreface sequence towards the north and west [*Gilham et al.*, 2005]. In the middle of the Heather Formation, a single turbidite channel sand has been deposited, an event known as the Heather Sand Member, which was sourced directly from the syn-sedimentary collapse of a younger shoreface system from the north or west of the Central Graben. The thickness of these turbidite channel sands is less than 10 metres, but their distribution is not uniform in the area, which is why it was not targeted as a producer, even though they are saturated with condensate. Covering this area, with a varying thickness controlled by the BCU erosion, are the organic–rich shales of the Kimmeridge Clay Formation, marking the maximum influence of the transgression in the basin.

6.4 Shale characterization

The shales in the Shearwater Field constitute the seal and overburden of the reservoir. The inclusion of the Heather and Kimmeridge Clay formations in the reservoir static and dynamic modelling allows us to evaluate the effect of pressure diffusion in the propagation of strains into the overburden as a consequence of reservoir (Fulmar Formation) depletion and compaction. The characterization of these units was performed mainly using well log data analysis and bibliographic references, as no rock samples, laboratory reports, or even static or dynamic models of the area were available for this case study. Both shales were deposited in marine conditions, under the influence of a major eustatic event, which was a marine transgression as a consequence of a rifting pulse causing subsidence and marine floor spreading. The energy conditions during the deposition of these units were relatively stable, with low oxygen circulation allowing organic matter to be preserved. At certain times, mass flows occurred into the basin, depositing some sand and silt intervals in both formations. The analysis of seismic reflectors associated with both units shows syntectonic activity associated with generation of accommodation space, which may have produced some lateral and vertical variability within the shaly sequence.

The Heather Formation is composed predominantly of medium to dark grey marine mudstones and siltstones with sporadic presence of concretions and limestone laminations [*Deegan and Scull*, 1977]. The lower interval (the thicker too) of the Heather Formation in the Shearwater Field presents a gradually coarsening-upwards electrofacies profile,

with even some fine laminations of sands (Figure 6-6). When present, the turbidite channels of the Heather Sand Member show clean sands with low density, due to high porosity and condensate saturation. The upper interval is more carbonaceous with higher occurrence of limestones but also higher silt content. The elastic behaviour of this interval (see acoustic impedance tract in the Figure 6-6) shows a very weak compaction trend for this unit, with relatively poor elastic contrast between the hydrocarbon saturated channel of the Heather Sand Member and the surrounding shales. Due to the high content of swelling smectite, a drilling geohazard has being reported for this unit.

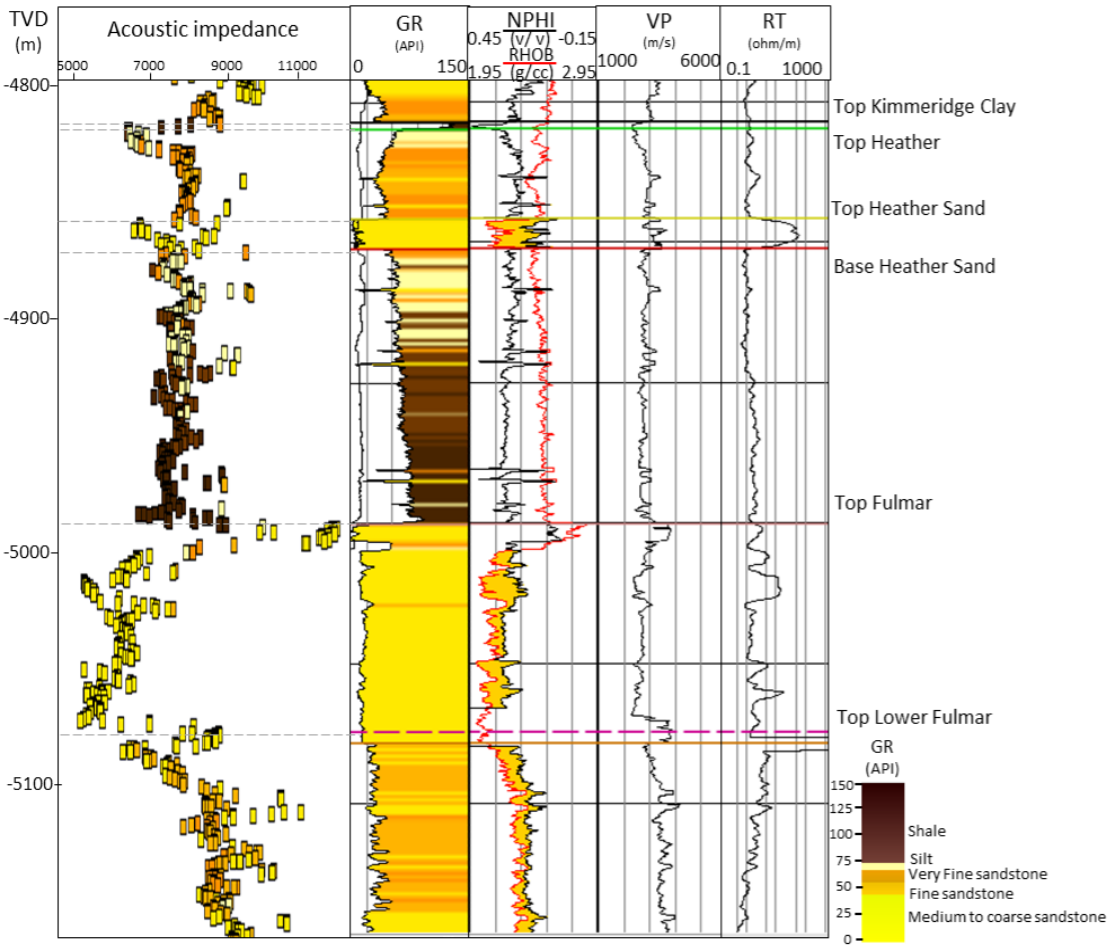

Figure 6-6 *Heather Formation electrofacies and acoustic impedance (colour coded using GR values).*

The Kimmeridge Clay Formation is predominantly comprised of dark-grey brown to black, non-calcareous to weakly calcareous, partly fissile, moderately to highly organic-rich mudstone, with local, thin laminae and streaks of siltstone and sandstone [*Deegan and Scull*, 1977]. Looking into the Kimmeridge Clay electrofacies it is easy to notice several patterns: the high gamma ray response should correspond to the fixed uranium of

the organic matter. Lower density values than those of the Heather Formation suggest higher porosity or less dense components (i.e. organic matter), which is corroborated by the much lower P-wave velocity of the Kimmeridge Clay interval, and finally the very uniform acoustic impedance behaviour in the interval is indicative of the absence of a compaction trend (Figure 6-7).

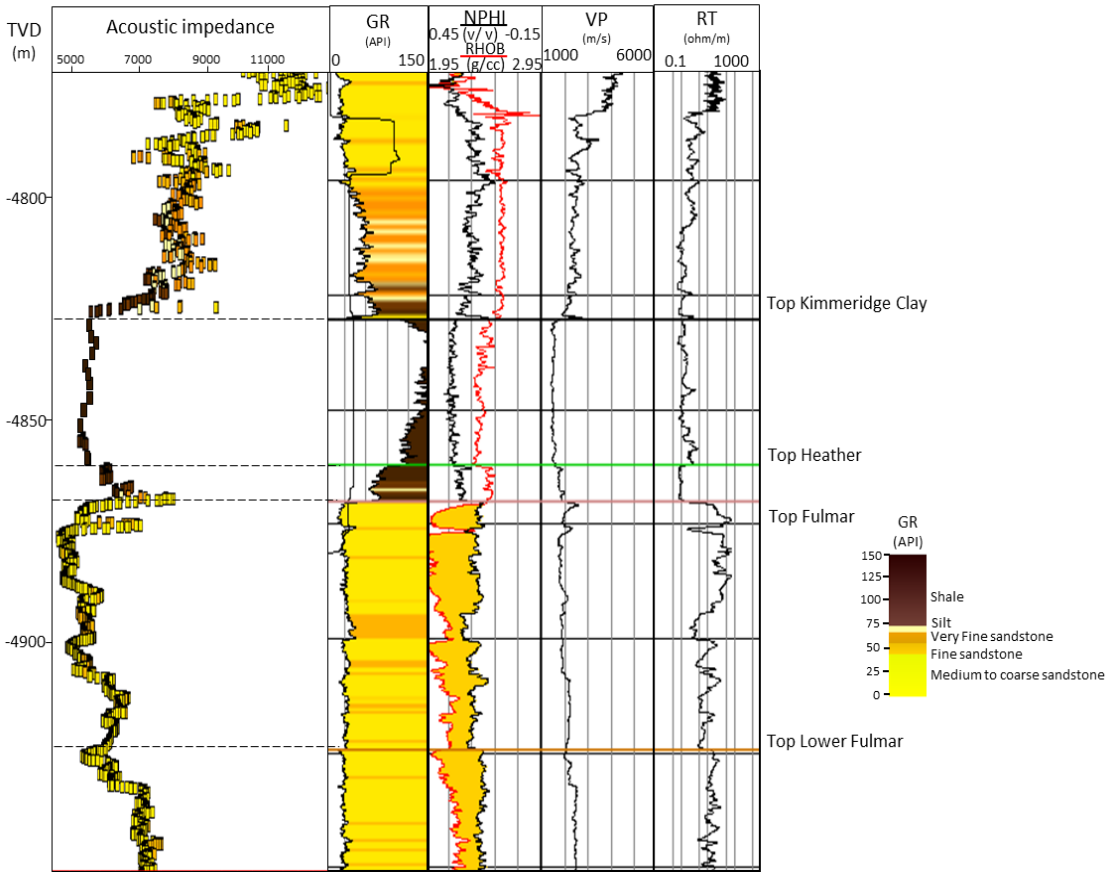

Figure 6-7 *Kimmeridge Clay Formation electrofacies and acoustic impedance (colour coded using GR values).*

6.4.1 Shale composition

Paleogeography and seismic reflection analysis determines that the direction of deposition for the Heather Formation is from west-northwest to southeast, with source provenance from the erosion of the emerged North Sea High and some plateaux lavas at the south of the Shetland Platform. Density, gamma ray and velocity well log averaged values, coupled with sediment provenance, are used as input for a basic material balance analysis (Equations 2.24 and 2.26) to determine shale composition, which was established for the Heather Formation as 60% clay fraction, 35% silt and 5% of calcite and organic matter. The clay fraction is, in turn, composed of illite (55%), smectite (40%) and

glauconite (5%). The same analysis was performed on Kimmeridge Clay Formation intervals, establishing a composition of the shale rock total volume of 65% of clay fraction (including 0.75 fraction content of illite and 0.25 smectite), 25% of silt (a mix of quartz and feldspar), 5% of calcite and 5% of organic matter.

6.5 Reservoir modelling

The dataset available for the Shearwater Field does not include static or dynamic reservoir simulation models, but only surfaces and faults in depth, wireline log data of 6 production wells, porosity-permeability relationships for the Fulmar Formation and some production reports, all provided by Shell. This information is used to build the static and dynamic model of the reservoir, with the inclusion of the overburden shales. The geometry of the model was defined using the available surfaces and faults, with the zones and number of layers based on the heterogeneity observed in the well log for each formation (Table 6-1). The grid geometry (56 x 33 x 50 cells) was established with a cell size of 100 x 100 metres (x, y) and variable thickness, depending on the layering. To have a better cell-fault polygon definition, the i and j axis directions were defined with a rotation of -5 degrees (N5°W), matching the direction of the majority of the reservoir faults.

Surface	Zone	Layers	Comments
BCU			
	Kimmeridge Clay	10	As the top of Kimmeridge Fm was not available, the layering was established following the base (Top Heather)
Top Heather Fm.			
	Upper Heather Shale	5	Layering follows the top, progradational stacking
Top Heather Sand			
	Heather Sand	2	Layering follows the top, progradational stacking
Base Heather Sand			
	Lower Heather Shale	7	Layering follows the top, progradational stacking
Top Fulmar			
	Upper Fulmar	16	Layering proportional to upper and lower limits (parallel), aggradational stacking
Top Lower Fulmar Mb			
	Lower Fulmar	10	Layering proportional to upper and lower limits (parallel), aggradational stacking
Base Fulmar Fm.			

Table 6-1 *Shearwater Field grid geometry for the simulation model*

6.5.1 Static properties

To express the reservoir heterogeneity, a variable distribution of NTG and porosity was modelled for the reservoir intervals and shales in the overburden, based on the upscaling of well log properties and the application of petrophysical workflows. Net to Gross estimation was made using the GR index linear relations for volume of shale and NTG computations (Equations 2.1, 2.3 and 2.7), based on the definition of rock type end members, with clean sand parameters defined from the upper member of Fulmar Formation and pure mudstone defined from the base of the Lower Heather Shale. I did not choose parameters inside the Kimmeridge Clay Formation, even though the energy during deposition of this unit was much lower than that for the Heather Formation, to avoid the effect of organic matter and residual kerogen saturation in the well log properties, as it may be more challenging to find a proper relation linking the effect of these components to the porosity and permeability estimation. The propagation of the computed NTG from the well location to the rest of the model (Figure 6-8) was carried out applying geostatistical methods (variograms) per interval, with parameters estimated from stratigraphic correlations along the field (Table 6-2). The use of spherical or exponential variograms is related to the zone homogeneity, evaluated on the analysis of the sedimentological environment, the facies dimensions and their spatial variability.

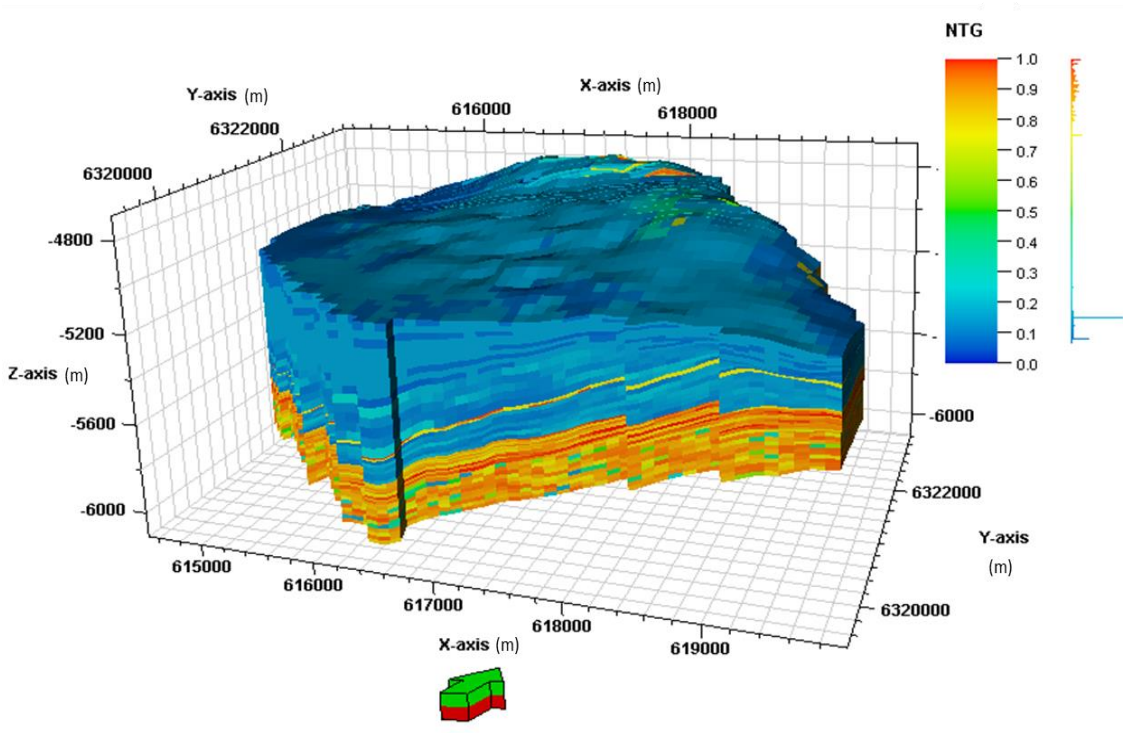

Figure 6-8 *Shearwater Field: static model showing NTG distribution.*

Zone	Method	Variogram	NTG range
Kimmeridge Clay	Gaussian random function	Spherical (deep marine conditions), azimuth 34° (major axis); anisotropy range 1500 m (major), 1050 m (minor) and 5 m (vertical).	Min = 0.07 Max = 0.15
Upper Heather Shale	Gaussian random function	Spherical (marine conditions); azimuth 34° (major axis); anisotropy range 1000 m (major), 1000 m (minor) and 5 m (vertical).	Min = 0.08 Max = 0.25
Heather Sand	Gaussian random function	Exponential (turbidite channels); azimuth 34° (major axis); anisotropy range 1500 m (major), 1000 m (minor) and 10 m (vertical).	Min = 0.4 Max = 0.9
Lower Heather Shale	Gaussian random function	Spherical (marine conditions); azimuth 34° (major axis); anisotropy range 1000 m (major), 1000 m (minor) and 5 m (vertical).	Min = 0.07 Max = 0.3
Upper Fulmar	Gaussian random function	Spherical (uniform shallow marine conditions); azimuth 34° (major axis); anisotropy range 2000 m (major), 1500 m (minor) and 30 m (vertical).	Min = 0.45 Max = 1
Lower Fulmar	Gaussian random function	Exponential (fluvial conditions; azimuth 34° (major axis); anisotropy range 1000 m (major), 300 m (minor) and 20 m (vertical).	Min = 0.2 Max = 0.9

Table 6-2 *Geostatistical parameters for NTG population in the Shearwater model. Azimuth defined on base of seismic data (continuity and distribution of reflectors) the anisotropy range was defined on the base of stratigraphic correlations according to the lateral and vertical variability of the identified layers in each formation, NTG ranges by Vsh computation using well logs data.*

For the porosity estimation were used two techniques according to the dominant lithology of the zone. For the Fulmar Formation and Heather Sand Member, as the clay content is very low, the porosity is based on the measures of the Neutron-Porosity (NPHI) well log, as no correction for clay bound water is needed. For the overburden shales, the hydrogen index measured by the NPHI is clearly biased by the water included in the crystalline structure of shales. Consequently, the porosity for the upper and lower Heather shales and Kimmeridge Clay Formation is estimated using shale composition, a library density for those components, saturated values for density and basic material balance analysis (Equations 2.20 and 2.24). Once the porosity has been computed for all zones, the values are averaged and upscaled to the grid layering geometry and then propagated from the well locations to all the model, applying geostatistical methods (Table 6-3) and using the NTG distribution as a guide to ensure a better consistency between properties.

Based on published literature [*Winefield et al.*, 2005] and Shell internal reports, early hydrocarbon migration and charge resulted in the Shearwater Field showing primary porosity preservation, which prevented compaction in the reservoir. To model this effect, a multiplier was created (with the numerical value of 1.05) above the condensate-water contact (located at -5150 metres TVD), to enhance the reservoir (Fulmar Formation and

Heather Sand Member) porosity by 5% [*De Gennaro et al.*, 2010] in the hydrocarbon saturated rock volumes (Figure 6-9).

Zone	Method	Variogram	Porosity range
Kimmeridge Clay	Moving Average	Using NTG trend. Orientation 34°; vertical range 5 m and major/minor ratio 1.	Min=0.08 Max= 0.19
Upper Heather Shale	Moving average	Using NTG trend. Orientation 34°; vertical range 5 m and major/minor ratio 1.	Min=0.08 Max= 0.15
Heather Sand	Moving average	Using NTG trend. Orientation 34°; vertical range 20 m and major/minor ratio 1.2.	Min=0.15 Max= 0.23
Lower Heather Shale	Moving average	Using NTG trend. Orientation 34°; vertical range 5 m and major/minor ratio 1.	Min=0.08 Max= 0.14
Upper Fulmar	Moving average	Using NTG trend. Orientation 34°; vertical range 30 m and major/minor ratio 1.4	Min=0.12 Max= 0.315
Lower Fulmar	Moving average	Using NTG trend. Orientation 34°; vertical range 20 m and major/minor ratio 2.	Min=0.08 Max= 0.247

Table 6-3 *Geostatistical parameters for porosity population of the Shearwater simulation model.*

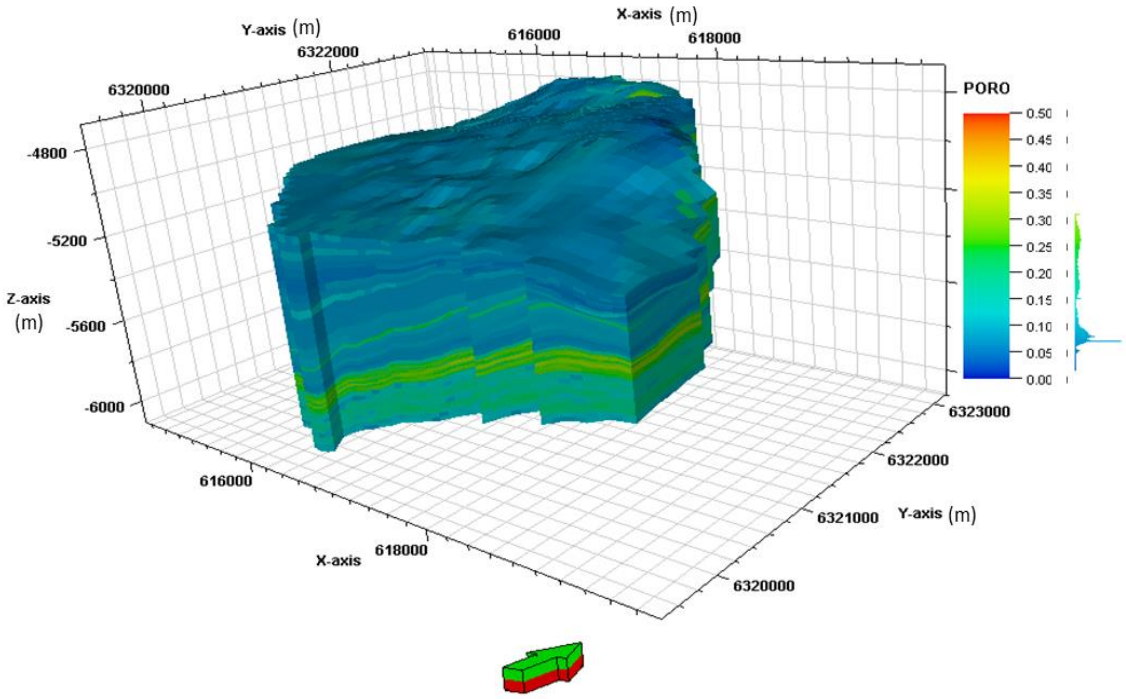

Figure 6-9 *Modelled porosity distribution for the Shearwater Field model.*

6.5.2 Dynamic properties

As several orders of magnitude separate the dynamic properties (permeability, mostly) of sand and shale, the modelling of these parameters was performed separately. For the producing reservoir units (Fulmar Formation and Heather Sand Member), the computed

continuous horizontal and vertical permeability logs were provided by Shell, together with the wireline log data. This information was core calibrated and used to determine a porosity-permeability relationship to propagate the sand's permeability from the well location to all entire model, based on the porosity distribution. For shales, the permeability is calculated using the empirical relationships of *Yang and Aplin* (2007) (Equations 2.28 and 2.29), based on pressure, clay content and shale porosity. The permeability modelling is performed using the porosity distribution as trend to propagate the property in the model, in order to have consistency between static and dynamic properties in the reservoir (Figure 6-10). As higher porosity is modelled for the reservoir units above the water- condensate fluid contact, permeability is also estimated as higher for those intervals.

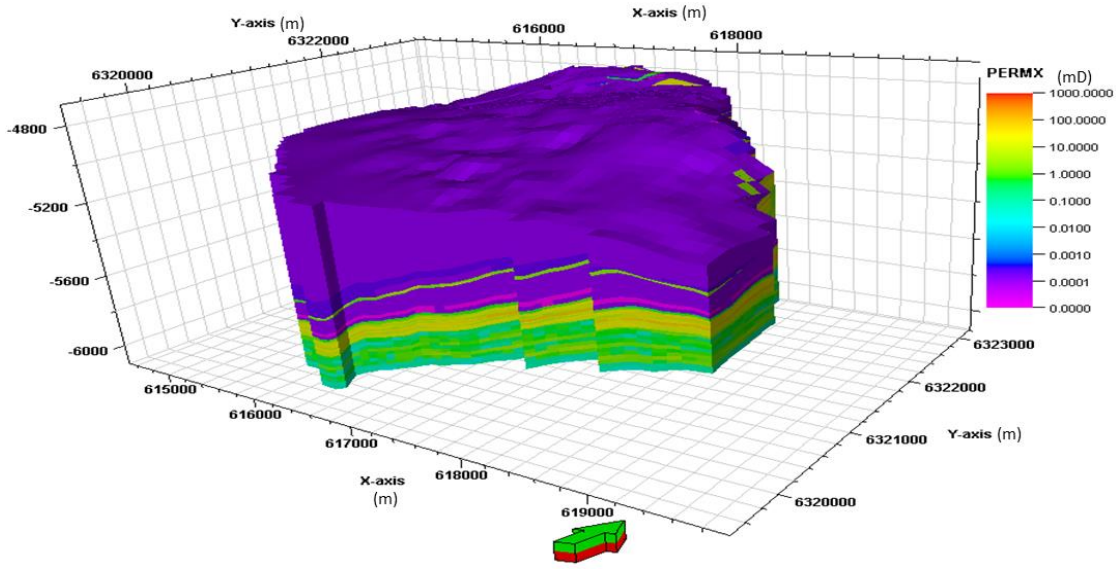

Figure 6-10 *Modelled Horizontal permeability for the Shearwater Field*

Initial (pre-production) conditions for the reservoir pressure and saturation are modelled through three different equilibrium regions, defined by the SATNUM keyword in the Eclipse software for numerical simulations. The first equilibrium region includes the Fulmar Formation, with a pressure datum defined as 1050 bars at 5000 metres TVD and a water-condensate contact at 5150 metres TVD. The second equilibrium region is defined for the Heather Formation, to model the reported overpressure of this interval as a consequence of the very fast shale deposition; for this, the pressure datum is defined as 1100 bars at 5000 metres TVD and, in order to make the shales water-saturated, an artificial water-condensate contact was created at 2000 metres TVD. Finally, the third

equilibrium zone was defined for the Kimmeridge Clay Formation with the same pressure gradient as the reservoir sands (pressure datum of 1050 bars at 5000 metres TVD) but with fluid contacts similar to those of the Heather Formation. Initial pressure and saturation distribution for the Shearwater Field model is shown in Figures 6-11 and 6-12.

To evaluate the effects of the overburden shales' inclusion into the numerical simulations results for pressure and saturation, four scenarios were considered: a) one control model without shales activated, b) a shale active model, with permeability estimated by the *Yang and Aplin*, (2007) method, c) another shale active model with shale permeability similar to the previous model but enhanced at the well location (cells intersected by the well trace), recreating drilling-induced fractures, and finally, d) a model where all overburden shale permeabilities were enhanced to recreate a shale high permeability model, a scenario that in a previous ETLP project [*HajNasser*, 2012] showed an excellent match between predicted overburden time shift and observed seismic data in the neighbouring Erskine Field. The specific parameters of all the models are shown in Table 6-4.

Model	Shale Kh	Shale Kv
Inactive shales	Not included	Not included
Active shales, estimated permeability	25–75 nD	7–14 nD
Active shales, fractures	25–75 nD, and up to 10 µD in the cell corresponding to the well location	7–14 nD, and up to 100 nD in the cell corresponding to the well location
Active shales' high permeability	Up to 100 µD	Up to 1 µD

Table 6-4 *Modelled scenarios for shale permeability variations. Kh= horizontal permeability and Kv= vertical permeability.*

The PVT fluid table properties were generated using a compositional model for the Shearwater Field condensate parameters, using the Petrel software. Similarly to previous field applications, shale capillary forces and relative permeabilities were modelled based on correlations of pore throat geometry with pressure (Equation 2.32) and results from shale gas laboratory tests for mercury injection [*Sigal*, 2013]. Well production data was built based on the internal production reports provided by the operator (Shell). The simulation model was initialised on October 1st of 2000 and stopped on December 1st of 2013, even though most wells failed due to geomechanical problems around the end of 2004 and production finished in November of 2007; however, as the latest seismic monitor was acquired at the end of 2013, the model was extended until that time.

6.6 Simulation results

As pressure and saturation changes are related to well production activity and most wells failed due to geomechanical issues before the end of 2004, (with just a few producing until the end of 2007), the pressure and saturation results are analysed in two time steps: at the end of 2004, considering the 2000 - 2004 period as a depletion stage, which conveniently has a seismic monitor acquired in 2004 recording the elastic changes corresponding to this time, and at the end of 2013, which corresponds to the latest seismic acquisition to evaluate the rehabilitation of the Shearwater Field. During this period (from 2004 to 2013) a natural pressure build-up process occurred in the reservoir, as consequence of the aquifer support and pressure equilibration within the reservoir units.

6.6.1 Pressure diffusion results

With depletion being the main production mechanism in this condensate reservoir, induced changes in the reservoir pore pressure are as high as 400 bars (from 1050 to 650 bars). Due to a smaller volume for pore pressure equilibration, during the depletion stage (at the end of 2004), the inactive shales model shows a higher depletion (up to 50 bars lower) in the Fulmar Formation at the crest of the structure where the wells are located (ovals in the Figure 6-11), when compared to the active shales models, whose response is smoother in the reservoir. Regarding pressure diffusion into the overburden shales, the model with estimated shale dynamic properties presents a pressure drop between 3 to 5 bars in the Heather Formation's layers adjacent to the reservoir, while for the high permeability scenario the pressure diffusion reaches the Kimmeridge Clay Formation layers, with the pressure drop being as high as 50 – 70 bars in the adjacent Heather Formation layers. Results corresponding to the active shale fractured scenario are not included in Figure 6-11, as they are similar to those from the shale estimated properties model, with only higher pressure diffusion in the shale cells corresponding to the well locations, where the enhanced vertical shale permeability representing fractures allows more connectivity with the reservoir, and hence more pressure diffusion. The implications of this local diffusion are shown in a further section of this chapter during the strain estimation at the well location. Figure 6-12 shows a sharp pressure gradient in 2004 at the water-condensate contact.

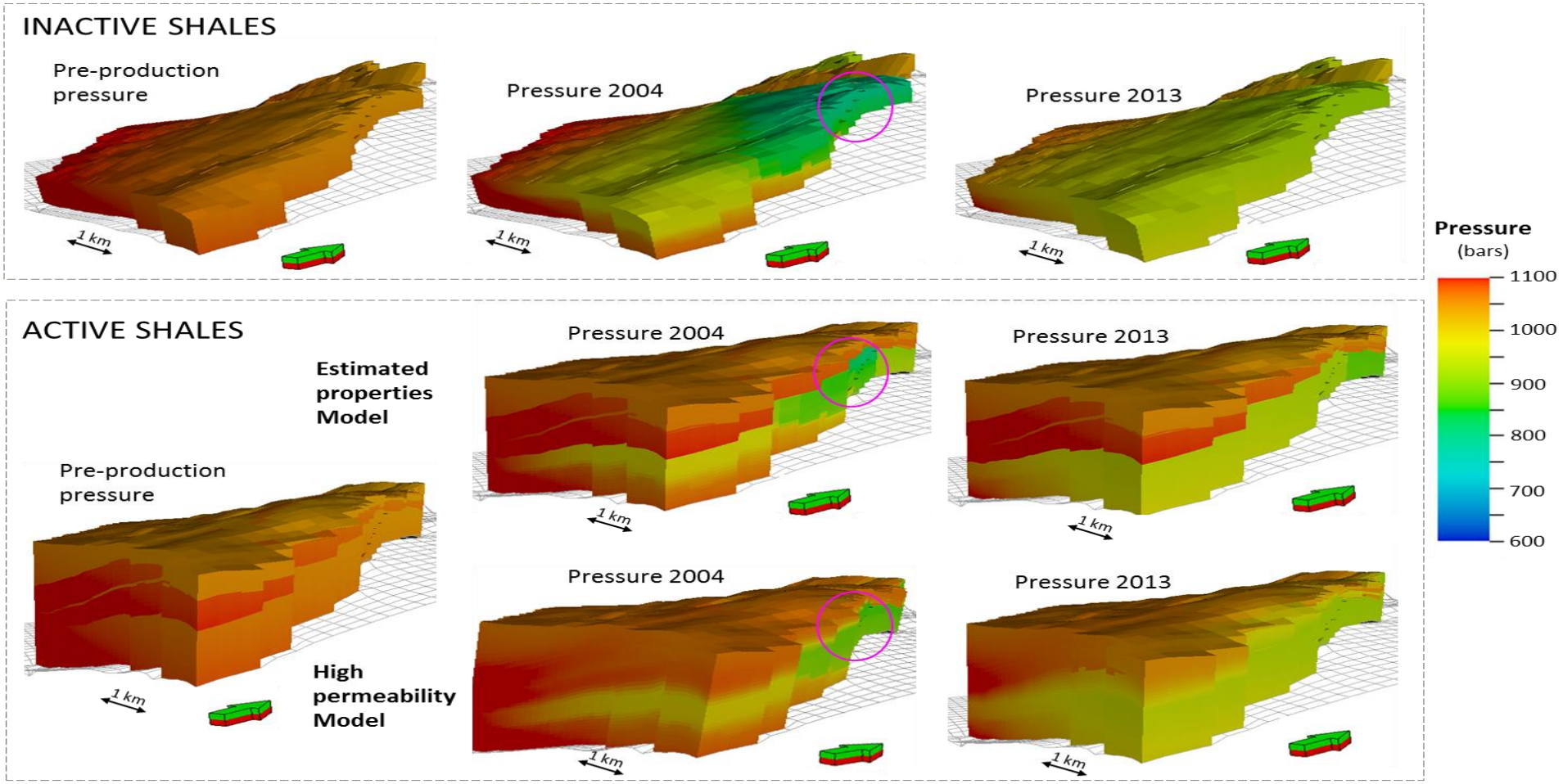

Figure 6-11 *Predicted pressure response for the modelled scenarios of the Shearwater Field, with and without overburden shales included in the simulation model.*

The combined effect of the changes in saturation at the fluid contact (from condensate to water), in porosity and permeability (modelled higher above the condensate-water contact) and the aquifer pressure support original front worked as an interface where the velocity of the pressure drop propagation becomes slower into lower levels of the Fulmar Formation.

The pressure build-up stage, evaluated in the 2013 time step after the geomechanical failure of all wells, shows a more similar response between the different models, with the predicted pressure still lower for the inactive shale model, and a uniform propagation of the depletion below the original condensate-water contact. The active shale models also show pressure equilibration within the Fulmar Formation intervals, with small extra pressure diffusion (between 1 and 2 bars) in the Heather Formation for the estimated properties model, while the high permeability scenario shows a tendency for pressure equilibrium between the reservoir and the overburden shales.

6.6.2 Saturation changes

As the induced pressure gradients were always above the Shearwater Field dew point (469 bars), the only changes of saturation involved in the reservoir are related to the water-condensate contact displacement and water breakthrough towards the producing wells. Active shale models show very similar saturation patterns (Figure 6-12), with a relatively uniform water-condensate contact displacement, with the higher permeability model having a slightly more efficient water sweep than the estimated properties model. On the other hand, the inactive shale scenario presents a water coning pattern with poor water sweep efficiency. Total oil and gas production volumes (in the separator at surface) for all the simulated models show a similar match with the historic production data, but for the total water production volume, the best match with the historic data is achieved by the inactive shales model.

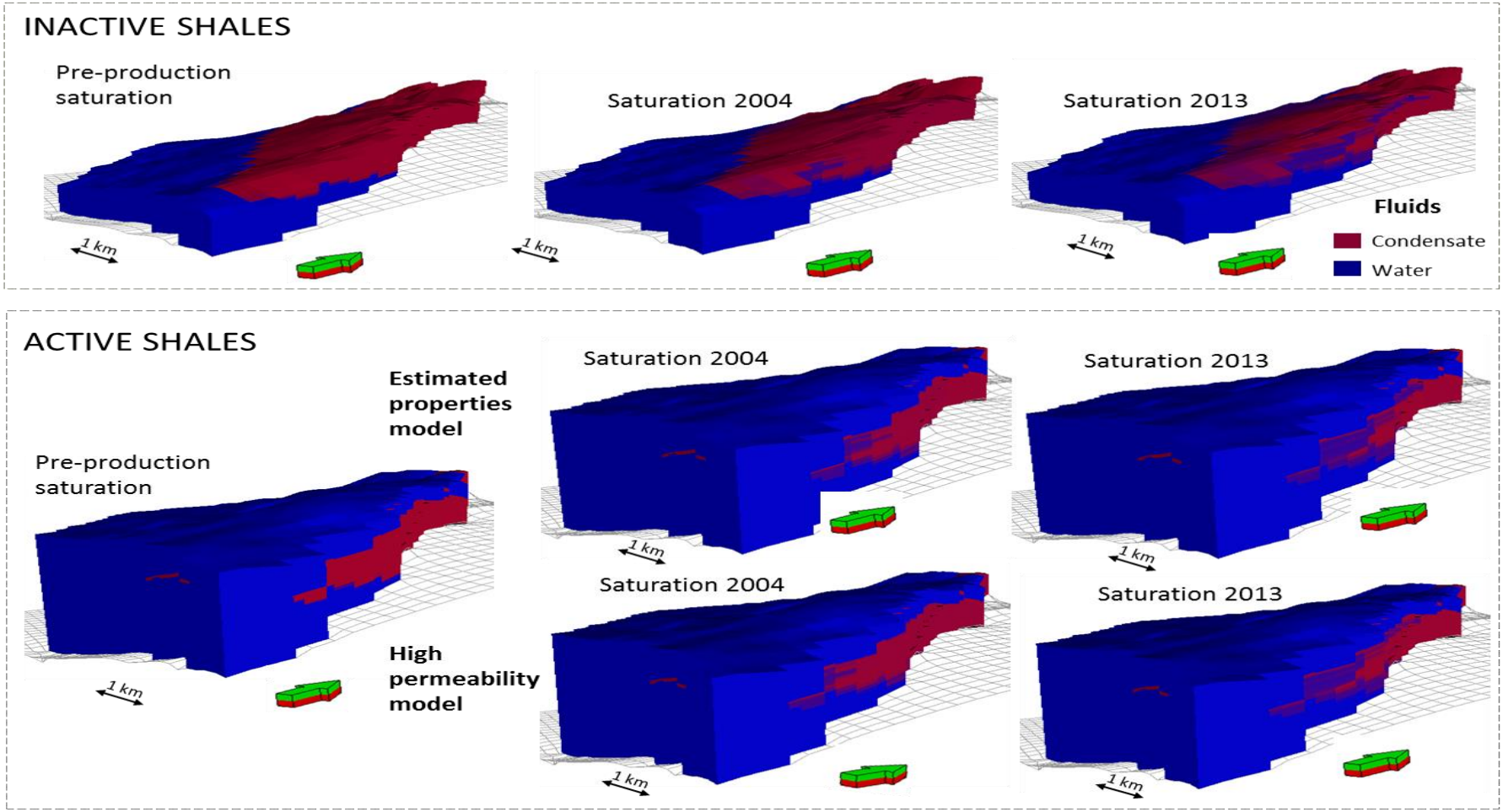

Figure 6-12 *Predicted saturation for the Shearwater Field, showing models with and without overburden shales included.*

6.7 The Shearwater Field time shift signal

The 4D seismic signal in the Shearwater Field was computed between the 2001, 2004 and 2013 full stack (0-40°) seismic vintages (pre and post stack parallel reprocessed in 2013 with a repeatability of 3% NRMS). The interpretation of the observed seismic monitors showed noticeable differences in the TWT positioning of the seismic events between time-lapse seismic vintages (base 2001 seismic survey and 2002, 2004 and 2013 monitors), both inside and outside the reservoir, with time shifts accumulated along the seismic ray path caused by changes in travel distance and seismic velocity. The distribution and values of those differences or time shifts is higher around the Upper Fulmar Member, which is the main target for condensate production and where compaction due to depletion was expected, but also the time-shift signal propagates towards the shales and even the chalk sequence of the overburden, and is high towards the underburden into the Pentland Formation.

The large time shifts in the Pentland Formation are unexpected, as the lithostatic weight of the entire rock column should not allow either considerable compaction or expansion in the underburden; thus, the expected time shift signals should show a decrease and not an increase, which is the opposite of what was observed in the Shearwater Field. This phenomenon is shown for two well locations over the extracted average trace in Figures 6-13 and 6-14. In both images one can appreciate the large time shift in the Upper Fulmar Member, where most wells are completed, decreasing in the lower Fulmar Member to almost null values, and then increasing again in the Pentland Formation. The stratigraphic variation in the overburden between wells 1 and 2, presents different signatures for the recorded time shift in the 2001, 2004 and 2013 seismic monitors, suggesting that the propagation of the strain in the overburden may be correlated with the stratigraphy, due to changes in the rocks' rheology and dynamic behaviour of these units under the induced effect of the reservoir compaction and its implication in the stress field of the area.

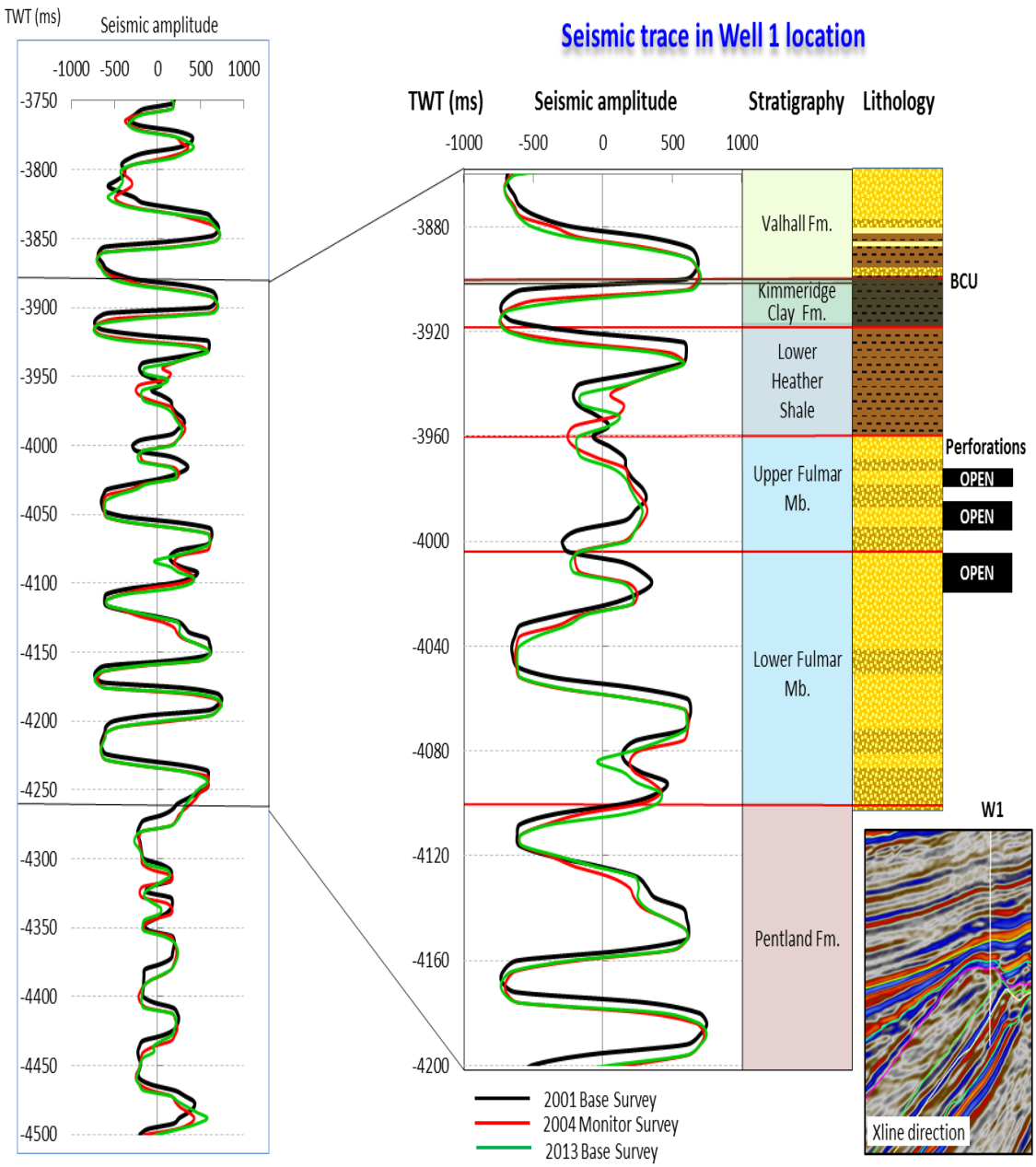

Figure 6-13 *Observed time shift in the well 1 location in extracted seismic traces from 2001, 2004 and 2013 seismic surveys.*

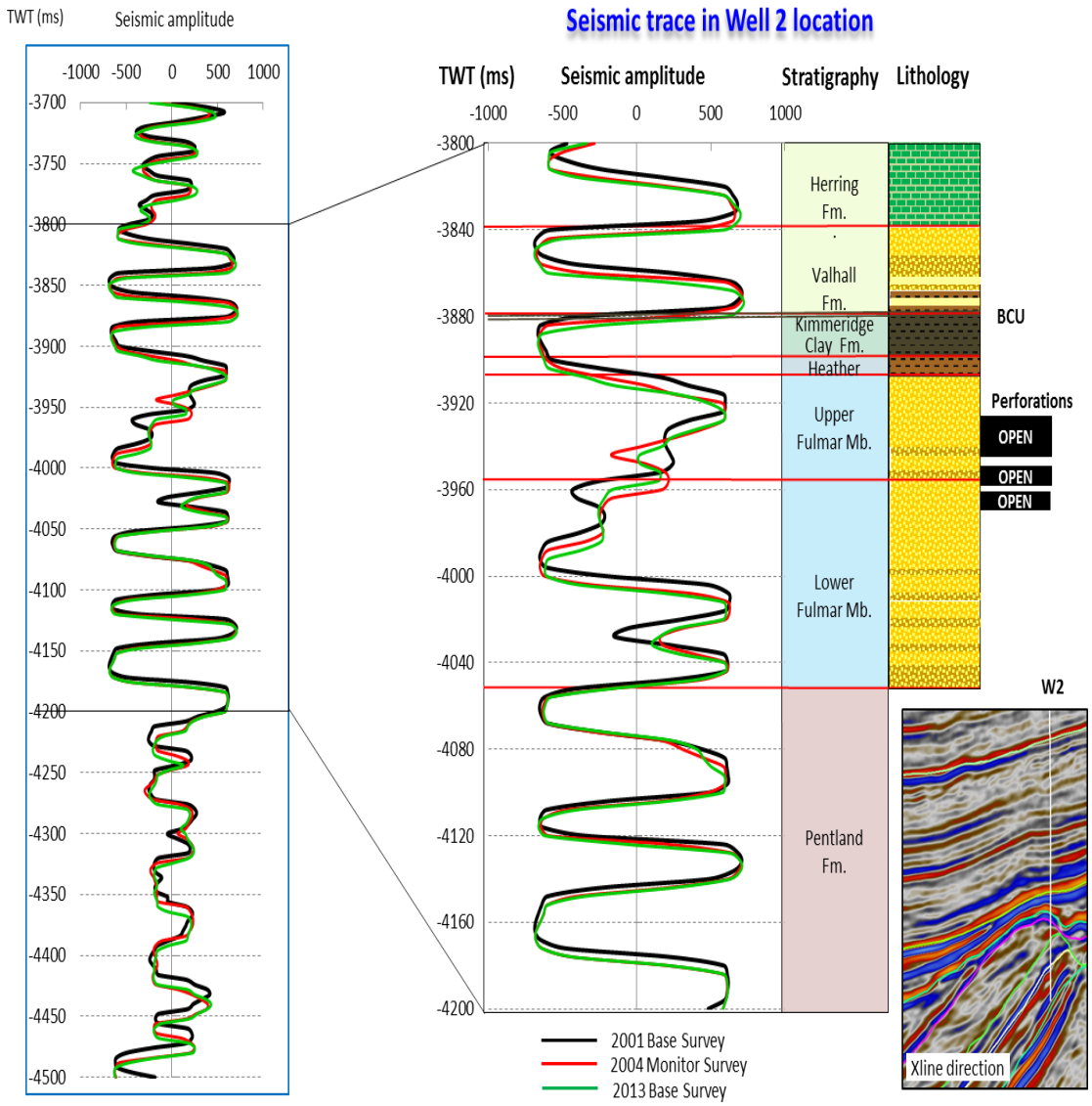

Figure 6-14 *Observed time shift in the Well 2 location in extracted seismic traces from 2001, 2004 and 2013 seismic surveys.*

The time shift estimation for the Shearwater Field is performed using an in-house code based on the Taylor series expansion and the cross-plotting concept of the Correlated Leakage Method [*Hoeber et al.*, 2005; *Whitcombe et al.*, 2010], a technique that assumes that there are no large amplitude or waveform changes between baseline and monitor, and time shifts between them are relatively small.

The method requires the definition of a TWT window (number of samples) for the correlation analysis. In order to choose a representative interval, the code was iterated to different time windows lengths and the results compared with a manually picked time shift, computing TWT differences between monitor and base for the same event in each sample (bold red line in Figures 6-15 and 6-16 that show time shift and time strain at two

well locations). The best fit to the manually picked time shift was achieved for correlation windows of 24 milliseconds (6 seismic samples). Time strain estimation was performed applying a non-linear inversion method [*Rickett et al.*, 2007] which reflects instantaneous rather than cumulative changes. The spatial distribution of the time shifts and time strain in the Shearwater Field are shown in Figure 6-17.

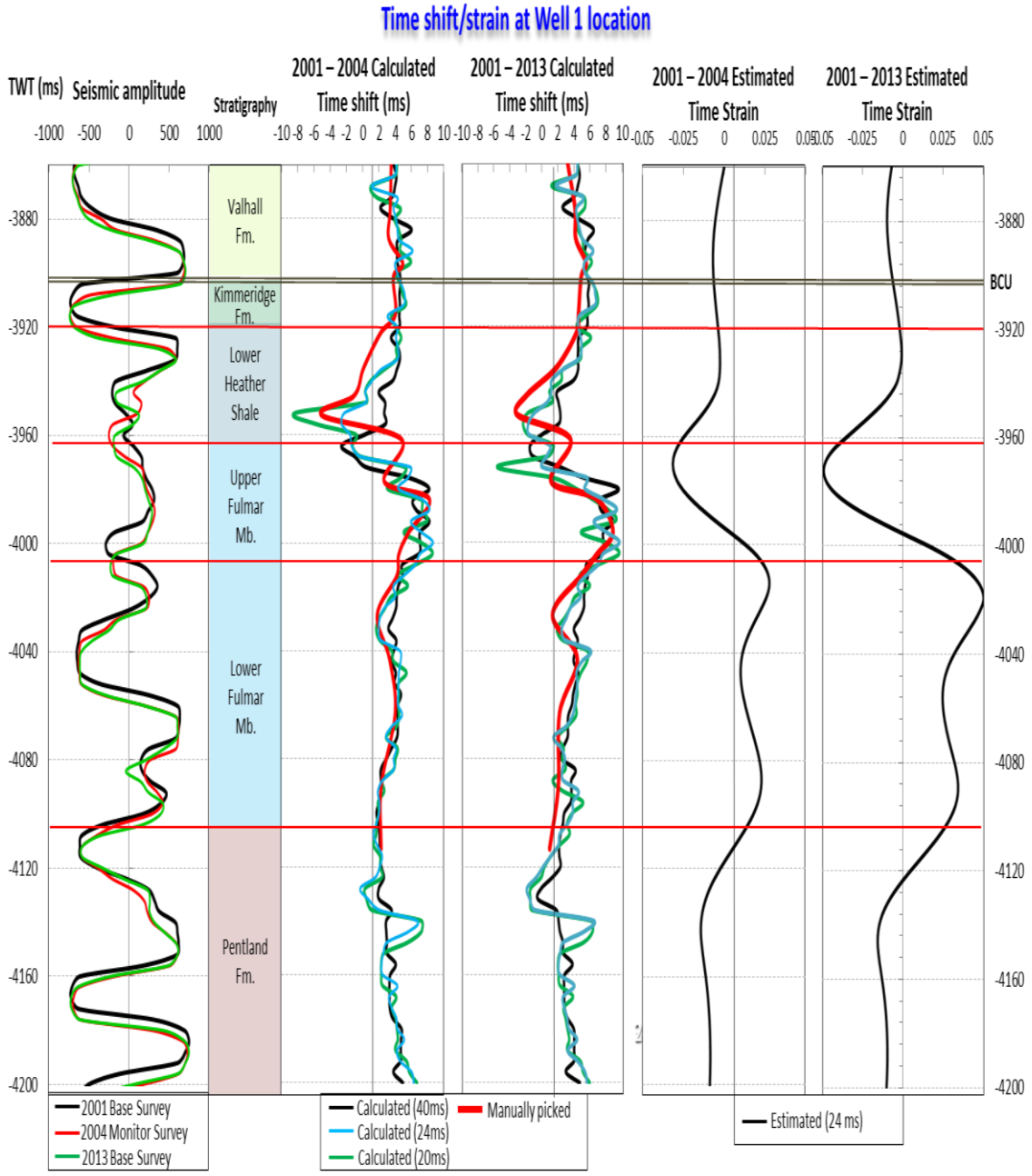

Figure 6-15 *Time shifts and time strain observed at the Well 1 location of Shearwater Field time lapse seismic, the image shows differences between 2001-2004 (main producing period) and 200-2013 (overall response). Time shift estimation was computed for several search windows, with the best fit (when compared to the manually picked, bold red line) at a 24 milliseconds window.*

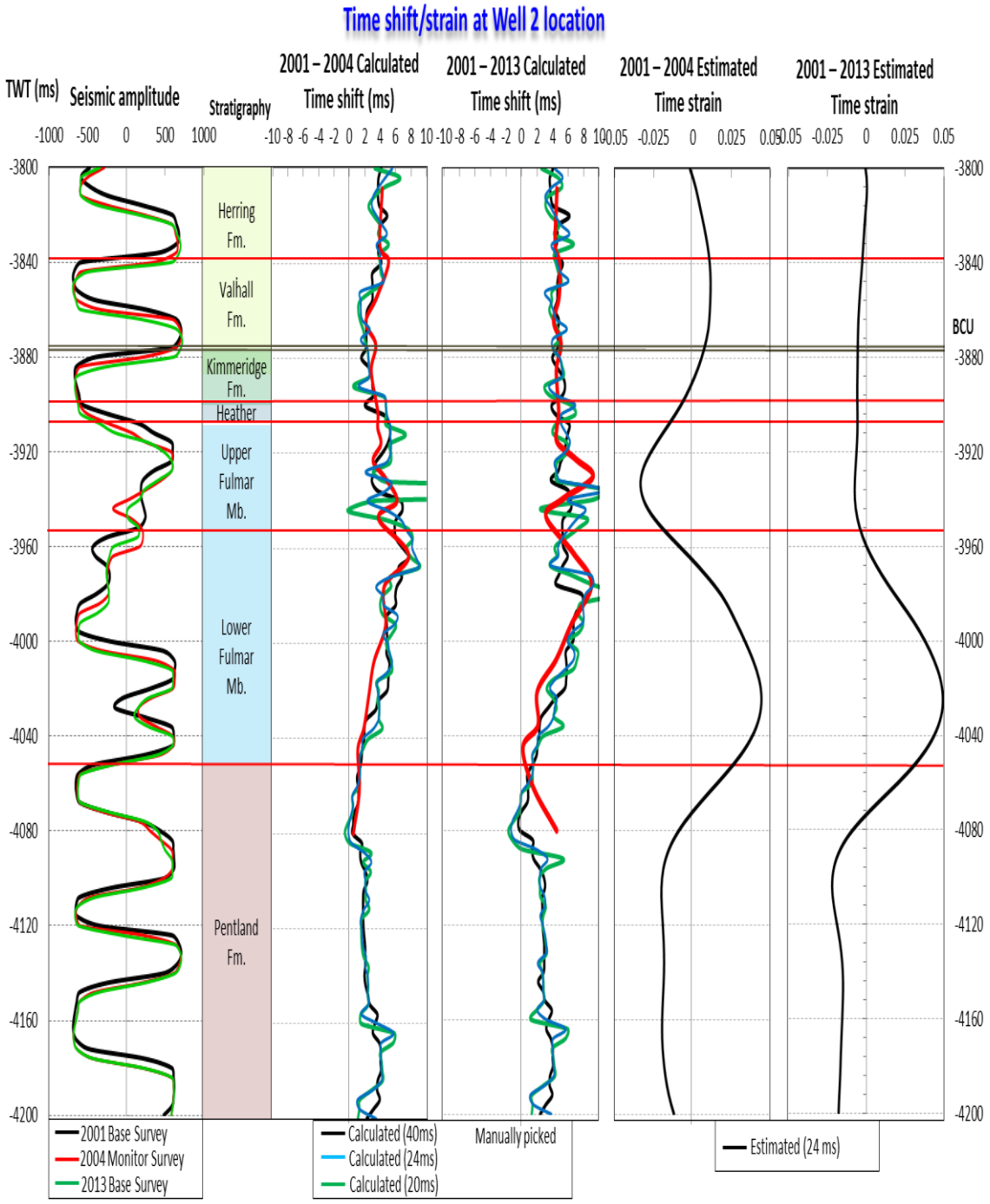

Figure 6-16 *Time shifts and time strain observed at the well 2 location of Shearwater Field time lapse seismic, the image shows differences between 2001-2004 (main producing period) and 2001-2013 (overall response).*

As the time shift is a cumulative measurement, it shows changes in signal polarity that are not necessarily located where changes in expansion/compaction occur, so the physical interpretation of the geomechanical processes occurring is based on the time strain. The observed strain behaviour in the overburden (Figures 6-15 and 6-16) suggests that the

response of the overlying shales is not uniform along the field, for instance, in Well 2, the strain behaviour indicates expansion in the overburden from the period 2001 to 2004, while the 2001 to 2013 response suggests compaction in the shales occurring after 2004, when most production stopped. Well 1 observed time strain shows only expansion in the overburden shales from the 2004 and 2013 studied periods, possibly due to stratigraphic changes in the overburden and other geomechanical parameters related to rock and wellbore stability. To study and validate these scenarios, in the next section, I explore a number of geomechanical models that replicate some of those conditions, and compare the predicted strain to the observed one, in order to validate the role of the overburden shales and pressure diffusion through them in the time lapse behaviour of the Shearwater Field.

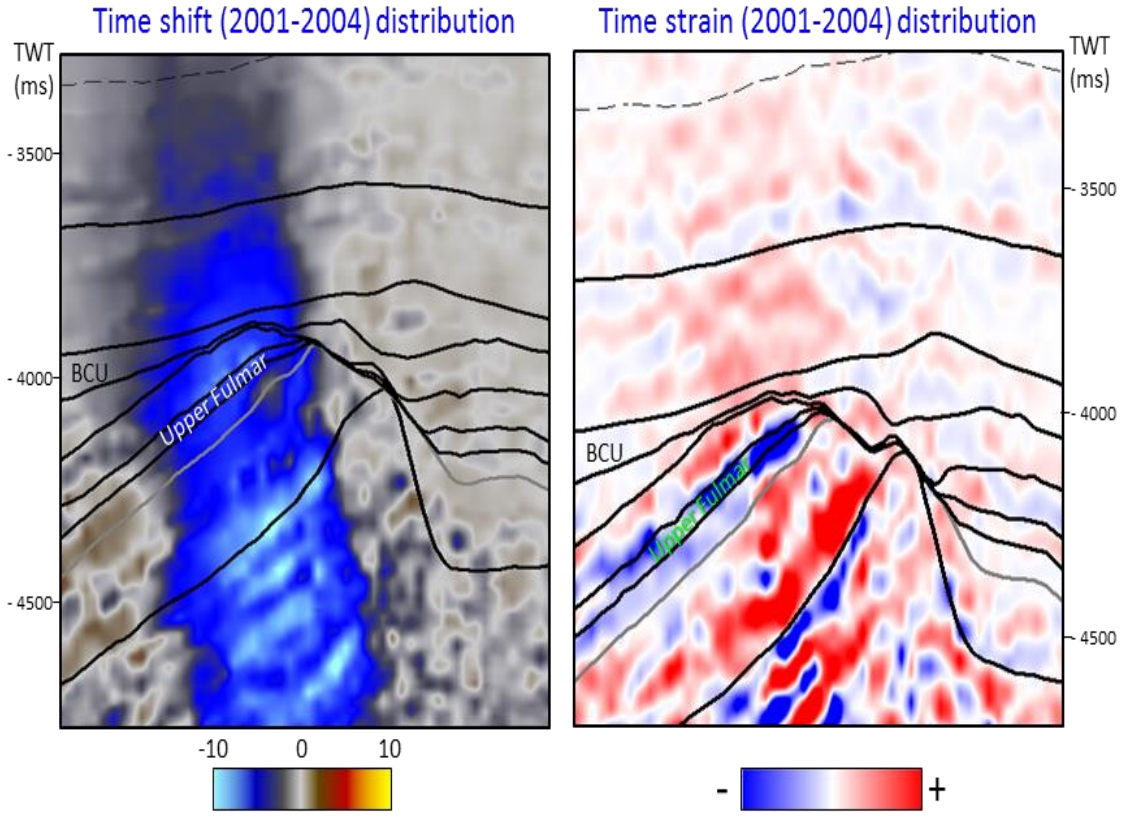

Figure 6-17 *Time shift and time strain distribution of the Shearwater Field, X-line views.*

6.8 Geomechanical modelling

The geomechanical modelling of the Shearwater Field is performed using the Visage Module of Petrel. The first step is to create a new grid for the geomechanical model: to do this, a number of zones and layers (see Table 6-5) are created in the overburden, underburden and sideburden (Figure 6-18), in order to satisfy the minimum geometry needed to have a consistent stress field and compute strain variations. As model and cell geometry requirements of the software are quite demanding, surfaces used for the zones and layering definition were smoothed, faults were removed and replaced by multipliers with null (0) transmissivity. Once the geometry of the model is defined, the next step is to create a material library (Table 6-6), which in this case was taken from previous studies in the field [*De Gennaro et al.*, 2010], which is used to populate the elastic parameters of each zone and layers, using wireline log data (density and velocity) to discriminate low and high bound values for each interval.

UNIT	Layers
Overburden	5
Sele	5
Tor	5
Hod	5
Early Cretaceous – base Chalk	5
Kimmeridge – Upper Jurassic	10
Upper Heather Shale	5
Heather Sand	2
Lower Heather Shale	7
Upper Fulmar	16
Lower Fulmar	10
Pentland	1
Triassic	1
Underburden	15

Table 6-5 *Zones and layers defined for the Geomechanical modelling.*

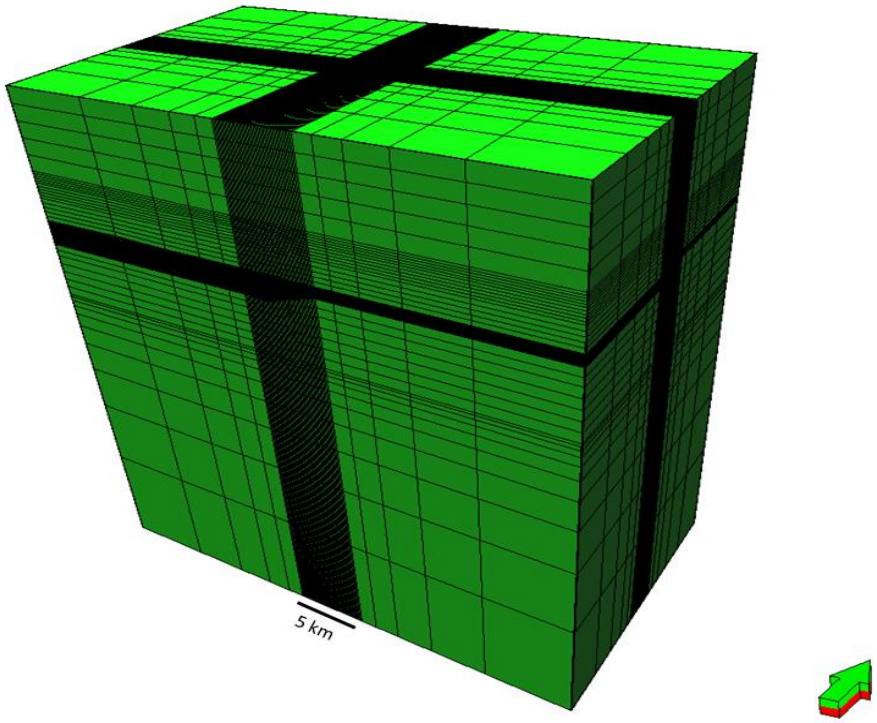

Figure 6-18 *Shearwater Field Geomechanical Model grid geometry.*

With the boundary conditions defined, the model stress field was established under an extensional regime [*De Gennaro et al.,* 2010], with the maximum horizontal stress direction at NW50^{o} (approximately Inline direction) and a vertical stress inclination of 90°. Predicted pressure and saturation from numerical simulations of the 2001, 2004 and 2013 time steps from the simulated scenarios were used as inputs to the geomechanical simulations, to estimate the strain response to production in the Shearwater Field.

	Young-Low GPa	Young-High GPa	Poisson-Low	Poisson-High
Overburden	3	7	0.25	0.40
Sele	3	22.7	0.25	0.30
Tor	26.4	53.3	0.25	0.25
Hod	11.5	42.6	0.25	0.28
Kimmeridge	3	12	0.25	0.25
Heather	2	18	0.25	0.27
Upper Fulmar	7	8	0.16	0.16
Lower Fulmar	15	16	0.25	0.25
Pentland	18.9	18.9	0.15	0.15
Triassic	22	22	0.25	0.25

Table 6-6 *Material library used to populate the elastic properties of the layers and units of the Shearwater geomechanical model; values taken from published literature [De Gennaro et al., 2010].*

6.9 Time strain results and interpretation

In order to compare the predicted strain results with the observed time strain, I convert strain to time strain using an approximation based on the R factor [*Hatchell and Bourne*, 2005]. This technique considers that the time strain can be defined as the multiplication of the strain by a variable number (equation 6.1). In empirical correlations the most used R factors correspond to 2 for reservoir intervals and 5 for overburden and underburden, but in some cases the match between predicted strain and observed time strain can only be achieved with large R factors (above 20). In this study I used conservative R factors (Table 6-7).

$$\varepsilon_{zz} = \frac{\Delta t}{t} * \frac{1}{(1+R)} \qquad \text{(where } \varepsilon_{zz} \text{ is the vertical strain)} \qquad (6.1)$$

	R factor
Overburden	5
Sele	5
Tor	5
Hod	5
Kimmeridge	5
Heather	5
Upper Fulmar	2
Lower Fulmar	2
Pentland	5
Triassic	5

Table 6-7 *R factors used for strain to time strain conversion*

Figure 6-19 shows, in a section along the production wells, the predicted time strain results for the 2004 time step of the models corresponding to inactive shale, active shale estimated properties, active shale with fractures (enhanced permeability around the wellbore), active shale high permeability scenarios and observed time strain between the 2004 and 2001 seismic surveys.

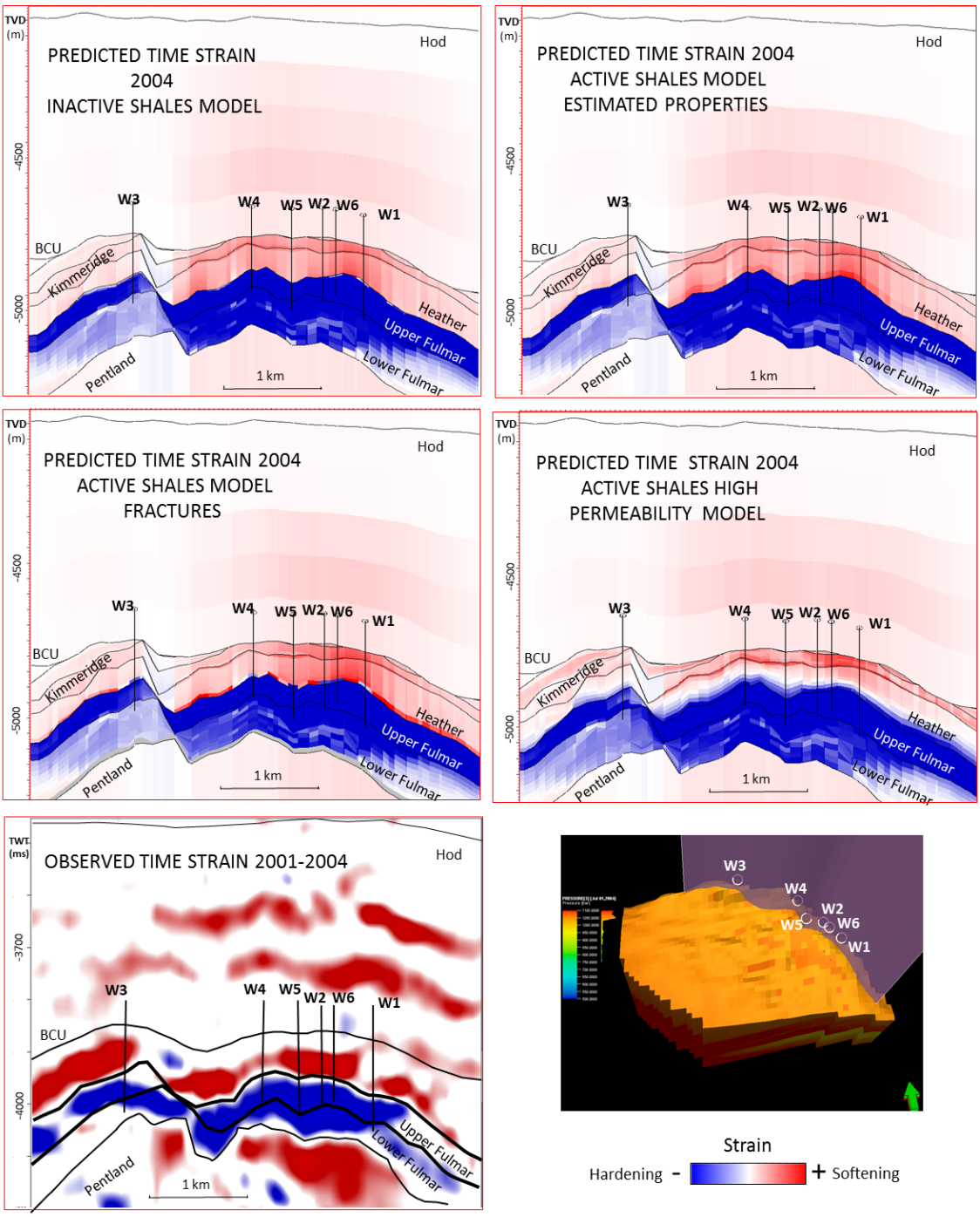

Figure 6-19 *Sections along the wells showing predicted and observed time strain for 2004 (after 3 years of production) in the Shearwater field for the modelled scenarios.*

The observed time strain between the 2001 and 2004 period (Figure 6-19, lower left picture) shows compaction in the reservoir, with stronger hardening signal above the condensate-water contact (mostly distributed in the Upper Fulmar Member). The softening signal linked to extension is observed in the Pentland Formation in the underburden and in the immediate overburden corresponding to the Heather Formation interval. The spatial distribution of the softening in the overburden is restricted to bands and appears to follow the bedding of the stratigraphy, suggesting that some lithological

intervals are more sensitive to the effects of the reservoir compaction. The predicted strain for the inactive shale model (Figure 6-19, top left picture) shows a good fit for the hardening signal corresponding to the reservoir compaction: however, the intensity of the signal linked to the overburden extension is very low when compared to the observed data. The propagation of the softening signal in the overburden for the 2001-2004 period extends further towards the top of the Hod Formation for the inactive shale model, suggesting that in the absence of overburden shale pressure diffusion, the compensation of the reservoir compaction takes place over a thicker section of the overburden.

The results for the estimated properties (Figure 6-19, top right picture) and fracture models (Figure 6-19, middle left picture) show a better match with the observed data (particularly the fractures model), capturing the extension and intensity of the softening signal in the overburden, especially in the immediate overburden interval, where the signature of extension is stronger. The hardening signal corresponding to the compaction inside the reservoir (mostly Upper Fulmar Member) is also represented in these two models.

The high permeability active shale model (Figure 6-19, middle right picture) shows an extended propagation of the hardening/compaction signal over the top of the Fulmar Formation into the lower Heather Formation, and the immediate overburden softening signal related to the extension is displaced to the base of the Kimmeridge Clay Formation. In addition, the predicted results of this model show connectivity through the faults between the hardening signals of the reservoir in the different blocks of the reservoir. As most of these features are not present in the observed time strain, the high permeability model has the lowest fit with the observed data at reservoir scale. Neither inactive nor active shale models could replicate the observed softening signal related to the extension in the underburden Pentland Formation.

In the observed 2013 time strain (Figure 6-20, lower left picture) it is obvious that the compaction is the dominant geomechanical process, with the propagation of the hardening signal within the entire Fulmar Formation (Upper and Lower members). After the initial expansion in the overburden, the rearrangement of the effective stress leads to decrease in the overall overburden softening signal, and then subsequent compaction of the immediate overburden; this is shown in the observed time strain, with the hardening signal extending over the top of the Fulmar Formation and into the lower Heather Formation, particularly in the area adjacent to the producers W4, W2, W5 and W6. The softening signal observed in the overburden adjacent to the producer W3, may be related

to still active extensional processes within the overburden shales, as a consequence of W3-induced depletion, as this was the latest well to fail and remained producing until the end of 2007.

The inactive shale (Figure 6-20, upper left picture) and estimated properties of active shale (Figure 6-20, upper right picture) showed a decrease in the overburden extension for the predicted 2013 strain and the propagation of the hardening signal within the Fulmar reservoir, but no signs of compaction at the base of the Heather Formation.

The active shale model with the inclusion of enhanced permeability associated with wellbore fractures (Figure 6-20, middle left picture) shows a similar compaction response within the reservoir, but also shows compaction at the Lower Shale from the Heather Formation and some softening in the immediate overburden in the vicinity of the W3, presenting the best fit with the observed data from all the modelled scenarios.

For the active shales high permeability model (Figure 6-20, middle right picture), the propagation of the compaction signal towards the overburden reaches the base of the Kimmeridge Clay Formation. This reduces the amount of compaction transmitted downwards to the Lower Fulmar Member, a clear mismatch between this modelled scenario and the observed seismic data. Similarly to the predicted results for 2004, in the 2013 data, the observed softening signal linked to extension in the Pentland Formation was not replicated in any modelled geomechanical scenario.

Analysing the response of the predicted scenarios and the observed time strain in vertical profiles, at the Well 1 and 2 locations (Figures 6-21, 6-22, 6-23 and 6-24), the first noticeable observation is the excellent correspondence between the predicted pressure depletion profile at the well location and the observed time strain, and it is also obvious that the predicted results for vertical time strain in active shale models show a better match with the observed time strain, in terms of the hardening, softening distribution and the time strain magnitude, when compared with the observed data.

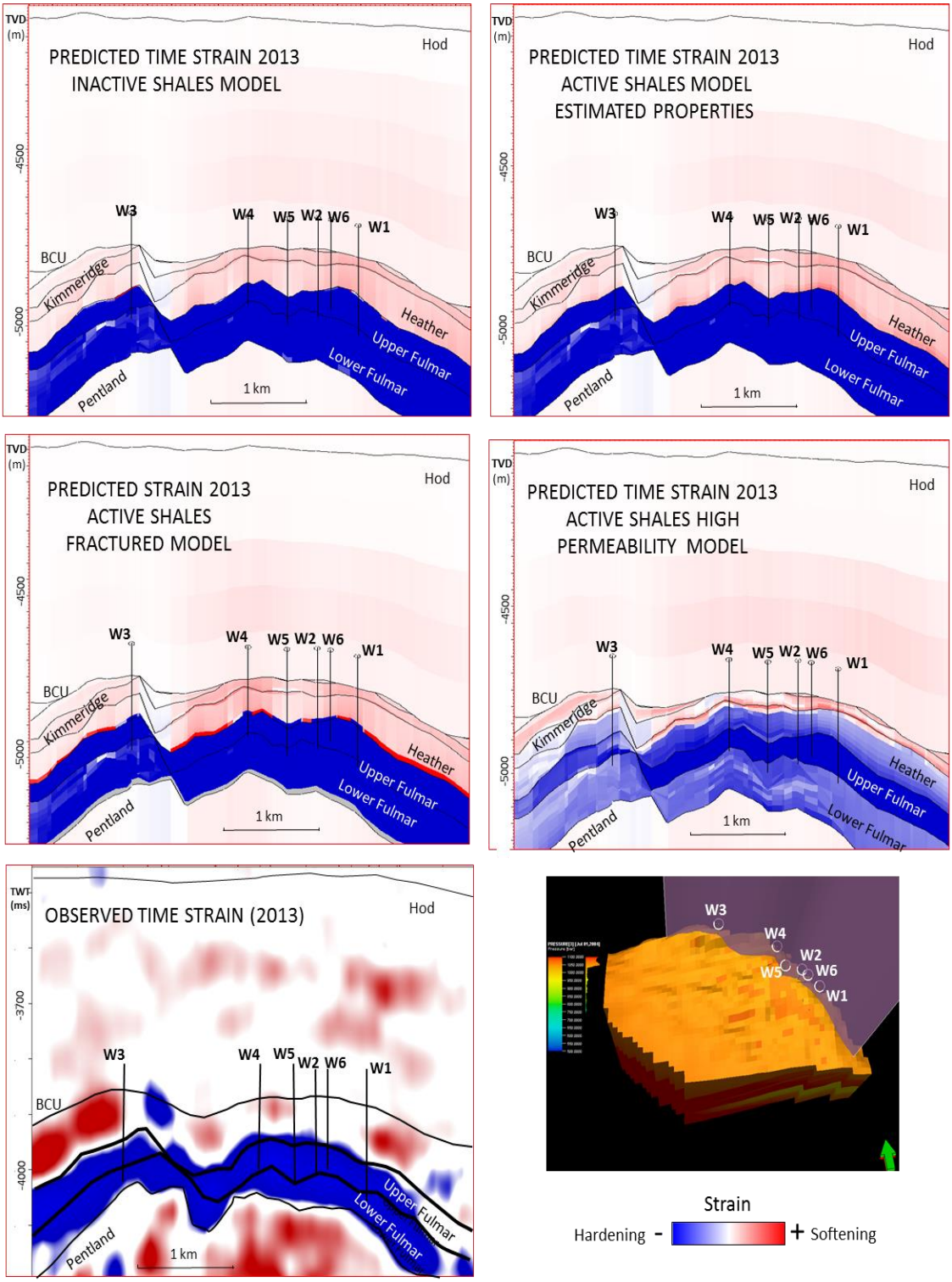

Figure 6-0-20 *Sections along the wells showing predicted and observed time strain for 2013 in the Shearwater field for the modelled scenarios.*

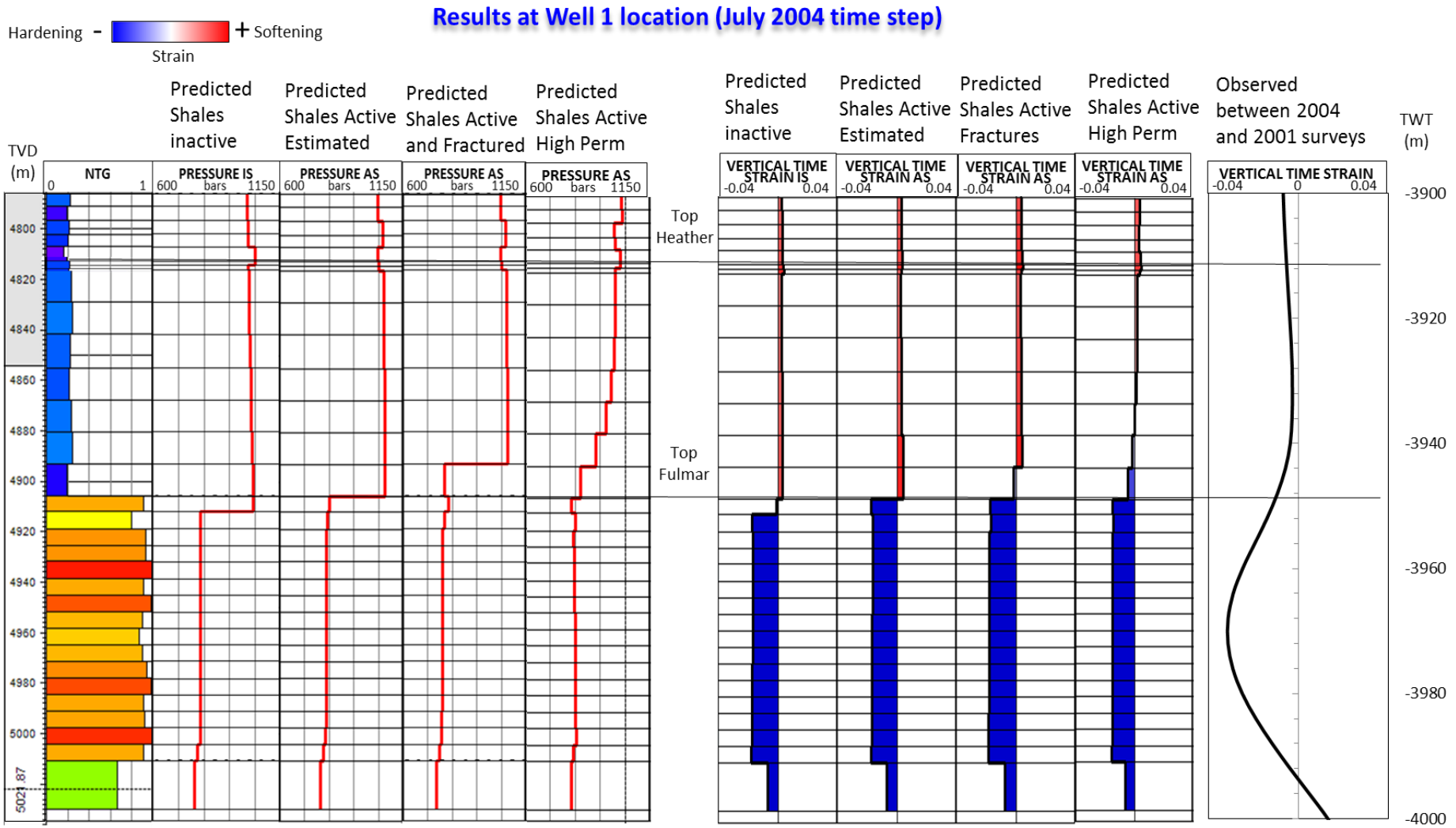

Figure 6-0-21 *Predicted pressure diffusion and time strain at the well 1 location for the July 2004 time step, for the modelled scenarios and observed seismic data*

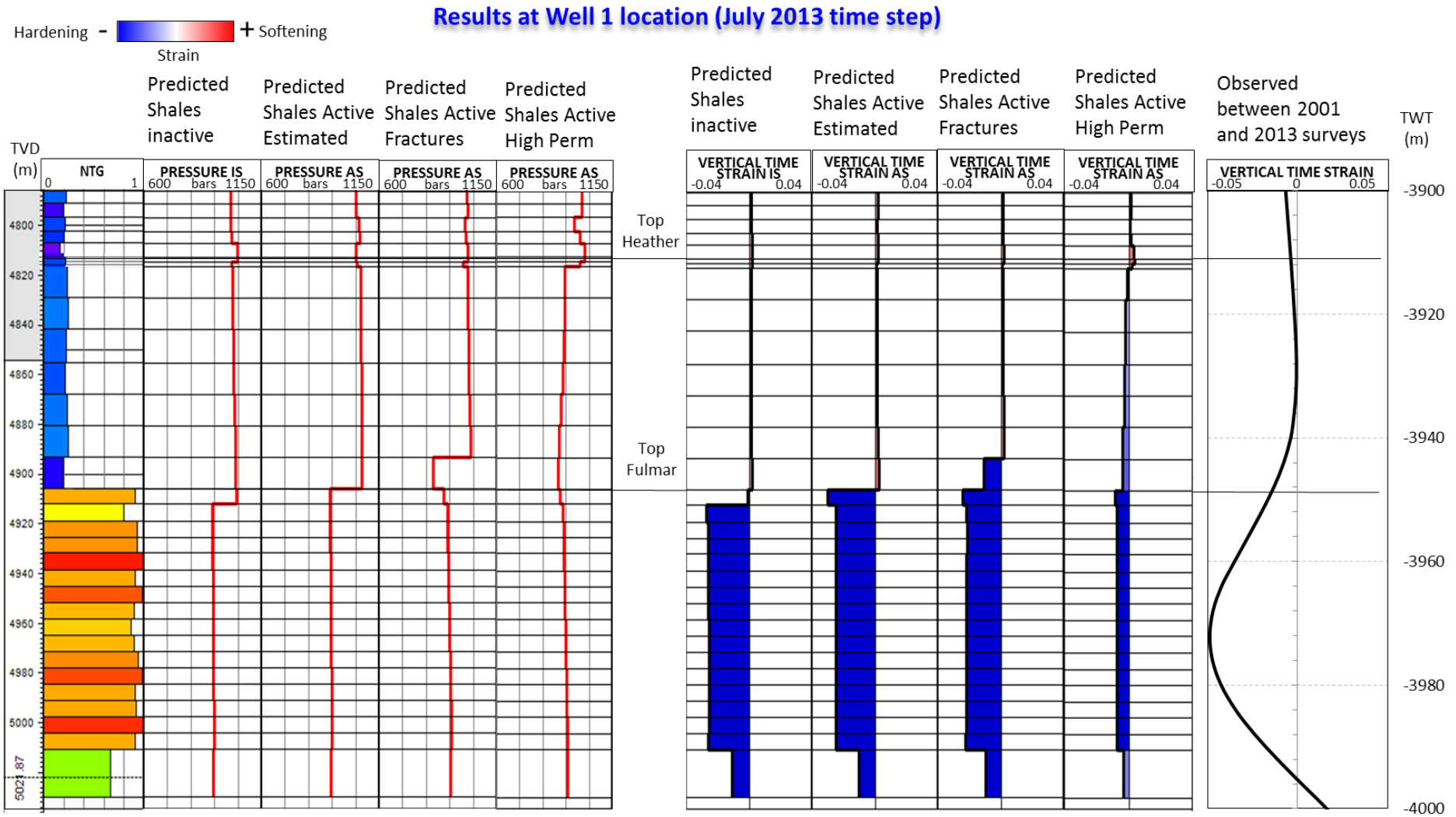

Figure 6-0-22 *Predicted pressure diffusion and time strain at the well 1 location for the July 2013 time step, for the modelled scenarios and observed seismic data*

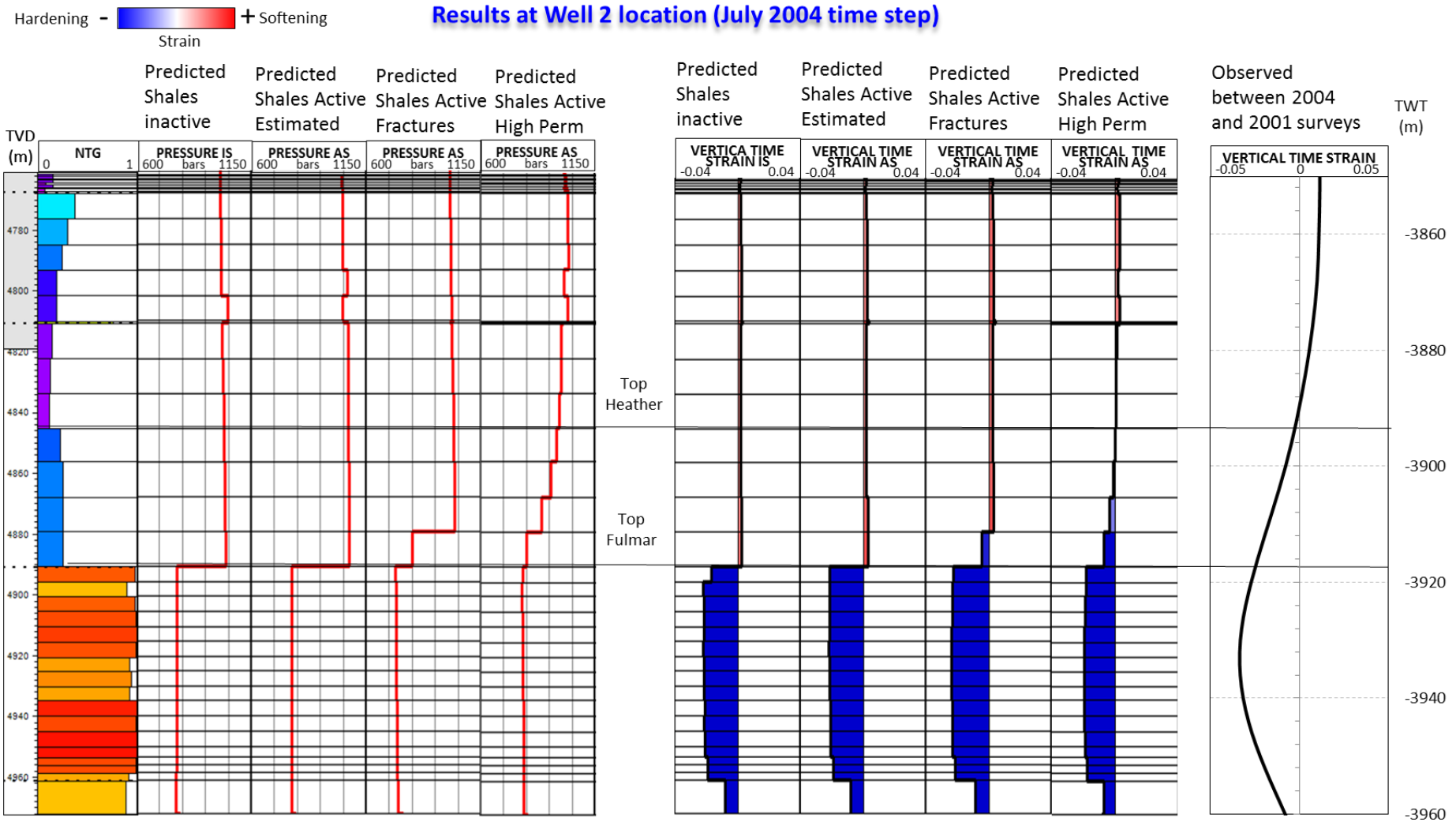

Figure 6-0-23 *Predicted pressure diffusion and time strain at the Well 2 location for the July 2004 time step, for the modelled scenarios and observed data*

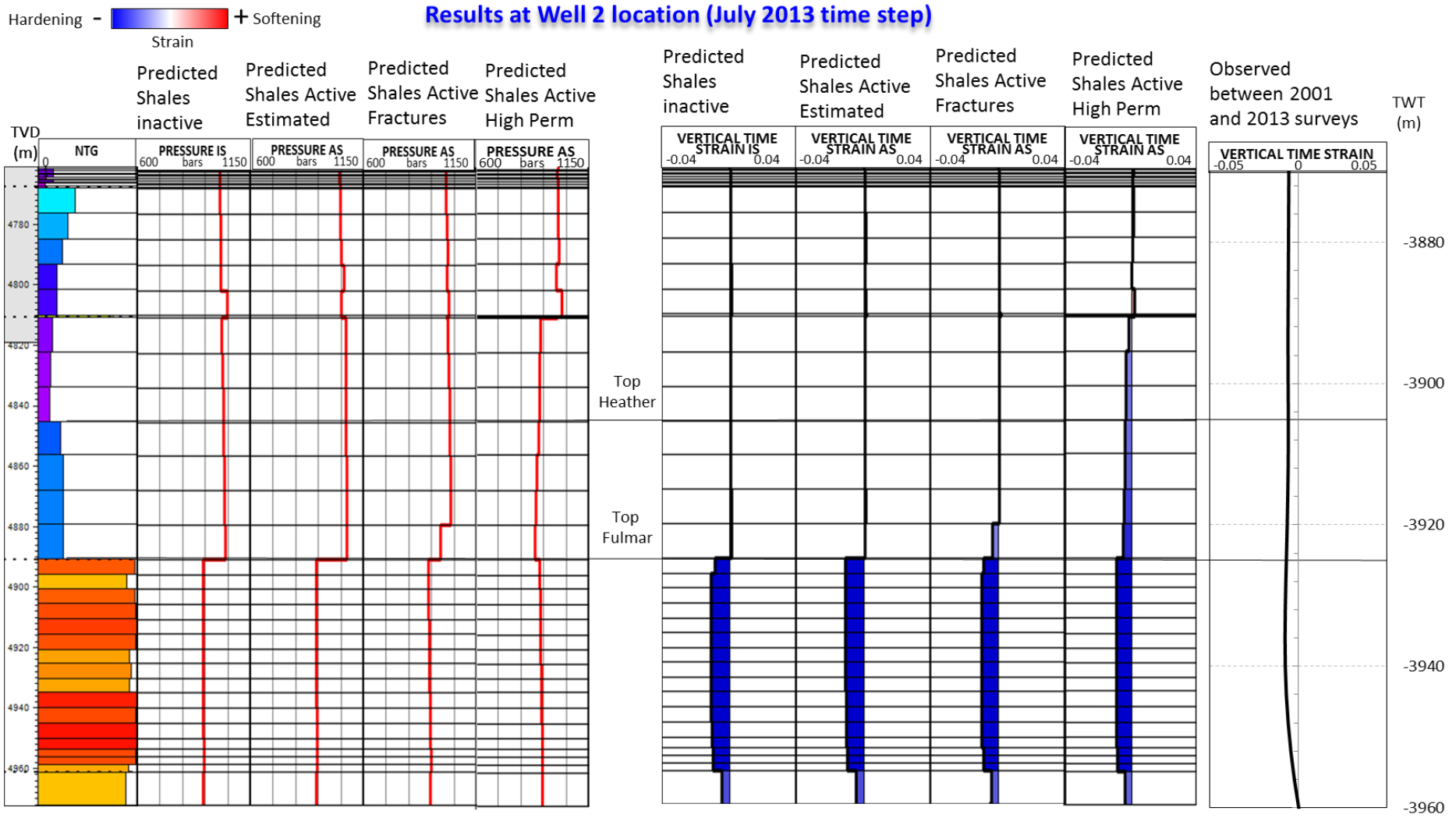

Figure 6-0-24 *Predicted pressure diffusion and time strain at the well 2 location for the July 2013 time step, for the modelled scenarios and the observed seismic data*

The results for Well 1 for the 2004 time step (Figure 6-21) show a strong correlation between the observed strain and the predicted shale pressure diffusion into the base of Heather Formation for the active shales with fractures in the wellbore and high permeability scenarios. The polarity of the observed strain indicates compaction in the immediate overburden layers (assuming that by the time of the 2004 monitor acquisition the initial shale expansion had already evolved to the compaction stage). Moreover, the predicted strain for larger shale permeability scenarios shows a better fit with the observed strain profile, which shows less compaction at the top of the Upper Fulmar Member, opposite to the strain behaviour of the inactive shale and active shale with estimated properties models, where the compaction at the top of the reservoir is equal to or even higher than the rest of the predicted Upper Fulmar Member compaction. The observed time strain for the 2013 time step at Well 1 (Figure 6-22) shows few changes for this stage, only an increase in the compaction within the Fulmar Formation (compared to the 2004 response), but without propagation towards the overburden, patterns that have a good fit with the predicted time strain for the model with shales active and fractures (even when the pressure profile does not match). The high permeability scenario for this stage shows a large mismatch, suggesting that pressure diffusion into the Heather Formation shales is restricted to the basal interval at this well location.

For Well 2, the predicted results for the model with shales activated with a high permeability show an excellent fit to the observed time strain data, for the 2004 (Figure 6-23) and 2013 (Figure 6-24) time strain predictions. This indicates that at Well 2 location, the extension of pressure diffusion into shales propagates even within the Kimmeridge Clay Formation, leading to higher compaction in the overburden shales, which agrees with the negative (hardening) time strain observed in the seismic data. The predicted strain for the active shale model with fractures for the 2004 time step shows a relatively good match with the observed data, but the 2013 prediction for this model shows little propagation of the compaction towards the overburden. The inactive shale and active shale estimation models show large mismatches with the observed data for the 2004 and 2013 periods, as the two predicted strains present extension for the immediate layers of the Heather Formation. Even though Figures 6-19 and 6-20 show how the best spatial distribution match with the time strain observed data is achieved for the shale active model with fractures (indeed, the high permeability model shows the worst fit with the seismic signature), the results for Well 2 suggest that, in specific areas (well location for example), the time strain signal behaviour can be explained only by assuming large

pressure diffusion towards the shaly overburden, through preferential permeability paths. These permeability paths may have a much higher fracture density than the model of enhanced borehole permeability, (see Table 6-4), allowing almost complete pressure equilibrium between the depleted reservoir and the shales of the overburden. Company reports for Well 2 describe an early geomechanical failure, evidencing a very active and dynamic reaction of the immediate overburden to the induced compaction and depletion of the Fulmar Formation reservoir, which may be related to the damage caused in the shales during the difficult process of drilling in this HP/HT reservoir, as a consequence of the complex pressure profile of the area and tough wellbore conditions. With the proven validity of the well location high permeability shale scenario, the reported depletion within the Heather Sand can also be explained, without this unit being completed for production in any well of the field. In any case, in general, the best fit for time strain prediction at any scale is achieved when shales are active, with conservative values for permeability, but with fractures enhancing the permeability around the wellbore.

6.10 Conclusions

The integrated analysis of the time strain signature at reservoir and well location scales, shows strong evidence that pressure diffusion into shales of the overburden (Heather and Kimmeridge Clay Formations) is an active process in the Shearwater Field, affecting the geomechanical behaviour of the reservoir and influencing the 4D seismic response and its interpretation. The irregular distribution of softening and hardening in the overburden, related to geomechanical processes, may be explained by the occurrence of shale pressure diffusion and its effects on the shale strain path, creating different elastic signatures (extension or compaction) in the observed 4D seismic responses recorded, depending on the monitor acquisition time-line and the stage of the effective stress rearrangement within shales and the reservoir. The occurrence and interpretation of these signals in the overburden may have important implications for future drilling activity, as pressure anomalies may be related to them.

The match achieved between the observed time strain and the predicted one for the active shale models with fractures, across different stages of the Shearwater Field lifetime, shows the influence of the drilling activity, as generated fractures enhance shale permeability around the wellbore, even to values similar to those of sands, which in turn

affects the pressure diffusion. In general terms, the observed and predicted time strain behaviour indicates that the pressure diffusion product of the sand-shale interface pressure interaction penetrates only the basal intervals of the Heather Formation, but the connection through fractures can be an important factor in the well vicinity and can cause depletion even into the Kimmeridge Clay Formation. The variable stratigraphic distribution of the overburden shale units in the Shearwater Field also contributes to generate extra anisotropy, which in some areas may enhance the connectivity between the reservoir and the overburden. Reservoir seal integrity evaluation analysis is beyond the scope of this case study, but I consider that high permeability scenarios linked to fractures may involve fluid flow interaction between the reservoir and the overburden units, especially considering the gas condensate mobility and the very high pressure gradients.

7 Chapter:

Conclusions and recommendations

This chapter summarises the findings of my studies on shale inclusion in reservoir simulation and 4D seismic, highlighting parameters such as reservoir architecture and connectivity, sand – shale geometry, permeability, pressure imbalance and timing influencing the contribution of shale pressure diffusion in the dynamic response and 4D seismic signature of each reservoir. I also discuss the applicability and generalisation of the developed workflow for the evaluation of shale pressure diffusion across different reservoirs and production scenarios. Finally, I present recommendations suggesting potential for future research related to this topic, based on the challenges encountered in this work and extension of increasingly complex aspects of the shale pressure diffusion process in conventional reservoirs and its impact on the 4D seismic interpretation.

7.1 Summary and general conclusions

The conventional reservoir-related shales in most of the field applications studied in my PhD Project exhibit clear dynamic behaviour. The inclusion of these shale intervals in the reservoir numerical simulations, honouring the shale's internal architecture in the 3D and 4D seismic modelling, enhances the understanding of the reservoir's elastic behaviour (Figure 7-1). Shale activation in the reservoir numerical simulations to enable pressure diffusion requires a proper characterization of this lithology, the differentiation between types of shales, its distribution and property variations, which all provide invaluable insights into understanding better the reservoir connectivity and its implications for the distribution and polarity of the 4D seismic response and its interpretation. The magnitude of the shale pressure diffusion and its contribution to the recorded elastic changes in the reservoir is the consequence of geology, the applied production mechanism and timing.

In the Heidrun Field case, the extensive reservoir compartmentalization and a deficient injection plan favoured pressure diffusion into the intra and inter-reservoir shales (Not Formation and Ile Shale Member). As result, pressure equilibrium was reached with the reservoir in the predicted scenarios after 9 years, for the thinner shales. Predicted scenarios with active shale showed a better fit to observed 4D seismic data (55.46% of match, 3.71% higher than inactive shale model), particularly in the hardening distribution, while the softening distribution showed small differences (0.05%) between active and inactive model. Also, in some particular blocks, the vertical connectivity through the shales between upper and lower sand bodies (Garn and Ile formations) resulted in no elastic changes related to pressure in the synthetic seismic volumes, a response that matches the observed 4D seismic data for the Heidrun Field area. In this dataset, predicted models without shales active show hardening in the synthetic 4D seismic response during the pressure depletion stage of the reservoir and softening in the build-up period, but these seismic signatures are absent in the observed 4D seismic data. With respect to volumetric predictions, shale pressure diffusion reduces the overall pressure imbalance between the Garn and Ile formations' sand reservoirs. As a result, the predicted scenarios with shale active show a better fit to the historical production data, especially in terms of gas volumes, because lower pressure compartmentalization reduces the process of gas exsolution in the oil column.

In the study of the Girassol Field, the large dimensions of the reservoir and the high connectivity between the coalescent turbidite sand channels, as a consequence of the

converging turbidite flows, does not favour significant pressure imbalance and diffusion towards the external shales. As shown in Chapter 4, the extension and magnitude of shale pressure diffusion is small and its elastic implications negligible, hence the predicted 4D seismic signal for active and inactive models shows very few differences when compared to the observed 4D seismic data. However, the predicted 4D seismic data showed a better (0.56% higher) fit to the observed 4D, probably due to the improved elastic modelling due to shale characterization. Both, active and inactive models showed low match with the 4D observed data, evidencing failures in the modelling of the reservoir connectivity and dynamic performance in the simulation model. The period of analysis that was covered by the available data was short, and time is a paramount parameter to evaluate shale pressure diffusion, as this is a quite slow process. Even when the simulation model was extended to more realistic periods where pressure diffusion in shales could be measurable, the predicted elastic changes were again very low, with only small and isolated sections of the reservoir showing differences related to shale activation and gas exsolution, a scenario which in this instance cannot be validated, due to lack of observed data. However, the unconsolidated conditions of the Girassol Field sands, does suggest that shales may have a more active role in the elastic behaviour of the reservoir in a more mature production stage of the field, as sand-induced compaction may trigger geomechanical effects in the shales (initial expansion and permeability improvement), which, in turn, may favour the process of pressure diffusion. In any case, the static characterization of shales in the Girassol Field, including the modelling of the pronounced effect that shale composition and its compaction trend have in the impedance contrast of the reservoir, show the importance of including shale in the synthetic seismic modelling, as the imaging of the amplitude contrast and the right placement of the seismic events was better captured when shales were included.

In the Schiehallion Field, shale activation improves clearly the model's fit to the 4D seismic data, predicted models with shales active have up to 5.8% better match with the observed data compared with the inactive shale models. Active shale models showed reduction in the hardening distribution match, but enhances considerably the distribution of the softening distribution, improving the understanding of the reservoir connectivity and reducing the dependence on transmissivity multipliers inserted into the simulation model. The specific pressure conditions of the reservoir, the compartmentalization caused by the presence of cemented intervals within the sand geobodies, and the geometric relationships between the shale and the reservoir, suggest that shale pressure diffusion

has a strong impact and is immediately visible via the process of gas exsolution. The distribution of the softening signal associated with the drop in pressure and subsequent gas exsolution in the levee and overbank facies of the turbidite complex is only explainable through the effects of pressure diffusion and connectivity through shales. The predicted oil, gas and water volumes for the modelled scenarios with shales active and without transmissitivy multipliers in the Schiehallion Field, Segment 1, showed a much better match with the history matched production data, evidencing that pressure connectivity through shales in this reservoir plays a very important role in the saturation distribution and its dynamic evolution under the production mechanisms applied in the reservoir.

In the first three case studies, the elastic implications of the shale pressure diffusion did not have any direct 4D seismic signature within the seismic interval corresponding to the shale itself. In the case of the homogeneously distributed shales of the Heidrun Field (layer cake architecture), the amplitude expression of the shale layers in the seismic was imprinted by the upper and lower sand reservoir static and dynamic elastic signature, whereas in the heterogeneously distributed shales of the turbidite reservoirs in Girassol and Schiehallion Fields, almost imperceptible changes within shale interval seismic expression were recorded by the 4D. Therefore the elastic changes were not recorded inside the shale, but instead within the reservoir, as the shale pressure diffusion changes the reservoir connectivity, in turn affecting the distribution of the reservoir saturation and pressure. If the sensitivity of the reservoir to minor changes of pressure is high (for example, the reservoir pressure being very close to the oil bubble point), the effect of shale pressure diffusion can cause considerable effects in the saturation and the distribution of the 4D seismic signature. The Schiehallion Field was particularly sensitive to the effect of pressure connectivity through shale. These findings were communicated to the operator's asset team in technical meetings and are currently being taken into account for the latest update of the simulation model of the reservoir.

With a clear difference from previous cases, in the Shearwater Field application, the 4D seismic signal records significant elastic changes within the seismic intervals corresponding to shale (overburden Heather and Kimmeridge Clay formations). The observed 4D time-shift signal, which in terms of time strain implies softening and expansion in the early stages of production and hardening and compaction after the mechanical failure of the wells and the ceasing of production, can be explained by the coupled effect of shale pressure diffusion (due to the Fulmar Formation reservoir induced

depletion) and the shale's geomechanical response to the effective stress variation as a consequence of the reservoir compaction and the shale strain path evolution (Figure 1-3) that goes from an initial expansion to a subsequent compaction. The results from the coupled pressure and saturation numerical simulation, with the geomechanical analysis considering overburden shales of the Shearwater Field as active, proved the validity of the modelled shale permeability scenarios, because the fit between the predicted strain from geomechanical modelling and the estimated time strain from the observed seismic data was better for active shale scenarios. The strain response analysis performed at well locations showed a better match between the observed seismic data and predicted models where high shale permeability values around the well location were modelled to represent drilling induced fractures, revealing the existence of preferential pressure diffusion paths and higher mechanical response to the reservoir compaction in the vicinity of the wellbore as a consequence of the formation damage caused to shales during drilling. Certainly, the failure due to geomechanical effects of every single production well in the field shows the dynamism in the stress field around the wellbore as consequence of very active shales.

In general, the developed workflow (Figure 7-1) improves the capacity of the 3D and the 4D seismic modelling and interpretation of conventional reservoirs. Shale's properties, its architecture, elastic response and interaction with the reservoir units are so variable that regarding them as inactive and homogeneous may be practical but far from accurate. The quantitative applications of 4D seismic using predicted synthetic seismic volumes only can be reliable if the elastic contrast within the reservoir and with the surrounding intervals is captured and represented properly, which is impossible if the shale static, dynamic and elastic properties are not correctly modelled. Although it is true that, computationally, the expansion in numbers of active cells in the simulation model may be difficult or increase the cost of performing multi-realisation analysis of history matched workflows (which is currently a very popular application of 4D seismic), the inclusion of shale analysis in the seismic modelling definitely enhances the quality of the outcomes. Of course, this inclusion may raise the engineering debate about scales and reasonable assumptions and simplifications in the models, but when the mismatch of the modelled scenarios with the observed data cannot be reduced, even with the overuse of engineering wildcards such as multipliers, it is worth trying with a more detailed representation of the geology in the model.

From the study of these datasets, it is clear that the role of shales as an active part of the reservoir and its sizeable effect on 4D seismic during production lifetime is going to vary

from one geological setting to another and with reservoir sensitivity to changes in pressure (see summary at Figure 7-2). It is difficult to generalise and establish hierarchies of specific scenarios where the process of shale pressure diffusion could have a larger contribution in the dynamic elastic behaviour of a conventional reservoir, as the shale pressure diffusion is a process that seems to respond to particular assemblage of parameters in the reservoir. Certainly, shale permeability and time are the paramount parameters, as inferred from the diffusion equations, but in these case studies, the shale-reservoir relationships, including the production mechanisms used in the reservoir, proved to be almost equally important. In the next section of this chapter, I describe and discuss some of those shale-sand interactions in an attempt to create a guide to evaluate the variables that favour shale pressure diffusion in conventional reservoirs and its implications in the 4D seismic response and its interpretation, based on the results and observation of the studied datasets.

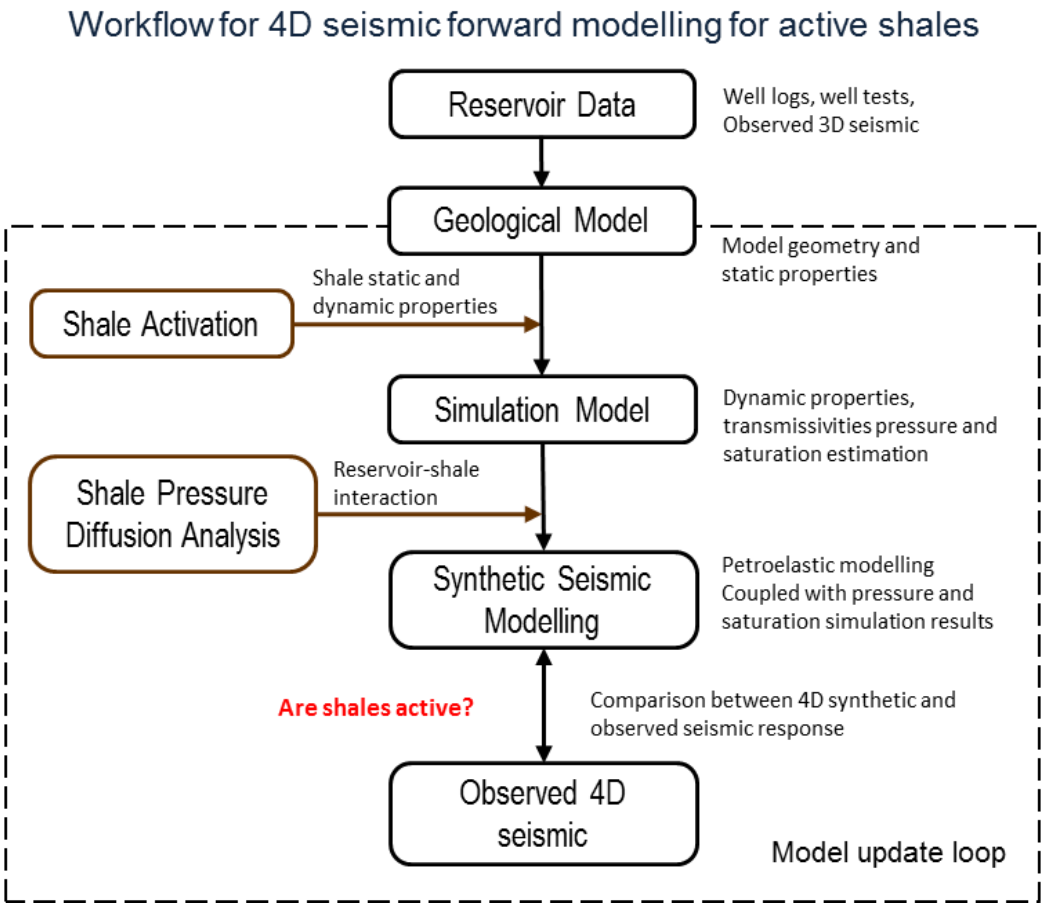

Figure 7-1 *Proposed workflow for the evaluation of the impact of shale pressure diffusion in the 4D seismic interpretation*

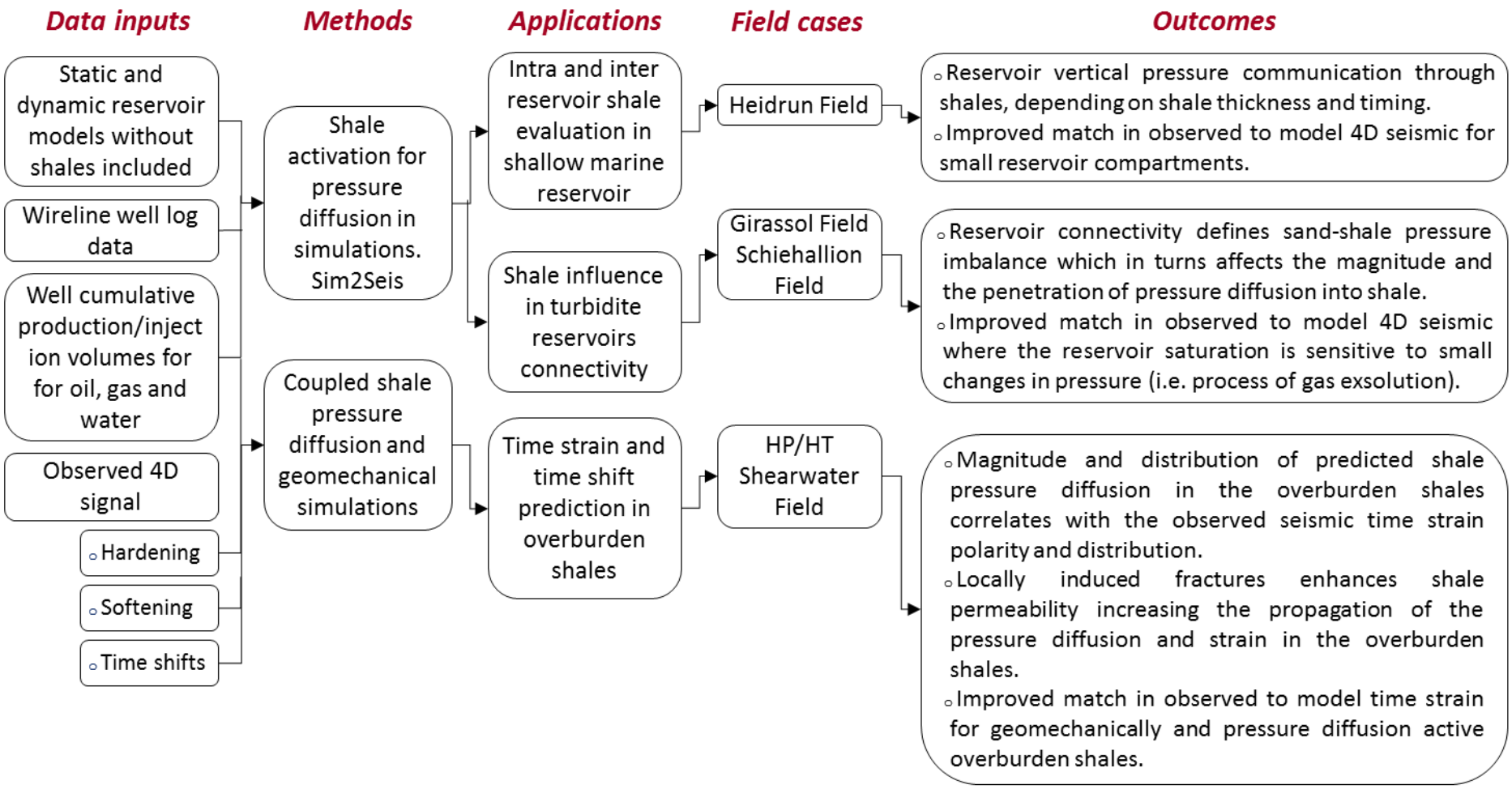

Figure 7-2 *Summary diagram showing the inputs, methods, applications and outcomes of the study cases of this work*

7.2 Parameters influencing shale pressure diffusion and its elastic response

The occurrence of measurable shale pressure diffusion and the possibility that its elastic effect could be recorded in the 4D seismic signature is the consequence of the conjunction of a series of parameters of a geological nature and the production mechanisms applied to the reservoir. According to the particular assembly of variables involved in a specific scenario, the incidence of the shale pressure diffusion could be anywhere between high and imperceptible.

7.2.1 Sand-shale pressure imbalance and reservoir connectivity

The pressure diffusion into shales depends basically on the shale-reservoir pressure imbalance (given that shales are not completely impermeable). Prior to production, shales and reservoir sands are in pressure equilibrium (unless shales were overpressured) as a consequence of the geological timescale processes such as compaction, diagenesis, hydrocarbon generation, migration and gravitational segregation of immiscible fluids. The induced depletion in the sands as a consequence of hydrocarbon production, causes pressure imbalance with the adjacent shales, depending on the reservoir connectivity, compartmentalization and the design and the effectiveness of the injection plan to maintain the reservoir pressure. If the effect of production in the pore space is compensated by injection, the pressure imbalance between shale and sand is very low and reservoir compaction will be null or negligible, and reservoir compaction is a key process for the beginning of shale pressure diffusion, as the readjustment of the stress field causes extension in the shales and improvement in the shale pore connectivity and permeability. The effectiveness of the plan to maintain pressure depends largely on the reservoir's homogeneity and connectivity, the relative mobility of the injected fluid compared to the hydrocarbons, and the balance between fluid volume extracted and fluid volume injected (at reservoir conditions). High reservoir heterogeneity, bad connectivity between injectors and producers due to lateral changes in facies or to the presence of impermeable barriers as faults, shale or cemented zones, leads to less interconnected pore space available to equilibrate the effect of depletion, causing pressure imbalance or a gradient between sands and shales.

Each field application in this thesis has particular conditions regarding the nature and the causes of the sand-shale pressure imbalance. The Heidrun Field, for instance, contains a very homogeneous sand reservoir, but the presence of intra and inter-reservoir shale intervals conditions the vertical connectivity, while the lateral connectivity is affected by the presence of two families of normal faults that results in the reservoir's tilted blocks configuration. The incomplete understanding of the complicated fault transmissivity in the field and the reservoir compartmentalization has led to the design and implementation of a top structure and down dip gas and water injection plan which was not very effective. Isolated compartments under production show much higher depletion than those connected to the injectors (Figure 3-10). Only with the interpretation of the acquired 4D seismic was the efficiency of the pressure maintenance plan improved, but even with an injection plan in place since the start of production, the pressure profile for the first 10 years of development of the Heidrun Field still showed a depletion trend (Figure 3-9). The predicted pressure results for this case study showed larger pressure diffusion in the reservoir shales located in those isolated blocks during the period when injection was not effective.

The opposite scenario is encountered in the Girassol Field, where the reservoir connectivity is excellent. The confinement of the turbidite flow into narrow areas, as a consequence of the structurally configured seafloor topography, restricted the lateral spreading of the turbidite flows, resulting in the deposition of stacked and coalescent sand turbidite channels. The massive reservoir dimensions and excellent channel connectivity mean that a very large network of interconnected pores is available to compensate the effect of depletion due to production, which also means that the injection plan for pressure maintenance in the field is very effective too. So the sand-shale pressure imbalance is low and for this reason, the predicted pressure diffusion in the shales of this reservoir is negligible.

The study of the Schiehallion Field's connectivity involves more parameters than the previous cases. With turbidite channels from different flows interconnected by the lateral coalescence of their overbank facies, the reservoir connectivity is complicated by the presence of cemented intervals inside the main sand channels. The distribution of those cemented intervals affects the connectivity along the channels, creating pressure imbalance and low effectiveness of water injection, but the cemented intervals mostly affect the connectivity between channels and levee and overbank facies. This effect is clearly evidenced by the spatially restricted hardening 4D seismic signal (channel shape)

corresponding to the effect and distribution of the injected water. So to match that response, the modelling of the transmissivity of the reservoir includes a lot of transmissivity multipliers to inhibit fluid flow between channels and overbank facies. The use of the multipliers does not explain the distribution of the softening signal observed in the overbank facies. On the other hand, isolated channels create more depletion and subsequent gas exsolution within the channels and, even when the predicted softening does not match the observed data, the predicted gas production is closer to the historical data. Shale pressure diffusion in this field connected channel depletion with the hydrocarbon saturated pore space of the sandy section of the overbank deposits, and due to the narrow window between the reservoir pressure and the bubble point, this causes gas exsolution, which explains the distribution of the softening signal observed in the real 4D seismic and in the predicted 4D for models with shales active.

Pressure imbalance between the reservoir and shales was already present between the overpressured overburden shales and the Fulmar reservoir in the Shearwater Field prior to production. But an overly large pressure gradient in this HP/HT field, induced by the condensate production (almost 400 bars of depletion), and the associated geomechanical effect of the Fulmar Formation compaction proved to be an excellent scenario to study shale pressure diffusion and its elastic implications. With no changes in saturation, as depletion is still above the condensate dew point, shale pressure diffusion does not have any expresion in the elastic changes within the reservoir, but only in the strain propagation to the overburden.

Large pressure diffusion in shale can definitely create its own elastic response and signal in the computed 4D differences, but the results of this project have shown that the contribution of this process is more important when a few bars in the reservoir pressure can change the fluid saturation. Thus, in general, shale pressure diffusion as consequence of the sand-shale pressure imbalance, reservoir connectivity and compartmentalization could have an important impact on the reservoir overall elastic response and 4D seismic interpretation only if the stress sensitivity of the reservoir to changes in pressure is very high.

7.2.2 Shale heterogeneity and internal architecture

Shale heterogeneity, reflecting changes in the energy during sedimentation and therefore grain size, creates large variations in the dynamic properties of shale, particularly in the

permeability and, hence, in the process of shale pressure diffusion. Due to intrinsic conditions associated with deposition, shale vertical heterogeneity is very large, when compared to the horizontal heterogeneity, as the lateral continuity of clay, silt and fine sand sheets, like laminations, often exceeds reservoir cell dimensions. Vertical granulometric gradation within shales could enhance the pressure interaction with the reservoir, depending on their position in relation to the sands. For instance, coarsening upwards shaly intervals at the base of a sand channel or fining upwards shaly intervals on the top of a sandy unit clearly represent scenarios where the transmissivity in the shale-sand interface is enhanced by a gradual decrease in the permeability. These types of contact are frequent in turbidite reservoirs, where the re-settlement of the fine fraction (suspended by the turbidite flow) over the channel facies results in a gradual and fining upwards profile, while at the base, the contact between the channels and shales tends to be abrupt and erosive, with basal pelagic and more homogeneous sequences, acting as an interface less prone to pressure diffusion. The existence of other geological features such as bioturbation can play a very important role in the pressure diffusion, as the biological destruction of the most important hydraulic structures, the laminations and bedding, creates preferential paths for pressure and even fluid interaction, as the vertical permeability which is the main constraint for shale pressure diffusion, is enhanced by several orders of magnitude.

The main challenge remains the comprehensive representation of shale heterogeneity and architecture at the simulation model scale, as grid cell thickness is in the range of metres, while shale internal variations are in the range of millimetres or centimetres. But if the patterns or trends in shales are clear, the modelling of the shale properties in the corresponding cells can be based on averaging and upscaling techniques from the well data to the simulation model.

7.2.3 Reservoir-Shale geometry

The spatial distribution of shale relative to the reservoir units is paramount, as this not only conditions the type of shale permeability (horizontal of vertical) acting at the reservoir- shale interface, it also defines the direction and the number of pressure diffusion fronts acting on a specific interval of shale. As a consequence of the higher shale horizontal permeability, it is expected that pressure diffusion propagates deeper in that preferential direction. The sideburden intervals and shales eroded by incised sandy

channels are the scenarios where shale pressure diffusion can penetrate larger distances. At the same time, the amount of pressure depletion inside the shale is controlled by an opposing front of build-up diffusion that attempts to re-establish the pressure equilibrium within the shales (Figure 7-3). This sort of restorative pressure diffusion effect can be also observed in the semi-infinite scenarios of shales in the overburden and in the underburden (Shearwater Field application). This process decreases the pressure imbalance within shale, but increases the imbalance with sands, giving the whole process a pulse dynamism.

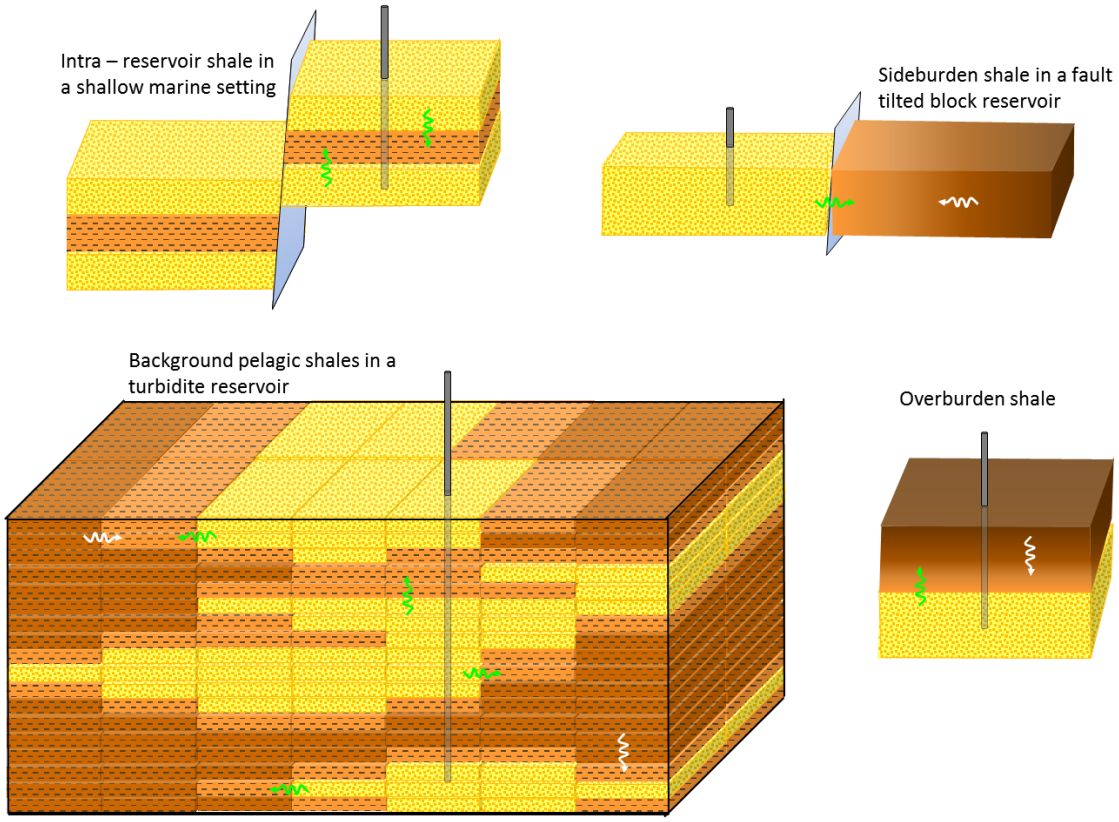

Figure 7-3 *Shale- reservoir geometry and its implications in the shale pressure diffusion process. Green arrows represent depletion diffusion fronts, while white arrows show pressure build up diffusion (the opposite reaction of the shale to re-establish pressure balance)*

Intra and inter-reservoir shales are, by their geometry, in the middle of two or more pressure diffusion fronts (depending on well completion and reservoir architecture). This implies that, depending on the amount of elapsed time and shale thickness, shales will experience a considerable amount of pressure depletion or even pressure equilibrium with the reservoir units, as was observed in the predicted numerical simulations of the Heidrun Field. Shales embedded within coalescent channels are also expected to experience

pressure diffusion relatively quickly, if a pressure imbalance between sands and shales exists. The architecture of the reservoir will also dictate the role of shale permeability anisotropy in the pressure diffusion process for the intra and inter-reservoir shales.

The shale-reservoir geometry defines most of the fluid flow barriers in the reservoir, and, with that, the majority of the spatial distribution of the recorded elastic changes in the observed 4D seismic, because 4D seismic signal related solely to pressure changes without saturation changes or major compaction processes is not very frequent in the 4D seismic data. Thus, in most cases, it is not the pressure diffusion that in itself results in a 4D signal, but the implications that it has for saturation.

The quest for ascertaining which parameters have the largest impact in the process of shale pressure diffusion and its role in the 4D seismic interpretation is not an easy task, as the final expression is a function of multiple geological parameters and production mechanisms. However, it is reasonable to conclude that as diffusion depends on permeability, shale heterogeneity is the paramount parameter, larger amounts of interbedded sand and silt within shaley intervals certainly increases the dynamic interaction with the reservoir. In second order will be the pressure imbalance as the presence of pressure gradients between the shale and the reservoir is the mechanism that will trigger the pressure diffusion.

But in terms of a measurable signal in the 4D seismic, the scenario where shale pressure diffusion have larger incidence in the elastic behaviour of the reservoir is when relatively small changes in pressure generate changes in saturation. So, one of the field scenarios where this workflow should highlight the expression of shale pressure diffusion in 4D is in highly compartmentalized reservoirs with pore pressure sensitivity to generate saturation changes, such as gas exsolution. Another scenario is reservoirs with strong compaction effects, as the study of shale pressure diffusion in this case can help to explain strain propagation in the overburden and the analysis of reservoir seal integrity.

7.3 Impact of shale pressure diffusion in the 4D seismic interpretation

As has been shown in this work, the influence of the shale pressure diffusion process in the 4D seismic interpretation can have a wide range of responses, from very low incidence to cases where this process can reveal the reservoir connectivity and explain the distribution and polarity of the 4D signature. The cases studied in this thesis were taken as representative of the geology and conditions of most of the fields under time lapse surveillance, so, assuming the validity of that representativeness and the compiled database of the 4D fields (Appendix A), this work will present now some statistics about how important the study of shale pressure diffusion should be in the 4D seismic workflow.

North Sea fields constitute the 45% (66 of 146, Appendix A) of the reservoirs under 4D surveillance. Out of those 66 fields, six are HP/HT Jurassic shallow marine condensate reservoirs in the central North Sea and Norwegian North Sea, with pressure depletion as production mechanism, and under strong compaction. Two of those fields (Shearwater and Erskine) had been studied in the ETLP finding that the inclusion of pressure diffusion in the immediate overburden shales for the time shift and time strain prediction workflows improve the fit to observed 4D seismic data, and is reasonable to assume that in the other four fields, shale pressure diffusion in the overlying late Jurassic shales may be an important process as well. The fault tilted configuration of the Jurassic shallow marine Heidrun Field is a geological scenario very common in the North Sea fields, indeed 26 fields have similar or equivalent stratigraphy (Jurassic Fangst or Brent groups, clean shallow marine sands with intra and inter-reservoir transgressive shales), configuration (fault tilted blocks - structural traps that created compartmentalization), depth (between -1800 and -2800 metres) and rock source (late Jurassic organic-rich shales). Shale activation in the Heidrun Field improved the prediction (up to 3.5%) of the 4D seismic signal of the field, but particularly in isolated blocks, fields with saturation changes more sensitive to pressure variations will exhibit larger elastic responses related to shale pressure diffusion. Doing the addition (32 out of 66 fields), at least the 48% of the North Sea 4D fields constitute candidates to study if the process of shale pressure diffusion is active and has expression in the 4D seismic signature.

Turbidite reservoirs under 4D seismic (53 fields, Appendix A) are less prone to have important responses as most of them are Tertiary (39 out of 53 fields) and located in relative passive margins (West Africa Atlantic Slope, North Sea Atlantic Slope and Gulf of Mexico), which reduce the presence of faults (except the faults linked to differential

compaction) and hence reservoir compartmentalization, also in most cases connectivity between reservoir facies (turbidite channels) is high, making injection and pressure maintenance more effective and reducing sand-shale pressure imbalance. But in the cases, where the turbidite reservoirs are compartmentalized due to the occurrence of geological features such as cemented reservoir intervals and faults (Schiehallion Field), shale pressure diffusion can play a very important role as the lateral contact between sideburden shales and depleted sandstones could have implications in process such as gas exsolution (if the saturation is sensitive to pressure variations) and its associated 4D seismic response. Assuming that at least 25% (no corroborated assumption) of the turbidites reservoirs have a structural component in their traps and present certain degree of compartmentalization, between shallow marine and turbidites an estimated of 60 fields (≈40% out of 146 fields in the database) could have responses in the 4D seismic signal associated to shale pressure diffusion.

Reservoirs deposited under higher energy conditions such as aeolian or fluvial environments are less prone to present the effect of shale pressure diffusion, due to less proportion of shale and reservoir – shale geometry.

7.4 Discussion of assumptions

With the aim of studying the effect of shale pressure diffusion, my work was based on assumptions and simplifications related to the physical processes that may occur in shales adjacent to or within conventional reservoirs as a consequence of the production and applied techniques to enhance the hydrocarbon recovery. Probably the most important assumption is that fluid flow from or into shale was not allowed during the numerical simulations of the case studies. Certainly, elevated shale capillary forces, higher than the induced depletion, forbid any change in shale saturation during the simulations. But shales are heterogeneous, and the capillary forces in the silt and fine sand laminations and beds may be below the pressure gradient, allowing some fluid flow. If the capillary pressure of these heterogeneities permits fluid flow, it is also plausible that these thin intervals may be hydrocarbon saturated. However, in the cases studied, the wireline log data available did not imply any change in the fluid saturation, so these intervals were modelled as water-saturated as well. As the scale of the silt and sand laminations embedded within shales is much lower than the minimum cell thickness, all these intervals were considered from the capillary pressure point of view as shale. This

assumption is valid in the context of averaging, as shale is the dominant lithology in the sequence and the upscaling of properties to the simulation grid dimension shows shale as the representative lithology of the interval. Therefore, in this work fluid flow was also forbidden for the heterogeneous thinly interbedded intervals within shale, without any change in the saturation (100% water), leaving pressure as the only shale dynamic parameter in the numerical simulations.

There is relative uncertainty in the established proportions of mineral components for shales in most of the fields studied. The mineral composition was estimated after extensive review of literature in the area and basin analysis, but the calibration of proportions was based on material balance equations (most of the times density related), taking as a reference the saturated properties measured in the well borehole with wireline tools.

Another major assumption in this work was the consideration of shale in the synthetic seismic modelling as equally stress sensitive as sandstones, using the same coefficients [*MacBeth,* 2004] and consolidation parameters for both lithologies. The lack of reliable stress sensitivity relationships for shales (especially a pressure-dependent relationship) is part of the generalised perception of the inactive role of shales that exists in the geoscientific community. As my research did not include laboratory analysis, and shale samples were not available, I was limited in performing the elastic modelling of shales, assuming equal behaviour for sands and shales under effective stress in response to pore pressure variations. If the reader is interested in this topic, previous work from the ETLP [*HajNasser*, 2012] evaluates the shale stress sensitivity using the same equations as in this work, but considering three scenarios where shales were regarded as: a) not stress sensible, b) with equal stress sensitive to sands and c) with stress sensitivity greater than that of sands.

Regarding the representativeness of scale and shale properties in the simulation model to assess shale pressure diffusion, one must always consider the positive effect of vertical grid refinement, as most simulation software computes the interactions from the centre of one cell to the centre of the contiguous cell, and if the distance between them is large, the time dependence of the pressure diffusion process increases. In this work, extra layering for higher vertical resolution was included in the shaly intervals, but I did not downscale the cell thickness to the shale heterogeneity scale; cell thicknesses between 1 and 3 metres were considered sufficient to evaluate pressure diffusion. However, to evaluate fluid flow, downscaling the vertical thickness to the shale heterogeneity scale, may bring some

interesting results for scientific purposes about the behaviour of the fluid flow at that scale; probably, as a practical implementation, one could perform a 1D or 2D analysis at the wellbore location or in a small test area. However, at the 3D full reservoir production scale, volumetric effects may be negligible, and probably without bringing any added value to reservoir prediction. With the high computational costs involved, such project would be impractical for the oil industry.

7.5 Recommendations and conjectures for future work

Probably the most important recommendation of this work is suggest the acquisition of data related to shale, laboratory analysis of shale samples will reduce the uncertainty related to shale composition, static and dynamic properties. Also the availability of 4D wireline well log data in the shale interval adjacent to depleted reservoirs. Such information would definitely show whether shale pressure diffusion is an active process or not in a particular reservoir. The range of applications of this type data would be tremendous, as penetration and timing of shale pressure diffusion could be corroborated, and the stress sensitivity relationships for shale and its geomechanical characterization could be extracted, based on time lapse velocity and density variations. Also petroelastic model calibration would be possible, and the uncertainties related to fluid flow between shales and the reservoir could be reduced. The credibility of research incorporating such data would be ground-breaking in changing the perception in industry and academia of shales in conventional reservoir characterization.

To cover a broader spectrum of the role of shale in 4D seismic interpretation, I believe that this work is missing a field application to evaluate shale pressure diffusion in a carbonate reservoir, particularly for a scenario under strong compaction to study the strain propagation in the overburden shales and the incidence of pressure diffusion in this process. As shale and carbonate deposition can coexist in terms of energy in some particular environments and the transition from one lithology to another could be more gradual, enhancing the connectivity and interaction between them.

The coupled geomechanical and pressure diffusion analysis, was missing in three of my field applications. This was done intentionally to isolate the impact of shale pressure diffusion, as the effect of two processes could overlap. Compaction was not a dominant process in the fields where the geomechanical analysis was excluded, but the inclusion of shales as geomechanically active in the numerical simulations and synthetic seismic

modelling can be used to differentiate the contribution to the 4D seismic signature from both physical processes.

The evaluation of the shale elastic response in the 4D seismic interpretation was performed with seismic attributes classically used to evaluate elastic changes in sandstones. As a suggestion for future research, a detailed seismic characterization of the shale intervals, based on the extraction of different amplitude or frequency seismic attributes, may capture the elastic changes related to shales, by highlighting the vertical and lateral variations in the time lapse seismic signature.

Lastly seismic inversion, which has been used in the shale gas industry to perform shale seismic characterization, based on the application of seismic inversion schemes to obtain attributes derived from impedance, such as Poisson' ratio, can be used as indicator of shale maturity, organic content and brittleness, to define shale gas pays.

7.6 Final remarks

The purpose of this research project was to evaluate with a practical approach the process of shale pressure diffusion in different geological and production scenarios, integrating geoscience and engineering characterization of shale with the 3D and 4D seismic modelling and interpretation. The different predicted responses and degrees of incidence of the shale pressure diffusion in the 4D seismic interpretation of each field gives the impression that the response of this process will vary from one field to another. So, Generalize about shale pressure diffusion response in the 4D seismic signature is a task with many limitations. This work constitute just another step into the study of shale in conventional reservoirs that will hopefully lead to further quantitative studies and will increase awareness among the community involved in the seismic characterization of regarding the active role of shales in the dynamic behaviour of conventional reservoirs and consequently the 4D seismic signature and its interpretation.

Appendix A

The geology of the 4D seismic fields

This appendix contains a database updated until 2014 with geological information about 146 fields around the word under time lapse seismic monitoring. This compendium was constructed with an extensive literature review of papers, web pages and reports from oil companies and news. The data included for each field have the limitation of being compiled from several sources (not all of them 100% verified) and the confidentiality policies of the oil companies.

A.1 Field Data

FIELD	GEOLOGY	OIL TYPE	RESERVOIR DEPTH	COUNTRY	OPERATOR	SURVEYS	USES OF 4D MONITORING
Abo	Turbidites (Miocene)	37° API	2250 - 2450 m TVDSS (450 -750 m under water)	Nigeria (offshore)	ENI - Agip	1993, 2011	Pressure monitoring
Agbami	Turbidites (Miocene)	30 - 40° API	4000 - 4500 m TVDSS (1550 m under water)	Nigeria (offshore)	Chevron	1996, 2009	Pressure monitoring. Shale Diapirism. OBN installed
Agbada	Fluvial - Deltaic (Eocene - Oligocene)	10 - 50° API	2500 - 3500 m TVDSS	Nigeria (onshore)	Shell	1993, 2006, 2010	4D seismic used to new discoveries in undrained sands
Akpo	Turbidite (Oligocene)	53° API (condensate) & gas	1350 m under water. Pressure 700 bar	Nigeria (offshore)	Total - Petrobras	1996, 2011	Water injection monitoring. Fans of distal Turbidites
Alba	Turbidites (Middle Eocene)	19° API	1875 - 2000 m TVDSS (138 m under water)	UK (offshore)	Chevron	1989, 1998, 2008	Water injection monitoring. OBC installed
Albatros / Snohvit	Fluvial - Deltaic (Jurassic)	gas	2300 - 2500 m TVDSS (310 - 340 m under water)	Norway (offshore)	Statoil - Petoro - Total	1997, 2003, 2006, 2009	CO2 re-injection and Pressure depletion monitoring
Alpine	Fluvial (Late Jurassic)	38 - 40° API	1820 - 1950 m TVD	Alaska (onshore)	Conoco Phillips	1996, 2001, 2012	Water and gas injection monitoring
Alve	Fluvial - Shallow marine (Jurassic)	Gas & condensate	3600 -3750 m TVDSS (400 m under water)	Norway (offshore)	Statoil - Petoro	2008, 2011	Gas monitoring and Pressure depletion
Alwyn North	Fluvial - Shallow marine (Brent Group - Jurassic and Triassic)	40 - 47° API & gas	3100 - 4000 m TVDSS (126 m under water)	UK (offshore)	Total	1981, 1996, 2001	Saturation monitoring, former projects of water and gas injection.
Amberjack	Deltaic (Pliocene)	22 - 25° API	1530 - 1830 m TVDSS (313 m under water)	USA - Gulf of Mexico (offshore)	Stone Energy	1994, 2002	Saturation monitoring, Highly compartmentalization. Undrained areas
Andrew	Turbidites (Palaeocene - Lower Cretaceous)	40° API & gas	2450 - 2554 m TVDSS	UK (offshore)	BP	1991, 2001, 2002	Pressure monitoring, infill wells
An Teallach	Turbidites (Palaeocene)	Gas	2000 - 2100 m TVDSS	UK (offshore)	BP	1993, 1999, 2000, 2002	ETLP Dataset
Atlantis	Turbidites (Plio - Pleistocene)	25 - 39° API	5670 - 5718 m TVDSS (1300 - 2200 m under water)	USA - Gulf of Mexico (offshore)	BP - BHP Billiton	2005, 2006, 2009	OBN installed. Water injection monitoring
Argonauta	Fluvial - Deltaic (Pliocene)	24° API	2800 - 2900 m TVDSS (1660 m under water)	Brazil (offshore)	Shell - Petrobras - ONGC	2013	LOFS monitoring, OBC installed. Water injection
Azeri	Fluvial - Deltaic (Pliocene)	36° API	2550 - 3308 m TVDSS (120 m under water)	Azerbaijan - Caspian Sea (offshore)	BP - Chevron - Statoil - ExxonMobil	2002, 2007, 2008(2), 2010	Permanent OBC monitoring. Water injection

FIELD	GEOLOGY	OIL TYPE	RESERVOIR DEPTH	COUNTRY	OPERATOR	SURVEYS	USES OF 4D MONITORING
Balol	Deltaic (Middle Eocene)	15.5° API (oil asphaltic)	996 - 1029 m TVD	India (onshore)	Hindustan Oil Exploration Company	2003, 2004, 2005	Monitoring in-situ combustion for thermal recovery. High porosity and permeability
Bittern	Turbidites (upper Paleocene - Lower Eocene)	39° API and gas	2055 m TVDSS (119 m under water)	UK (offshore)	Dana - Shell - Esso	1991, 2000, 2006	Water injection monitoring
Blake	Turbidite (Lower Cretaceous)	31° API	1500 m TVDSS (100 m under water)	UK (offshore)	BG (now Shell) - Talisman	1992 - 2007	Gas and water injection monitoring
Bonga	Turbidites (Miocene)	29° API	3800 - 4150 m TVDSS (1000 m under water)	Nigeria (offshore)	Shell - ExxonMobil - ENI	1993, 2000, 2008	High porosity - permeability sands
Brage	Fluvial - deltaic - shallow marine (Jurassic)	33.7° API 7 gas	2000 - 2300 m TVDSS (140 m under water)	Norway (offshore)	Statoil - Petoro - Talisman	1992, 2003, 2007	Shallow gas caps over the reservoir. Gas injection monitoring
Burgan	Carbonates and shallow marine sandstones (Upper Cretaceous)	28 - 33° API	1090 - 1360 TVDSS	Kuwait (onshore)	Kuwait Oil Company	1996, 1998	A major field composed by several structures. Pressure monitoring
Cantarell	Carbonate breshia (Upper Cretaceous)	19 - 22° API	2600 - 3550 TVDSS (40 - 50 m under water)	Mexico (offshore)	Pemex	1996, 2004	Change for OBC to OBN. Nitrogene injection monitoring. Breshia caused by meteorite impact
Cervia	Shallow - Marine (Pliocene)	Gas	2800 - 4800 m TVDSS	Italy (offshore)	ENI - Agip	1987, 1992	Gas monitoring
Chirag	Fluvial - Deltaic (Pliocene)	35° API	2400 - 3108 m TVDSS (100 m under water)	Azerbaijan - Caspian Sea (offshore)	BP - Chevron - Statoil - ExxonMobil	2007, 2008, 2010	Permanent OBC monitoring. Water injection
Clair	Fluvial - Aeolian (Devonian - Carboniferous)	23° API	1550 - 2100 TVDSS (140 m under water)	UK (offshore)	BP - Conoco Phillips - Crevron - Shell - Hess	1995, 2006, 2 more surveys after	Permanent OBC monitoring. Water injection
Cold Lake	Fluvial sands (Cretaceous)	7° API (bitumen)	80 - 150 m TVD.	Canada (onshore)	Suncor Mine, Syncrude Mine	1999, 2009, 2010	Monitoring steam injection in oil sands
Cormorant	Fluvial - Shallow marine (Brent Group - Jurassic)	36° API & gas	2895 - 3000 m TVDSS (150 m under water)	UK (offshore)	Abu Dhabi National Energy Company - Shell	1979, 1984, 1991, 1998	Water injection monitoring
Curlew	Shallow marine (Jurassic)	39 - 44° API & gas	3045 - 3288 m TVDSS (92 m under water)	UK (offshore)	Shell	1981, 1991	Pressure Monitoring
Dalia	Turbidites (Miocene)	21 - 23° API	2000 - 2500 m TVDSS (1200 - 1500 m under water)	Angola (offshore)	Total - Statoil - ExxonMobil - BP	2009, 2010	Unconsolidated reservoir. OBN intalled. Permeability >1D

FIELD	GEOLOGY	OIL TYPE	RESERVOIR DEPTH	COUNTRY	OPERATOR	SURVEYS	USES OF 4D MONITORING
Diana/ Hoover/ Madison and Marschall)	Turbidites (Plio-Pleistocene)	30° API	3300 - 3800 m TVDSS (1463 m under water)	USA - Gulf of Mexico (offshore)	ExxonMobil - Plains E&P	1972, 2005, 2006	The Diana field 4D seismic monitoring is inside of the Hoover Project
Draugen	Deltaic - shallow marine bars (Jurassic)	38° API	1600 - 1800m TVDSS (250 m under water)	Norway (offshore)	Norske - Shell - Petoro - BP - Chevron	1990, 1998, 2001 and 2004	RF= >60%. Water injection monitoring
Dikanza	Turbidites (Mioceno)	25 - 29° API	2400 - 2700 m TVDSS (1100 m under water)	Angola (offshore)	ExxonMobil - BP -ENI - Statoil	1997, 2002, 2008	Water injection monitoring
Duri	Deltaic (tidal) Miocene	22° API	160 - 300 m TVD	Indonesia - Sumatra (onshore)	PT Caltex Pacific Indonesia	1992, 1993(3), 1994, 1995, 1996	4D seismic used to monitoring steam inyection. High viscosity oil
Edvard Grieg (formerly Luno Field)	Fluvial and Eolian (Triassic)	34° API	1800 - 2200 m TVDSS(110 m under water)	Norway (offshore)	Lundin	2008, 2009, 2010, 2012, 2013, 2014	Water injection monitoring and dranaige pattern for oil and gas
Ekofisk	Chalk (Cretaceous)	30 - 40° API & gas	2900 - 3250 m TVDSS (70 m under water)	Norway (offshore)	Conoco Phillips - Petoro - Statoil - ENI - Total	1989, 1999, 2003, 2006, 2008, 2010, 2011, 2012, 2014, 2015	ETLP Dataset. Subsidence - water injection monitoring. LOFS
Eldfisk	Chalk (Cretaceous and Palaeocene)	39° API	2700 - 2900 m TVDSS (75 m under water)	Norway (offshore)	Conoco Phillips - Petoro - Statoil - ENI - Total	1999, 2012	water injection monitoring. OBC installed
Elgin	Fluvial - Shallow marine (Jurassic)	40° API & gas & condensate	5800 - 6100 m TVDSS (93 m under water)	UK (offshore)	Total - ENI - BG Group - GDF SUEZ	1989, 1996, 2005	High pressure, high temperature reservoir. Pressure depletion monitoring
Enfield	Turbidites (Late Jurassic)	22° API	2060 m TVDSS (500 - 550 m under water)	Australia (offshore)	Woodside - Western Australian - Mitsui	2004, 2007, 2008, 2011	Monitoring gas and water injection
Erha	Turbidites (Terciary)	32.8° API	2900 - 3570 m TVDSS (1200 m under water)	Nigeria (offshore)	ExxonMobil - Shell	2000, 2005, 2009	Water and gas injection monitoring
Erskine	Shallow marine (Jurassic)	Gas	3600 - 5000 m TVDSS (91 m under water)	UK (offshore)	Chevron - BG Group - BP	1989, 2001, 2007	Compactation time shift monitoring
Eugene Island	Deltaic (Pleistocene)	23° API	700 - 3660 m TVDSS (64 - 81 m under water)	USA - Gulf of Mexico (offshore)	Crevron Texaco - ExxonMobil - Shell	1988, 1994	The field recharge oil fron a fault. Water injection monitoring
Foinaven	Turbidites (Palaeocene)	26° API	2000 - 2200 m TVDSS (500 m under water)	UK (offshore)	BP - Marathon Oil	1992, 1995, 1997, 1998, 1999, 2000	Very differents RF for each unit. Previous ETLP Dataset

FIELD	GEOLOGY	OIL TYPE	RESERVOIR DEPTH	COUNTRY	OPERATOR	SURVEYS	USES OF 4D MONITORING
Forties	Fluvial - deltaic (Palaeocene)	32.6° API	2100 - 3400 m TVDSS (110 m under water)	UK (offshore)	Apache	1988, 2000, 2005, 2010	High porosity - permeability sands
Fram	Fluvial - Shallow marine (Jurassic)	38.3° API & gas	2300 - 2500 m TVDSS (350 m under water)	UK (offshore)	Statoil - ExxonMobil	2005, 2010	Gas and water injection monitoring
Franklin	Fluvial - Shallow marine (Jurassic)	40° API & gas & condensate	5500 - 5800 m TVDSS (93 m under water)	UK (offshore)	Total - ENI - BG Group - GDF SUEZ	1987, 1996, 2005	High pressure, high temperature reservoir. Pressure depletion monitoting
Fulmar	Shallow marine (Jurassic)	39° API	3050 m TVDSS (82 m under water)	UK (offshore)	Talisman Energy ExxonMobil - Amerada Hess	1977, 1992	Dome shaped structure. Water and Gas monitoring
Gannet	Turbidites (Eocene)	20 - 43° API	1768 - 2728 m TVDSS (95 m under water)	UK (offshore)	Shell - Esso	1993, 1998, 2004	Salt diapirism. Undrained areas monitoring, recompletion
Garoupa / Namorado	Shallow marine carbonates and turbidites (Early Cretaceous)	31° API	3000 -3100 m TVDSS (100 -304 m under water)	Brazil (offshore)	Petrobras	1986 - without extra data	Water injection monitoring
Genesis	Turbidites (Plio - Pleistocene)	31° API	3350 - 4560 m TVDSS (740 - 910 m under water)	USA - Gulf of Mexico (offshore)	Chevron Texaco - ExxonMobil - BHP Billiton	1991, 2002	Compactation time shift monitoring
Girassol	Turbidites (Oligocene)	32° API	2300 - 2650 m TVDSS (1350 m under water)	Angola (offshore)	Total - Esso - BP - Statoil	1999, 2002, 2004	Faulted system. ETLP dataset. Water injection monitoring
Gjoa	Fluvial - Shallow marine (Jurassic)	44° API and condensate	2200 m TVDSS (360 m under water)	Norway (offshore)	Statoil - GDF SUEZ - Petoro - Shell	2007, 2012	Gas monitoring
Glitne	Deep marine fans (Palaeocene)	32° API	2150 m TVDSS (110 m under water)	Norway (offshore)	Statoil - Total	1993, 2008	Saturation monitoring. Water injection
Grane	Turbidites (Palaeocene)	18.7° API	1700 m TVDSS (128 m under water)	Norway (offshore)	Statoil - Petoro - ExxonMobil - Conoco Phillips	2005, 2007, 2009	Water injection monitoring. Very high porosity (33%) and permeability (5 - 10 D)
Greater Gorgon	Fluvial (Triassic) - Turbidites (Jurassic)	Gas	3200 - 4600 m TVDSS (800 - 1200 m under water)	Australia (offshore)	Chevron Texaco - Shell - BP - Mobil	2004, 2006, 2009	Plume of CO_2 migration prediction. CO_2 storage monitoring
Gryphon	Submarine fan system (Eocene)	26° API and gas	1450 - 1500 m TVDSS (113 m under water)	UK (offshore)	Maersk - Sojitz	1990/1995, 2002, 2011	OBC installed. Reservoir connectivity
Gullfaks	Fluvial - deltaic (Middle Jurassic) Brent Group	37° API	1700 - 2000 m TVDSS (130 - 220 m under water)	Norway (offshore)	Statoil - Petoro	1985, 1995, 1996, 1999	RF from 46% (in 1986) to 70% (2010). Water and gas injection monitoring
Guillemot	Turbidites (upper Paleocene - Lower Eocene)	35 - 38° API	2200 m TVDSS (87 m under water)	UK (offshore)	Dana - Esso	1991, 2000, 2005, 2013	Water front mapping, depletion monitoring

FIELD	GEOLOGY	OIL TYPE	RESERVOIR DEPTH	COUNTRY	OPERATOR	SURVEYS	USES OF 4D MONITORING
Gunashli	Fluvial - Deltaic (Pliocene)	36° API	2700 - 3400 m TVDSS (175 m under water)	Azerbaijan - Caspian Sea (offshore)	BP - Chevron - Statoil - ExxonMobil	2002, 2007, 2008, 2010	Permanent OBC monitoring. Water injection
Hall - Gurney	Shallow marine shelf carbonates (Carboniferous)	38° API	880 m TVD	USA (onshore)	Kinder Morgan - Murfin Company	2003, 2004(3), 2005(3), 2006(2)	CO2 injection monitoring to enhance RF
Harding	Deltaic - Shallow marine (Eocene)	19.5° API	1580 - 1750 m TVDSS (109 m under water)	UK (offshore)	Taqa - Maersk	1990, 2000, 2002, 2005, 2011	Water re-injection monitoring
Heidrun	Fluvial - deltaic - shallow marine (Lower Jurassic)	25° API	2175 - 2475 m TVDSS (350m under water)	Norway (offshore)	Statoil - Petoro - ENI - Conoco Phillips	1986, 2001, 2004	ETLP Dataset. Water and gas injection monitoring
Hibernia	Fluvial (braided) Early Cretaceous	32 - 34° API	2400 - 3700 m TVDSS (80 m under water)	Canada (offshore)	ExxonMobil - Crevron - Suncor - Murphy - Statoil	1981, 1991, 2001	Water and gas inyection monitoring
Holt	Shallow marine (Carboniferous-Permian)	14° API	718 - 900 m TVD	USA (onshore)	ARCO (now BP)	1981,1982, 1983	Monitoring of combustion in-situ (burnfront propagation)
Jansz / Io	Shallow marine sandstones (Jurassic - Creataceous)	Gas	2900 - 3300 m TVDSS (1350 m under water)	Australia (offshore)	ExxonMobil - Crevron Texaco - BP - Shell	2004, 2011	Gas production and Pressure depletion monitoring. CO2 injection
Jasmin/ Carmelia/ Pazflor/ Rosa	Turbidite (Oligocene)	30° API	2400 - 3000 m TVDSS (1400 m under water)	Angola (offshore)	Total - Esso - BP - Statoil	1999, 2012	water injection ad production monitoring
Jubarte	Turbidites (Cretaceous)	17 - 28° API	2500 m (Shallow reservoirs), 5000 - 7000 m TVDSS pre salt reservoirs (1350 m under water)	Brazil (offshore)	Petrobras	2001, 2013, 2015	Pre salt reservoir. High porosity (28%) - permeability sands. Production monitoring. OBC installed
Ketzin	Fluvial - Transitional (Upper Triassic)	Gas	650 - 750 m TVD	Germany (onshore)	CO2MAN Project - Shell	2005, 2009, 2012	CO2 storage monitoring
Kilauea	Turbidites (Pleistocene and Eocene)	22 - 32° API & gas	1250 - 2000 m (shallow), 3460 m TVDSS for Eocene reservoir (150 - 190 m under water)	USA - Gulf of Mexico (offshore)	Texaco	1985, 1995	Monitoring gas saturation
Kristin	Shoreface - Shallow marine (middle Jurassic)	Gas & condesate	4600 - 5000 m TVDSS (370 m under water)	Norway (offshore)	Statoil - Petoro - ExxonMobil - ENI - Total	2003, 2007	High pressure and temperature reservoir. Pressure depletion monitoring

FIELD	GEOLOGY	OIL TYPE	RESERVOIR DEPTH	COUNTRY	OPERATOR	SURVEYS	USES OF 4D MONITORING
Kolo Creek	Deltaic - Shallow marine (Miocene)	39° API	3550 - 3620 m TVD	Nigeria (onshore)	Shell	1997, 2006, 2008	Water injection monitoring
Lavrans	Shallow marine (Jurassic)	Gas & condesate	4500 - 5100 m TVDSS (250 m under water)	Norway (offshore)	Statoil - Petoro	2008, 2012	Gas monitoring, pressure depletion
Leismer	Fluvial sands (Cretaceous)	6 - 15° API	100 - 550 m TVD	Canada (onshore)	Statoil	2011, 2012	Oil sand reservoir
Lena	Unconsolidated channels of turbidites (Pliocene)	25 - 35° API	3000 - 3600 m TVDSS (310 m under water)	USA - Gulf of Mexico (offshore)	ExxonMobil	1983, 1995	Salt dome structure
Liaohe	Deltaic (Plio - Pleistocene)	10 - 26° API	1300 - 1700 m TVD	China (onshore)	CNPC	1992, 1993, 1994, 2009, 2011	Steam injection monitoring
Loyal	Turbidites (Palaeocene)	22 - 28° API	2160 - 2397 m TVDSS (500 m under water)	UK (offshore)	BP - Shell - Hess - Statoil	1992, 1996, 1999, 2000	Field northwards to Schiehallion
Maclure	Submarine fan (Eocene)	27° API	1450 -1500 m TVDSS (100 m under water)	UK (offshore)	Taqa - Maersk	1990/1995, 2002, 2011	Reservoir connectivity, fluid movement monitoring
Magnus	Turbidites (jurassic)	39° API	2800 - 3160 m TVDSS (185 m under water)	UK (offshore)	BP - Nippon Oil E&P - ENI	1992, 2001	Gas injection monitoring
Marlim	Turbidites (Oligocene)	18-21° API	3400 m TVDSS (650 - 1050 m under water)	Brazil (offshore)	Petrobras	1997, 2005	NTG=0.8 - 1 (very clean sands) RF= 25%
Mars	Turbidites (Oligocene to Plio-Pleistocene)	30° API	4877 - 5791 m TVDSS (896 m under water)	USA - Gulf of Mexico (offshore)	Shell - BP - Agip - Conoco	2004, 2005	More than 10,000 feets of stacked turbidites sands with some influence of salt diapirism
Meren	Deltaic (wave dominated) Middle Miocene	35° API	1460 - 2892 m TVDSS (15 m under water)	Nigeria (offshore)	Chevron - Texaco	1987, 1996	Field in shallow waters
Midgard	Fluvial - Shallow marine (Jurassic)	Gas	4850 m TVDSS (240 - 300 m under water)	Norway (offshore)	Statoil - Petoro - ENI - Total - ExxonMobil	2001, 2006, 2009	Gas monitoring
Mikkel	Fluvial - Shallow marine (Jurassic)	Gas & condesate	2500 m TVDSS (220 m under water)	Norway (offshore)	Statoil - ExxonMobil - ENI - Total	1998, 2012	Gas movement monitoring High porosity high permeability. Pressure depletion
Minagish	Open Marine Carbonates (Late Jurassic)	20 - 35° API	3000 - 3600 TVD	Kuwait (onshore)	Kuwait Oil Company	1996, 1998	Oolitic and high porosity carbonate
Moho Bilondo	Turbidites (Upper Miocene)	22 - 29° API	2340 - 2645 m TVDSS (600 - 900 m under water)	Congo (offshore)	Total - Chevron - SNPC	2001, 2012	water injection monitoring

FIELD	GEOLOGY	OIL TYPE	RESERVOIR DEPTH	COUNTRY	OPERATOR	SURVEYS	USES OF 4D MONITORING
Mungo	Submarine fan system - Chalk (Upper Cretaceous - Palaeocene)	39 - 41° API	1200 - 2500 m TVDSS (88 m under water)	UK (offshore)	BP	1991, 2001, 2005, 2007, 2008, 2009, 2010, 2011	HD OBC installed. Reservoir characterization and fluid movement monitoring
Neelam	Shelf Carbonates (open - shallow marine) Eocene - Miocene	40° API & gas	1400 - 1480 m TVDSS (110 m under water)	India (offshore)	ONGC (Oil and Natural Gas Corporation)	1989, 1999	Monitoring water injection
Nelson	Turbidite (Palaeocene)	40° API	2190 - 2280 m TVDSS (83 m under water)	UK (offshore)	Shell - ELF - Esso	1985, 1990, 1997, 2000, 2003, 2006, 2009	History matching. Previous ETLP Dataset
Njord	Shallow marine (Jurassic)	47° API & gas	2850 m TVDSS (330 m under water)	Norway (offshore)	Statoil - GDF SUEZ - E.ON Ruhrgas	2001, 2004, 2007, 2011	Initial gas injection project, suspended in 2007
Norne	Shallow marine (Lower - Middle Jurassic)	30 - 40° API & gas	2525 - 2688 m TVDSS (380 m under water)	Norway (offshore)	Statoil - Petoro ENI	1992, 2001, 2003, 2004, 2006, 2008	ETLP Dataset. OWC monitoring. History matching and water injection
Ormen Lange	Turbidites (Palaeocene)	Gas & condesate	2700 - 2900 m TVDSS (800 - 1100 m under water)	Norway (offshore)	Shell - Petoro - Statoil - ExxonMobil	1996, 2007, 2009	Gas production and pressure depletion monitoring
Oseberg	Prograding Delta (Brent Group) Middle Jurassic	38° API	2300 - 2700 m TVDSS (100 m under water)	Norway (offshore)	Statoil - Petoro - Total - ExxonMobil - Conoco Phillips	1982 (2D), Surveys 3D 1989, 1991, 1992, 1999, 2004, 2009	Porosities between 20 - 30%. Very high permeabilities. Water and gas injection monitoring
Otway/ Thylacine/ Geographe/ Casino/ Minerva	Fluvial - Deltaic (Jurassic - Lower Cretaceous)	Gas	2000 - 2400 m TVDSS (60 - 100 m under water)	Australia (offshore)	BHP Billiton - Woodside - Mitsui - Santos	1991, 1997, 2000, 2008(2), 2009, 2010	CO2 storage monitoring. Gas monitoring
Peace River	Fluvial sands (Cretaceous)	7 - 41° API (bitumen)	600 m TVD	Canada (onshore)	Shell - Penn West Energy Trust	2002, 2009, 2010, 2014	Steam injection monitoring in oil sands. Seismovie technology
Pierce	Submarine fan system and Chalk (Upper Cretaceous - Palaeocene)	40° API and gas	2100 - 3100 TVDSS (85 m under water)	Uk (offshore)	Shell - Summit Petroleum	1992, 2003, 2009	Fluid movement monitoring
Pluto / Xena	Fluvial - Deltaic (Upper Triassic - Jurassic - Lower Cretaceous)	Gas	3000 - 3400 m TVDSS (830 - 1000 m under water)	Australia (offshore)	Woodside - Tokyo Gas	2005, 2011	Liquefied natural gas project
Raudhatain	Carbonates and shallow marine sandstones (Lower - Middle Cretaceous)	28 - 40° API	2620 - 3000 m TVD	Kuwait (onshore)	Kuwait Oil Company	1996, 1999	Irregular OWC. Water injection monitoring

FIELD	GEOLOGY	OIL TYPE	RESERVOIR DEPTH	COUNTRY	OPERATOR	SURVEYS	USES OF 4D MONITORING
Ravva	Turbidites (Miocene)	31° API	820 - 2620 m TVDSS (80 m under water)	India (offshore)	Cairn - ONGC	1990,2010, 2011	4D Seismic for find remaining oil zones
Ringhorne	Fluvial - Shallow marine (Jurassic)	38° API	1940 m TVDSS (130 m under water)	Norway (offshore)	ExxonMobil - Statoil	2001, 2006, 2009	Gas and water movement monitoring. High porosity high permeability.
Rosebank	Fluvial - Deltaic - Shallow marine (intra and sub basalt) Palaeocene	27 - 38° API	2740 - 2810 m TVDSS (1120 m under water)	UK (offshore)	Chevron - Statoil - OMV	2010, 2011	OBC installed. Subvolcanic reservoir
Rulison	Fluvial (Upper Cretaceous)	gas	2100 - 2740 m TVD	USA (onshore)	Williams RMT Company	1996, 2003, 2004, 2006	Heterolithic reservoir
Sabriyah	Carbonates and shallow marine sandstones (Middle Cretaceous)	28 - 32° API	2500 - 2900 m TVDSS	Kuwait (onshore)	Kuwait Oil Company	1996, 1998	Irregular OWC. Water injection monitoring
Salah	Shallow marine (Devonian - Carboniferous)	Dry gas	1800 - 1900 m TVD	Algeria (onshore)	Sonatrach - BP - Statoil	2003, 2005, 2006, 2008, 2009, 2010	Co2 storage monitoring
Sarawak / Natura	Carbonates (Miocene)	44° API & gas	1610 - 1800 m TVDSS (45 m under water)	Malaysia (offshore)	Shell - Petronas	1992, 2001, 2002, 2006, 2008	Monitoring of gas in carbonates
Scarborough	Deltaic - Turbidites (Triassic - Jurassic)	Gas	1800 - 2068 m TVDSS (900 m under water)	Australia (offshore)	ExxonMobil - BHP Billiton	1996, 2004, 2007, 2012	Gas monitoring
Schiehallion	Turbidites (Palaeocene)	22 - 26° API	2064 m TVDSS (300 m under water)	UK (offshore)	BP - Shell - Hess	1993, 1996, 1999, 2000, 2002, 2004, 2006, 2008, 2013	ETLP Dataset. Water injection monitoring
Schoonebeek	Fluvial (Cretaceous)	25° API	650 - 900 m TVD	Netherland (onshore)	Shell	2005 - 2010	Reactivated field. Permanent steam injection monitoring, Seismovie
Shearwater	Shallow marine (Jurassic)	40° API & condensate	4545 m TVDSS (90 m under water)	UK (offshore)	Shell - ExxonMobil - BP - BG Group	1992, 1996, 2002, 2004, 2013	High pressure, high temperature reservoir. Pressure depletion monitoring. ETLP Dataset
Sleipner	Fluvial - deltaic (Mio - Pliocene)	63.2° API (condensate and gas)	3450 m TVDSS (110 m under water)	UK (offshore)	Statoil - ExxonMobil - Gassco (CO2 storage)	1994, 1999	CO2 injection and pressure depletion monitoring
Snorre	Fluvial (Late Triassic - Lower Jurassic)	40 - 42° API	2000 - 2700 m TVDSS (300 - 350m under water)	Norway (offshore)	Statoil - Petoro - ExxonMobil - Total	1997, 2001, 2006, 2009	Water and gas injection monitoring

FIELD	GEOLOGY	OIL TYPE	RESERVOIR DEPTH	COUNTRY	OPERATOR	SURVEYS	USES OF 4D MONITORING
South Arne	Chalk (Cretaceous)	32.4° API 7 Gas	2700 - 2940 m TVDSS (60 m under water)	Denmark - North Sea (offshore)	Hess - Danoil - Dong	1995, 2005	Porosity exceed 40%. ETLP Dataset. Water injection monitoring
South Timbalier	Turbidites (Plio - Pleistocene)	29° API	2130 - 4570 m TVDSS (20 m under water)	USA - Gulf of Mexico (offshore)	Energy XXI - Crevron	1988, 1994	Field affected by salt diapirism. 4D monitoring of gas and oil saturations
Statfjord	Fluvial - deltaic (Middle Jurassic) Brent Group	39.5° API	2500 - 3000 m TVDSS (150 m under water)	Norway - Uk (offshore)	Statoil - ExxonMobil - Conoco Phillips	1979, 1992, 1997, 2001, 2004, 2006	Water and gas injection monitoring
Steepbank	Fluvial (lower Cretaceous)	6 - 8° API	260 - 320 m TVD	Canada (onshore)	Chevron	1985, 1991, 1992	Steam injection monitoring. Previous ETLP dataset
Stybarrow	Turbidites (Early Cretaceous)	17 - 22° API & gas	2000 - 2200 m TVDSS (825 m under water)	Australia (offshore)	BHP Billiton - Woodside	2000, 2008, 2011	Monitoring production, water and gas injection
Tarn / Kuparuk River	Shallow marine - Turbidite (Jurassic)	38° API & gas	1580 - 1700 m TVD	Alaska (onshore)	Conoco Phillips	1994, 2001, 2008, 2011	Gas reinjection monitoring
Teal South	Turbidites (Oligocene - Miocene)	37° API	1370 - 2400 m TVDSS (85 m under water)	USA - Gulf of Mexico (offshore)	Texaco	1995, 1997, 1999,	ETLP Dataset. OBC monitoring. Undrained areas, saturation monitoring
Tordis	Fluvial - deltaic (Middle Jurassic) Brent Group	37,5° API	2000 - 2500 m TVDSS (200 m under water)	Norway (offshore)	Statoil - Petoro - ExxonMobil - Total	1984, 1997, 2001, 2006, 2009	Very high RF. Water injection monitoring
Troll	Shallow marine sandstones (Jurassic)	40 - 45° API & gas	1330 m TVDSS (300 m under water)	Norway (offshore)	Statoil - Petoro - Conoco Phillips - Total	1989, 1991, 1995, 1998, 2000, 2001, 2003	The major gas field of Norway. Pressure depletion monitoring
Tullich	Submarine fan system (Eocene)	25° API and gas	1450 - 1500 m TVDSS (113 m under water)	UK (offshore)	Maersk	1990/1995, 2002, 2011	OBC installed. Reservoir connectivity
Vacuum	Shelf carbonates (Permian)	25° API	1210 - 1430 m TVD	USA - New Mexico (onshore)	Conoco Phillips - Texaco - ExxonMobil	1995, 1997, 1998	Monitoring of CO2 injection
Valhall	Chalk (Cretaceous)	34° API	2400 m TVDSS (70 m under water)	Norway (offshore)	BP - Hess	11 surveys 2003 - 2008	Water injection monitoring. Pressure depletion and compaction monitoring. ETLP Dataset
Veslefrikk	Fluvial - Shallow marine (Jurassic)	38° API	2800 - 3200 m TVDSS (185 m under water)	Norway (offshore)	Statoil - Talisman - Petoro	2003, 2005, 2010	Water injection monitoring
Vigdis	Fluvial - deltaic (Middle Jurassic) Brent Group	37° API	2200 - 2600 m TVDSS (280 m under water)	Norway (offshore)	Statoil - Petoro - ExxonMobil - Total	1997, 2001, 2006, 2009	Very high RF. Water injection monitoring

FIELD	GEOLOGY	OIL TYPE	RESERVOIR DEPTH	COUNTRY	OPERATOR	SURVEYS	USES OF 4D MONITORING
Vilje	Deep marine fans (Palaeocene)	37° API & gas	2150 m TVDSS (120 m under water)	Norway (offshore)	Statoil - Marathon - Total	1996, 2012	Production and OWC monitoring
Visund	Fluvial - Shallow marine (Jurassic)	35° API & gas	2900 - 3000 m TVDSS (335 m under water)	Norway (offshore)	Statoil - Petoro - Total - Conoco Phillips	2004, 2007, 2010	Gas and water injection monitoring
West Brae	Turbidites (Palaeocene)	22° API	1630 - 1721 m TVDSS	UK (offshore)	Marathon Oil - BP	1993, 2007	Intern Shale distribution that control the fluid column. Water injection monitoring
Weyburn	Carbonates (Carboniferous)	24 - 34° API	1400 - 1450 m TVD	Canada (onshore)	Cenovus Energy - Encana	2000, 2001, 2002	CO2 injection monitoring (to increase RF). High permeability (vuggy)
Wheatstone / Lago	Fluvial - Deltaic (Upper Triassic - Jurassic - Lower Cretaceous)	Gas & condesate	3354 - 3410 m TVDSS (118 m under water)	Australia (offshore)	Chevron	2006, 2009, 2012	Liquefied natural gas project
Widuri	Fluvial (Oligocene - Miocene)	31° API	1075 - 1130 m TVDSS	Sumatra (offshore)	CNOOC SES Ltd	1991, 2000	High porosity, high permeability and RF (almost 70%). OWC monitoring

To this list should be added the Lula (before Tupi), Peroba, Franco and Piracuca fields from the Santos Basin in Brazil, but the lack of published data in the area due to Petrobras' very strict confidentiality policies, makes impossible to build a database of those fields. Also in the Alaskan North Slope Area, ConocoPhillips have several projects of 4D seismic acquisitions in progress. Woodside, in alliance with Tokyo Gas, are also increasing the number of their gas fields with time lapse monitoring in Australia.

A.2 Statistics

Is very possible that this database leaves out some fields with 4D seismic monitoring, but perhaps those presented here are the most important projects of 4D seismic in the world. This list contains 146 fields, with information about their location, reservoir sedimentology, age, depth, oil gravity, number and date of seismic surveys, companies operating the field and main uses of the 4D seismic technique.

Onshore vs offshore

Number of Fields	146
Offshore 4D seismic	122
Onshore 4D seismic	24

Age, geology and depth of 4D reservoirs

Age of Reservoirs	# of 4D fields
Plio - Pleistocene	16
Miocene	13
Oligocene	4
Eocene	11
Palaeocene	18
Cretaceous	25
Jurassic	42
Triassic	8
Permian	2
Carboniferous	5
Devonian	2

Geology of the Reservoirs	# of 4D fields
Turbidites	53
Fluvio - Deltaic	43
Shallow marine	32
Carbonate shelf	16
Aeolian	2

Depth of the Reservoirs	# of fields
0 - 1000 m	8
1000 - 2000 m	29
2000 - 3000 m	65
3000 - 4000 m	37
4000 - 5000 m	12
> 5000 m	6

Type of oil

Gravity of oil (API)	# of 4D fields
< 10° API	3
10 - 20° API	10
20 - 30° API	33
30 - 40° API	60
> 40° API	17
Condensate & gas	23

Geographic distribution

Area or country	# of 4D fields
North Sea (Norway, UK and Denmark) and Atlantic slope of Norway	66
Europe (Italy, Netherland and Germany)	3
Gulf of Mexico USA - Mexico	15
West Africa (Angola, Congo, Nigeria)	16
Middle East and North Africa (Algeria, Kuwait)	5
Brazil	4
North America (USA, Alaska and Canada, mostly onshore)	13
Australia and Southeast Asia (India, Sumatra, Indonesia, Malaysia)	20
Caspian Sea (Azerbaijan)	3
China	1

Applications of the 4D seismic

Use of the 4D seismic	# of 4D fields
Water injection	48
CO2 injection	5
CO2 Storage	6
Gas (caps and injection)	31
Oil - water saturation (OWC)	60
Steam injection	7
Nitrogen injection	1
Pressure depletion	14
Combustion in-situ	2
Compaction	4

Main 4D seismic operators

Companies with 4D seismic fields	# of fields
ExxonMobil	44
Statoil	39
Shell	30
BP	25
Chevron - Texaco	23
Total	22
Petoro	19
ConocoPhillips	13
ENI	10
Woodside	6
Kuwait Oil Company	4
Hess	4
GDF Suez	4
BG Group (now Shell)	4
Petrobras	4
Taqa	3
Marathon	2
BHP Billiton	2

Database references

Anderson R., et al, 1997. *4D Time-Lapse Seismic Monitoring in the South Timbalier 295 Field, Gulf of Mexico.* Offshore Technology Conference, May 1997, Houston - Texas.

Aquino J., et al, 2003. *The Sihil Field: Another giant below Cantarell, offshore Campeche, Mexico*. AAPG Memoir 78, pp. 141 – 150.

Bloomer C., 2009. *Agbami Project: People and partnerships delivering a world-scale field development.* Offshore Technology Conference 2009, Houston – Texas.

Clifford P., et al, 2003. *Integration of 4D Seismic Data into the Management of Oil Reservoirs with Horizontal Wells between Fluid Contacts.* Offshore Conference Europe September 2003, Aberdeen UK.

Daher B., et al, 2007. *Jubarte Field – Development Strategy*. Offshore Technology Conference. Houston Texas May 2007.

Dan W., et al, 2009. *4D viability demonstration in SAGD test area – Liaohe Oil Field*. SEG Beijing 2009 International Geophysical Conference & Exposition.

Dolberg D., et al, 2000. *Porosity prediction from seismic inversion, Lavrans Field, Halten Terrace, Norway*. The Leading Edge. April 2000, pp. 392 – 399.

Eastwood J., et al, 1999. *Time-Lapse-Seismic Processing and Analysis: Gulf of Mexico Example, Lena Field*, Offshore Technology Conference, May 1999, Houston – Texas.

El-Emam A., 2006. *Time Lapse (4D) Seismic Studies in the State of Kuwait: History and Future*. 2006 SEG Annual Meeting, October 1 - 6, 2006, New Orleans, Louisiana.

Eneyok G., et al, 2003. *The Curlew Field, Block 29/7, UK North Sea.* Geological Society, London, Memoirs 2003, Vol. 20, pp. 509- 522.

Foster D., et al, 2008. *Building on BP's large-scale OBC monitoring experience—The Clair and Chirag-Azeri projects*. The Leading Edge, December 2008, pp. 1632 – 1637.

Hanson R., et al, 2009. *Analysis of time-lapse data from the Alba Field 4C/4D seismic survey*. Petroleum Geoscience January 2003 Vol. 9 no. 1, pp. 103-111.

Hamson G., 2012. *Leveraging 4D Seismic and Production Data to Advance the Geological Model of the Enfield Oil Field, Western Australia*. AAPG Annual Convention and Exhibition, California, April 2012.

Hudson T., et al, 2006. *Preliminary results of the Genesis Field Time-Lapse Seismic Project, Gulf of Mexico*. Offshore Technology Conference, May 2006, Houston – Texas.

Hurren C., et al, 2012. *Successful Application ff 4D Seismic in the Stybarrow Field, Western Australia.* SPE Asia Pacific Oil & Gas Conference and Exhibition, October 2012, Perth, Australia.

Jenkins C., et al, 2008. *Reservoir Definition at the Jansz/Io Gas Field, NW Shelf, Australia: A Case Study of an Integrated Project from Exploration to Development*. International Petroleum Technology Conference, December 2008. Kuala Lumpur – Malaysia.

Johann P., et al, 2009. *4D seismic in heavy-oil turbidite reservoir offshore Brazil*. The Leading Edge, June 2009, pp. 718 – 729

Kaleta N., 2001. *Time-Lapse (4D) Seismic investigation of the I3 and TA2 sands, Kilauea Field, Green Canyon Block 6, Gulf of Mexico*. Master Thesis in Pennsylvania State University.

Kovacic L. and Poggiagliomi E., 2003. *Integrated time-lapse reservoir monitoring and characterization of the Cervia Field: a case study*. Petroleum Geoscience, January 2003, Vol. 9, pp. 43 – 52.

Landro M., et al, 1999. *The Gullfaks 4D seismic study.* Petroleum Geoscience, Vol.5 no. 3, August 1999, pp. 213 – 226.

Li R., el al, 2006. *Prediction of 4D seismic responses for the Otway Basin CO2 sequestration site.* SEG 2006 Annual Meeting, New Orleans USA.

Lumbantobing S., et al, 2011. *Improving Oil Recovery and Injection Strategy in Shallow Reservoir (Rindu Reservoir) of Area 3,4 Duri Steam Flood.* SPE Asia Pacific Oil & Gas Conference and Exhibition, September 2011, Jakarta, Indonesia.

Lumley D., 2000. *Meren Field, Nigeria: A 4D seismic case study*. Offshore Technology Conference, May 2000, Houston, Texas.

Lumley D., 2010. *4D seismic monitoring of gas production and CO_2 sequestration, North West Australia.* PESA News, February-March 2010, pp. 14 – 17.

Magnus, K., et al, 2011. *Onshore 4D Processing: Niger Delta Example: Kolo Creek Case Study. 2011 SEG* Annual Meeting. Society of Exploration Geophysicists.

McGillivray P., 2004. *Microseismic and Time-Lapse Monitoring of heavy oil. Extraction process at Peace River*. SEG 2004, Expanded Abstracts.

Meyer R., 2001. *4-D seismic and time-lapse reservoir geology*. CREWES Research Report, Vol. 13, 2001, pp. 895 - 906.

Mitchell P., et al, 2009. *4D seismic in deep water at the Dikanza field, offshore Angola, West Africa*. SEG Expanded Abstracts 2009, Vol. 28

Moneam A., et al, 2004. *4D seismic monitoring of the miscible CO2 flood of Hall-Gurney Field, Kansas, U.S.* The Leading Edge, November 2004, pp. 1171 – 1176.

Mudi K., et al, 2012. *Effective an innovative approach to integrating static and dynamic data: a key to volumes optimization in Erha Field.* SPE Nigerian Annual International Conference and Exhibition, August 2012, Abuja, Nigeria.

Narayanasamy R., et al, 2010. *Wellbore-instability predictions within the Cretaceous Mudstones of Clair Field, west of Shetlands*. SPE Drilling & Completion, Vol. 25, no. 4, pp. 518 – 529.

Onuwaje A., et al, 2009. *The Bonga 4D – Shell Nigeria´s First Deep Water Monitor.* 71st EAGE Conference & Exhibition, Amsterdam 2009.

Ritchie B., et al, 2002. *The impact of new 4D Seismic technology on the Magnus Field.* SEG International Exposition and Annual Meeting, October 2002, Salt Lake City, Utah.

Roggero F., et al, 2012. *History Matching of Production and 4D Seismic Data: Application to the Girassol Field, Offshore Angola*. Oil & Gas Science and Technology – Rev. IFP Energies nouvelles, Vol. 67 no. 2, 2012, pp. 237-262

Saller A., et al, 2012. *Contrasting Styles of San Andres Reservoirs: Vacuum versus Slaughter Fields, Middle Permian, West Texas and Southeast New Mexico.* AAPG Annual Convention and Exhibition, Long Beach, California, USA, April 2012.

Sullivan M., et al, 2004. *An integrated approach to characterization and modeling of deep-water reservoirs, Diana field, western Gulf of Mexico, in Integration of outcrop and modern analogs in reservoir modelling*: AAPG Memoir 80, pp. 215– 234.

Vedanti N. and Sen M., 2009. *Seismic inversion tracks in situ combustion: A case study from Balol oil field, India.* GEOPHYSICS, Vol. 74(4), July 2009.

Vedanti N., et al,, 2009. *Time Lapse (4D) Seismic: Some Case Studies. Journal Earth Science India,* Vol.2 (IV) October, 2009, pp. 230 – 248.

Verlo S. and Hetland M., 2008. *Development of a field case with real production and 4D data from the Norne Field as a benchmark case for future reservoir simulation models testing.* Master Thesis, NTNU, Norway.

Woock R., et al, 2011. *Quantifying bypassed pay through 4D post-stack inversion*. AAPG, April 2011.

www.abarrelfull.wikidot.com

www.bg-group.com

www.bp.com

www.chevronaustralia.com

www.cggveritas.com

www.conocophillips.com

www.exxonmobile.com

www.ng.total.com

www.offshore-technology.com

www.petoro.no

www.petrobras.com

www.seg.org

www.statoil.com

www.wgpgroupltd.com

www.woodside.com.au

Appendix B

Concepts of Shale Pressure Diffusion

This appendix contains the general equations that describe the process of pressure diffusion in shales, for the different sand-shale geometries presented in this work: linear depletion for a semi-infinite model and linear depletion for a single layer (interbedded between sands).

B.1 Pore pressure diffusion

Assuming the presence of a homogeneous porous medium containing one or more slightly compressible fluid phases, the analytic 1D solution to the pressure diffusion can be solved by the equation [*Crank*, 1975]

$$\frac{\partial P}{\partial t} = D\frac{\partial^2 P}{\partial X^2} \tag{B.1}$$

where P is the pore pressure, t the time, X the spatial coordinate. D is the diffusivity coefficient that is given by the relation

$$D = \frac{\lambda}{\phi C_t} \tag{B.2}$$

where ϕ is porosity, C_t is total compressibility (rock + fluid) and λ is the fluid mobility given by

$$\lambda = \frac{k.k_r}{\mu} \tag{B.3}$$

where k is permeability, k_r is relative permeability and μ is the fluid viscosity.

B.2 Shale pressure diffusion scenarios

According to the sand-shale geometry (see figure below), the pore pressure diffusion in shales can be modelled analytically as a linear process.

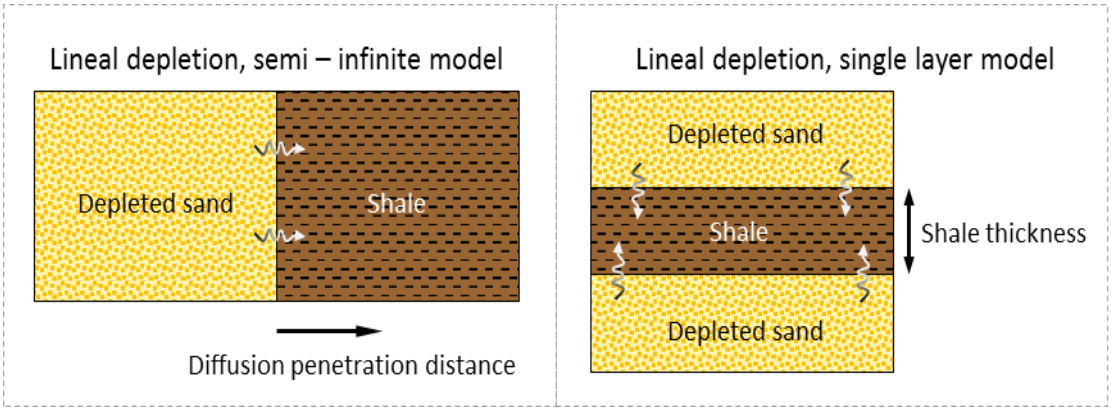

B.2.1 Linear depletion: semi-infinite model

This model represents the pressure diffusion for sideburden, overburden and underburden shales. If the depletion is considered as homogeneous, the pore pressure in the shales as a consequence of their interaction with the reservoir sands will decrease linearly as a function of time. Considering a period of time t =0 < than time of depletion, Tp, the solution to the semi-infinite problem is [*Crank*, 1975]

$$P_{sh}(x,t) - P_{sand} = t\left(\frac{\Delta P}{T_p}\right)\left|\left(1+\frac{x^2}{2Dt}\right)\left(1-erf\left(\frac{x}{2\sqrt{Dt}}\right)\right) - \frac{x}{2\sqrt{\pi Dt}}exp\left(-\frac{x^2}{4Dt}\right)\right| \quad \text{(B.4)}$$

where P_{sh} is shale pore pressure, P_{sand} is sand pore pressure, ΔP is the amount of depletion in shale and Dt is the elapsed time for depletion.

Yesser HajNasser, a previous ETLP student who worked on this topic, derived an equation to estimate the penetration of a pressure drop in the shale equivalent to 10% of sand depletion.

$$X = \left(1-\frac{T_p}{t}\right)\sqrt{\frac{k.t}{\phi C_t \mu}} \quad \text{(B.5)}$$

where X is the distance of penetration

B2.2 Linear depletion: single shale layer

Under this model the analytical solution for the pressure diffusion in intra and inter-reservoir shales with a layer of thickness L and $0 \leq z \leq L$ is represented. The depletion can be estimated by a series of damped sinusoids [*Crank*, 1975]

$$P_{sh}(z,t) - P_{sand} = \Delta P\left|1 - \sum_{n=0}^{\infty} b_n e^{-\frac{(2n+1)^2\pi^2\alpha t}{L^2}} \sin\big((2n+1)\pi z\big)\right| \quad \text{(B.6)}$$

where

$b_n = 4/(2n+1)\pi$. (B.7)

Appendix C

Wavelet extraction procedure

This section show the workflow used in the Hampson & Rusell Suite software to perform the wavelet extraction in each field application, using two methods, *Statistical Extraction* using seismic data and *Extraction Using Wells* and seismic data.

To define the wavelet used as input in the Sim2Seis convolutional workflow, the Hampson&Rusell Suite software was used to perform the wavelet extraction in each field application, using two methods, *Statistical Extraction* using seismic data and *Extraction Using Wells* and seismic data. The extracted wavelets were used to produce several well-tie in the field using always the pre-production full-stack seismic volumes and the cross-correlation (degree of match between produced synthetic traces with the wavelet and the observed seismic in the well location for a specific time window) was evaluated for both methods. The wavelet with the best correlation coefficient in each field was selected as the most representative of the seismic volume and used as Sim2Seis input.

Statistical Extraction method

The first step is to selectin the basic tab (see figure below) the seismic volume (pre-production), trace range (all the volume or just the area of interest), the time window interval (usually 200 ms above and below the reservoir interval), name and wavelet length (200 ms).

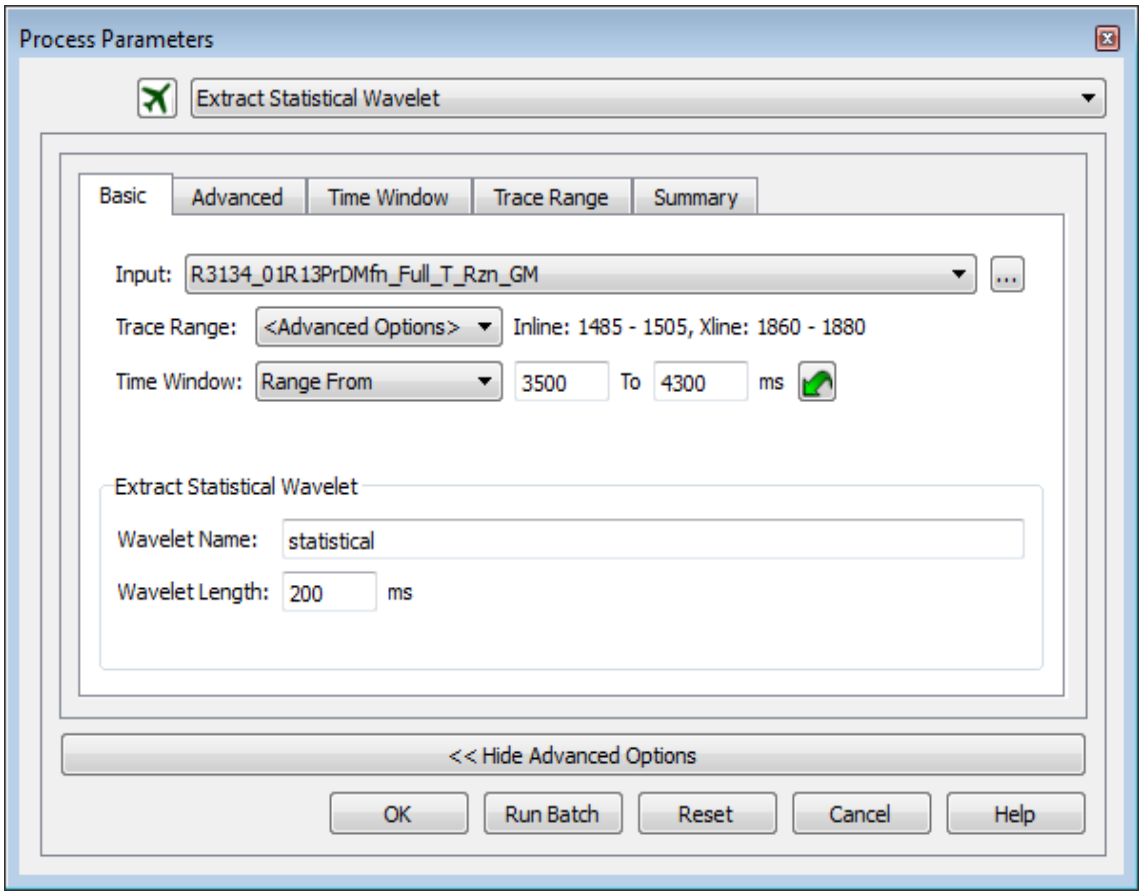

In the advanced tab, the taper length, phase rotation and phase type can be defined and then run the Extract Statistical Wavelet workflow.

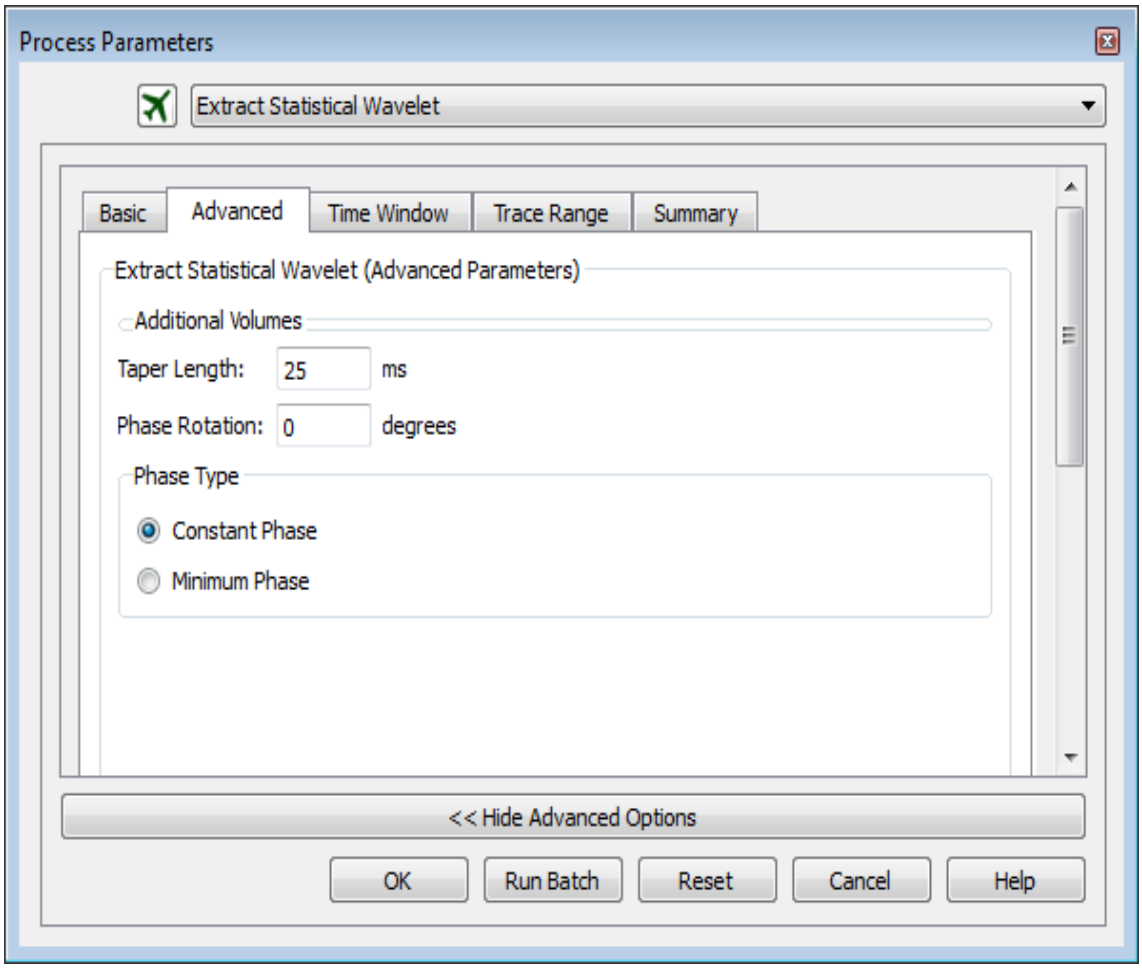

Statistical Extraction method

The first step is to selectin the basic tab (see figure below) the seismic volume (pre-production), the time window interval (usually 200 ms above and below the reservoir interval), select the well or wells used for extraction, name, wavelet length (200 ms) and extraction type (in this project the Roy White Algorithm was used).

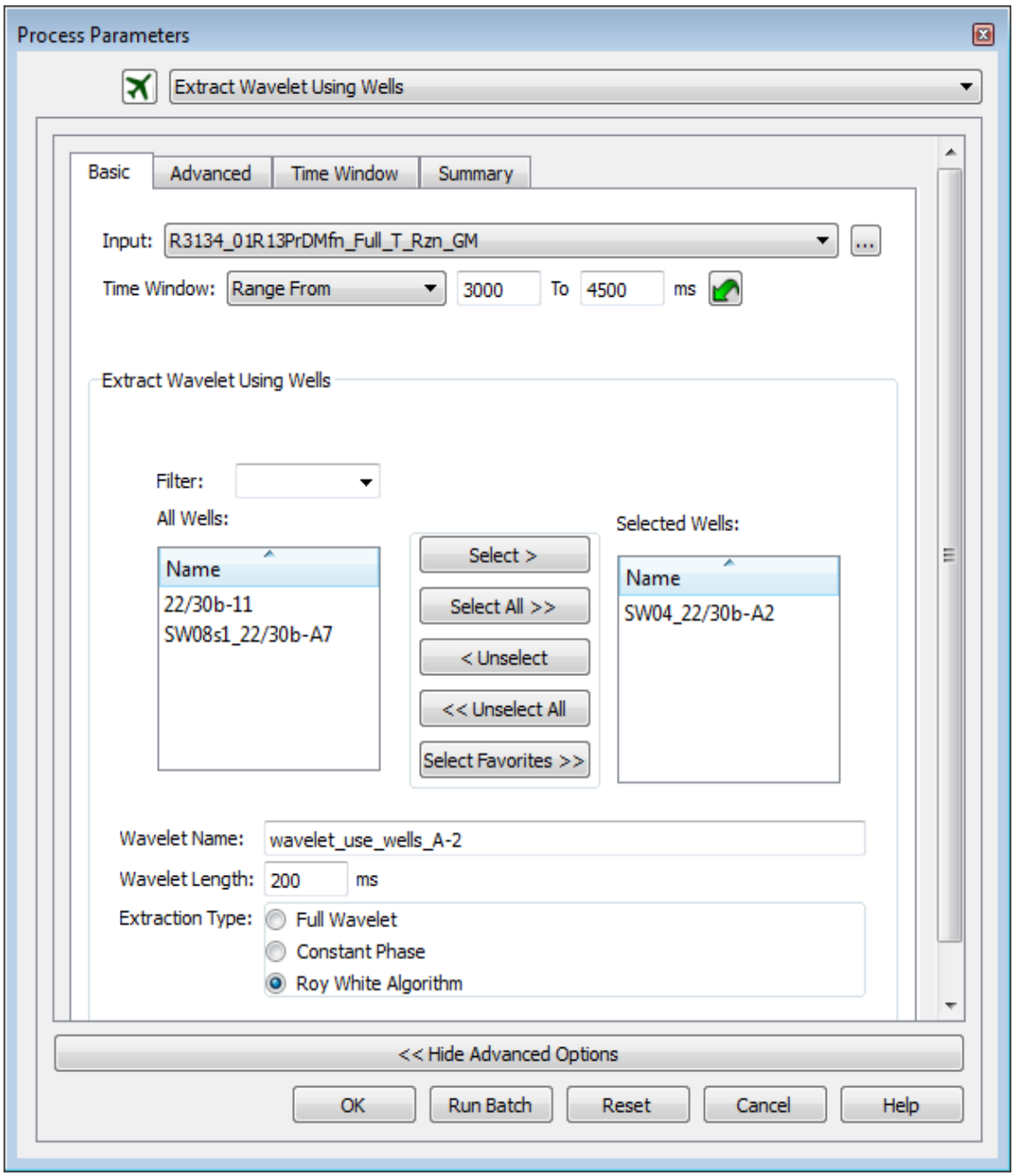

Then in the advanced tab, the taper length, frequency smoother, white noise factor and neighbourhood radius (or distance), and then run the workflow

According to the highest correlation coefficient achieved by a specific method, the Heidrun Field wavelet was extracted by statistical method, while Girassol, Schiehallion and Shearwater were extracted using wells and the Roy White extraction method.

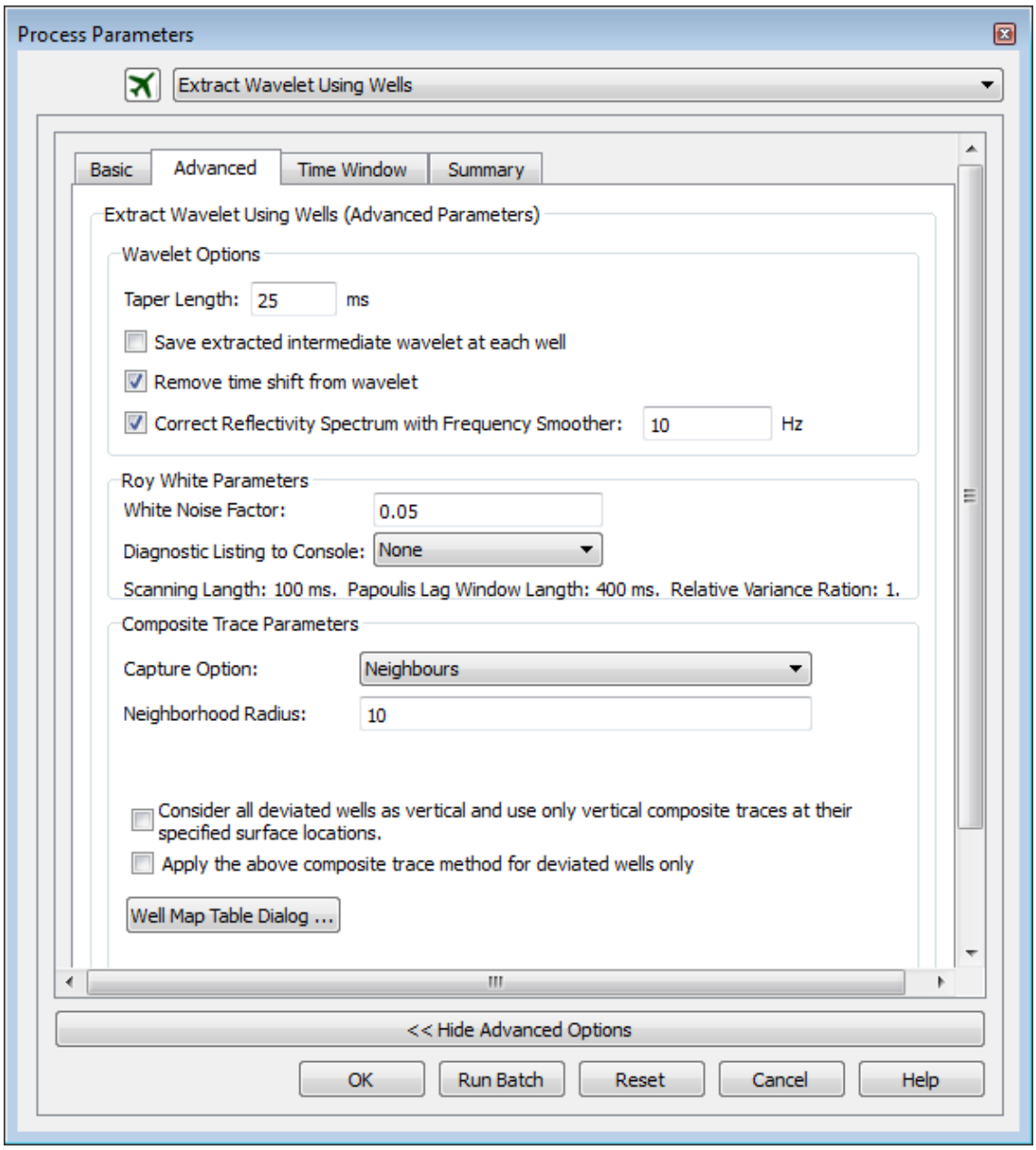
Process Parameters
Extract Wavelet Using Wells
Basic
Advanced
Time Window
Summary
Extract Wavelet Using Wells (Advanced Parameters)
Wavelet Options
Taper Length: 25 ms
Save extracted intermediate wavelet at each well
Remove time shift from wavelet
Correct Reflectivity Spectrum with Frequency Smoother: 10 Hz
Roy White Parameters
White Noise Factor: 0.05
Diagnostic Listing to Console: None
Scanning Langth: 100 ms. Papoulis Lag Window Langth: 400 ms. Relative Variance Ration: 1.
Composite Trace Parameters
Capture Option: Neighbours
Neighborhood Radius: 10
Consider all deviated wells as vertical and use only vertical composite traces at their specified surface locations.
Apply the above composite trace method for deviated wells only
Well Map Table Dialog ...
<< Hide Advanced Options
OK
Run Batch
Reset
Cancel
Help

Appendix D

Publications

This section comprises two conference papers presented at the Society of Exploration Geophysicists (SEG) Annual Meeting and Exhibition at New Orleans in 2015 and the European Association of Geoscientists & Engineers (EAGE) Annual Meeting and Exhibition at Vienna in 2016

.

The role of shale pressure diffusion in 4D seismic reservoir monitoring – case studies

Ricardo Rangel and Colin MacBeth, Edinburgh Time Lapse Project – Heriot Watt University*

Summary

The low but non-negligible permeability of shale enables pressure diffusion; the elastic implications of this process are sizeable over the production lifetime and can be recorded by time-lapse seismic monitoring (Ricard et al. 2012). To assess this effect our study include the internal architecture analysis of the shale in the 3D and 4D seismic modeling of two field applications: a shallow marine and a turbidite reservoir, where shale permeability, sand – shale geometry, time, reservoir connectivity and compartmentalization, determinate the impact of pressure diffusion in generating 4D signal related to changes in saturation (gas coming out of solution) and pressure.

Introduction

Intrinsic properties have made shales regarded as impermeable rocks, and certainly conventional fluid flow through pure shales is almost negligible during hydrocarbon production time scale. This is the reason why they are not represented in reservoir simulation models (inactive cells). Classical reservoir characterization treats all shales as pure mudstones (almost 100% clay), when most intra and inter-reservoir shales are heterogeneous and anisotropic. Shale permeability, even when it's in the order of few nanodarcys allow pressure diffusion, which impacts the production induced elastic changes in the reservoir recorded in time – lapse seismic monitoring (MacBeth et al. 2011, Ricard et al. 2012).

To evaluate pressure diffusion in shale and its effect on the reservoir 4D signal, the approach of this study is to include the internal sedimentological structure of the shale in the classical 3D and 4D seismic modeling workflow (figure 1). The start point is to recognize how the geological and simulation models represents shales and how these make them active, populating shale cells with static (NTG, porosity) and dynamic properties (permeability and transmissivity), estimated with a detailed geological analysis, upscaling and honoring the log data. Including lithological and fluid flow heterogeneity inside shales in the simulation model enables pressure and fluid interaction (flow almost null) with the reservoir. To analyze the effect of this process, simulation outputs and rock physics analysis applied to shale are integrated in synthetic seismic modeling.

Comparison of 4D synthetic seismic responses of active and inactive shale models with the real 4D seismic, will test the effect of the pressure diffusion process in shales in order to determine if they are really active or not, improving the understanding of the reservoir elastic behavior, its compartmentalization and connectivity.

To show how different shale architecture and sand – shale geometry interphase can impact in the pressure diffusion evolution and its elastic implications, in this study we are presenting two field applications: a Middle Jurassic Norwegian Sea shallow marine – deltaic reservoir with a fault tilted block configuration where sand and shale are distributed in a simple layer cake model geometry; and an unconsolidated Oligocene turbidite reservoir from West Africa Offshore that consists in stacked and amalgamated turbidite sand channels with shale as background. Shale activation in both fields produce interesting results in the 4D signal related to changes in saturation (gas coming out of solution) and pressure.

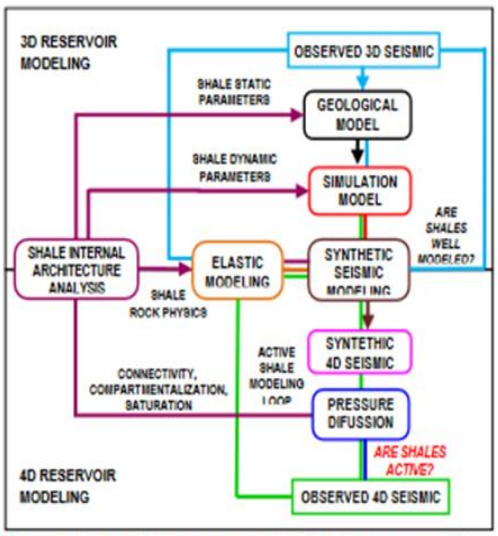

Figure 1: Shale architecture analysis in 3D&4D seismic modeling.

Shale internal architecture analysis

Compared with sandstones that are usually regarded as monomineralic (quartz) rocks with a saturated pore space, shale composition and heterogeneous properties are more complex and require a detailed characterization. The first step is to recognize that most intra and inter-reservoir shales are not pure mudstones, the 'shale base line' commonly used in petrophysical evaluations to represent 100% pure shale, had to be redefined because most shales do have NTG ≠ 0, common interbedded silt and fine sand laminations inside of shales constitute preferential permeability paths favoring pressure diffusion and fluid

DOI http://dx.doi.org/10.1190/segam2015-5705931.1

flow through this lithology. When shale characterization is performed it is necessary to differentiate between overburden, underburden, sideburden, intra and inter-reservoir shale, because sedimentary processes involved in each shale type deposition usually are different depending on shale composition and internal architecture. As laboratory data was not available for the study cases to determinate shale composition, a regional analysis was done coupled with an intensive log data characterization to establish mineralogy and clay provenance. Once that clay type and content was established, shale property estimation was performed following these equations (figure 2) and using log data.

NTG estimation

$$NTG = 1 - V_{sh}$$

$$V_{sh} = \frac{GR - GR_{clean}}{GR_{shale} - GR_{clean}}$$

where
V_{sh} is volume of shale
GR_{clean} is value for cleanest sand
GR_{shale} is value for purest shale

Porosity estimation

$$\phi = \frac{\rho_m - \rho_{sat}}{\rho_m - \rho_w}$$

where
ρ_{sat} is saturated density from log
ρ_m is shale's matrix density
ρ_w is water density

$$\rho_m = (\rho_{clay\,mixture} * Vol_{clay}) + (\rho_{silt\,mixture} * Vol_{silt})$$

Permeability estimation (Yang & Aplin, 2007)

$$Kv = 10^{19.21} J_v^{1.110} r^{1.074} \quad \text{(vertical permeability)}$$

$$Kh = (c\tan(\alpha))^{2.236} Kv \quad \text{(horizontal permeability)}$$

$$J_v = \frac{9}{8} \phi (\sin\alpha)^2 \frac{J_1^3}{(1 + J_1 + J_1^2)^2}$$

$$J_1 = 2.371 \quad 1.62CF^2 + 153.8\phi^4$$

(ratio of the largest radius of a pore to its throat radius)

where
CF = Clay fraction (from total volume rock)
ϕ = Porosity (fraction)
r = Pore throat ratio (nm)

$$r = \frac{746}{P} \quad \text{(Lapierre et al., 1990)}$$

P is pressure (MPa)
α is pore alignment angle relative to bedding direction (degree)

$$\alpha = 45° - 10.24°(e_{100} - e) \qquad \sigma > 100kPa$$

$$\alpha = 45° \qquad \sigma \leq 100kPa$$

$$e = \frac{\phi}{1 - \phi} \text{ (void ratio)} \qquad e_{100} = \frac{\phi_0}{1 - \phi_0} \text{ (void ratio at 0.1 MPa)}$$

$$\phi_0 = 0.8 \frac{Vol_{clay}}{Vol_{solids}} + 0.4 \frac{Vol_{quartz}}{Vol_{solids}} \quad \text{(Ruud et al., 2003)}$$

Figure 2: Equations for shale property estimation

Study cases

Norwegian Sea shallow marine reservoir:

Field description: Producing since 1995, this offshore oil (28° API) & gas reservoir consists of good quality sandstones deposited in Middle Jurassic in deltaic and shallow marine environments separated by episodic transgressive shales. As result of the stratigraphic and structural (fault tilted blocks) configuration the reservoir is highly compartmentalized. The field dataset available for this study consist of geological and simulation models (production data from 1995 to 2011), well logs, four 3D seismic surveys and five 4D seismic surveys (2001, 2004, 2006, 2008 and 2011).

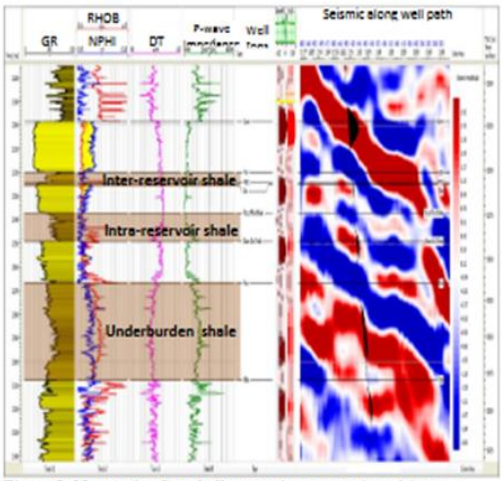

Figure 3: Norwegian Sea shallow marine reservoir architecture

Shale modeling: with clay fraction established as an illite (60%) – montmorillonite (40%) mixture, shale properties estimation was performed and inactive cells (in simulation model) populated with averaged and upscaled values. For shale relative permeability and capillary pressure tables, laboratory data from shale gas injection tests (Sigal, 2013) was used to correlate pore throat geometry between shales.

Pressure and saturation results: with vertical permeabilities as low as 5nD, after 9 years of production, pressure equilibrium between reservoir sands and shales start to be reached (figure 4), first in thinner shales (6 metres thick inter-reservoir shale) in small blocks and then (after 11 years) in thicker ones (15 metres thick intra-reservoir shales).

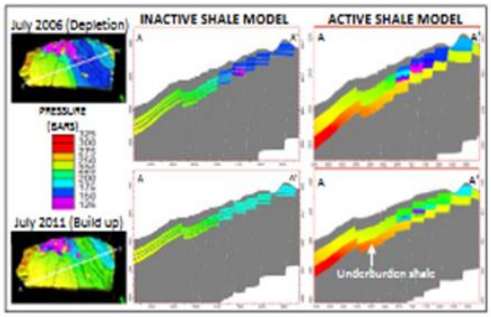

Figure 4: Pressure evolution for inactive and active shale models

DOI http://dx.doi.org/10.1190/segam2015-5705931.1

After 16 years of production, none pressure diffusion was observed in the underburden shale. Control simulation model with shales inactive, showed more gas coming out of solution in small reservoir compartments and higher pressure depletion in top structure blocks.

West Africa turbidite reservoir

Field description: producing since 2001. This offshore oil (32° API) field consists in unconsolidated, stacked and amalgamated turbidite sand channels with shale as background deposited during Oligocene. Due thickness (250 metres) shale compaction trend has important elastic implications. The field dataset for this study include simulation model (production data from 2001 to 2004), well logs, a preproduction 3D seismic survey (1999) and two 4D monitors (2002 and 2004).

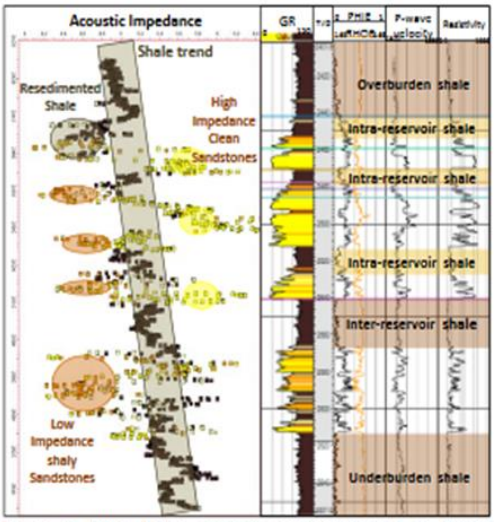

Figure 5: West Africa reservoir architecture and its P-wave impedance expression

Shale modeling: water saturated shales elastically softer than light oil saturated sands (figure 5), not only have to be unconsolidated; also the clay fraction needs to be light as well. Regional clay provenance analysis established shale's clay fraction for this field in 50% kaolinite (slow clay material, Mavko et al 2009) and 50% illite. Following the elastic behavior, overburden, inter-reservoir and underburden shales where modeled with the same compaction trend (deposition dominated for pelagic processes); while intra-reservoir shales (deposited as re-settle particles, suspended from the turbidite flow) where modeled with higher clay content and with a different compaction trend (even softer). Relative permeabilities and capillary pressure also was correlated from shale gas laboratory data.

Pressure and saturation results: Initiating with computed permeability values of Kv =7 nD and Kh = 20 nD, none pressure diffusion into shales was appreciated. Rising permeability values over Kv = 25nD and Kh = 200nD pressure diffusion start to happen after 8.5 years, changes occurs in shale cells nearby sands (almost only direct contact, figure 6). Pressure diffusion was in the range of 10 – 20 bars, with maximum vertical penetration of 20 metres and horizontal of 100 metres (2 cells). Diffusion was observed only in intra-reservoir shales (probably because overburden and underburden cells grid are too coarse. There was no substantial change in saturation between inactive and active shale models.

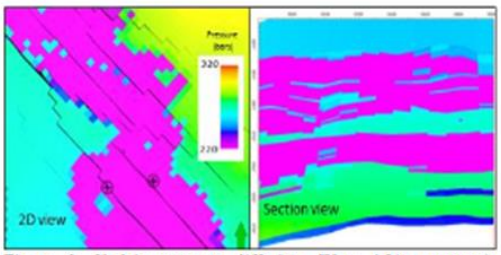

Figure 6: Shale's pressure diffusion, West Africa reservoir (pressure scale saturated to show diffusion)

Elastic modeling

To perform synthetic seismic model for inactive and active shale models in both fields we use Sim2Seis (in-house simulator to seismic code). As each reservoir simulation model represented heterogeneity in a particular way, the elastic modeling was different for each study case; for the shallow marine reservoir we define elastic properties for the lithological end members (cleanest sand and purest shale), and for each cell the code perform sand – shale property mixing (according to NTG distribution); while for the turbidite reservoir the elastic parameters were defined by saturation regions, additional regions were created for shales, one for overburden, sideburden underburden and inter-reservoir shales, and another for intra-reservoir ones. For both fields, the stress sensitivity was modeled using MacBeth (2004) effective pressure dependent equations, including shale compaction trends for the turbidite reservoir.

Results

Including shales active in the 3D seismic modeling improves the quality of the synthetic seismic for both study cases; sand – shale amplitude contrast is captured better, and reservoir seismic thickness is more accurate. The seismic analysis for the Norwegian Sea reservoir, shows 4D signal pressure related above seismic noise level for the inactive shale model in the highest reservoir block (green

DOI http://dx.doi.org/10.1190/segam2015-5705931.1

oval on figure 7), where depletion is stronger, signal that is absent in the real 4D seismic and in active shale synthetic seismic, in fact, 4D signal related with depletion is not commonly reported; in this case, better reservoir connectivity in terms of pressure is indicative of the active character of shales in this field.

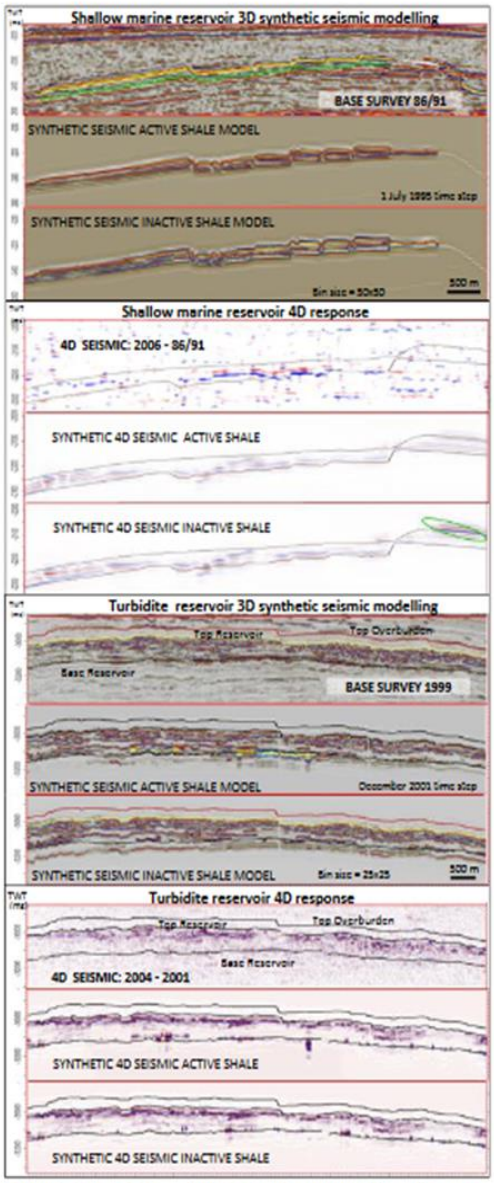

Figure 7: 3D and 4D synthethic seismic responses for study cases

In the case of the West Africa turbidite reservoir, the 4D signals for synthetic seismic with active and inactive shale are quite similar (differences at the base reservoir are related to grid changes during shale activation process, figure 7) even extending the simulation to 2009 (2001 to 2004 is a period too short to evaluate 4D signal related to pressure diffusion on shale). As in this field sands are very well connected, depletion induced by production is quickly equilibrated along the reservoir, the pressure imbalance between sand and shale is lower and shales activation is not producing any effect in the 4D seismic signal (at least with the data available for this study).

Conclusions

Honoring shale internal architecture in the 3D and 4D seismic modeling enhances the understanding of the reservoir's elastic behavior; differentiation between types of shales, its distribution and property variations allows better synthetic seismic imaging. With the study of these datasets it is clear that pressure diffusion in shales not only depends on the shale permeability, but also time. Other factors are shale – reservoir geometry (that define pressure diffusion fronts), connectivity and reservoir compartmentalization (figure 8). The role of shales as active part of the reservoir and its sizeable effect on 4D seismic during production lifetime is going to vary from one geological scenario to another and with reservoir sensitivity to changes in pressure.

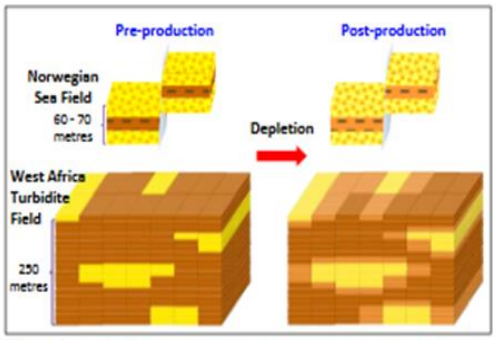

Figure 8: Sand–shale geometry and reservoir compartmentalization as determinant parameters for pressure diffusion into shales.

Acknowledgments

We thank the sponsors of the Edinburgh Time Lapse Project, Phase V, for their support (BG, BP, Chevron, CGG, ConocoPhillips, ENI, ExxonMobil, Hess, Ikon Science, Landmark, Maersk, Nexen, Norsar, RSI, Petoro, Petrobras, Shell, Statoil, Suncor, Taqa, TGS and Total). Thanks are extended to Schlumberger for providing the Petrel and Eclipse software.

DOI http://dx.doi.org/10.1190/segam2015-5705931.1

EDITED REFERENCES

Note: This reference list is a copyedited version of the reference list submitted by the author. Reference lists for the 2015 SEG Technical Program Expanded Abstracts have been copyedited so that references provided with the online metadata for each paper will achieve a high degree of linking to cited sources that appear on the Web.

REFERENCES

Lapierre, C., S. Leroueil, and J. Locat, 1990, Mercury intrusion and permeability of Louiseville clay: Canadian Geotechnical Journal, **27**, no. 6, 761–773, http://dx.doi.org/10.1139/t90-090.

MacBeth, C., 2004, A classification for the pressure-sensitivity properties of a sandstone rock frame: Geophysics, **69**, 497–510, http://dx.doi.org/10.1190/1.1707070.

MacBeth, C., Y. HajNasser, K. Stephen, and A. Gardiner, 2011, Exploring the effect of meso-scale shale beds on a reservoir's overall stress sensitivity to seismic waves: Geophysical Prospecting, **59**, no. 1, 90–110, http://dx.doi.org/10.1111/j.1365-2478.2010.00897.x.

Mavko, G., T. Mukerji, and J. Dvorkin, 2004, The rock physics handbook: Cambridge University Press.

Ricard, L., C. MacBeth, Y. HajNasser, and P. Schutjens, 2012, An evaluation of pressure diffusion into a shale overburden and sideburden induced by production-related changes in reservoir fluid pressure: Journal of Geophysics and Engineering, **9**, no. 3, 345–358, http://dx.doi.org/10.1088/1742-2132/9/3/345.

Ruud, B., M. Jakobsen, and T. A. Johansen, 2003, Seismic properties of shales during compaction: 73rd Annual International Meeting, SEG, Expanded Abstracts, 1294–1297, doi:10.1190/1.1817522.

Sigal, R. F., 2013, Mercury capillary pressure measurements on Barnett core: SPE Reservoir Evaluation & Engineering, **16**, no. 4, 432–442, http://dx.doi.org/10.2118/167607-PA.

Yang, Y., and A. Aplin, 2007, Permeability and petrophysical properties of 30 natural mudstones: Journal of Geophysical Research, **112**, B03206, http://dx.doi.org/10.1029/2005JB004243.

DOI http://dx.doi.org/10.1190/segam2015-5705931.1

Th LHR2 01

The Effect of Shale Activation on 4D Seismic Interpretation of a UKCS Field

R. Rangel* (ETLP - Heriot-Watt University), C. MacBeth (ETLP - Heriot-Watt University) & M. Mangriotis (ETLP - Heriot-Watt University)

SUMMARY

Shale typically has a low but non-negligible permeability of the order of nanodarcys that could affect magnitude and pattern of pressure diffusion over the lifetime of a producing field. The implications of this phenomenon for reservoir monitoring by 4D seismic can be significant, but depend on the geology of the field, the time-lines for production and recovery, and the timing of the seismic surveys. This study assesses pressure diffusion effects for an offshore Paleocene turbidite reservoir in the UKCS. First, we evaluate the petrophysical characteristics of the overburden, intra-reservoir and underburden shales. Next, we adjust the simulation model to activate the shale-related contributions, and then perform 3D and 4D seismic modelling. In our reservoir of interest, fluid flow simulation results indicate that gas dominates the 4D seismic signature. It is found that activation of the shale improves the overall reservoir connectivity, which in turn impacts strongly on the breakout and distribution of gas liberated from solution and improves the fit to the observed seismic data.

Introduction

Well known intrinsic property values have contributed to shales being regarded as impermeable rocks during modelling and simulation. This is considered valid as conventional fluid flow through pure shales is almost negligible during the hydrocarbon production time scale. This is the reason why they are represented in reservoir simulation models as inactive cells. Classical reservoir characterisation treats all shales as pure mudstones (almost 100% clay), when most intra and inter-reservoir shales are heterogeneous and anisotropic. It has been shown that shale permeability, even an order of a few nanodarcys, permits pressure diffusion that impacts production induced elastic changes in the reservoir recorded in time–lapse seismic monitoring (MacBeth et al. 2011). To further evaluate pressure diffusion in shales and the effect on 4D reservoir signatures, the approach of this study is to include the internal architecture of the shale in the classical 3D and 4D seismic modelling workflow. The start point is to recognize how the geological and simulation models represent shales and how to make them active, populating shale cells with static (NTG, porosity) and dynamic properties (permeability and transmissivity), estimated with a detailed geological analysis, upscaling, and honouring the log data. In this workflow, the modelling of shale's capillary pressure inhibit fluid interaction between shales and reservoir (pressure gradient is not high enough to change shale's saturation). Activating shales in the simulation model enables pressure diffusion with the reservoir, to analyse the effect of this process, simulation model outputs are used to perform synthetic seismic modelling. The mismatch between the observed 4D and the synthetic seismic responses for inactive and active shale models is compared to determinate the degree of shale contribution to the reservoir dynamic behaviour.

Field dataset

Our field of interest is an offshore oil and gas field located in the United Kingdom Continental Shelf, approximately 130 kilometres West of Shetland Islands in the North Atlantic Ocean. Discovered in 1993 and on stream since 1998, the reservoir is a Tertiary live black oil accumulation (25° API) with small local gas caps, developed under a down-dip water injection plan. The reservoir consist in stacked turbidite channels with good quality (porosities between 25 – 30% and permeabilities between 200 – 1000 mD). The turbidite sequences were deposited from North to South and are cross-cut by several W-E normal faults that divides the reservoir in four compartmentalised segments (Figure 1). In this case study, shales were activated only for Segment 1.

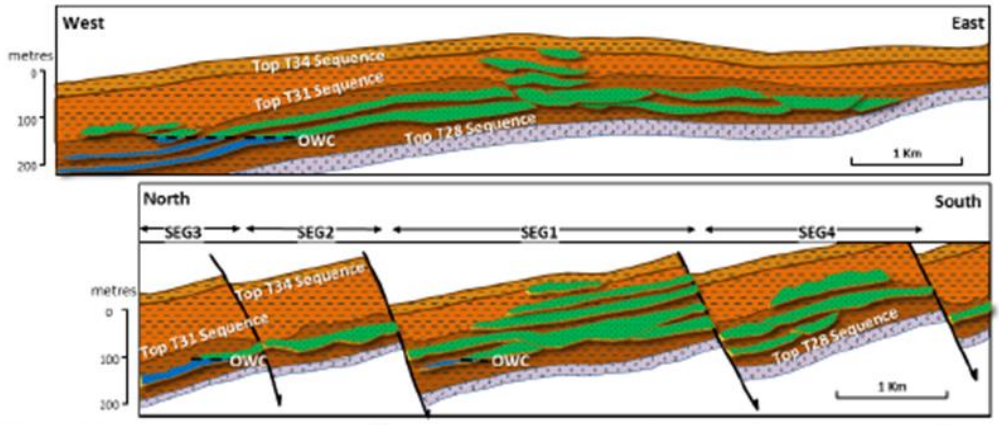

Figure 1 Structural configuration for UKCS field used in this study. Redrawn from Leach et al. 1999.

For the shale activation workflow, the dataset available for this study consisted of well log data, simulation model history matched to production data from August 1998 to January 2009, and the seismic data (1996 baseline, 2004, 2006 and 2008 monitor surveys).

Shale internal architecture and properties

Deep marine sediments are usually very well sorted. The distance from sediment source influx and frequency of high energy events are the parameters that determine the vertical variability in the sediments (lateral distribution can be very uniform). The internal architecture of shales associated with turbidite reservoirs is the consequence of the mixture of the energy regimes, between the permanent pelagic conditions (clay flocculation and settlement process never stops) and the episodic turbidite flows. To analyse the characteristics of shales in our field we use gamma ray well logs and compute volume of shale to establish lithological heterogeneity. Density and P-wave velocity logs determinate acoustic properties that are useful to identify sedimentation settlement patterns and compaction trends. According to these variations, shales in this field can be categorised from top to base in the following groups: overburden, inter-reservoir, intra-reservoir and underburden shales. An equal number of geobodies were created to represent these and to establish their transmissivities with the reservoir. As laboratory data is not available for this study to determinate shale composition, a regional analysis is performed coupled with an intensive log data characterisation to establish mineralogy and clay provenance. Shales in this field have an average composition of 65% clays and 35% of silt. Paleogeographic and sediment source analysis established that the clay fraction of shales in this area are dominated by illite (around 60% of clay volume), with a variable distribution of montmorillonite (more abundant at the base) and chlorite. Once that clay type and content was defined, shale static and dynamic properties are calculated by rock physics analysis and applying the empirical equations of Yang and Aplin (2007). The range of estimated values for the properties used to populate shale cells in simulation models is given in the table 1.

NTG	Porosity	Horizontal Permeability	Vertical Permeability
0.07 – 0.16	0.14 – 0.16	30 – 100 nD	7 – 14 nD

Table 1 Range values for the static and dynamic properties for the shales in our field of interest.

Reservoir modelling

In order to evaluate the effect of shales in this dataset, not only are inactive cells activated, but also the geometry of the simulation model is modified. 20 layers with constant thickness (1 metre) are added at the top of the reservoir as overburden, also 20 layers more are added to the base as the underburden. The lateral geometry and boundaries of the selected field segment are kept as originally delineated. The shale fluid-flow properties of capillary pressure and relative permeability are calculated using results from shale gas injection tests (Sigal, 2013) with similar pore throat geometry. Shale saturation (100% water) and pressure, were modelled creating an additional for the geobodies containing the different types of shales. Transmissivities were defined as only permeability dependent, so the value assigned for shale transmissibility was 1 between shale geobodies and the reservoir. Rock compaction tables and stress sensitivity were modelled using the equations of MacBeth (2004) for pressure dependence. To determine the impact on the reservoir connectivity four models were considered: an inactive (control), active shale model, and two equals' models (active and inactive shale) with all transmissivity multipliers removed.

Pressure and saturation and production results

Because time dependency of shale pressure diffusion process, saturation and pressure results were studied at the end of the simulated period (10 years of production/injection). Regarding pressure changes, in the active shale models the build-up signal corresponding to water injection is spatially more extended and production induced depletion is lower due the addition of extra volume to the reservoir. Variations in saturation for active shale models display less gas exsolution in channels facies, but more in the overbank/levee deposits. Total oil, gas and water production (Figure 2) for the models without the transmissivity multipliers gave a better match to the historical production data when shales are activated. This indicated that for this field, the use of some multipliers appeared to be compensating for the effect of the shale.

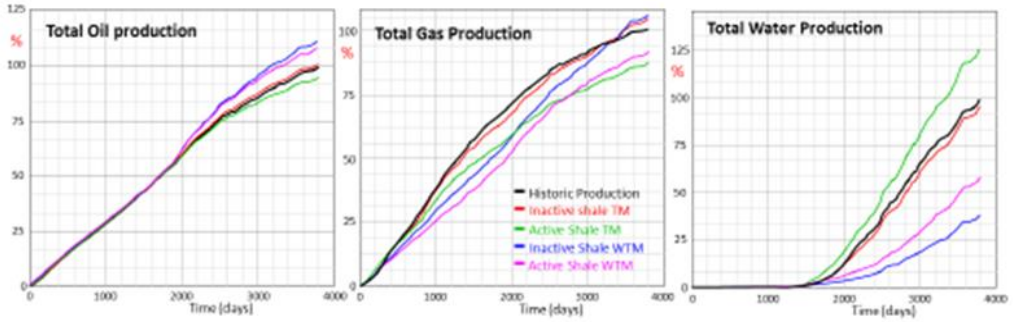

Figure 2 Total oil, gas and water normalized production for the modelled scenarios, historic production data displayed as reference (black line that represent the accumulated 100%).TM=transmissivity multipliers included, WTM=transmissivity multipliers removed.

Synthetic seismic modelling and 4D response

Simulator to seismic modelling is performed for the four scenarios, and 4D seismic differences computed between pre-production in August 1998 and August 2008, and these are compared with the observed 4D seismic response (Figure 3). The predicted 4D signal for active shale models not only better fits the hardening response (that is strongly influenced by the application of transmissivity multipliers), also the distribution of the softening signal is more accurate. This implies that pressure connectivity between reservoir facies through shales plays an important role in the process of gas exsolution. Indeed the distribution of the observed softening (Figure 3) matches the spatial distribution of the levee facies very well (see dark blue facies with NTG=0.2 in Figure 4). In the original model these are not connected to channel geobodies. Shale activation, creates a degree of pressure connectivity between those facies and as the reservoir's pressure (200 bars) is very close to bubble point (194 bars), any induced depletion will produce gas exsolution and consequently soften the 4D seismic signal.

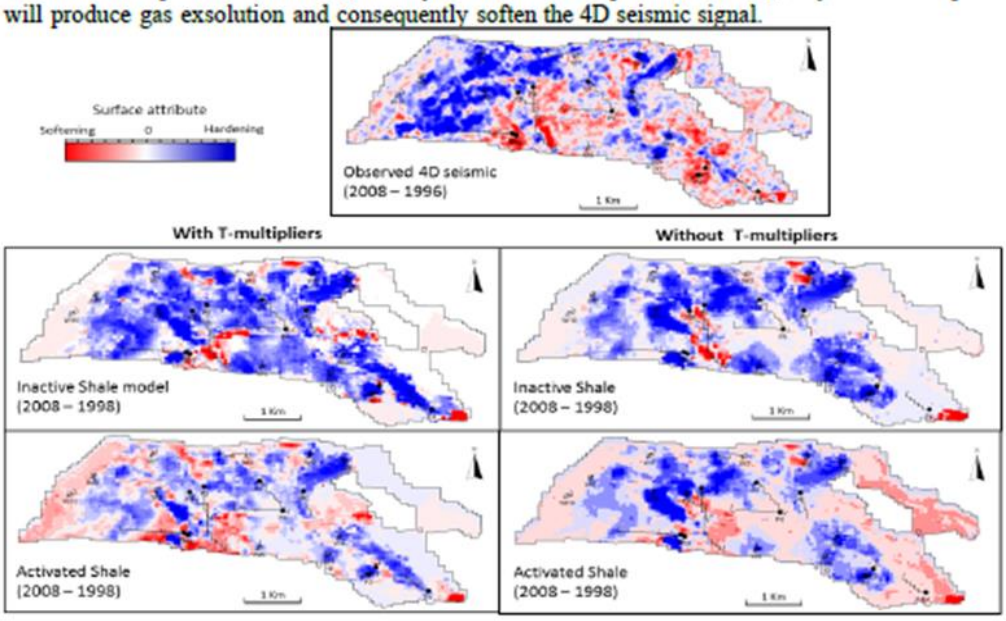

Figure 3 Comparison between observed and synthetic 4D seismic response (differences between RMS Amplitudes from 1998 and 2008).

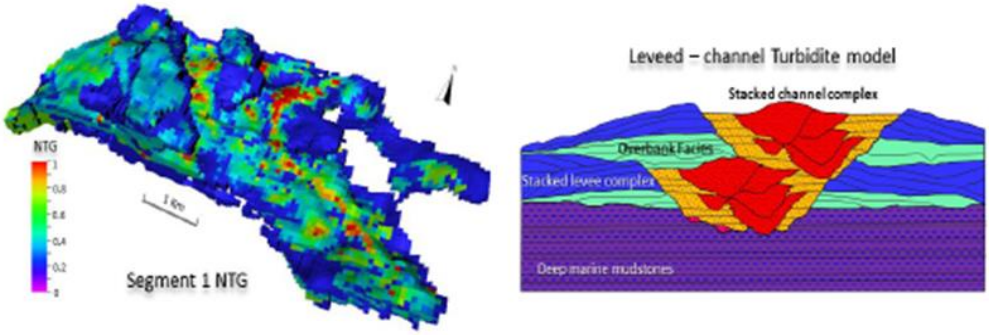

Figure 4 Left: net to gross distribution in the segment of our study. Right: schematic model of a levee – channel turbidite model.

Conclusions

The reservoir-related shales in the UKCS field studied indicate clear dynamic behavior. Their activation improves model fit to the 4D seismic data and helps to understand the reservoir connectivity by reducing the dependence on transmissivity multipliers inserted into the simulation model. Shale characterization provides a more accurate modelling of the synthetic seismic data. The specific pressure conditions of our field and the geometric relationships between the shale and reservoir sands, mean that shale pressure diffusion has a strong impact and is immediately visible via the process of gas exolution. Shales can therefore impact the distribution and polarity of the 4D seismic response and its consequent interpretation.

Acknowledgments

We thank BP and partners for providing the field dataset and permission to publish this paper, also we thank to all the sponsors of the Edinburgh Time Lapse Project, Phase V and VI, for their support (BG, BP, Chevron, CGG, ConocoPhillips, ENI, ExxonMobil, Hess, Ikon Science, Landmark, Maersk, Nexen, Norsar, RSI, Petoro, Petrobras, Shell, Statoil, Suncor, Taqa, TGS and Total). Thanks are extended to Schlumberger for provision of the Petrel and Eclipse software.

References

Leach, H., Herbert, N., Los, A. and Smith, R. [1999] The Schiehallion development. Petroleum Geology of Northwest Europe. *Proceedings of the 5th Conference*. Geological Society, London, 683-692.

MacBeth, C. [2004] A classification for the pressure-sensitivity properties of a sandstone rock frame. *Geophysics*, **69**(2), 497-510.

MacBeth, C., HajNasser, Y., Stephen, K. and Gardiner, A. [2011] Exploring the effect of meso - scale shale beds on a reservoir's overall stress sensitivity to seismic waves. *Geophysical Prospecting*, **59**(1), 90-110.

Sigal, R.F. [2013] Mercury capillary pressure measurements on Barnett core. *SPE Reservoir Evaluation & Engineering*, **16**(04), 432-442.

Yang, Y. and Aplin, A. C. [2007] Permeability and petrophysical properties of 30 natural mudstones. *Journal of Geophysical Research: Solid Earth (1978-2012)*, **112**(B3).

References

Addis, M., X. Choi, and J. Gunning (1998), *The influence of the reservoir stress-depletion response on the lifetime considerations of well completion design*. SPE/ISRM Rock Mechanics in Petroleum Engineering, SPE.

Allen, J. (2012), *Principles of physical sedimentology*, Springer Science & Business Media.

Amini, H. (2014), *A pragmatic approach to Simulator to Seismic Modelling for 4D sismic interpretation*, PhD Thesis, Heriot-Watt University.

Anderson, A. V., D. K. Sickafoose, T. R. Fahrer, and R. R. Gottschalk (2012), *Interaction of Oligocene–Miocene deep-water depositional systems with actively evolving structures: The Lower Congo Basin, offshore Angola*. AAPG Special Volumes 2012.

Arain, A. H. (2015), *Theoretical study of Osmotic and Swelling Pressures with Experimental Investigation of Threshold Capillary Pressure in Shales*. Master Thesis, Norges Teknisk-Naturvitenskapelige Universitet.

Asef, M., and M. Farrokhrouz (2013), *Shale engineering: Mechanics and mechanisms*, CRC Press.

Asquith, G. B., D. Krygowski, and C. R. Gibson (2004), *Basic well log analysis*, AAPG Tulsa, OK.

Beaubouef, R. (2004), *Deep-water leveed-channel complexes of the Cerro Toro Formation, Upper Cretaceous, southern Chile*, AAPG bulletin, 88(11), 1471-1500.

Bell, R., C. Jackson, G. Elliott, R. Gawthorpe, I. R. Sharp, and L. Michelsen (2014), *Insights into the development of major rift-related unconformities from geologically constrained subsidence modelling: Halten Terrace, offshore mid Norway*, Basin Research, 26(1), 203-224.

Bhuyan, K., and Q. Passey (1994), Clay estimation from GR and neutron-density porosity logs, paper presented at SPWLA 35th Annual Logging Symposium, Society of Petrophysicists and Well-Log Analysts.

Biscaye, P. E. (1965), *Mineralogy and sedimentation of recent deep-sea clay in the Atlantic Ocean and adjacent seas and oceans*, Geological Society of America Bulletin, 76(7), 803-832.

Boggs, S. (2006), *Principles of sedimentology and stratigraphy*, Pearson Prentice Hall.

Bouchet, R., B. Levallois, G. Mfonfu, and J.-F. Authier (2004), *Girassol field optimized development*, paper presented at AAPG International conference, October.

Bouma, A. H., P. H. Kuenen, and F. P. Shepard (1962), *Sedimentology of some flysch deposits: a graphic approach to facies interpretation*, Elsevier Amsterdam.

Box, G. E., J. S. Hunter, and W. G. Hunter (2005), *Statistics for experimenters: design, innovation, and discovery*, Wiley-Interscience New York.

Brace, W. F., J. Walsh, and W. Frangos (1968), *Permeability of granite under high pressure*, Journal of Geophysical research, 73(6), 2225-2236.

Calvert, R. (2005), *Insights and methods for 4D reservoir monitoring and characterization*. SEG 2005 Distinguished Instructor Short Course.

Castagna, J. P., M. L. Batzle, and R. L. Eastwood (1985), *Relationships between compressional-wave and shear-wave velocities in clastic silicate rocks*, Geophysics, 50(4), 571-581.

Chen, J. a., and T. Larson (2013), *Modeling Net-to-gross in Deepwater Reservoirs*, paper presented at EAGE Annual Conference & Exhibition incorporating SPE Europec, SPE.

Chitale, D. V. (2009), *Simplified and More Accurate Clay Typing Enhances the Value Added by Petrophysical Evaluation of Shale and Tight Gas Sand Plays*, AAPG Convention Denver, Colorado.

Clavier, C., W. Hoyle, and D. Meunier (1971), *Quantitative interpretation of thermal neutron decay time logs: part I. Fundamentals and techniques*, Journal of Petroleum Technology, 23(06), 743-755.

Crank, J. (1975), *The Mathematics of Diffusion: 2d Ed*, Clarendon Press.

Da Fontoura, S., E. Muniz, and R. Lomba (2007), *Pressure diffusion and ion diffusion properties of terciary shales*, paper presented at 11th ISRM Congress, International Society for Rock Mechanics.

Dalland, A., Augedahl, H. O., Bomstad, K., &, and K. Ofstad (1988), *The Post-Triassic Succession of the mid-Norwegian Shelf. Lithostratigraphic scheme for the Mesozoic and Cenozoic succession offshore mid- and northern Norway*, NPD Bulletin(4), 5-42.

Davies, D., and K. G. Maver (2004), *4d time-lapse studies and reservoir simulation to seismic modeling*, paper presented at Offshore Technology Conference, Offshore Technology Conference.

De Gennaro, S., P. Schutjens, M. Frumau, M. Fuery, J. Ita, and P. Fokker (2010), *The Role of Geomechanics in the Development of an HPHT Field*, paper presented at 44th US Rock Mechanics Symposium and 5th US-Canada Rock Mechanics Symposium, American Rock Mechanics Association, Salt Lake City, UT, USA.

Deegan, C., and J. Scull (1977), *A proposed standard lithostratigraphic nomenclature for the central and Northern North-Sea:* Bull, NPD(1).

Dewan, J. T. (1983), *Essentials of modern open-hole log interpretation*, PennWell Books.

Dewhurst, D., A. Siggins, U. Kuila, M. Clennell, M. Raven, and H. Nordgard-Bolas (2008), *Elastic, geomechanical and petrophysical properties of shales*, paper presented at The 42nd US Rock Mechanics Symposium (USRMS), American Rock Mechanics Association.

Dvorkin, J., and A. Nur (1998), *Time-average equation revisited,* Geophysics, 63(2), 460-464.

Egbele, E., I. Ezuka, and M. Onyekonwu (2005), *Net-To-Gross Ratios: implications in integrated reservoir management studies,* paper presented at Nigeria Annual International Conference and Exhibition, SPE.

Eggenberger, K., D. Hill, D. Lowden, S. Sonika, and M. Paydayesh (2015), *High-Fidelity 4D Forward Modelling as part of a Redefined Closed-Loop Seismic Reservoir Monitoring Framework: A Case Study,* paper presented at 2015 SEG Annual Meeting
.
Erratt, D., G. Thomas, N. Hartley, R. Musum, P. Nicholson, and Y. Spisto (2010), *North Sea hydrocarbon systems: some aspects of our evolving insights into a classic hydrocarbon province,* paper presented at Geological Society, London, Petroleum Geology Conference series, Geological Society of London.

Fagel, N. (2007), *Clay minerals, deep circulation and climate,* Developments in marine geology, 1, 139-184.

Fam, M., and M. Dusseault (1998), *Borehole stability in shales: a physico-chemical perspective,* paper presented at SPE/ISRM Rock Mechanics in Petroleum Engineering, SPE.

Gassmann, F. (1951), *Elastic waves through a packing of spheres,* Geophysics, 16(4), 673-685.

Geertsma, J. (1973), *Land subsidence above compacting oil and gas reservoirs*, Journal of Petroleum Technology, 25(06), 734-744.

Gilham, R., C. Hercus, A. Evans, and W. De Haas (2005), *Shearwater (UK Block 22/30b): managing changing uncertainties through field life,* paper presented at Geological Society, London, Petroleum Geology Conference series, Geological Society of London.

Gonzalez-Carballo, A., P.-Y. Guyonnet, B. Levallois, A. Veillerette, and R. Deboiasne (2006), *Repeated 4D Monitoring of the Girassol Field (Angola): Impact on Reservoir Understanding and Economics,* paper presented at Offshore Technology Conference, Offshore Technology Conference.

Grasso, J.-R. (1992), *Mechanics of seismic instabilities induced by the recovery of hydrocarbons,* Pure and Applied Geophysics, 139(3-4), 507-534.

HajNasser, Y. (2012), *The implications of shale geomechanics and pressure diffusion for 4D interpretation,* PhD Thesis, Heriot-Watt University.

Haldorsen, H. H., and L. W. Lake (1984), *A new approach to shale management in field-scale models,* Society of Petroleum Engineers Journal, 24(04), 447-457.

Harris, N. B. (1989), *Reservoir geology of Fangst Group (Middle Jurassic), Heidrun Field, offshore Mid-Norway,* AAPG Bulletin, 73(11), 1415-1435.

Hatchell, P., and S. Bourne (2005), *Rocks under strain: Strain-induced time-lapse time shifts are observed for depleting reservoirs,* The Leading Edge, 24(12), 1222-1225.

Hatchell, P., A. Van Den Beukel, M. Molenaar, K. Maron, C. Kenter, J. Stammeijer, J. Van Der Velde, and C. Sayers (2003), *Whole earth 4D: Reservoir monitoring geomechanics,* paper presented at 73rd SEG Meeting, Dallas, USA, Expanded Abstracts.

Herwanger, J. V., and S. A. Horne (2009), *Linking reservoir geomechanics and time-lapse seismics: Predicting anisotropic velocity changes and seismic attributes,* Geophysics, 74(4), W13-W33.

Hettema, M., P. Schutjens, B. Verboom, and H. Gussinklo (1998), *Production-induced compaction of sandstone reservoirs: the strong influence of field stress*, paper presented at European Petroleum Conference, SPE.

Hoeber, H., D. Lecerf, H. Zaghouani, and D. Whitcombe (2005), *Matching of multiple time-lapse data using multi-coherence analysis,* paper presented at 67th EAGE Conference & Exhibition.

Hooson, W. (1747), *The Miners Dictionary*, W. Hooson and T. Payne.

Hornby, B. E. (1998), *Experimental laboratory determination of the dynamic elastic properties of wet, drained shales,* Journal of Geophysical Research: Solid Earth, 103(B12), 29945-29964.

Horsrud, P., R. M. Holt, E. F. Sonstebo, G. Svano, and B. Bostrom (1994), *Time dependent borehole stability: Laboratory studies and numerical simulation of different mechanisms in shale,* paper presented at Rock Mechanics in Petroleum Engineering, SPE.

Johnston, D. H. (2013), *Practical applications of time-lapse seismic data,* Distinguished Instructor Short Course, SEG, 16, 270.

Keller, L. (2014), *Pore Space Relevant of Gas Transport in Opalinus Clay-Homogeneity, Percolation and Capillary Properties,* paper presented at Fourth EAGE Shale Workshop.

Kloosterman, H., R. Kelly, J. Stammeijer, M. Hartung, J. Van Waarde, and C. Chajecki (2003), *Successful application of time-lapse seismic data in Shell Expro's Gannet Fields, Central North Sea, UKCS,* Petroleum Geoscience, 9(1), 25-34.

Kragh, E., and P. Christie (2002), *Seismic repeatability, normalized rms, and predictability,* The Leading Edge, 21(7), 640-647.

Landrø, M., O. A. Solheim, E. Hilde, B. O. Ekren, and L. K. Strønen (1999), *The Gullfaks 4D seismic study,* Petroleum Geoscience, 5(3), 213-226.

Lapierre, C., S. Leroueil, and J. Locat (1990), *Mercury intrusion and permeability of Louiseville clay,* Canadian Geotechnical Journal, 27(6), 761-773.

Larionov, V. (1969), *Borehole radiometry,* Nedra, Moscow.

Lasocki, J., J. Guemene, A. Hedayati, C. Legorjus, and W. Page (1999), *The Elgin and Franklin fields: UK Blocks 22/30c, 22/30b and 29/5b*, paper presented at Geological Society, London, Petroleum Geology Conference series, Geological Society of London.

Leach, H., N. Herbert, A. Los, and R. Smith (1999), *The Schiehallion development*, paper presented at Geological Society, London, Petroleum Geology Conference series, Geological Society of London.

Lisitzin, A. (1996), *Oceanic Sedimentation–Lithology and Sedimentation*, American Geophysical Union, Washington.

Lumley, D. E. (2001), *Time-lapse seismic reservoir monitoring*, Geophysics, 66(1), 50-53.

Lumley, D. E. (2004), *Business and technology challenges for 4D seismic reservoir monitoring*, The Leading Edge, 23(11), 1166-1168.

MacBeth, C. (2004), *A classification for the pressure-sensitivity properties of a sandstone rock frame*, Geophysics, 69(2), 497-510.

MacBeth, C., Y. HajNasser, K. Stephen, and A. Gardiner (2011), *Exploring the effect of meso-scale shale beds on a reservoir's overall stress sensitivity to seismic waves*, Geophysical Prospecting, 59(1), 90-110.

MacLellan, A., P. Rowbotham, R. Rogers, and J. Millington (2006), *Integrated 3D/4D structural and stratigraphic interpretation on Nelson accounts for variable fluid contact levels*, paper presented at 68th EAGE Conference & Exhibition.

Marsh, N., J. Imber, R. Holdsworth, P. Brockbank, and P. Ringrose (2010), *The structural evolution of the Halten Terrace, offshore Mid-Norway: extensional fault growth and strain localisation in a multi-layer brittle–ductile system*, Basin Research, 22(2), 195-214.

Mavko, G., T. Mukerji, and J. Dvorkin (2009), *The rock physics handbook: Tools for seismic analysis of porous media*, Cambridge university press.

Mbia, E. N., I. L. Fabricius, P. Frykman, A. Krogsbøll, and F. Dalhoff (2014), *Quantifying Porosity, Compressibility and Permeability in Shale*, paper presented at Fourth EAGE Shale Workshop.

Meysman, F. J., J. J. Middelburg, and C. H. Heip (2006), *Bioturbation: a fresh look at Darwin's last idea*, Trends in Ecology & Evolution, 21(12), 688-695.

Morton, A., C. Hallsworth, D. Strogen, A. Whitham, and M. Fanning (2009), *Evolution of provenance in the NE Atlantic rift: the Early–Middle Jurassic succession in the Heidrun Field, Halten Terrace, offshore Mid-Norway*, Marine and Petroleum Geology, 26(7), 1100-1117.

Olden, P., P. Corbett, R. Westerman, J. Somerville, B. Smart, and N. Koutsabeloulis (2001), *Modeling combined fluid and stress change effects in the seismic response of a producing hydrocarbon reservoir*, The Leading Edge, 20(10), 1154-1163.

Pang, J., J. Zuo, D. Zhang, and L. Du (2013), *Effect of porous media on saturation pressures of shale gas and shale oil*, paper presented at IPTC 2013: International Petroleum Technology Conference.

Park, C. B., R. D. Miller, D. W. Steeples, and R. A. Black (1996), *Swept impact seismic technique (SIST)*, Geophysics, 61(6), 1789-1803.

Pedersen, T., J. Harms, N. Harris, R. Mitchell, and K. Tooby (1989), *The role of correlation in generating the Heidrun Field geological model*, in Correlation in Hydrocarbon exploration, edited, pp. 327-338, Springer.

Petschick, R., G. Kuhn, and F. Gingele (1996), *Clay mineral distribution in surface sediments of the South Atlantic: sources, transport, and relation to oceanography*, Marine Geology, 130(3), 203-229.

Potter, P. E., J. B. Maynard, and P. J. Depetris (2005), *Mud and mudstones: Introduction and overview*, Springer Science & Business Media, Berlin Germany.

Potter, P. E., J. B. Maynard, and W. A. Pryor (1980), *Sedimentology of shale*, Springer Science & Business Media.

Prasad, M., T. Mukerji, M. Reinstaedler, and W. Arnold (2009), *Acoustic signatures, impedance microstructure, textural scales, and anisotropy of kerogen-rich shales*, paper presented at SPE annual technical conference and exhibition, SPE

Rangel, R., and C. MacBeth (2015), *The Role of Shale Pressure Diffusion in 4D Seismic Reservoir Monitoring–Case Studies*, paper presented at 2015 SEG Annual Meeting, SEG.

Rattey, R., and A. Hayward (1993), *Sequence stratigraphy of a failed rift system: the Middle Jurassic to Early Cretaceous basin evolution of the Central and Northern North Sea*, paper presented at Geological Society, London, Petroleum Geology Conference series, Geological Society of London.

Ricard, L. P., C. MacBeth, Y. HajNasser, and P. Schutjens (2012), *An evaluation of pore pressure diffusion into a shale overburden and sideburden induced by production-related changes in reservoir fluid pressure*, Journal of Geophysics and Engineering, 9(3), 345.

Rickett, J., L. Duranti, T. Hudson, B. Regel, and N. Hodgson (2007), *4D time strain and the seismic signature of geomechanical compaction at Genesis*, The Leading Edge, 26(5), 644-647.

Rider, M., and Kennedy M. (2013), *The Geological Interpretation of well logs*, Third ed., Rider-French Consulting Ltd. , Glasgow - UK.

Roggero, F., O. Lerat, D. Y. Ding, P. Berthet, C. Bordenave, F. Lefeuvre, and P. Perfetti (2012), *History Matching of Production and 4D Seismic Data: Application to the Girassol Field, Offshore Angola*, Oil & Gas Science and Technology–Revue d'IFP Energies nouvelles, 67(2), 237-262.

Ruud, B. O., M. Jakobsen, and T. A. Johansen (2003), *Seismic properties of shales during compaction*, paper presented at 2003 SEG Annual Meeting, SEGs.

Saputra, I. (2008), *Shale Volume Calculation,* CCGVeritas Technical Report.

Sayers, C. (2010), *Geophysics under stress: Geomechanical applications of seismic and borehole acoustic waves,* SEG DISC.

Sayers, C., and D. Dewhurst (2008), *Introduction to this special section—Shale geophysics,* The Leading Edge, 27(6), 736-737.

Schieber, J., W. Zimmerle, and P. S. Sethi (1998), *Shales and Mudstones,* Vols. I and II.

Schön, J. (2011), *Physical properties of rocks: A workbook*, Elsevier.

Séranne, M. (1999), *Early Oligocene stratigraphic turnover on the west Africa continental margin: a signature of the Tertiary greenhouse-to-icehouse transition?,* Terra Nova-Oxford, 11(4), 135-140.

Serra, O. (2008), *Well logging handbook*, Editions Technip.

Sigal, R. F. (2013), *Mercury capillary pressure measurements on Barnett core,* SPE Reservoir Evaluation & Engineering, 16(04), 432-442.

Simpson, J., and H. Dearing (2000), *Diffusion Osmosis-An unrecognized cause of shale instability*, paper presented at IADC/SPE Drilling Conference, SPE.

Singh, P., R. Slatt, G. Borges, R. Perez, R. Portas, K. Marfurt, M. Ammerman, and W. Coffey (2009), *Reservoir characterization of unconventional gas shale reservoirs: example from the Barnett Shale, Texas, USA.* AAPG, The shale Shaker, Vol. 60.

Sondergeld, C. H., and C. S. Rai (2011), *Elastic anisotropy of shales,* The Leading Edge, 30(3), 324-331.

Staples, R., A. Cook, J. Braisby, B. Hodgson, and A. Mabillard (2006), *Integration of 4D seismic data and the dynamic reservoir model reveal new targets in Gannet C,* The Leading Edge, 25(9), 1126-1133.

Stieber, S. (1970), *Pulsed Neutron Capture Log Evaluation-Louisiana Gulf Coast,* paper presented at Fall Meeting of the SPE of AIME, SPE.

Thambynayagam, M. (2011), *The Diffusion Handbook: Applied Solutions for Engineer*s *by RK.*

Thomsen, L. (1986), *Weak elastic anisotropy,* Geophysics, 51(10), 1954-1966.

Tourtelot, H. A. (1960), *Origin and use of the word "shale*", American Journal of Science, 258, 335-343.

Vermeer, G. J. (2003), *3D seismic survey design optimization,* The Leading Edge, 22(10), 934-941.

Vernik, L., and A. Nur (1992), *Ultrasonic velocity and anisotropy of hydrocarbon source rocks,* Geophysics, 57(5), 727-735.

Walia, R. (2004), *Time Lapse Processing for Reservoir Characterization,* paper presented at PGCE 2004.

Wei, M.-q., Y.-g. Duan, Q.-t. Fang, R. Wang, B.-m. Yu, and C.-s. Yu (2013), *Mechanism model for shale gas transport considering diffusion, adsorption/desorption and Darcy flow,* Journal of Central South University, 20, 1928-1937.

Whitcombe, D., P. Paramo, N. Philip, A. Toomey, T. Redshaw, and S. Linn (2010), *The Correlated Leakage Method–It's Application to Better Quantify Timing Shifts on 4D Data,* paper presented at 72nd EAGE Conference and Exhibition incorporating SPE EUROPEC 2010.

Winefield, P., R. Gilham, and R. Elsinger (2005), *Plumbing the depths of the Central Graben: towards an integrated pressure, fluid and charge model for the Central North Sea HPHT play*, paper presented at Geological Society, London, Petroleum Geology Conference series, Geological Society of London.

Worthington, P. F. (2010), *Net Pay--What Is It? What Does It Do? How Do We Quantify It? How Do We Use It?,* SPE Reservoir Evaluation & Engineering, 13(05), 812-822.

Wu, P., and R. Aguilera (2013), *Uncertainty Analysis of Shale Gas Simulation: Consideration of Basic Petrophysical Properties,* paper presented at SPE Unconventional Resources Conference Canada, SPE.

Yang, Y., and A. C. Aplin (2007), *Permeability and petrophysical properties of 30 natural mudstones,* Journal of Geophysical Research: Solid Earth (1978–2012), 112(B3).

Ziegler, P. A. (1988), *Evolution of the Artic-North Atlantic and the Western Tethys - a visual interpretattion of a series of Paleogeographic - Paleotectonic maps,* AAPG memoir, 43, 164-196.